Alma Mater Studiorum - Università di Bologna

DOTTORATO DI RICERCA IN

CHIMICA

Ciclo 34

**Settore Concorsuale:** 03/A2 - MODELLI E METODOLOGIE PER LE SCIENZE CHIMICHE

**Settore Scientifico Disciplinare:** CHIM/02 - CHIMICA FISICA

# SIMULATION OF PHOTOINDUCED PROCESSES IN ORGANIC CHROMOPHORES: MAPPING PHOTOCHEMICALLY RELEVANT STATES FOR ACCURATE DYNAMICS

**Presentata da:** Flavia Aleotti

**Coordinatore Dottorato**

Luca Prodi

**Supervisore**

Marco Garavelli

**Co-supervisore**

Elisabetta Venuti

**Esame finale anno 2022**

# Contents

# Abstract

The simulation of ultrafast photoinduced processes is a fundamental step towards the understanding of the underlying molecular mechanism and interpretation or prediction of experimental data. Indeed, dynamics simulations is at present the only way to visualise the motion of the system perturbed out of equilibrium by the absorption of light. Performing a computer simulation of a complex photoinduced process is only possible introducing some approximations (e.g. the classical treatment of the nuclei and the stochastic non adiabatic events in mixed quantum/classical dynamics or the reduction of the number of degrees of freedom and/or simplification of the energy profiles to low order terms of a series expansion in quantum dynamics). In order to obtain reliable results, the need to reduce the complexity must balance with the accuracy of the model, which should include all the relevant degrees of freedom and a quantitatively correct description of all the electronic states involved in the process.

This work presents new computational protocols and strategies for the parameterisation of accurate models for photochemical/photophysical processes based on state-of-the-art multiconfigurational wavefunction-based methods. The required ingredients for a dynamics simulation include potential energy surfaces (PESs) as well as interstate couplings between the electronic states, which must be mapped across a wide range of geometries. Indeed, due to kinetic energy, the nuclear wavepacket/trajectory may explore regions quite far from ground and excited states equilibrium structures during the propagation. The developed procedures allow to obtain solid and extended databases reducing as much as possible the computational cost, thanks to, e.g., specific tuning of the level of theory for different PES regions and/or direct calculation of only the needed components of vectorial quantities (like gradients or non adiabatic couplings, NACs).

The presented approaches were applied to three case studies, all requiring an accurate parameterisation but for different reasons, i.e. (a) the need to simulate transient experiments based on wavepacket propagation (azobenzene), (b) the delicate interplay of a large number of excited states of different nature (pyrene) and (c) the presence of a complex environment (visual rhodopsin). The resulting models and simulations allowed to elucidate the mechanism and time scale of the internal conversion, reproducing or even predicting new transient experiments. The general applicability of the developed protocols to systems with different peculiarities and the possibility to parameterise different types of dynamics on an equal footing (classical vs purely quantum) prove that the developed procedures are flexible enough to be tailored for each specific system, and pave the way for exact quantum dynamics with multiple degrees of freedom.

# Chapter 1

# Introduction

Light is the main source of energy for life on Earth. Sunlight photons reaching our planet trigger a number of fundamental processes for life like plant photosynthesis or stratospheric ozone production. This is made possible by the ability of some molecules to absorb its energy and transform it into e.g. chemical or mechanical energy. The study of such light-induced processes is the central topic of photochemistry and photophysics. A deep insight into the molecular mechanisms initiated by light absorption is indeed fundamental not only to improve our knowledge on natural processes, but also to suggest strategies to improve or exploit them to perform useful tasks.

An experimental study of a photoinduced physical or chemical process requires the use of a light pulse of proper wavelength to excite the sample and some techniques to retrieve information about the populated excited state(s). The simplest example is probably given by linear absorption spectroscopy, in which the change in the incident light intensity is measured as a function of frequency/wavelength to obtain information about the energy of the absorbed light, i.e. the energy of the photoexcited state(s). Many more sophisticated experimental techniques exist, relying on the use of multiple pulses interacting with the sample at precisely controlled time delays, which allow to determine excited state properties and/or to keep track of their evolution in time. The major hurdle in the experimental study of photoinduced processes is however given by their ultrafast timescales. Indeed, molecular motions triggered by light absorption take place in the femto- to picosecond regime ($10^{-15}$-$10^{-12}$ s), while modifications in the electron density surrounding the atoms nuclei are even faster ($10^{-18}$ s). In particular, the ultrafast deactivation of excited states is typically driven by the so called conical intersections[1, 2], i.e. points of degeneracy between the potential energy surfaces of different electronic states sharing the same spin multiplicity, where population transfer between them is extremely rapid and efficient. Such points acts as special transition states for photochemical reactions and are found with unsuspected frequency, eventually acting as population funnels driving the photoinduced processes. Following the ultrafast nuclear dynamics in real time (e.g bond breaking and formation) requires sufficient time resolution to sample the signatures of the atomic motions and, despite the tremendous progress in the generation of femto- or even attosecond laser pulses[3–5], interpretation of experimental spectra as well as a full understanding of the underlying mechanisms cannot yet prescind from a computational study. In addition, experiments do not directly observe the geometrical/conformational changes of molecules, but rather record the temporal change of observables which are functions of the molecular deformations. Their interpretation would require knowledge of the electronic structure of the system as a function of the dynamics, that can only be accessed through quantum mechanical calculations. Computational quantum chemistry tools allow to obtain excited states energies and other fundamental properties by solving the Schrödinger equation at some level of approximation, yielding valuable insights into the topology of the electronic potential energy surfaces as a function of nuclear coordinates (e.g. conical intersections, barrier heights, ground state products etc.). However, the characterisation of crossing and stationary points is often not enough to predict or explain the outcome of a photoprocess, as this is intrinsically a dynamic event due to the effect of kinetic energy that, in a real experiment, can drive the molecular system away from such geometries. In these cases, nuclear dynamics simulations can be performed at various level of approximation to reproduce the time evolution of the system based on quantum chemistry data. This is the ultimate and, in principle, most reliable description of a photoinduced chemical process.

In my three-years research activity I have focused on the development of accurate models for the simulation of photoactive molecules using state-of-the-art multireference perturbative electronic structure methods such as complete or restricted active space second order perturbation theory (CASPT2[6] or RASPT2[7]) in its different flavours. The final aim was to develop new protocols and smart strategies to produce all the necessary data for the simulation of photoinduced processes. The developed strategies can be tailored for the parameterisation of different kinds of non adiabatic dynamics (i.e. dynamics involving the passage through different electronic states via their conical intersections): from classical molecular dynamics based on Newton's equations for the nuclear motion to purely quantum dynamics in which all particles in the system obey the time-dependend Schrödinger equation. The calculation of potential energy surfaces and all the needed interstate couplings over the wide range of geometries that can be explored during a dynamics can be computationally very demanding, and I have worked on the development of ad-hoc strategies to produce highly accurate sets of data at a fair computational cost. This involves a careful selection of the fundamental coordinates describing the molecular motion (as well as their faithful representation in terms of atomic displacements) and the development of computational tools to reduce as much as possible the cost associated with the accurate multireference perturbative methods employed (e.g. through direct computation of vectorial components along the pre-selected reactive coordinates).

This work is organised as follows: the basic theoretical concepts of the applied methods are introduced in Chapter 2, while Chapter 3 explains the developed computational strategies for the parameterisation of model potential energy surfaces (PESs) and couplings for photoactive systems. Following, the results of the application of such strategies to three compounds are presented. Chapter 4 is dedicated to the study of azobenzene, a simple chromophore undergoing *cis-trans* photoisomerization that has extensively been studied for applications as a molecular photoswitch (i.e. a type of molecule that can change its structural geometry and physical/chemical properties upon light irradiation). Our protocol allowed to run the quantum dynamics of its photoinduced isomerization process and gain better insight into its longly debated isomerization mechanism as well as to simulate transient diffraction and spectroscopy experiments with unprecedented accuracy. Moreover, we have also investigated the effect of chemical substitution on azobenzene, and how it could alter the photochemical outcome. In Chapter 5, a new parameterisation protocol for a linear vibronic coupling (LVC) model for quantum dynamics based on multiconfigurational electronic structure methods is presented and successfully applied to the pyrene molecule and its complex photophysics. Eventually, Chapter 6 shows the application of our modelling strategies to a more complicated and realistic case including environment effects: the retinal chromophore inside rhodopsin, a light-sensitive protein of the retina whose structural change upon irradiation is the first step in the process of vision. We mapped potential energy surfaces and electronic state couplings of different types along reactive coordinates taking into account the effect of the protein embedding through hybrid quantum mechanics/molecular mechanics (QM/MM) scheme[8]. Such an accurate and extended database has never been reported before, and paves the road to to future dynamics simulations of this fascinating system.

## References

[1] M. Garavelli, "Computational Organic Photochemistry: Strategy, Achievements and Perspectives," *Theoretical Chemistry Accounts*, vol. 116 (1-3), pp. 87–105, **2006**.

[2] D. R. Yarkony, "Diabolical conical intersections," *Reviews of Modern Physics*, vol. 68, pp. 985–1013, 4 **1996**.

[3] T. Popmintchev, M.-C. Chen, P. Arpin, M. M. Murnane, and H. C. Kapteyn, "The attosecond nonlinear optics of bright coherent X-ray generation," *Nature Photonics*, vol. 4 (12), pp. 822–832, **2010**.

[4] K. Ramasesha, S. R. Leone, and D. M. Neumark, "Real-Time Probing of Electron Dynamics Using Attosecond Time-Resolved Spectroscopy," *Annual Review of Physical Chemistry*, vol. 67 (1), pp. 41–63, **2016**.

[5] F. Zamponi, Z. Ansari, M. Woerner, and T. Elsaesser, "Femtosecond powder diffraction with a laser-driven hard X-ray source," *Optics Express*, vol. 18 (2), pp. 947–961, **2010**.

[6] K. Andersson, P. A. Malmqvist, B. O. Roos, A. J. Sadlej, and K. Wolinski, "Second-order perturbation theory with a CASSCF reference function," *The Journal of Physical Chemistry*, vol. 94 (14), pp. 5483–5488, **1990**.

[7] V. Sauri, L. Serrano-Andrés, A. R. M. Shahi, L. Gagliardi, S. Vancoillie, and K. Pierloot, "Multiconfigurational Second-Order Perturbation Theory Restricted Active Space (RASPT2) Method for Electronic Excited States: A Benchmark Study," *Journal of Chemical Theory and Computation*, vol. 7 (1), pp. 153–168, **2011**.

[8] A. Warshel and M. Levitt, "Theoretical studies of enzymic reactions: Dielectric, electrostatic and steric stabilization of the carbonium ion in the reaction of lysozyme," *Journal of Molecular Biology*, vol. 103 (2), pp. 227–249, **1976**.

# Chapter 2

# Theoretical Background

External stimuli (such as light) perturb instantly (i.e. on the attosecond timescale, $10^{-18}$ s) the electron density of a system bringing it out of equilibrium, in a process known as excitation. As a consequence, the heavier (and thus slower) nuclei respond to the perturbed electronic density in the femtosecond regime ($10^{-15}$ s), initiating vibrational dynamics. The aim of this thesis is to show how it is possible to model and simulate photochemical and photophysical processes taking place in the femtosecond timescale. These involve the interaction of light with the electrons of a molecular system, therefore, quantum chemical methods are the necessary tool to get an accurate description of the system. The basis of quantum mechanics is the time-dependent Schrödinger equation (TDSE):

$$i\hbar\frac{\partial}{\partial t}\Psi(\mathbf{r},\mathbf{R},t) = \hat{H}\,\Psi(\mathbf{r},\mathbf{R},t) \tag{2.1}$$

where $\Psi(\mathbf{r},\mathbf{R},t)$ is the wavefunction bearing all the information about the system, that depends on the coordinates of the electrons $\mathbf{r}$ and nuclei $\mathbf{R}$ and on the time $t$. $\hat{H}$ is the Hamiltonian operator

$$\hat{H} = -\frac{\hbar^2}{2m}\nabla^2 + V \tag{2.2}$$

The potential $V$ in equation (2.2) can in general depend on time, however, for a freely evolving system, $\hat{H}$ is generally assumed to be time-independent, and consists of the sum of kinetic and potential terms:

$$\hat{H} = \underbrace{-\sum_{\alpha}\frac{\hbar^2}{2m_\alpha}\nabla^2_{\mathrm{N},\alpha}}_{\hat{T}_\mathrm{N}} \underbrace{-\sum_{i}\frac{\hbar^2}{2m_\mathrm{e}}\nabla^2_{e,i}}_{\hat{T}_\mathrm{e}} \underbrace{-\sum_{\alpha,i}\frac{Z_\alpha e^2}{R_{\alpha i}}}_{\hat{V}_\mathrm{eN}} + \underbrace{\sum_{\alpha,\beta}\frac{Z_\alpha Z_\beta e^2}{R_{\alpha\beta}}}_{\hat{V}_\mathrm{N}} + \underbrace{\sum_{i,j}\frac{e^2}{r_{ij}}}_{\hat{V}_\mathrm{e}} \tag{2.3}$$

where $i$, $j$ label the electrons, $\alpha$, $\beta$ the nuclei, $m_\alpha$, $m_\mathrm{e}$ are the masses of nucleus $\alpha$ and of the electron, respectively, $Z_\alpha$, is the atomic number of nucleus $\alpha$ and $e$ is the electronic charge in Coulomb. The first two terms in equation (2.3) account for the kinetic energy of nuclei ($\hat{T}_\mathrm{N}$) and electrons ($\hat{T}_\mathrm{e}$), respectively, the third terms gives the electron-nuclear attraction ($\hat{V}_\mathrm{eN}$) and the last two terms give the nuclear ($\hat{V}_\mathrm{N}$) and electron ($\hat{V}_\mathrm{e}$) repulsion, respectively. Inserting the Hamiltonian of equation (2.3) into TDSE (2.1) yields a partial differential equation, which is generally solved by separation of variables. Thus, we adopt a tentative wavefunction of the form

$$\Psi(\mathbf{r},\mathbf{R},t) = \psi(\mathbf{r},\mathbf{R})\,\theta(t) \tag{2.4}$$

Inserting this trial form into equation (2.1) and dividing both sides by $\psi(\mathbf{r},\mathbf{R})\theta(t)$ yields

$$\frac{i\hbar}{\theta(t)}\frac{\partial}{\partial t}\theta(t) = \frac{\hat{H}\psi(\mathbf{r},\mathbf{R})}{\psi(\mathbf{r},\mathbf{R})} \tag{2.5}$$

The left-hand side of equation (2.5) is a function of time only, while the right-hand side depends only on the spatial coordinates of the electrons and nuclei. The only way for the two terms to be equal for any values of $t$, $\mathbf{r}$ and $\mathbf{R}$ is that they are both equal to the same constant, that we set to $E$, i.e. the energy of the system. In this way, two differential equations are obtained, one for the temporal part:

$$i\hbar\frac{\mathrm{d}}{\mathrm{d}t}\theta(t) = E\,\theta(t) \tag{2.6}$$

and one of the spatial part:

$$\hat{H}\,\psi(\mathbf{r},\mathbf{R}) = E\,\psi(\mathbf{r},\mathbf{R}) \tag{2.7}$$

The solution to equation (2.6) is

$$\theta(t) = \theta(0)\,e^{-\frac{i}{\hbar}Et} = \theta(0)\left[\cos\left(\frac{Et}{\hbar}\right) - i\sin\left(\frac{Et}{\hbar}\right)\right] \tag{2.8}$$

this tells us that the time-evolution of the system is purely oscillatory, since $\theta(t)$ never changes in magnitude. Thus, the total wavefunction

$$\Psi(\mathbf{r},\mathbf{R},t) = \psi(\mathbf{r},\mathbf{R})\,\theta(0)\,e^{-\frac{i}{\hbar}Et} \tag{2.9}$$

differs from $\psi(\mathbf{r},\mathbf{R})$ only by a phase factor of constant magnitude.

Equation (2.7) is not as straightforward to solve, and is called time-independent Schrödinger equation (TISE). It is an eigenvalue equation whose solutions depend on the form of the potential $V$. For bound potentials of molecules (equation (2.3)), physically meaningful solutions exist only for discrete values of E, while for unbound potentials solutions exist over a continuous range of E.

One important feature of the total wavefunction $\Psi(\mathbf{r},\mathbf{R},t)$ shown in equation (2.9) is that the quantity $|\Psi(\mathbf{r},\mathbf{R},t)|^2$, which defines the probability density function, is time independent, as we can easily show:

$$\begin{aligned}
|\Psi(\mathbf{r},\mathbf{R},t)|^2 &= \Psi^\dagger(\mathbf{r},\mathbf{R},t)\,\Psi(\mathbf{r},\mathbf{R},t)\\
&= \psi^\dagger(\mathbf{r},\mathbf{R})\,\theta^\dagger(0)\,e^{\frac{i}{\hbar}Et}\,\psi(\mathbf{r},\mathbf{R})\,\theta(0)\,e^{-\frac{i}{\hbar}Et}\\
&= \psi^\dagger(\mathbf{r},\mathbf{R})\,\psi(\mathbf{r},\mathbf{R})\,\theta^\dagger(0)\,\theta(0)
\end{aligned} \tag{2.10}$$

In contrast to the system wavefunction (which is a mathematical construct), the density of equation (2.10) is an observable. Moreover, by the same reasoning, the expectation value $\int \Psi^\dagger(\mathbf{r},\mathbf{R},t)\,\hat{A}\,\Psi(\mathbf{r},\mathbf{R},t)$ for any time-independent operator $\hat{A}$ is also time-independent.

It is important to stress the fact that the solutions obtained with the trial wavefunction in equation (2.4) (i.e. by space and time variable separation) are only particular solutions of TDSE which, for the property of predicting the expectation values of time-independent observables, are called *stationary states.* A general solution to TDSE is a superposition of stationary states, e.g:

$$\Psi(\mathbf{r}, \mathbf{R}, t) = a\, \psi_E(\mathbf{r}, \mathbf{R})\, \theta_E(0)\, e^{-\frac{i}{\hbar}Et} + b\, \psi_{E'}(\mathbf{r}, \mathbf{R})\, \theta_{E'}(0)\, e^{-\frac{i}{\hbar}E't} \tag{2.11}$$

Indeed, TDSE is a linear differential equation, and any linear combination of solutions will be a solution itself. The linear combination of particular solutions, each with its time-dependent phase factor, induces time dependence in the probability density, which for the simple case of equation (2.11) gives:

$$\begin{aligned} |\Psi(\mathbf{r}, \mathbf{R}, t)|^2 =& |a|^2\, |\psi_E(\mathbf{r}, \mathbf{R})|^2\, |\theta_E(0)|^2 + |b|^2\, |\psi_{E'}(\mathbf{r}, \mathbf{R})|^2\, |\theta_{E'}(0)|^2 + \\ &+ 2\Re\left\{ a^\dagger\, b\, \psi_E^\dagger(\mathbf{r}, \mathbf{R})\, \psi_{E'}(\mathbf{r}, \mathbf{R})\, \theta_E^\dagger(0)\, \theta_{E'}(0)\, e^{-i\frac{(E'-E)t}{\hbar}} \right\} \end{aligned} \tag{2.12}$$

The third term in equation (2.12) arises from interference between the two stationary states and contains all the time dependence of the probability density and other observable quantities. Although the “separated-variable solutions” are stationary, particles in general are not. Systems in equilibrium relax to a stationary state and exhibit no time evolution, while systems perturbed out of their equilibrium (e.g. by interaction with an external stimuli such as light) exist in a superposition of stationary states which gives rise to time evolution, i.e. dynamics.

For the study of the static electronic structure of molecules, time dependence is typically neglected and the main goal is to obtain the stationary states which solve TISE (or a good approximation to them). Such “time-independent methods” are introduced in the next section 2.1, with particular interest in multiconfigurational wavefunction-based methods. On the other hand, when the aim is to describe the time evolution of a system which is not in a stationary state (e.g. dynamics of a molecule undergoing a photoinduced process), time-dependent methods must be applied, which are introduced in section 2.2.

## 2.1 Time-independent methods: electronic structure

For time-independent problems, such as the determination of the electronic structure of a molecule, the phase factor introduced by the temporal part of $\Psi(\mathbf{r}, \mathbf{R}, t)$ is usually neglected, and the starting point is TISE (equation (2.7)). The spatial wavefunction $\psi(\mathbf{r}, \mathbf{R})$ is a function of the electronic and nuclear coordinates, that is in general practically impossible to obtain analytically for molecular systems with more than three degrees of freedom. To get an approximate solution to TISE, we can consider the electronic Hamiltonian $\hat{H}_\mathrm{e}$

$$\hat{H}_\mathrm{e} = \hat{T}_\mathrm{e} + \hat{V}_\mathrm{eN} + \hat{V}_\mathrm{e} + \hat{V}_\mathrm{N} \tag{2.13}$$

and write the electronic TISE at a fixed nuclear configuration $\mathbf{R}$:

$$\hat{H}_\mathrm{e}\, \varphi(\mathbf{r}; \mathbf{R}) = E_\mathrm{e}(\mathbf{R})\, \varphi(\mathbf{r}; \mathbf{R}) \tag{2.14}$$

The formal solutions to equation (2.14) form a complete orthonormal basis, that we can conveniently use to express the full spatial wavefunction:

$$\Psi(\mathbf{r},\mathbf{R}) = \sum_k \varphi_k(\mathbf{r};\mathbf{R})\,\chi_k(\mathbf{R}) \tag{2.15}$$

where $\chi_k(\mathbf{R})$ play the role of expansion coefficients. In the last two equations (2.14) and (2.15) the semicolon in $\varphi(\mathbf{r};\mathbf{R})$ indicates the parametric dependence on the nuclear positions. Substituting equation (2.15) into the full TISE (2.7), multiplying both sides by $\varphi_l^\dagger(\mathbf{r};\mathbf{R})$ and integrating over the electronic coordinates gives a set of $k$ coupled eigenvalue equations which represent the TISE for the nuclei:

$$\begin{aligned}\sum_k \Bigg( & E_{\mathrm{e},k}(\mathbf{R})\,\delta_{kl} + \sum_\alpha -\frac{\hbar^2}{2m_\alpha}\nabla^2_{\mathrm{N},\alpha}\,\delta_{kl} + \\ & + \sum_\alpha -\frac{\hbar^2}{2m_\alpha}\Bigg[\underbrace{\int \mathrm{d}\mathbf{r}\,\varphi_l^\dagger(\mathbf{r};\mathbf{R})\,\nabla^2_{\mathrm{N},\alpha}\,\varphi_k(\mathbf{r};\mathbf{R})}_{\text{scalar coupling}} + \\ & + 2\underbrace{\int \mathrm{d}\mathbf{r}\,\varphi_l^\dagger(\mathbf{r};\mathbf{R})\,\nabla_{\mathrm{N},\alpha}\,\varphi_k(\mathbf{r};\mathbf{R})\,\nabla_{\mathrm{N},\alpha}}_{\text{derivative coupling}}\Bigg]\Bigg)\chi_k(\mathbf{R}) = E\sum_k \chi_k(\mathbf{R})\,\delta_{kl}\end{aligned} \tag{2.16}$$

Up to this point no approximation has been introduced, and equation (2.16) is formally exact. $\hat{H}_\mathrm{e}$ is diagonal in the $\{\varphi(\mathbf{r};\mathbf{R})\}$ basis, while $\hat{T}_\mathrm{N}$ originates the $k,l$ scalar and derivative coupling terms in the last two lines of equation (2.16), which together form the so-called non adiabatic coupling (NAC):

$$\mathrm{NAC}_{lk} = \sum_\alpha -\frac{\hbar^2}{2m_\alpha}\left[\int \mathrm{d}\mathbf{r}\,\varphi_l^\dagger(\mathbf{r};\mathbf{R})\,\nabla^2_{\mathrm{N},\alpha}\,\varphi_k(\mathbf{r};\mathbf{R}) + 2\int \mathrm{d}\mathbf{r}\,\varphi_l^\dagger(\mathbf{r};\mathbf{R})\,\nabla_{\mathrm{N},\alpha}\,\varphi_k(\mathbf{r};\mathbf{R})\right] \tag{2.17}$$

It describes the change of the electronic wavefunction with the nuclear displacement, i.e. correlates nuclear and electronic motions. Focusing on the derivative coupling, its matrix representation in the $\{\varphi(\mathbf{r};\mathbf{R})\}$ basis is anti-hermitian, as it is easily demonstrated by considering that $\int \mathrm{d}\mathbf{r}\,\varphi_l^\dagger(\mathbf{r};\mathbf{R})\,\varphi_k(\mathbf{r};\mathbf{R}) = \delta_{kl}$ for any nuclear configuration. Therefore, the derivative of this overlap with respect to the nuclear coordinates must be zero, and it follows that

$$\begin{gathered}\nabla_\mathrm{N}\int \mathrm{d}\mathbf{r}\varphi_l^\dagger(\mathbf{r};\mathbf{R})\varphi_k(\mathbf{r};\mathbf{R}) = \int \mathrm{d}\mathbf{r}\nabla_\mathrm{N}\varphi_l^\dagger(\mathbf{r};\mathbf{R})\varphi_k(\mathbf{r};\mathbf{R}) + \int \mathrm{d}\mathbf{r}\varphi_l^\dagger(\mathbf{r};\mathbf{R})\nabla_\mathrm{N}\varphi_k(\mathbf{r};\mathbf{R}) = 0 \\ \int \mathrm{d}\mathbf{r}\nabla_\mathrm{N}\varphi_l^\dagger(\mathbf{r};\mathbf{R})\varphi_k(\mathbf{r};\mathbf{R}) = -\int \mathrm{d}\mathbf{r}\varphi_l^\dagger(\mathbf{r};\mathbf{R})\nabla_\mathrm{N}\varphi_k(\mathbf{r};\mathbf{R})\end{gathered} \tag{2.18}$$

and

$$\int \mathrm{d}\mathbf{r}\,\varphi_k^\dagger(\mathbf{r};\mathbf{R})\,\nabla_\mathrm{N}\,\varphi_k(\mathbf{r};\mathbf{R}) = 0 \tag{2.19}$$

i.e. the derivative coupling is anti-hermitian in the basis of the electronic wavefunctions. Additionally, it can be shown that the $k,l$ coupling is inversely proportional to the $k-l$ energy gap. To prove this, we can differentiate the electronic Schrödinger equation (2.14) with respect to each nuclear coordinate $\alpha$ and subsequently multiply both sides by $\varphi_l^\dagger(\mathbf{r};\mathbf{R})$ and integrate over the electronic coordinates obtaining

$$\begin{aligned}\int \mathrm{d}\mathbf{r}\, \varphi_l^\dagger(\mathbf{r};\mathbf{R}) \left(\nabla_{\mathrm{N},\alpha}\hat{H}_\mathrm{e}\right) \varphi_k(\mathbf{r};\mathbf{R}) &= \left(E_{\mathrm{e},k} - E_{\mathrm{e},l}\right) \int \mathrm{d}\mathbf{r}\, \varphi_l^\dagger(\mathbf{r};\mathbf{R}) \nabla_{\mathrm{N},\alpha}\, \varphi_k(\mathbf{r};\mathbf{R}) \\ \int \mathrm{d}\mathbf{r}\, \varphi_l^\dagger(\mathbf{r};\mathbf{R}) \nabla_{\mathrm{N},\alpha}\, \varphi_k(\mathbf{r};\mathbf{R}) &= \frac{\int \mathrm{d}\mathbf{r}\, \varphi_l^\dagger(\mathbf{r};\mathbf{R}) \left(\nabla_{\mathrm{N},\alpha}\hat{H}_\mathrm{e}\right) \varphi_k(\mathbf{r};\mathbf{R})}{\left(E_{\mathrm{e},k} - E_{\mathrm{e},l}\right)}\end{aligned} \tag{2.20}$$

This tells us that the derivative coupling term has a local nature, and becomes large when the two electronic states come close. Large couplings induce an efficient and rapid population transfer between electronic states during the nuclear motion. This is a non classical effect that originates as a consequence of the fact the system can exist in multiple (and coupled) electronic states simultaneously. Indeed, energetically-accessible regions of degeneracy are responsible for nonradiative decay down the ladder of excited states, known as internal conversion. These special points of degeneracy are known as Conical Intersections (CIs), and are frequently observed in photochemical reactions. The NACs become singular at degeneracy points, and their spiky and localised nature makes their numerical treatment quite difficult.

In the approach that we have followed, vibronic (i.e. nuclear and electronic) coupling is through nuclear kinetic energy terms. When the coupling terms cannot be neglected, a diabatic transformation is often applied (see section 2.2.4), in which the kinetic term is diagonalised. However, the transformation creates coupling terms in the potential as the off-diagonal elements of $\hat{H}_\mathrm{e}$. The diabatic representation is easier to deal with, because it results in smoother electronic potentials and vibronic couplings, compared to the adiabatic states (and corresponding non adiabatic couplings).

### 2.1.1 Born-Oppenheimer approximation

The coupled equations 2.16 are formally exact and take into account the nuclear-electronic coupling. The $\hat{T}_\mathrm{N}$ terms (including the scalar and derivative couplings of equation (2.17)) are inversely proportional to the nuclear mass, therefore, the NACs will only produce small corrections in the energy levels as a consequence of the heaviness of the nuclei. Indeed, for the same displacement, the electronic wavefunctions usually change much slower than the vibrational ones, making the NACs orders of magnitude smaller than the other terms in equation (2.16). Therefore, they can be neglected, and hence the whole matrix is effectively zero. The scalar coupling term can approximately be written as the square of the derivative coupling and, accordingly, it is significantly smaller in magnitude (and negligible in the same way). Only the diagonal kinetic energy term in equation (2.16) is retained in the case of well separated states

$$\sum_k \left( E_{\mathrm{e},k}(\mathbf{R})\, \delta_{kl} + \sum_\alpha -\frac{\hbar^2}{2m_\alpha} \nabla^2_{\mathrm{N},\alpha} \delta_{kl} \right) \chi_k(\mathbf{R}) = E \sum_k \chi_k(\mathbf{R})\, \delta_{kl} \tag{2.21}$$

Such approximation is called the Born-Oppenheimer (BO) approximation or adiabatic approximation, and it represents the fundamental assumption in quantum chemistry. In this view, the nuclei are considered stationary with respect to the electrons, which is justified by the high mass and velocity difference between the two types of particles. Therefore, electrons can adapt almost instantaneously to a new nuclear arrangement.

Under the BO approximation it is possible to solve the electronic problem in equation (2.14) for a large set of nuclear positions, obtaining adiabatic potential energy surfaces (PESs) which can be used to solve the TISE for the nuclei (2.21) and eventually to propagate them, i.e. to simulate their time resolved dynamics with the TDSE. Based on the BO approximations, many electronic structure methods have been developed to find approximate solutions to the electronic TISE (2.14). Indeed, analytical solutions are impossible to find for more than two particles (i.e. many-electron systems), which require approximate methods. Among these, the main distinction is between *wavefunction-based* and *density-based* methods. The former rely on the computation of the multi-electronic wavefunction of the system (to a certain level of approximation), an abstract quantity which satisfies some physically-meaningful conditions. On the other hand, density-based methods rely on the electron density $\rho(\mathbf{r})$ which, in contrast to the wavefunction (whose complexity grows rapidly with the number of electrons in the system, is a function of three spatial coordinates only). For the ground state, this approach is justified by the celebrated Hohenberg-Kohn (HK) theorems, which state that the exact ground state total energy of any many-electron system is given by a functional of the electron density only[1]. In contrast, for the calculation of excited states energies and properties, wavefunction-based methods are in general more reliable, although the price to pay is a higher computational cost, which limits their application to small-medium size systems.

Following, some wavefunction-based methods will be outlined, with particular focus of Complete Active Space Self-Consistent Field (CASSCF) and Complete Active Space Perturbation Theory (CASPT2) which were used for the works described in this thesis.

### 2.1.2 The Hartree-Fock method

The idea behind the Hartree-Fock (HF) method is to obtain the best approximation to the lowest-energy $N$-electron solution of TISE through variational minimisation of its energy expectation value $\int \mathrm{d}\mathbf{r}\, \varphi^{\dagger}(\mathbf{r};\mathbf{R})\, \hat{H}_{\mathbf{e}}\, \varphi(\mathbf{r};\mathbf{R})$. In accordance with molecular orbital (MO) theory, the $N$-electron wavefunction is approximated with a combination of one-electron solutions (orbitals). These are made up of a spatial part, named *spatial orbital* $\phi(x, y, z)$ and a spin function $\sigma(s)$ describing the spin component of the electron. MOs are chosen to be orthogonal to each other, as they are solution of the one-electron eigenvalue problem, and normalised, in order to satisfy the physical requirement that the probability of finding the electron anywhere in space is unity. Their final shape depends on the system and is determined variationally to minimise the total energy. The spatial component of the one-electron MOs $\phi(x, y, z)$ are obtained as Linear Combinations of Atomic Orbitals $\Theta(x, y, z)$ (LCAO)

$$\phi_i(x, y, z) = \sum_j c_{ij}\Theta_j(x, y, z) \tag{2.22}$$

The atomic orbitals (AOs) can be either of Slater type (STO) or Gaussian type (GTO): the former are hydrogen-like and thus more accurate, the latter are represented by gaussian functions, which make integral calculation considerably faster. GTOs are the most common choice in quantum chemical calculations, as Slater type AOs become quickly difficult to treat for increasing molecular sizes. Due to the inaccurate description at very short and large distances from the nuclei, each $\Theta_j(x,y,z)$ is represented as a non-variable contraction of several primitive GTOs

$$\Theta_j(x,y,z) = \sum_k d_{jk} G_k(x,y,z) \tag{2.23}$$

where the $d_{jk}$ coefficients (called *contraction coefficients*) are fixed constants within a given basis set. Basis functions of this type are called *contracted gaussians*, the individual $G_k$ being termed *primitive gaussians*. The quality of the basis set (that, in general, improves with the number of primitive GTOs included in the contraction) is of fundamental importance for the accuracy of the final results, and the use of finite basis sets represents an error source that must not be underestimated.

In order to account for the electron indistinguishability, the wavefunction has to be anti-symmetric with respect to the exchange of any pair of particles due to Pauli exclusion principle applied to the electrons (fermions), i.e.

$$\varphi(\mathbf{x}_1, \mathbf{x}_2, \cdots, \mathbf{x}_n) = -\varphi(\mathbf{x}_2, \mathbf{x}_1, \cdots, \mathbf{x}_n) \tag{2.24}$$

where $\mathbf{x}_n$ labels the coordinates of the $n$-th electron (spatial and spin). The molecular spin-orbitals are therefore combined in a mathematical construct named Slater determinant (SD) that satisfies such requirement:

$$\begin{aligned}\Phi^{\mathrm{SD}}(\mathbf{x}_1, \mathbf{x}_2, \cdots, \mathbf{x}_n) &= \frac{1}{\sqrt{N!}} \begin{vmatrix} \phi_1(\mathbf{x}_1) & \phi_1(\mathbf{x}_2) & \dots & \phi_1(\mathbf{x}_N) \\ \phi_2(\mathbf{x}_1) & \phi_2(\mathbf{x}_2) & \dots & \phi_2(\mathbf{x}_N) \\ \vdots & \vdots & \ddots & \vdots \\ \phi_N(\mathbf{x}_1) & \phi_N(\mathbf{x}_2) & \dots & \phi_N(\mathbf{x}_N) \end{vmatrix} \\ &= \frac{1}{\sqrt{N!}} \sum_P^{N!} (-1)^P \hat{P} \phi_1(\mathbf{x}_1) \phi_2(\mathbf{x}_2) \cdots \phi_N(\mathbf{x}_N)\end{aligned} \tag{2.25}$$

where $\hat{P}$ represents a permutation operator of $N$ objects (electrons, in our case), $(-1)^P$ stands for the parity of the permutation and $\Phi^{\mathrm{SD}}$ stands for the SD wavefunction. Such wavefunction has the property of antisymmetry, because swapping two electrons correspond to interchanging two rows of the determinant, which will have the effect of changing its sign. Moreover, it is not possible for a spin-orbital to be occupied by two electrons of the same spin, because the determinant would vanish if two columns are identical. The only problem with SDs is that they are not necessarily eigenstates of the $\hat{S}^2$ spin operator (in contrast with what the many-electron wavefunction is expected to be). To solve this, couples of SDs are linearly combined with ± sign to form configuration state functions (CSFs), which are pure spin states.

To show how the HF method works, it is convenient to express the electronic Hamiltonian $\hat{H}_{\mathrm{e}}$ in terms of one-electron and two-electron operators:

$$\hat{H}_{\mathrm{e}} = \sum_i \hat{f}_i + \sum_{i,j} \hat{g}_{ij} \tag{2.26}$$

$$\hat{f}_i = -\frac{\hbar^2}{2m_{\mathrm{e}}} \nabla^2_{e,i} - \sum_\alpha \frac{Z_\alpha e^2}{R_{\alpha i}} \tag{2.27}$$

$$\hat{g}_{ij} = \frac{e^2}{R_{ij}} \tag{2.28}$$

The nuclear repulsion is a constant and has now been excluded from $\hat{H}_\mathrm{e}$. In the Hartree-Fock method, the variational method is applied to the expectation value of the electronic Hamiltonian, with the constraint that the varied spin-orbitals should remain orthogonal:

$$\frac{\delta}{\delta\phi_k}\left(\int \mathrm{d}\mathbf{x}_1 \cdots \mathrm{d}\mathbf{x}_N\, \Phi^\dagger(\mathbf{x}_1, \cdots, \mathbf{x}_N)\, \hat{H}_\mathrm{e}\, \Phi(\mathbf{x}_1, \cdots, \mathbf{x}_N) - \sum_k \epsilon_k \int \mathrm{d}\mathbf{x}_1 \phi_k^\dagger(\mathbf{x}_1)\phi_k(\mathbf{x}_1)\right) = 0 \tag{2.29}$$

where $\epsilon_k$ are the Lagrange multipliers to be determined. This yields a set of coupled eigenvalue equations called the Hartree-Fock equations:

$$\hat{f}_1\, \phi_k(\mathbf{x}_1) + \sum_j \int \phi_j^\dagger(\mathbf{x}_2)\, \hat{g}_{12}\, \left[\phi_k(\mathbf{x}_1)\, \phi_j(\mathbf{x}_2) - \delta_{\sigma_k\sigma_j}\, \phi_j(\mathbf{x}_1)\, \phi_k(\mathbf{x}_2)\right] \mathrm{d}\mathbf{x}_2 = \epsilon_k\, \phi_k(\mathbf{x}_1) \tag{2.30}$$

The N-electron problem has therefore turned into $N$ one-electron problems, in which the electron is subject to an interaction with the mean field generated by the remaining $N-1$ electrons (whose coordinates have been integrated out of the equation). The solutions to the Hartree-Fock equations represent the MOs that, combined in a SD wavefunction, minimise the energy of the system. The MOs are expressed as linear combinations of AOs (equation (2.22)), therefore the solution of the HF problems reduces to finding the optimal set of expansion coefficients $c_{ij}$ that minimise the energy expectation value.

The total energy can be found by adding all the MO energies $\epsilon_k$ (which correspond to the Lagrange multipliers of the variational problem), removing the pair contribution form $\hat{g}_{12}$ to avoid double counting of the $k, j$ and $j, k$ interaction:

$$\begin{aligned} E &= \sum_k \epsilon_k - \sum_{j\neq k} \int \phi_k^\dagger(\mathbf{x}_1)\, \phi_j^\dagger(\mathbf{x}_2)\, \hat{g}_{12} \left[\phi_k(\mathbf{x}_1)\, \phi_j(\mathbf{x}_2) - \delta_{\sigma_k\sigma_j}\, \phi_j(\mathbf{x}_1)\, \phi_k(\mathbf{x}_2)\right] \mathrm{d}\mathbf{x}_1\, \mathrm{d}\mathbf{x}_2 \\ &= \sum_k \epsilon_k - \sum_{j\neq k} \left(J_{jk} - K_{jk}\right) \end{aligned} \tag{2.31}$$

The two integrals $J_{jk}$ and $K_{jk}$ in equation (2.31) are called Coulomb and exchange intergals, respectively. The Coulomb integral

$$J_{kj} = \int \phi_k^\dagger(\mathbf{x}_1)\, \phi_j^\dagger(\mathbf{x}_2)\, \hat{g}_{12}\, \phi_k(\mathbf{x}_1)\, \phi_j(\mathbf{x}_2)\, \mathrm{d}\mathbf{x}_1\, \mathrm{d}\mathbf{x}_2 \tag{2.32}$$

gives the electrostatic repulsion between the two electrons occupying the $\phi_k$ and $\phi_j$ spin-orbitals. It is independent of the electron spin and has a classical interpretation. In contrast, the exchange integral $K_{jk}$ does not have a classical counterpart:

$$K_{kj} = \int \phi_k^\dagger(\mathbf{x}_1)\, \phi_j^\dagger(\mathbf{x}_2)\, \hat{g}_{12}\, \phi_k(\mathbf{x}_2)\, \phi_j(\mathbf{x}_1)\, \delta_{\sigma_k\sigma_j}\, \mathrm{d}\mathbf{x}_2\, \mathrm{d}\mathbf{x}_2 \tag{2.33}$$

It looks like the repulsion between the two "mixed" charge distributions $\phi_k^\dagger(\mathbf{x}_1)\phi_j(\mathbf{x}_1)$ and $\phi_j^\dagger(\mathbf{x}_2)\phi_k(\mathbf{x}_2)$, however, it originates from the use of an SD as wavefunction and its nature is purely quantistic (i.e. it is due to the need to consider all possible permutations of electrons in the MOs). $K_{kj}$ is non-vanishing only for electrons with different spins, and accounts for the fact that they "repel more" (i.e. electrons with the same spin cannot occupy the same spatial orbital, while electrons with different spin can share the same region of space).

The main problem in solving the HF equations is that the energy of the $i$-th solution depends on the interaction with all the other electrons whose energy, in turn, depends on the energy of the $i$-th electron itself. Therefore, the equations must be solved iteratively, starting with some guess spin-orbitals which are varied until the self-consistency is reached (within a determined threshold). For this reason, the Hartree-Fock method is also called the self-consistent field (SCF) method.

Despite the underlying approximations, the Hartree-Fock SD is a good representation to the ground state wavefunction. The obtained MOs behave as if each particle were subjected to the mean field created by all other electrons, therefore, the electron-electron repulsion is accounted for only in an average fashion. In a sufficiently large basis set, the HF wavefunction accounts for ~ 99% of the total energy. The remaining 1%, however, is often very important to describe chemical phenomena. The difference between the exact and the HF energies is called the *correlation energy*, and is due to to the correlation in the electronic motion (which is not accurately described by an average repulsion). One way to retrieve the correlation energy is through the use of a multideterminant (i.e. multiconfigurational) wavefunction, which provides the necessary flexibility to describe the correlated motion of the electrons. This is of of particular importance to describe electronically excited states, and electron correlation methods typically use the Hartree-Fock SD as starting point for improvements. The basis set of AOs determines the size of the MO basis for the determinant construction, while the number of possible determinants (i.e. electronic configurations within the MOs) determines the size of the multiconfigurational wavefunction, and thus limits the description of the electron correlation.

$$\begin{array}{ccccccccccc} G & \longrightarrow & \Theta & \longrightarrow & \phi & \longrightarrow & \Phi^{\mathrm{SD}} & \longrightarrow & \Phi & \longrightarrow & \varphi \\ \text{primitive GTO} & & \text{AO} & & \text{MO} & & \text{SD} & & \text{CSF} & & \text{many elec. WF} \end{array}$$

### 2.1.3 Retrieving electron correlation: Configuration Interaction

The Hamiltonian in the Hartree-Fock method depends on all the occupied MOs. The total number of MOs, however, is not limited by the number of electrons, but rather it depends on the size of the basis set used to construct them. Thus, if a sufficiently large basis set is used, the Hartree-Fock equations yield $N$ occupied and $K - N$ *virtual* (i.e. unoccupied) spin-orbitals, where $K$ is the total number of MOs determined by the basis set size. In order to improve the HF results, it is possible to replace one or more occupied spin-orbitals with virtual ones, obtaining the so-called *excited determinants*. The virtual orbitals extend further away from the core, therefore their inclusion in the wavefunction is equivalent to allowing electrons to explore more space and, thus, to better avoid the other electrons. All the possible determinants or CSFs (i.e. electronic configurations) that can be formed out of the $K$ HF orbitals form a complete basis (within the basis set used) in which the $N$-electron wavefunction can be expanded

$$|\varphi\rangle = \sum_i c_i \, |\Phi_i\rangle \tag{2.34}$$

For convenience, Dirac notation will be used throughout the rest of this chapter, in which the determinant/CSF $\Phi_i$ composed of the $N$ spin orbitals $\{\phi_1, \phi_2, \cdots, \phi_N\}$ is indicated as $|\Phi_i\rangle = |\phi_1 \phi_2 \cdots \phi_N\rangle$ and $\langle\Phi_i|$ is the complex conjugate of $|\Phi_i\rangle$.

Depending on the number of replacements with respect to the HF configuration, excited determinants are classified into *singly-excited* or *singles* $|\Phi_a^r\rangle$, *doubly-excited* or *doubles* $|\Phi_{ab}^{rs}\rangle$, *triply-excited* or *triples* $|\Phi_{abc}^{rst}\rangle$ and so on, in which $a, b, c$ label occupied HF spin-orbitals while $r, s, t$ label virtuals. The $N$-electron wavefunction then becomes

$$|\varphi\rangle = c_0 |\Phi_0^{\text{HF}}\rangle + \sum_{a,r} c_a^r |\Phi_a^r\rangle + \sum_{\substack{a<b \\ r<s}} c_{ab}^{rs} |\Phi_{ab}^{rs}\rangle + \sum_{\substack{a<b<c \\ r<s<t}} c_{abc}^{rst} |\Phi_{abc}^{rst}\rangle + \cdots \tag{2.35}$$

The configuration interaction (CI) method uses the variational method to find the best set of coefficients that minimises the energy expectation value of the $N$-electron wavefunction expanded in a basis of Slater determinants

$$\langle\varphi| \hat{H} |\varphi\rangle = \sum_{i,j} c_i^* c_j \langle\Phi_i| \hat{H} |\Phi_j\rangle = \sum_i c_i^2 E_i + \sum_{i,j\neq i} c_i^* c_j \langle\Phi_i| \hat{H} |\Phi_j\rangle \tag{2.36}$$

with the constraint that the total CI wavefunction is normalised. This corresponds to a diagonalisation of the molecular Hamiltonian in the basis of the CI wavefunctions: lowest eigenvalue $\mathscr{E}_0$ is an approximation to the ground state energy, with $\mathscr{E}_0 - E_0^{\text{HF}}$ representing the correlation energy $E_{\text{corr}}$ (within the approximation imposed by the basis set). Higher eigenstates (and eigenvalues) represent excited state wavefunctions (and energies). The matrix representation of the Hamiltonian in the $\{\Phi_i\}$ basis is called the CI matrix.

In the limit of an infinite and complete determinant basis, CI provides an exact solution to the $N$-electron problem. In practise, however, we can only handle a finite set of trial functions, whose limit is imposed by the basis set size, and CI provides upper bounds to the exact energies.

If all the possible configurations are included in the expansion the method is called full-CI, and it yields the best possible results within the basis set approximation. Unfortunately, even for small molecules and moderate-size one-electron basis, the number of possible determinants is too big to make CI computationally affordable. Thus, the CI expansion is usually truncated in some way, excluding some determinants (or CSFs). To this aim, there are few useful observations about coefficients $c_i$ and CI matrix element $\langle\Phi_i| \hat{H} |\Phi_j\rangle$ appering in the expectation value (equation (2.36)):

- in the CI expansion, a large number of coefficients vanish because there is no mixing between states of different spin (e.g. triplet configurations do not contribute to the expansion of singlet wavefunctions and vice versa);

- if the system is symmetric, additional coefficients vanish due to the fact that only determinants with the same symmetry as the considered state can contribute;

- all the CI matrix elements $\langle\Phi_0^{\text{HF}}| \hat{H} |\Phi_a^r\rangle$ involving the HF determinant and any singly-excited determinant are null, as they are equivalent to the off-diagonal elements of the Fock matrix (i.e. the matrix representation of the one-electron hamiltonian in the spin-orbital basis), which is diagonal in the converged HF orbital basis. This is known as Brillouin's theorem and implies that the contribution of single excitations to the ground state correlation energy is small (although non zero, due to the indirect contribution through their interaction with other contributing determinants e.g. double excitations);

- the Hamiltonian operator consists of a sum over one- and two-electron operators, thus, if two configurations differ by more than two spin orbitals, the corresponding CI element $H_{ij} = \langle\Phi_i|\hat{H}|\Phi_j\rangle$ vanishes because the integration will always include the overlap between two different MOs, which is zero.

The most common truncated CI methods include single excitations (CIS[2]) or singles and doubles (CISD[3]). Higher order expansions (CISDT, CISTQ etc.) approach the full-CI limit, but they are computationally unaffordable for most systems, as the size of the determinant basis grows rapidly for multiple excitations.

### 2.1.4 The CASSCF method

Empirical studies have shown the that CI wavefunction converges slowly, and requires a large number of configurations that impact on the computational cost (singles are not enough, double and triples are required). The CI wavefunction is indeed missing flexibility, due to the fixed MOs used. An improvement to the CI method is the multiconfigurational self-consistent field (MCSCF) method, in which both the CI coefficients and the MOs used for constructing the determinants are simultaneously optimised. The MCSFC procedure is iterative (if the "multiconfiguration" includes only one determinant, it reduces to the HF method) and achieves accurate results. However, the additional effort emerging from the complexity of the simultaneous optimisation of CI and MO coefficients makes it necessary to restrict in some way the number of excitations included.

Among the MCSCF methods, the most popular is probably the complete active space self-consistent field (CASSCF) method[4] in which, instead of limiting the order of the excitations, a full-CI is performed in a subspace of orbitals, referred to as the active space. The active space size and composition is left to the chemical intuition of the user, and depends on the problem at hand and on the computational expense. Typically, the active space should include those orbitals that are involved in the chemical transformation, or whose occupation number changes significantly when exciting from the ground to the excited state(s) included in the model. The CASSCF MOs are therefore divided in three subspaces: the *inactive* MOs are doubly-occupied in all the configurations, the *active* MOs have a variable occupation number and are used to generate the excited determinants, the *secondary* or *virtual* MOs are always empty and do not contribute (see Figure 2.1, left).

The number of CSFs generated from a given active space is determined by Weyl's formula:

$$\mathrm{N}_{\mathrm{CAS}} = \frac{2S+1}{n+1}\binom{n+1}{N/2-S}\binom{n+1}{N/2+S+1} \tag{2.37}$$

where $n$ is the number of active (spatial) MOs, $N$ the number of active electrons, and $S$ is the total spin. The number of CSFs included in the expansion grows rapidly with the active space size, and the CASSCF wavefunction and CI matrix become unmanageably large for more than 18 active orbitals/electrons. The restricted version of the method (RASSCF[5]) represents a valid alternative for bigger systems. In RASSCF, the active orbitals are further partitioned into three subspaces: RAS1, RAS2 and RAS3 (see

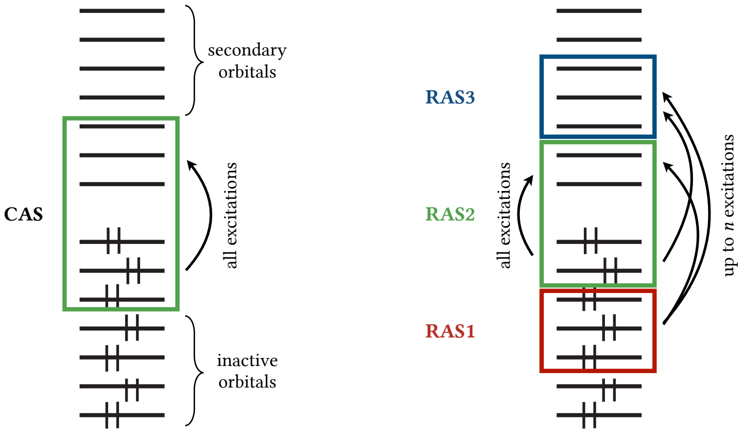

**Figure 2.1:** CASSCF (left) and RASSCF (right) orbital partitioning and possible excitations.

Figure 2.1, right). The full-CI scheme is applied to RAS2, while RAS1/RAS3 have restrictions on the maximum number of holes/electrons (i.e. excitations) allowed. The more general extensions GASSCF[6] (general active space SCF) and ORMAS[7] (occupation restricted multiple active spaces) also exist, in which an arbitrary number of subspaces can be defined.

One problem with the orbital optimisation in (C/R/G)ASSCF is that the final set of MOs depends on the optimised state, which makes the various solutions non-orthogonal. To deal with this problem, a state-averaged (SA) variant of the methods was developed. Here the optimisation objective is not the energy of a single state, but rather a weighted average of $N$ states of interest:

$$\tilde{E} = \sum_{i}^{N} \omega_i E_i \quad \text{with} \quad 0 \leq \omega_i \leq 1 \quad \text{and} \quad \sum_{i} \omega_i = 1 \tag{2.38}$$

this yields a unique and average set of MOs, which ensures that all desired states are orthogonal and described on an equal footing. However, it must be remembered that in this way the energy of one state becomes a function of the state-averaging parameters (i.e. number of states and relative weights), and that the average description goes at the expenses of the accuracy on each particular state, especially when the optimal MOs for the different wavefunctions differ significantly.

Current CASSCF(RASSCF/GASSCF) sizes do not allow to fully describe electron correlation and consequent errors can be of several eV. However, they provide a qualitatively correct description of multiconfigurational states, especially in degeneracy regions, where two or more determinants become isoenergetic. The fraction of the correlation energy retrieved by adding enough flexibility in the wavefunction to give a qualitatively correct description of the system is often referred to as *static* or *non-local* correlation. Indeed, excitations can promote an electron far away in e.g. in charge-transfer (CT) transitions. This non-local effect is described at (C/R/G)ASSCF level. On the other hand, the remaining part of the $E_{\text{corr}}$ is called *dynamic* or *local* correlation, and is addressed to the response of the electrons to the changes of their immediate (local) environment as a consequence of the excitation (e.g. positive and negative charges created upon CT). Dynamic/local correlation contribution is different for each electronic state, therefore CASSCF could even predict wrong state order or artificial state mixing due to wrong near-degeneracies.

In the multi-determinant approach, static correlation is recovered by the inclusion of a relatively small number of determinants bearing the highest contributing coefficients in the description of a particular state. In contrast, retrieving dynamic correlation requires the inclusion of many configurations with small contribution, in particular those involving promotion to higher-lying virtual orbitals (which are usually not included in the active space). Around the ground state equilibrium structure, the closed shell HF determinant is the dominant configuration, and all other terms can be treated perturbatively (see MP2 method, section 2.1.6). The multiconfigurational description is instead more important for excited states. However, even along the ground state potential there are regions where the HF description fails, e.g. bond breaking, torsion around double bonds. Correlation effects not described by the CASSCF wavefunction are generally recovered by subsequent Multi–Reference–CI (MRCI[8]) or Complete–Active–Space–Perturbation–Theory (CASPT2[9]) treatments that use the CASSCF wavefunction as zeroth order approximation. Both methods extend the expansion space by including higher order excitations from the CASSCF wavefunction. The MRCI is a variational approach, similar to CIS and CISD, but using a CASSCF reference function instead of a HF one. CASPT2 treats higher order excitations as perturbation to the CASSCF wavefunction. Both techniques provide accurate results, however, at the expense of huge computational effort.

To conclude, it must be mentioned that in recent years a number of new methods have been developed to tackle the exponential scaling problem in the MCSCF procedure: among them, the Stochastic-CASSCF[10] method (based on the FCI Quantum Monte Carlo approach[11–15] as the CI eigensolver), the density matrix renormalization group DMRG-SCF[16, 17] method and the variational-2RDM[18] method are gaining popularity.

### 2.1.5 Rayleigh–Schrödinger perturbation theory

In Perturbation Theory (PT) we consider the Hamiltonian $\hat{H}$ as the sum of a reference Hamiltonian $\hat{H}_0$ and a perturbation $\hat{V}$, which is assumed to be much smaller than $\hat{H}_0$.

$$\hat{H}(\lambda) = \hat{H}_0 + \lambda \hat{V} \tag{2.39}$$

The solutions of the reference Hamiltonian are known

$$\hat{H}_0 \, |\varphi_n^{(0)}\rangle = E_n^{(0)} \, |\varphi_n^{(0)}\rangle \tag{2.40}$$

and denoted as unperturbed reference energies ($E_n^{(0)}$) and wavefunctions ($|\varphi_n^{(0)}\rangle$).

The extent of the perturbation is represented by the parameter $\lambda$, of which the full Hamiltonian becomes a function, as well as its eigenvalues and eigenfiunctions:

$$\hat{H}(\lambda) \, |\varphi_n(\lambda)\rangle = E_n(\lambda) \, |\varphi_n(\lambda)\rangle \tag{2.41}$$

If we assume that the perturbation is small, we can express $|\varphi_n(\lambda)\rangle$ and $E_n(\lambda)$ as a Taylor series around $|\varphi_n^{(0)}\rangle$ and $E_n^{(0)}$, respectively:

$$|\varphi_n(\lambda)\rangle = |\varphi_n^{(0)}\rangle + \lambda \, |\varphi_n^{(1)}\rangle + \lambda^2 \, |\varphi_n^{(2)}\rangle + \ldots \tag{2.42}$$

$$E_n(\lambda) = E_n^{(0)} + \lambda E_n^{(1)} + \lambda^2 E_n^{(2)} + \ldots \tag{2.43}$$

the terms $|\varphi_n^{(k)}\rangle$ and $E_n^{(k)}$ represent the $k$-th derivatives with respect to $\lambda$ of $|\varphi_n(\lambda)\rangle$ and $E_n(\lambda)$, respectively.

Equation (2.41) then becomes:

$$\left(\hat{H}_0 + \lambda\hat{V}\right)\left[|\varphi_n^{(0)}\rangle + \lambda\,|\varphi_n^{(1)}\rangle + \lambda^2\,|\varphi_n^{(2)}\rangle + \ldots\right] = \\ \left[E_n^{(0)} + \lambda E_n^{(1)} + \lambda^2 E_n^{(2)} + \ldots\right] \times \left[|\varphi_n^{(0)}\rangle + \lambda\,|\varphi_n^{(1)}\rangle + \lambda^2\,|\varphi_n^{(2)}\rangle + \ldots\right] \quad (2.44)$$

For the left and right hand polynomials to be equal for every value of $\lambda$, the only possibility is that they are the very same polynomial. Therefore, we can write an equation for each power order of $\lambda$, setting equal its coefficients on the left and right hand sides of equation (2.44):

- **Order 0**:
$$\hat{H}_0\,|\varphi_n^{(0)}\rangle = E_n^{(0)}\,|\varphi_n^{(0)}\rangle \quad (2.45)$$
  This is just the time-independent Schrödinger equation for the reference Hamiltonian, whose solutions are known.

- **Order 1**:
$$\hat{H}_0\,|\varphi_n^{(1)}\rangle + \hat{V}\,|\varphi_n^{(0)}\rangle = E_n^{(1)}\,|\varphi_n^{(0)}\rangle + E_n^{(0)}\,|\varphi_n^{(1)}\rangle \quad (2.46)$$

- **Order 2**:
$$\hat{H}_0\,|\varphi_n^{(2)}\rangle + \hat{V}\,|\varphi_n^{(1)}\rangle = E_n^{(2)}\,|\varphi_n^{(0)}\rangle + E_n^{(1)}\,|\varphi_n^{(1)}\rangle + E_n^{(0)}\,|\varphi_n^{(2)}\rangle \quad (2.47)$$

The terms $|\varphi_n^{(1)}\rangle$, $|\varphi_n^{(2)}\rangle$, $E_n^{(1)}$, $E_n^{(2)}$, etc., represent the first-, second-, ..., $n$-th order perturbative corrections of the wavefunction and energy, respectively.

To find $E_n^{(1)}$ and $|\varphi_n^{(1)}\rangle$ we can project equation (2.46) onto the $m$-th solution of $\hat{H}_0$ obtaining

$$E_m^{(0)}\langle\varphi_m^{(0)}\,|\varphi_n^{(1)}\rangle + \langle\varphi_m^{(0)}|\,\hat{V}\,|\varphi_n^{(0)}\rangle = E_n^{(1)}\delta_{m,n} + E_n^{(0)}\,\langle\varphi_m^{(0)}|\varphi_n^{(1)}\rangle \quad (2.48)$$

- if $\mathbf{m} = \mathbf{n}$:
$$E_n^{(1)} = \langle\varphi_n^{(0)}|\,\hat{V}\,|\varphi_n^{(0)}\rangle \quad (2.49)$$
  so the first-order energy correction for state $n$ only requires the zeroth-order wavefunction to be calculated.

- if $\mathbf{m} \neq \mathbf{n}$:
$$\begin{aligned} E_m^{(0)}\,\langle\varphi_m^{(0)}|\varphi_n^{(1)}\rangle + \langle\varphi_m^{(0)}|\,\hat{V}\,|\varphi_n^{(0)}\rangle &= E_n^{(0)}\,\langle\varphi_m^{(0)}|\varphi_n^{(1)}\rangle \\ \langle\varphi_m^{(0)}|\varphi_n^{(1)}\rangle &= \frac{\langle\varphi_m^{(0)}|\,\hat{V}\,|\varphi_n^{(0)}\rangle}{\left(E_n^{(0)} - E_m^{(0)}\right)} \end{aligned} \quad (2.50)$$
  The left-hand side is nothing but the $m$-th coefficient of the first-order correction to the wavefunction ($|\varphi_n^{(1)}\rangle$) when it is expressed in the basis of the known solutions of $\hat{H}_0$, and it can be calculated from known quantities.

Knowing all the coefficients, we would have a complete knowledge of $|\varphi_n^{(1)}\rangle$. Unfortunately, equation (2.50) was derived assuming $m \neq n$ so the $n$-th coefficient is missing. To fix this, it is convenient to work with a wavefunction subject to an intermediate normalisation, i.e. $\langle\varphi_n^{(0)}|\varphi_n(\lambda)\rangle = 1$ (the renormalisation of a vector is a step that can always be done without changing the outcome of any experiment), obtaining

$$\langle\varphi_n^{(0)}|\varphi_n^{(k)}\rangle = \delta_{0,k} \tag{2.51}$$

which means that the missing $\langle\varphi_n^{(0)}|\varphi_n^{(1)}\rangle$ is null, so we already have a full description of $|\varphi_n^{(1)}\rangle$, and we can write the first-order correction of the wavefunction in terms of the known solutions of $\hat{H}_0$:

$$|\varphi_n^{(1)}\rangle = \sum_{m\neq n} |\varphi_m^{(0)}\rangle \langle\varphi_m^{(0)}|\varphi_n^{(1)}\rangle = \sum_{m\neq n} |\varphi_m^{(0)}\rangle \frac{\langle\varphi_m^{(0)}|\,\hat{V}\,|\varphi_n^{(0)}\rangle}{\left(E_n^{(0)} - E_m^{(0)}\right)} \tag{2.52}$$

In most of the cases, the first-order correction of the energy is not sufficient to include dynamic correlation, therefore, the second-order term $E_n^{(2)}$ is needed. Again, we start by projecting equation (2.47) onto $|\varphi_n^{(0)}\rangle$:

$$\begin{gathered}
\cancel{\langle\varphi_n^{(0)}|\,\hat{H}_0\,|\varphi_n^{(2)}\rangle} + \langle\varphi_n^{(0)}|\,\hat{V}\,|\varphi_n^{(1)}\rangle = E_n^{(2)}\,\langle\varphi_n^{(0)}|\varphi_n^{(0)}\rangle + E_n^{(1)}\,\langle\varphi_n^{(0)}|\varphi_n^{(1)}\rangle + \cancel{E_n^{(0)}\,\langle\varphi_n^{(0)}|\varphi_n^{(2)}\rangle} \\
\langle\varphi_n^{(0)}|\,\hat{V}\,|\varphi_n^{(1)}\rangle = E_n^{(2)}\,\langle\varphi_n^{(0)}|\varphi_n^{(0)}\rangle + E_n^{(1)}\,\langle\varphi_n^{(0)}|\varphi_n^{(1)}\rangle
\end{gathered} \tag{2.53}$$

The $E_n^{(1)}$ term on the right vanishes using intermediate normalisation, therefore

$$\begin{aligned}
E_n^{(2)} &= \langle\varphi_n^{(0)}|\,\hat{V}\,|\varphi_n^{(1)}\rangle \\
&= \sum_{m\neq n} \frac{\left|\langle\varphi_m^{(0)}|\,\hat{V}\,|\varphi_n^{(0)}\rangle\right|^2}{\left(E_n^{(0)} - E_m^{(0)}\right)}
\end{aligned} \tag{2.54}$$

Equation (2.54) shows the expression for the second-oder energy correction of state $n$. This equation can be used to correct the energies of all the eigenstates of the reference Hamiltonian $\hat{H}_0$, except for the case of degenerate solutions. Indeed, when two eigenstates of the unperturbed Hamiltonian come to be degenerate, the denominator of the left-hand side vanishes, and the corresponding term in the sum becomes infinite. In such cases, the only possibility to get a physically meaningful result would be to have $\langle\varphi_m^{(0)}|\,\hat{V}\,|\varphi_n^{(0)}\rangle = \langle\varphi_n^{(0)}|\,\hat{V}\,|\varphi_m^{(0)}\rangle = 0$. It can be demonstrated that, given a set of degenerate eigenstates, it is always possible to combine them linearly to obtain a new set of states that satisfies such requirement. Moreover, any linear combination of such degenerate states is still an eigenstate of $\hat{H}_0$ sharing the same eigenvalue. In the limit case of an Hamiltonian with all degenerate solutions, $\hat{H}_0$ is a multiple of the identity matrix $\mathbb{I}$: this implies that $\hat{H}_0$ is invariant with respect to a change of basis in which the new basis is a linear combination of the starting eigenfunctions. In this new basis, both $\hat{H}_0$ and $\hat{V}$ are diagonal: $\hat{H}_0$ is a multiple of $\mathbb{I}$, while the diagonal elements of $\hat{V}$ can be different. The final hamiltonian $\hat{H} = \hat{H}_0 + \hat{V}$ will still be diagonal but with diagonal terms which are not necessarily equal, therefore the perturbation has removed the degeneration between the eigenstates. In this case, the second-order energy correction is null, because all off-diagonal terms of $\hat{V}$ appearing in equation (2.54) vanish.

More frequently, only some subsets of eigenstates of $\hat{H}_0$ are degenerate, as represented in Figure 2.2 In such situations, it is possible to work on each block separately, treating it as a separate Hamiltonian with all degenerate solutions and getting the energy correction for the subset of eigenstates. Moreover, the change of basis relative to a single block is not influencing the energy correction of the others. This means that it is possible to work only on the blocks including the states of interest without affecting the remaining parts of $\hat{H}_0$.

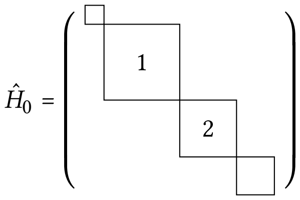

**Figure 2.2:** Reference Hamiltonian with subsets of degenerate eigenstates.

### 2.1.6 Møller-Plesset perturbation theory

In Møller-Plesset perturbation theory (MPPT), the perturbational treatment is applied to a single-determinant reference wavefunction. This method is often applied to the HF results in order to get an accurate approximation of the ground state energy, truncating the correction at the second order as higher-order corrections do not constitute a significant enough improvement to compensate the additional complexity and computational expense. The resulting method is called MP2 method.

The reference function is thus the HF determinant, composed of canonical orbitals obtained diagonalising the Fock operator $\hat{f}$ (i.e. the energy of one spin-orbital). The molecular Fock operator $\hat{F}$ is defined as

$$\hat{F}(\varphi_{\text{HF}}^{(0)}) = \sum_i \hat{f}(\varphi_{\text{HF}}^{(0)}) \tag{2.55}$$

We have explicitly indicated the $\hat{F}$ and $\hat{f}$ dependence on the reference density of $|\varphi_{\text{HF}}^{(0)}\rangle$ to stress the fact that the electronic interaction (i.e. Coulomb and exchange terms) is a function of the HF occupied spin orbitals. The expectation value of the molecular Fock operator over the reference wavefunction is the sum of the energies of occupied spin-orbitals

$$E^{(0)} = \langle\varphi_{\text{HF}}^{(0)}|\,\hat{F}(\varphi_{\text{HF}}^{(0)})\,|\varphi_{\text{HF}}^{(0)}\rangle = \sum_i \epsilon_i \tag{2.56}$$

The perturbation is defined as the difference between the exact Hamiltonian and the Fock operator, i.e. as the sum of Coulomb and exchange interactions defined in section 2.1.2 (here labelled $\hat{v}_{ij}$ with $i, j$ being HF occupied orbitals).

$$\hat{H} = \hat{F} - \lambda \left( \sum_{ij} \hat{v}_{i,j} \right) = \hat{F} + \lambda \hat{V} \tag{2.57}$$

With this formulation, the MPPT energy corrected to first order ($E^{(0)} + E^{(1)}$) is simply the HF energy, as the expectation value $\langle \varphi^{(0)}_{\mathrm{HF}} | \hat{H} | \varphi^{(0)}_{\mathrm{HF}} \rangle$ removes the double counting of electron-electron interactions (i.e. $E_{\mathrm{HF}}$, see section 2.1.2). As a consequence, the first improvement with respect to HF results comes with the second-order MP2 correction $E^{(2)}$, which is obtained through

$$E^{(2)} = \langle \varphi^{(0)}_{\mathrm{HF}} | \hat{V} | \varphi^{(1)} \rangle \tag{2.58}$$

In order to obtain the second-order energy correction, the missing ingredient is the explicit resolution of the first-order correction to the HF wavefunction. In the general formulation of equation (2.52), $|\varphi^{(1)}\rangle$ is expanded in the basis of all the excited states (i.e. $\hat{H}_0$ solutions orthogonal to the reference state), therefore, the MP2 procedure can be summarised as follows:

1. construct the excited states;
2. obtain their coefficients in the first-order corrected wavefunction;
3. compute the second-order correction of the energy.

Excited states for a particular Fock operator $\hat{F}$ are generated through replacements of the occupied orbitals with the virtual (unoccupied) orbitals. This is a good approximation to them, however, it must be remembered that such “excited states” do not correspond to the true self-consistent excited states of the SCF procedure, because that would require to iteratively redefine the electronic density of the Fock operator to be self-consistent.

From equation (2.52) it follows that, out of the full expansion of $|\varphi^{(1)}\rangle$, only excited states which interact with the reference state over the perturbation potential have non-zero coefficients. We call this space the *first-order interacting space*, and it is much smaller than the full Hilbert space: for the HF reference determinant, the first-order interacting space contains determinants which at most correspond to doubly-excited configurations, because the perturbation is a two-electron operator (see section 2.1.3). Moreover, singly-excited determinants do not contribute, as a consequence of Brillouin’s theorem (section 2.1.3). Only double excitations contribute to $|\varphi^{(1)}\rangle$, and their individual coefficients can be computed as

$$c_{ijab} = \frac{\langle \varphi^{(0)}_{\mathrm{HF}} | \hat{V} | \varphi^{ab}_{ij} \rangle}{E^{(0)} - E^{ab}_{ij}} \tag{2.59}$$

The denominator trivially reduces to $\epsilon_i + \epsilon_j - \epsilon_a - \epsilon_b$ as $E^{ab}_{ij} = E^{(0)} - \epsilon_i - \epsilon_j + \epsilon_a + \epsilon_b$. The numerator is computed as

$$\begin{aligned} \langle \varphi^{(0)}_{\mathrm{HF}} | \hat{V} | \varphi^{ab}_{ij} \rangle &= - \int \phi^{\dagger}_i(\mathbf{x}_1)\, \phi^{\dagger}_j(\mathbf{x}_2)\, \hat{g}_{12} \Big[ \phi_a(\mathbf{x}_1)\, \phi_b(\mathbf{x}_2) - \phi_a(\mathbf{x}_2)\, \phi_b(\mathbf{x}_1) \Big] \mathrm{d}\mathbf{x}_2\, \mathrm{d}\mathbf{x}_2 \\ &= -\Big( \langle \phi_i \phi_j | \phi_a \phi_b \rangle - \langle \phi_i \phi_j | \phi_b \phi_a \rangle \Big) \end{aligned} \tag{2.60}$$

Thus, the first-order correction to the wavefunction is expressed as

$$|\varphi^{(1)}\rangle = \sum_{\substack{a>b \\ i>j}} \frac{-\Big(\langle\phi_i\phi_j|\phi_a\phi_b\rangle - \langle\phi_i\phi_j|\phi_b\phi_a\rangle\Big)}{\epsilon_i + \epsilon_j - \epsilon_a - \epsilon_b} |\varphi_{ij}^{ab}\rangle \tag{2.61}$$

and the second-order energy correction is

$$E^{(2)} = \langle\varphi_{\mathrm{HF}}^{(0)}| \hat{V} |\varphi^{(1)}\rangle = \sum_{\substack{a>b \\ i>j}} \frac{\Big[\langle\phi_i\phi_j|\phi_a\phi_b\rangle - \langle\phi_i\phi_j|\phi_b\phi_a\rangle\Big]^2}{\epsilon_i + \epsilon_j - \epsilon_a - \epsilon_b} \tag{2.62}$$

The procedure described above gets a bit more complicated if the excited configurations are generated taking care of the spin, to guarantee that the generated states have the same eigenvalues of the spin operators as the reference functions. In such case, the excited states are neither normalised nor strictly orthogonal, and an additional orthonormalisation step has to be included before calculating the coefficients, in which excited determinants are linearly combined to form singlet and triplet CSFs.

### 2.1.7 CASPT2

Single-reference methods, such as Møller–Plesset perturbation theory, have been successful in modelling molecular systems close to their equilibrium structure. However, in cases of, e.g., bond breaking, excited states etc. a single-configuration reference function is qualitatively incorrect, and perturbation theory will not be able to recover a good approximation to the true state. Hence, a theory based on multiconfigurational reference functions is needed. Several approaches exist, among which the most popular and affordable is probably the complete active space second-order perturbation theory (CASPT2), that uses a CASSCF reference function.

Before moving to the description of the CASPT2 procedure, a short introduction to the second quantization formalism is needed, as this makes the CASPT2 equations simpler.

### 2.1.8 Second quantization formalism

In first quantization (i.e. traditional formulation), the Hamiltonian is expressed in terms of operators which are sums over particles (equations (2.27) and (2.28)). On the other hand, in the second quantization formalism, the summations run over the orbital space, and the Hamiltonian operator is expressed in terms of operators that "probe" whether a particle (electron) is present in some orbital and if so, include the contribution of that particular orbital.

The basics of second quantization are represented by creation ($\hat{a}_i^\dagger$) and annihilation operators ($\hat{a}_i$):

$$\hat{a}_i^\dagger |\phi_j, \phi_k, \ldots, \phi_N\rangle = |\phi_i, \phi_j, \phi_k, \ldots, \phi_N\rangle \tag{2.63}$$

$$\hat{a}_i |\phi_i, \phi_j, \phi_k, \ldots, \phi_N\rangle = |\phi_j, \phi_k, \ldots, \phi_N\rangle \tag{2.64}$$

in which $|\phi_j, \phi_k, \ldots, \phi_N\rangle$ represents a SD composed of the $\{\phi_j, \phi_k, \ldots, \phi_N\}$ spin-orbitals. As suggested by the above equations, $\hat{a}_i^\dagger$ creates a particle in spin-orbital $\phi_i$, while $\hat{a}_i$ annihilates it. The outcome of $\hat{a}_i^\dagger$ ($\hat{a}_i$) acting on a SD in which $\phi_i$ is already occupied (empty) is zero:

$$\hat{a}_i^\dagger |\phi_i, \phi_j, \phi_k, \ldots, \phi_N\rangle = 0 \tag{2.65}$$

$$\hat{a}_i |\phi_j, \phi_k, \ldots, \phi_N\rangle = 0 \tag{2.66}$$

As a result, any SD in second quantization can be expressed as the result of successive creation operators acting on the vacuum state:

$$|\phi_j, \phi_k, \ldots, \phi_N\rangle = \hat{a}_j^\dagger \hat{a}_k^\dagger \ldots \hat{a}_N^\dagger |\rangle \tag{2.67}$$

One- and two-electron operators in second quantization are expressed as summations over creation/annihilation operators:

$$\hat{f} = \sum_{i,j} f_{ij} \hat{a}_i^\dagger \hat{a}_j = \sum_{i,j} \langle\phi_i| \hat{h} |\phi_j\rangle \hat{a}_i^\dagger \hat{a}_j \tag{2.68}$$

$$\hat{g} = \frac{1}{2} \sum_{i,j,k,l} g_{ijkl} \hat{a}_i^\dagger \hat{a}_j^\dagger \hat{a}_k \hat{a}_l = \frac{1}{2} \sum_{i,j,k,l} \langle\phi_i\phi_j|\phi_k\phi_l\rangle \hat{a}_i^\dagger \hat{a}_j^\dagger \hat{a}_k \hat{a}_l \tag{2.69}$$

Thus, the electronic Hamiltonian in a second-quantized form is

$$\hat{H} = \sum_{i,j} f_{ij} \hat{E}_{ij} + \frac{1}{2} \sum_{i,j,k,l} g_{ijkl} \hat{e}_{ijkl} \tag{2.70}$$

where $\hat{E}_{ij}$ and $\hat{e}_{ijkl}$ are the one- and two-electron spin-adapted excitation operators, respectively:

$$\hat{E}_{ij} = \sum_{\sigma=\alpha}^{\beta} \hat{a}_{i\sigma}^\dagger \hat{a}_{j\sigma} \tag{2.71}$$

$$\hat{e}_{ijkl} = \hat{E}_{ij}\hat{E}_{kl} - \delta_{jk}\hat{E}_{il} \tag{2.72}$$

The expectation value of the electronic Hamiltonian operator (2.70) over a second-quantized wavefunction can be expressed as follows:

$$\begin{aligned} \langle\varphi| \hat{H} |\varphi\rangle &= \sum_{r,s} \sum_{i,j} C_r C_s f_{ij} \langle\Phi_r| \hat{E}_{ij} |\Phi_s\rangle + \frac{1}{2} \sum_{r,s} \sum_{i,j,k,l} C_r C_s g_{ijkl} \langle\Phi_r| \hat{e}_{ijkl} |\Phi_s\rangle \\ &= \sum_{i,j} f_{ij} \mathrm{D}_{ij} + \frac{1}{2} \sum_{i,j,k,l} g_{ijkl} \Gamma_{ijkl} \end{aligned} \tag{2.73}$$

where $C_r$, $C_s$ are the CI expansion coefficient and $\mathrm{D}_{ij}$, $\Gamma_{ijkl}$ are matrix elements of the one- and two-electron density matrices $\mathbf{D}$ and $\mathbf{\Gamma}$

$$\mathrm{D}_{ij} = \sum_{r,s} C_r C_s \langle\Phi_r| \hat{E}_{ij} |\Phi_s\rangle \tag{2.74}$$

$$\Gamma_{ijkl} = \sum_{r,s} C_r C_s \langle\Phi_r| \hat{e}_{ijkl} |\Phi_s\rangle \tag{2.75}$$

### 2.1.9 State-Specific (SS) CASPT2

In the SS-CASPT2 method each reference state is treated independently. In general this will work very well if the original CASSCF states are good qualitative representatives of the final states. However, if the reference states are poor (e.g. artificial mix of states in CASSCF wavefunctions due to lack of dynamic electron correlation) convergence is slow, and the obtained results are quantitatively wrong. In such cases, multi-state versions of CASPT2 must be applied (see below).

The SS-CASPT2 method is based on (i) a multi-configurational CASSCF reference wavefunction, and (ii) a partitioning of the Hamiltonian, such that it reduces down to MP2 partitioning if the CASSCF wavefunction is reduced down to a single-determinant wavefunction.

The reference Hamiltonian is defined to be the generalised molecular Fock operator

$$\hat{F}(\mathbf{D}) = \sum_{i,j} f_{ij}(\mathbf{D})\hat{E}_{ij} \tag{2.76}$$

which, for a multideterminant CASSCF wavefunction, depends on the density matrix of the reference state as

$$f_{ij}(\mathbf{D}) = h_{ij} + \sum_{k,l} \mathrm{D}_{kl}\Big[\langle\phi_i\phi_j|\phi_k\phi_l\rangle - \frac{1}{2}\langle\phi_i\phi_j|\phi_l\phi_k\rangle\Big] \tag{2.77}$$

In the case of a closed-shell single-determinant wavefunction, the $f_{ij}$ elements are identical to the HF case, and the reference Hamiltonian coincides with the MP2 one.

Concerning the generation of the excited states that define the first-order correction to the reference wavefunction, the configuration space (spanned by all possible CSFs within the molecular orbitals) is divided into four subspaces:

- $V_0$: including configurations that appear in $|\varphi^{(0)}\rangle$;
- $V_{\mathrm{K}}$: including all other configurations that are possible within the CASSCF active space but that give a zero contribution to $|\varphi^{(0)}\rangle$;
- $V_{\mathrm{SD}}$: single and double replacement CSFs generated from $V_0$;
- $V_{\mathrm{TQ...}}$: higher order replacement CSFs generated from $V_0$.

Again, due to the one- and two-electron operators present in the Hamiltonian, only states in $V_{\mathrm{SD}}$ interact with the reference state through $\hat{H}$ and contribute to the first order wavefunction. The CSFs in $V_{\mathrm{SD}}$ are generated by the spin-averaged excitation operators acting on $|\varphi^{(0)}\rangle$, excluding the excited configurations within the active space, which belong to $V_{\mathrm{K}}$. The $V_{\mathrm{SD}}$ subspace can be further divided into eight subspaces:

The single excitations can be generated by linear combinations of the double excitations, however, they do not contribute to the first-order correction due to Brillouin's theorem (see above).

| | | | |
|---|---|---|---|
| **interal** | $\hat{E}_{\text{act-inact}}\hat{E}_{\text{act}'\text{-act}''}$ | | (a) |
| | $\hat{E}_{\text{act-inact}}\hat{E}_{\text{act}'\text{-inact}'}$ | | (b) |
| **semi-internal** | $\hat{E}_{\text{virt-act}}\hat{E}_{\text{act}'\text{-act}''}$ | | (c) |
| | $\hat{E}_{\text{virt-inact}}\hat{E}_{\text{act-act}'}$ | $\hat{E}_{\text{act-inact}}\hat{E}_{\text{virt-act}'}$ | (d) |
| | $\hat{E}_{\text{act-inact}}\hat{E}_{\text{virt-inact}'}$ | | (e) |
| **external** | $\hat{E}_{\text{virt-act}}\hat{E}_{\text{virt}'\text{-act}'}$ | | (f) |
| | $\hat{E}_{\text{virt-inact}}\hat{E}_{\text{virt}'\text{-act}}$ | | (g) |
| | $\hat{E}_{\text{virt-inact}}\hat{E}_{\text{virt}'\text{-inact}'}$ | | (h) |

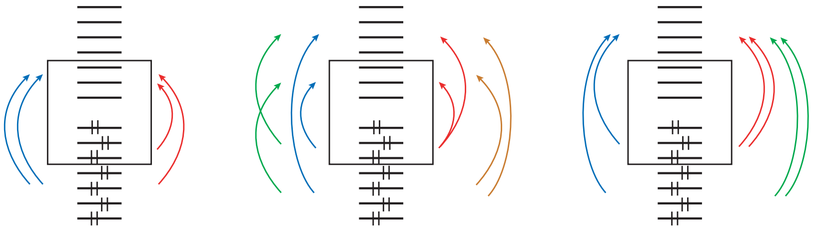

(a) **internal** (b) **semi-internal** (c) **external**

**Figure 2.3:** Classification of excitations generating the $V_{\text{SD}}$ subspaces based on the number of virtual indices in (a) internal, 0 virtual indices; (b) semi-internal, 1 virtual index; (c) external, 2 virtual indices.

At this point, two issues have to be resolved, which are common to most versions of multiconfigurational reference perturbation theory beyond MPPT:

1. the reference wavefunction is no more an eigenfunction of the reference Hamiltonian defined in equation (2.76);
2. we have only exact knowledge about the reference functions, and not about the complementary functions that extend to the full Hilbert space (i.e. complete infinite set of excited states).

The latter problem is addressed by construction of an artificial set of functions $\{\varphi_i\}$ with properties

$$\langle\varphi_i|\varphi_j\rangle = \delta_{ij} \quad \text{and} \quad \langle\varphi_i|\varphi^{(0)}\rangle = 0 \tag{2.78}$$

In SS-CASPT2 the complementary functions are built using configurations in the $V_{\text{SD}}$ space.

The first problem is solved by using projection operators. A projection operator $\hat{P}_{\text{X}}$ is defined for each subspace $V_{\text{X}}$

$$\hat{P}_{\text{X}} = \sum_{i\in \text{X}} |\varphi_i\rangle\langle\varphi_i| \tag{2.79}$$

in terms of which the reference Hamiltonian is now expressed as

$$\hat{H}_0 = \hat{P}_0\hat{F}(\mathbf{D})\hat{P}_0 + \hat{P}_{\text{K}}\hat{F}(\mathbf{D})\hat{P}_{\text{K}} + \hat{P}_{\text{SD}}\hat{F}(\mathbf{D})\hat{P}_{\text{SD}} + \hat{P}_{\text{TQ...}}\hat{F}(\mathbf{D})\hat{P}_{\text{TQ...}} \tag{2.80}$$

for which it is trivial to verify that both the reference and the complementary space functions are eigenstates. However, in contrast with MP2, the reference Hamiltonian (2.80) will not be diagonal, but rather block-diagonal as follows:

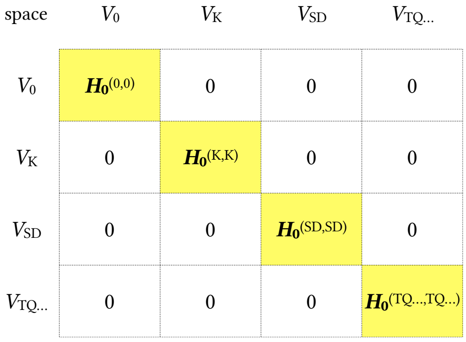

| space | $V_0$ | $V_K$ | $V_{SD}$ | $V_{TQ...}$ |
|---|---|---|---|---|
| $V_0$ | $\boldsymbol{H_0}^{(0,0)}$ | 0 | 0 | 0 |
| $V_K$ | 0 | $\boldsymbol{H_0}^{(K,K)}$ | 0 | 0 |
| $V_{SD}$ | 0 | 0 | $\boldsymbol{H_0}^{(SD,SD)}$ | 0 |
| $V_{TQ...}$ | 0 | 0 | 0 | $\boldsymbol{H_0}^{(TQ...,TQ...)}$ |

The first order wavefunction is then expanded into a set of functions $|\varphi_j\rangle$ from $V_{\text{SD}}$:

$$|\varphi^{(1)}\rangle = \sum_{j=1}^{M} C_j\, |\varphi_j\rangle \qquad |\varphi_j\rangle = 1, \ldots, M \text{ in } V_{SD} \tag{2.81}$$

If we now use this ansatz in equation (2.46) and project both sides onto $\langle\varphi_i|$ we obtain an equation for the expansion coefficients:

$$\sum_{j=1}^{M} C_j \, \langle\varphi_i|\, \hat{H}_0 - E^0 \,|\varphi_j\rangle = -\,\langle\varphi_i|\, \hat{V}\, |\varphi^{(0)}\rangle \qquad |\varphi_j\rangle = 1, \ldots, M \tag{2.82}$$

or, in matrix form

$$(\mathbf{H}_0 - E^0 \mathbb{I})\, \mathbf{C} = -\mathbf{V} \tag{2.83}$$

The $|\varphi_j\rangle$ functions are neither normalised not necessarily orthogonal and may also be linearly dependent, therefore their number $M$ can also be grater than the dimension of $V_{\text{SD}}$. Hence, orthonormalisation and elimination will have to be carried out to generate a non-redundant set of orthonormalised excited states. The overlap matrix $\text{S}_{ij} = \langle\varphi_i|\varphi_j\rangle$ is then diagonalised

$$\mathbf{s} = \mathbf{U}^{\dagger}\mathbf{S}\mathbf{U} \tag{2.84}$$

and the output orthogonal vectors normalised:

$$\tilde{\mathbf{U}} = \mathbf{U}\mathbf{s}^{-\frac{1}{2}} \tag{2.85}$$

We now have a set of orthonormalised doubly excited states which are computed as

$$|\tilde{\varphi}_i\rangle = \sum_j \tilde{\text{U}}_{ji}\, |\varphi_j\rangle \tag{2.86}$$

All other matrices and vectors are transformed to the space of the orthonormalised excited states

$$\tilde{\mathbf{H}}_0 = \tilde{\mathbf{U}}^{\dagger}\mathbf{H}_0\tilde{\mathbf{U}} \quad \text{and} \quad \tilde{\mathbf{V}} = \tilde{\mathbf{U}}^{\dagger}\mathbf{V} \tag{2.87}$$

The coefficients $\tilde{\mathbf{C}}$ in the expression for the first-order correction to the wavefunction are then found by solving

$$(\tilde{\mathbf{H}}_0 - E^0 \mathbb{I})\, \tilde{\mathbf{C}} = -\tilde{\mathbf{V}} \tag{2.88}$$

Due to the non-diagonal form of the operator on the left-hand side and because of the size of the problem, the solution has to be found iteratively starting from a trial vector of coefficients.

Eventually, the second-order correction to the energy can be computed as

$$E^{(2)} = \langle \varphi^{(0)} | \hat{V} | \varphi^{(1)} \rangle = \tilde{\mathbf{V}}^{\dagger} \tilde{\mathbf{C}} = -\tilde{\mathbf{V}}^{\dagger} (\tilde{\mathbf{H}}_0 - E^0 \mathbb{I})^{-1} \tilde{\mathbf{V}} \tag{2.89}$$

From equation (2.89) it follows that $V_{\mathrm{SD}}$ configurations with energies close to the reference energy $E^{(0)}$ will lead to an overestimation or even singularities of the perturbation energy. This is know as the "intruder state" problem[19]. As perturbation theory holds only for small perturbations, such configurations should be included already in the preceding CASSCF calculation. If this is not practicable, a level shift technique can be applied, adding a finite shift (normally $0.1 - 0.3$ a.u.) to $E^{(0)}$ which removes the effect of the intruder state. Caution is required that no new intruder states arise by accidental degeneracy of the shifted reference energy with energies of other configurations.

The SS-RASPT2[20] and SS-GASPT2 methods also exists, which use restricted and general active space reference functions. They are equivalent to CASPT2, however, in the generation of the $V_{\mathrm{SD}}$ subspace, an additional class of excitations has to be considered, in which all indices are active (this was not present in CASPT2 as all excitations within the active orbitals was already included in $V_0$ or $V_{\mathrm{K}}$). This small difference implies significant computational challenges in defining the $V_{\mathrm{SD}}$ space, therefore, in the current implementations of both RASPT2 and GASPT2, an approximation is employed in removing the active–active excitations from the first-order interacting space. The effect of this approximation is a degradation in the accuracy of the perturbative treatment compared to CASPT2, however, it is expected that the possibility of using larger active spaces for the reference RASSCF/GASSCF functions will compensate for it.

As mentioned at the beginning of this section, SS-CASPT2 is not reliable in case the reference CASSCF wavefunction is qualitatively wrong due to the lack of dynamic correlation. If this is the case, a bigger active space would be a trivial but expensive (or not even feasible) solution. In order to overcome this problem, a multi-state version of perturbation theory was developed, that allows the reference states to mix with each other as the perturbation is introduced order by order (something that was not contemplated in SS-CASPT2). This is done through an "effective Hamiltonian" that gives corrected energies acting on corrected model states, which are linear combinations of the original reference states. Multi-state CASPT2 methods are based on quasi-degenerate perturbation theory (QDPT) and make use of Bloch equation, which is introduced in the next section.

### 2.1.10 Quasi-degenerate perturbation theory: the Bloch equation.

Modern applications of the perturbation technique are often based on the effective operator formalism introduced by Bloch in 1958[21]. In this formalism, we consider a subset of the eigenstates of the system, called the *model space*. The basic idea is that the effect of the true operator $\hat{H}$ operating in the entire Hilbert space can be reproduced by an "effective" operator $\hat{H}_{\mathrm{eff}}$ operating only within the model space.

Out of the complete set of orthonormal solutions of the unperturbed Hamiltonian $\hat{H}_0$, some will be part of (and define) the *model space* $P$, while the remaining eigenfunctions will be part of (and define) the so called *orthogonal space* $Q$. It is assumed that all eigenfunctions of $\hat{H}_0$ sharing the same eigenvalue are part of the same subspace. Each of the two subspaces has a projector operator:

$$\hat{P} = \sum_{a \in \mathrm{P}} |\varphi_a^{(0)}\rangle \langle \varphi_a^{(0)}| \tag{2.90}$$

$$\hat{Q} = 1 - \hat{P} = \sum_{r \notin \mathrm{P}} |\varphi_r^{(0)}\rangle \langle \varphi_r^{(0)}| \tag{2.91}$$

with the properties:

$$\hat{P} = \hat{P}^\dagger = \hat{P}\hat{P} \qquad \hat{P}\hat{Q} = \hat{Q}\hat{P} = 0 \qquad \left[\hat{P}, \hat{H}_0\right] = \left[\hat{Q}, \hat{H}_0\right] = 0 \tag{2.92}$$

$\hat{P}$ can be used to project the exact wavefunction of state $\alpha$ onto the the model space

$$\hat{P}\,|\varphi_\alpha\rangle = \sum_{j=1}^{d} c_{\alpha j}\,|\varphi_j^{(0)}\rangle = |\varphi_\alpha^{(0)}\rangle \qquad \alpha = 1, 2, \dots, d \tag{2.93}$$

The projections $|\varphi_\alpha^{(0)}\rangle$ are called the *model states* or *model functions* and are not solutions of $\hat{H}_0$. They are expressed by linear combinations of the reference states in the model space.

If the model space includes $d$ states, it can be shown that there is a one-to-one correspondence between the $d$ eigenfunctions of the full Hamiltonian $|\varphi_\alpha\rangle$ and their projection onto the model space $|\varphi_\alpha^{(0)}\rangle$. If the perturbation is gradually reduced until it is switched off, the $|\varphi_\alpha\rangle$ states must reduce to the reference states $|\varphi_a\rangle$. If we turn on the perturbation again, the model states change due to the mixing within the model space, but they are still expected to be distinct. Therefore, there is a one-to-one correspondence between them and the eigenfunctions of $\hat{H}$. This correspondence allows to write an operator (called the wave operator, $\hat{\Omega}$) that transforms the model states into the real eigenfunctions:

$$|\varphi_\alpha\rangle = \hat{\Omega}\,|\varphi_\alpha^{(0)}\rangle \qquad \alpha = 1, 2, \dots, d \tag{2.94}$$

$\hat{\Omega}$ is the same for all model states and has the following properties:

- it gives a null result if applied to the orthogonal space:

$$\hat{\Omega}\,\hat{Q} = 0 \tag{2.95}$$

- Since $\hat{P} + \hat{Q} = 1$, and $\hat{\Omega}\,\hat{Q} = 0$, it follows directly that

$$\hat{\Omega}\,\hat{P} = \hat{\Omega} \tag{2.96}$$

- transforming the model functions into the $|\varphi_\alpha\rangle$ and then re-projecting them onto the model space, leaves the model states unchanged, therefore

$$\hat{P}\,\hat{\Omega} = \hat{P} \tag{2.97}$$

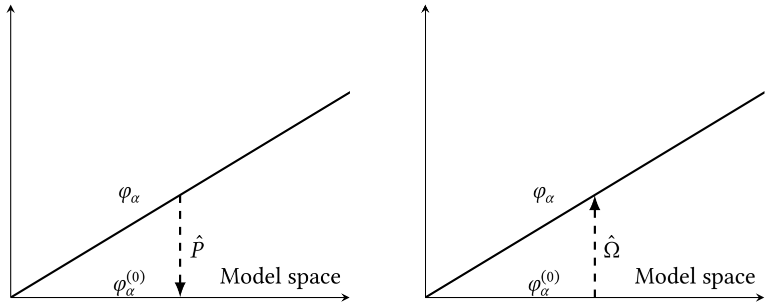

**Figure 2.4:** Illustration of the projection and wave operators.

Even though $\hat{P}$ transforms the $|\varphi_\alpha\rangle$ into the $|\varphi_\alpha^{(0)}\rangle$, while $\hat{\Omega}$ performs exactly the opposite transformation, this does not mean that $\hat{\Omega}$ is the inverse of $\hat{P}$ in the ordinary sense. Figure 2.4 illustrates the action of the two operators.

We can plug equation (2.94) in the Schrödinger equation for the full Hamiltonian and operate with $\hat{P}$ to the left on both sides obtaining

$$\hat{P}\hat{H}\hat{\Omega}\,|\varphi_\alpha^{(0)}\rangle = E_\alpha \hat{P}\hat{\Omega}\,|\varphi_\alpha^{(0)}\rangle = E_\alpha\,|\varphi_\alpha^{(0)}\rangle \qquad \alpha = 1, 2, \ldots, d \tag{2.98}$$

$\hat{P}\hat{H}\hat{\Omega}$ is the expression for the effective Hamiltonian operator $\hat{H}_{\text{eff}}$ which generates $d$ exact eigenvalues when operating on the model space:

$$\hat{H}_{\text{eff}} = \hat{P}\hat{H}\hat{\Omega} = \hat{P}\hat{H}\hat{\Omega}\hat{P} \tag{2.99}$$

Its eigenfunctions are the projection of the real eigenstates onto the model space. These projections are not necessarily orthogonal and, therefore, $\hat{H}_{\text{eff}}$ is generally non hermitian.

The exact energy is given by:

$$E_\alpha = \langle\varphi_\alpha^{(0)}|\,\hat{H}_{\text{eff}}\,|\varphi_\alpha^{(0)}\rangle \tag{2.100}$$

To get get an expression of the wave operator that is independent of the unknown energy $E_\alpha$, we can operate operate with $\hat{\Omega}$ to the left on Schrödinger's equation and make use of the properties listed above to obtain:

$$(E_\alpha - \hat{\Omega}\hat{H}_0\hat{P})\,|\varphi_\alpha\rangle = \hat{\Omega}\hat{V}\,|\varphi_\alpha\rangle \tag{2.101}$$

This allows to eliminate $E_\alpha$ by subtracting the last result to Schrödinger's equation:

$$\begin{aligned}
(E_\alpha - \hat{H}_0)\,|\varphi_\alpha\rangle - (E_\alpha - \hat{\Omega}\hat{H}_0\hat{P})\,|\varphi_\alpha\rangle &= \hat{V}\,|\varphi_\alpha\rangle - \hat{\Omega}\hat{V}\,|\varphi_\alpha\rangle \\
\cancel{E_\alpha|\varphi_\alpha\rangle} - \hat{H}_0\,|\varphi_\alpha\rangle - \cancel{E_\alpha|\varphi_\alpha\rangle} + \hat{\Omega}\hat{H}_0\hat{P}\,|\varphi_\alpha\rangle &= \hat{V}\,|\varphi_\alpha\rangle - \hat{\Omega}\hat{V}\,|\varphi_\alpha\rangle \\
\hat{\Omega}\hat{H}_0\,|\varphi_\alpha^{(0)}\rangle - \hat{H}_0\hat{\Omega}\,|\varphi_\alpha^{(0)}\rangle &= \hat{V}\hat{\Omega}\,|\varphi_\alpha^{(0)}\rangle - \hat{\Omega}\hat{V}\hat{\Omega}\,|\varphi_\alpha^{(0)}\rangle \\
(\hat{\Omega}\hat{H}_0 - \hat{H}_0\hat{\Omega})\,|\varphi_\alpha^{(0)}\rangle &= (\hat{V}\hat{\Omega} - \hat{\Omega}\hat{V}\hat{\Omega})\,|\varphi_\alpha^{(0)}\rangle
\end{aligned} \tag{2.102}$$

The last result is called the Bloch equation, which can be also written as

$$[\hat{\Omega}, \hat{H}_0] = \hat{V}\hat{\Omega} - \hat{\Omega}\hat{V}\hat{\Omega} \tag{2.103}$$

Moreover, since $\hat{\Omega}$ gives zero when operating on the orthogonal space, it follows that the above relation holds in the entire space.

Usually, the wave operator is also expanded in powers of the perturbation with $\hat{\Omega}^{(0)} = \hat{P}$, which leads to a series of equations (one for each power of the perturbation parameter):

$$[\hat{\Omega}^{(n)}, \hat{H}_0] = \hat{Q}\hat{V}\hat{\Omega}^{(n-1)} - \sum_{k=1}^{n-1} \hat{\Omega}^{(n-k)}\hat{V}\hat{\Omega}^{(k-1)} \tag{2.104}$$

Using the expansion of $\hat{\Omega}$, the effective Hamiltonian up to second order is

$$\hat{H}^{[2]}_{\text{eff}} = \hat{H}^{(0)}_{\text{eff}} + \hat{H}^{(1)}_{\text{eff}} + \hat{H}^{(2)}_{\text{eff}} = \hat{P}\hat{H}\hat{P} + \hat{P}\hat{H}\hat{\Omega}^{(1)}\hat{P} \tag{2.105}$$

with matrix elements

$$\langle \varphi^{(0)}_a | \hat{H}^{[2]}_{\text{eff}} | \varphi^{(0)}_a \rangle = E^{[2]}_a \tag{2.106}$$

$$\langle \varphi^{(0)}_a | \hat{H}^{[2]}_{\text{eff}} | \varphi^{(0)}_b \rangle = \langle \varphi^{(0)}_a | \hat{H} | \varphi^{(0)}_b + \varphi^{(1)}_b \rangle \tag{2.107}$$

The effective Hamiltonian can eventually be diagonalised to derive the model states of the model space.

### 2.1.11 Multi-State (MS) CASPT2

QDPT requires $\hat{H}_0$ and $\hat{H}^{[2]}_{\text{eff}}$ to be unique for all the reference states. The multi-state CASPT2 method proposed in 1998 Finley and co-workers[22] is a hybrid approach between QDPT and SS-CASPT2 which resolves cases where the reference CASSCF wavefunctions do not meet the qualitative requirements for a fast convergence of the perturbation expansion. It is an application of the above described *perturb-then-diagonalise* technique (i.e. in which the final step is the diagonalisation of $\hat{H}_{\text{eff}}$) in which the model space is defined by a group of CASSCF reference functions.

In the construction of the effective Hamiltonian (equations (2.106) and (2.107)) the diagonal elements are the SS-CASPT2 energies

$$\langle \varphi^{(0)}_a | \hat{H}^{[2]}_{\text{eff},\,a} | \varphi^{(0)}_a \rangle = E^{\text{SS-CASPT2}}_a \tag{2.108}$$

However, the SS-CASPT2 energies are computed with a reference Hamiltonian which is state-specific, and this raises a problem when calculating the off-diagonal elements of the resulting $\hat{H}_{\text{eff}}$, which is consequently not symmetric:

$$\langle \varphi^{(0)}_a | \hat{H}^{[2]}_{\text{eff},\,b} | \varphi^{(0)}_b \rangle = \langle \varphi^{(0)}_a | \hat{H} | \varphi^{(1)}_b \rangle \neq \langle \varphi^{(0)}_b | \hat{H}^{[2]}_{\text{eff},\,a} | \varphi^{(0)}_a \rangle = \langle \varphi^{(0)}_b | \hat{H} | \varphi^{(1)}_a \rangle \tag{2.109}$$

In the current implementation this problem is fixed with a simple symmetrisation of the matrix with the limitation that results should be questioned if corresponding off-diagonal elements are large and different. It has been demonstrated that the MS-CASPT2 method resolves cases with accidental degeneracy at the CASSCF level if it does not persist at the SS-CASPT2 level. On the other hand, the MS-CASPT2 can provide erroneous behaviour around conical intersections and other cases of near-degeneracy, due to the rapid changes in the wavefunction for small geometrical displacements observed around CIs (which induces changes in the reference “SS-based” hamiltonian and, therefore, in the perturbation, resulting in discontinuities of the PESs). The latter problem is known to be a consequence of the use of state-specific effective operators, and the extended multi-state version of the method (XMS-CASPT2) was later suggested to overcome these problems.

### 2.1.12 Extended Multi-State (XMS) CASPT2

One of the qualitative criteria which a quasi-degenerate perturbation theory should satisfy is that the eigenvalues of the effective Hamiltonian should be invariant to the particular basis functions selected to span the model space, as long as they span the same subspace. To fulfil such requirement, Granovsky[23] suggested that, in the calculation of the diagonal elements for $\hat{H}_{\text{eff}}$, the $\hat{H}_0$ operator of SS-CASPT2 should be constructed including all the reference states in the $V_0$ space, i.e. the $\hat{H}_0^{(0,0)}$ block should be extended from

$$\hat{H}_0^{(0,0)} = \sum_i |\varphi_i\rangle \langle\varphi_i| \hat{F} |\varphi_i\rangle \langle\varphi_i| \tag{2.110}$$

to

$$\hat{H}_0^{(0,0)} = \sum_{i,j} |\varphi_i\rangle \langle\varphi_i| \hat{F} |\varphi_j\rangle \langle\varphi_j| \tag{2.111}$$

In this way, $\hat{H}_0$ is explicitly independent of the selection of the basis functions spanning a particular model space. The $\hat{H}_0$ matrix is then diagonalised and the "traditional" MS procedure is then continued in the basis of these new eigenfunctions[24].

The use of an average $\hat{H}_0$ operator common to all states resolves the problem of discontinuity of the PES at the MS-CASPT2 level, however, at the expenses of the accuracy of the results in regions where the reference states are well-separated in energy. For this reason, SS- or MS-CASPT2 are typically more reliable for the prediction of vertical excitation energies far from crossing regions, while XMS-CASPT2 should be trusted close to CIs. Recently, a new method called extended dynamically weighted CASPT2 (XDW-CASPT2) has been proposed[25], that performs similarly to MS-CASPT2 where the electronic states are energetically well separated and is equivalent to XMS-CASPT2 in case the underlying zeroth-order references are near-degenerate. It basically interpolates between the two methods based on the coupling (mixing) between the reference SS-CASPT2 states, and it has proven to be a very promising method.

## 2.2 Time-dependent methods: nuclear dynamics

The separation of time and space variables introduced at the beginning of this chapter is a valid strategy to study the electronic structure at the key geometries determining a photochemical/photophysical event (e.g. energy minima, conical intersections, transition states). The static studies alone, however, are often insufficient to get a complete picture of the mechanism behind because, in a real experiment, the kinetic energy will drive the molecules away from energy minima, visiting other regions of the PESs. Therefore, dynamics simulations are necessary to get accurate predictions of excited state lifetimes, photoreaction quantum yields and accessibility of the various decay channels.

The simulation of the nuclear and electronic dynamics can be done at several levels of theory: one extreme is represented by classical molecular dynamics (MD) in which the nuclei move classically subject to a force field (FF) which is parameterised specifically for an electronic state based on QM calculations or experimental data. Classical MD simulations are very powerful tools for ground state processes, while they are more difficult to adapt to excited states and photochemical reactions. The other extreme is represented by quantum dynamics (QD) in which both nuclei and electrons are treated quantum mechanically. QD simulations are very accurate and allow to predict quantum effects in the nuclear dynamics like coherence phenomena, tunnelling processes, branching at conical intersections or the interaction with light, but they are also very expensive and applicable only to small systems. Indeed, such an accurate treatment of nuclei and electrons requires either to reduce significantly the number of nuclear degrees of freedom, or to treat many nuclear coordinates but in approximate way (e.g. harmonic approximation). The former approach is briefly described in the next section 2.2.1, while the leading technique in multidimensional QD (i.e. MCTDH) is introduced in section 2.2.2.

In between classical and quantum dynamics, a plethora of techniques exist. One of the most popular is the trajectory surface-hopping (TSH) technique, in which the nuclei are propagated classically on a QM electronic potential which is either precomputed or calculated on-the-fly, and the non adiabatic events are treated stochastically. Such methods are introduced in section 2.2.3.

### 2.2.1 Exact quantum dynamics in a reduced-coordinate space

One technique to perform QD for molecular systems is grid-based quantum dynamics, in which the molecular wavepacket (i.e. the continuous nuclear wavefunction $\chi(\mathbf{R}, t)$) is represented in terms of a discrete set of time-evolving complex amplitudes at a set of grid points. Comparing this method to the representation of the wavefunction in terms of conventional basis of orthogonal functions (called the *spectral basis*, e.g. in the basis of stationary vibrational eigenfunctions), the amplitudes at grid points can be interpreted as the coefficients of localised basis functions derived from unitary transformation of the spectral basis (the so called *pseudospectral basis*). This approach is only feasible in few dimensions due to exponential computational cost: assuming that each degree of freedom requires $n$ grid points, an exact (i.e. full-dimensional) wavepacket representation of a non-linear molecule with $3N - 6$ nuclear degrees of freedom requires $n^{3N-6}$ total grid points, which rapidly becomes unfeasible, even for small molecules. This issue is known as “the curse of dimensionality”, and it is the motivation behind the biggest approximation in grid-based quantum dynamics: the number of coordinates included in the model must be significantly reduced. This approximation, however, is not so crude in the case of ultrafast (i.e. sub-ps) chemical processes like photochemical reactions, as the system does not have time to redistribute the energy in many modes (a process that typically requires several ps). As a consequence, photoinduced processes are often well described by only few (1-3) relevant coordinates. Figure 2.5 shows the necessary steps for a grid-based QD simulation. The preliminary steps to the propagation are needed to set up the complete Hamiltonian in arbitrary reduced coordinates, i.e. computation of PESs and NACs as well as a general transformation protocol for the kinetic energy operator from Carte-

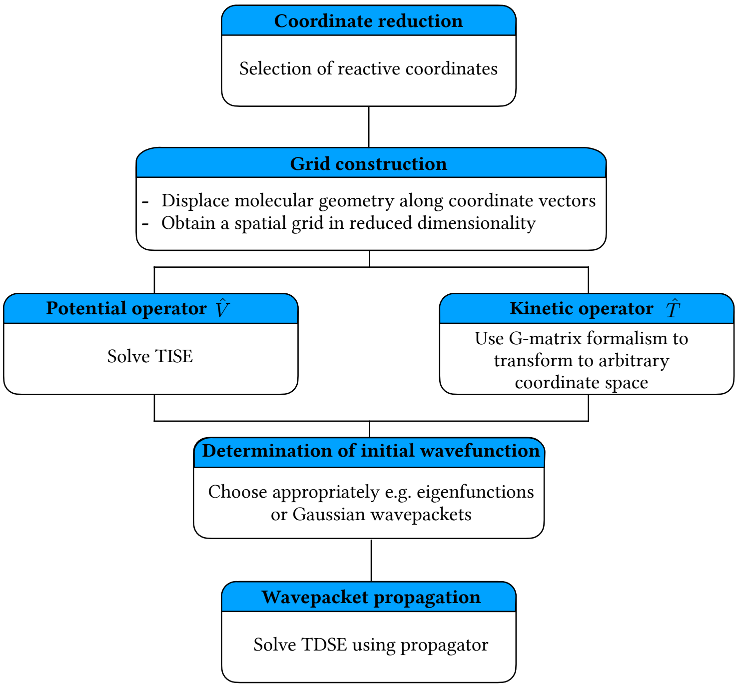

**Figure 2.5:** Overview of the necessary steps to set up a wavepacket simulation in reduced coordinates on pre-calculated PESs. Adapted from reference[19].

sian to arbitrary coordinates.

The starting point for QD is the TDSE (2.1), whose solution yields the time evolution of the molecular system. Due to the complexity of quantum dynamical simulations, analytical solutions are rarely possible and numerical propagation schemes are needed. As shown at the beginning of this chapter, the time evolution of a molecular system is due to the superposition of stationary states (i.e. a wavepacket), which creates an interference (third term in equation (2.12)) containing all the time dependence of the probability density and other observable quantities. The Born-Oppenheimer approximation leads to the separation of electronic and nuclear degrees of freedom, allowing to calculate electronic energy in all the grid points, using the methods described in the previous section. Subsequently, the nuclear wavefunction can be propagated in time on the pre-calculated PES.

The time dependence in the nuclear TDSE

$$i\hbar\frac{\partial}{\partial t}\chi(\mathbf{R},t) = \hat{H}\,\chi(\mathbf{R},t) \tag{2.112}$$

is determined by the action of a propagator $\hat{U}(t,t_0)$ on the nuclear wavefunction:

$$\chi(\mathbf{R},t) = \hat{U}(t,t_0)\,\chi(\mathbf{R},t_0) = e^{-\hat{H}(t-t_0)}\,\chi(\mathbf{R},t_0) \tag{2.113}$$

In the grid method, the propagator can be implemented in several ways, originating different propagation schemes (e.g. expansion of the exponential in Taylor series or Chebychev polynomials, see reference[19]).

The dynamics of ultrafast photochemical processes is started by the interaction with light, typically with femto-second laser pulses. After the excitation, $n$ electronic states my be involved in the process, and the TDSE may be represented in matrix form:

$$i\hbar\frac{\partial}{\partial t}\begin{pmatrix} a_1(t)\chi_1(\mathbf{R},t) \\ \vdots \\ a_n(t)\chi_n(\mathbf{R},t) \end{pmatrix} = \begin{pmatrix} H_{11} & \cdots & H_{nn} \\ \vdots & \ddots & \vdots \\ H_{1n} & \cdots & H_{nn} \end{pmatrix} \begin{pmatrix} a_1(t)\chi_1(\mathbf{R},t) \\ \vdots \\ a_n(t)\chi_n(\mathbf{R},t) \end{pmatrix} \tag{2.114}$$

The nuclear wavefunction is then distributed over several PESs according to the time-dependent expansion coefficients $a_n(t)$. The diagonal elements of the Hamiltonian matrix describe the uncoupled dynamics on the individual PES

$$H_{ii} = T_{ii} + V_{ii}(\mathbf{R}) \tag{2.115}$$

where $V_{ii}(\mathbf{R})$ is the pre-calculated PES of state $i$, and $T_{ii}$ the kinetic energy, which is equal for all states. Coupling between the different electronic states is described by the off-diagonal elements. They may reflect the interaction with the laser light, an intramolecular coupling like non-adiabatic and spin–orbit coupling, or all couplings simultaneously.

When the aim is to perform dynamics in a reduced coordinate space, both diagonal and off-diagonal Hamiltonian elements must be expressed in the reduced coordinates. Chapter 3 is fully dedicated to the parameterisation protocol for the Hamiltonian, starting from the selection of the reactive coordinates and following with PESs and coupling calculation/projection onto the reduced coordinates. Concerning the kinetic term $T_{ii}$, the G-matrix formalism is a powerful technique to convert the cartesian kinetic energy operator

$$\hat{T}_x = -\frac{\hbar^2}{2}\sum_{i=1}^{3N}\frac{1}{m_i}\frac{\partial^2}{\partial x^2} \tag{2.116}$$

to any arbitrary set of coordinates. Given a set of $3N$ ($N$ = number of atoms) cartesian coordinates $\{x\}$ which must be reduced to $M$ reactive coordinates $\{q\}$, the G-matrix (i.e. metric tensor) of the new set of coordinates can be written as

$$G_{rs} = \sum_{i}^{3N}\frac{i}{m_i}\frac{\partial q_r}{\partial x_i}\frac{\partial q_s}{\partial x_i} \tag{2.117}$$

where the summation is conducted over all three cartesian degrees of freedom of each atom $i$ with mass $m_i$. Using the G-matrix elements (and with some simplifying assumptions detailed in referece[19]), the kinetic operator can be written as

$$\hat{T}_q \approx -\frac{\hbar^2}{2}\sum_{r=1}^{M}\sum_{s=1}^{M}\frac{\partial}{\partial q_r}\left[G_{rs}\frac{\partial}{\partial q_s}\right] \tag{2.118}$$

This is a very general formulation of the kinetic energy operator in arbitrary coordinates $q$. In contrast to $\hat{T}_x$ (equation (2.116)), $\hat{T}_q$ contains cross partial derivatives with respect to $q_r$ and $q_s$, which represent a kinetic coupling between two coordinates. These cross terms originate from non-orthogonal connections of cartesian components and mean that a motion along $q_r$ induces a motion along $q_s$ with a certain amplitude corresponding to the degree of the kinetic coupling.

The exact QD outlined here can only be performed in very few coordinates. If it is not possible to reduce the dimensionality of the problem, alternative methods like MCTDH are able to include more modes. The inclusion of many coordinates, however, goes at the expense of the topographical information of the PES, and the best QD method must be carefully chosen for each specific process.

### 2.2.2 Quantum dynamics in many coordinates: the MCTDH method

The Multi-Configuration Time-Dependent Hartree (MCTDH) method[26–28] keeps a fully quantum mechanical picture while removing the scaling problem of standard QD methods, that rely on time-independent nuclear basis sets. Its power lies in the fact that it efficiently yields approximate solutions to TDSE using time dependent basis functions, whose equations of motions are derived through application of a variational principle. The time evolution of the basis functions ensures that the basis set remains optimal and small, that is, the wavefunction representation is very compact, allowing up to 50 or more degrees of freedom. The MCTDH method can be considered as the time-dependent analogue of the CASSCF methods in electronic structure theory (in which both the CI expansion coefficients and the MO basis function are optimised).

The first idea of a time-dependent basis was introduced by McLachlan in the 60s[29], who used a simple Hartree product as wavefunction, with one basis function for each degree of freedom of the system. The resulting method is known as the time-dependent Hartree (TDH) method. For a system with two degrees of freedom ($x$ and $y$), the TDH wavefunction is

$$\mathrm{X}(x, y, t) = a(t)\chi_1(x, t)\chi_2(y, t) \tag{2.119}$$

where $a(t)$ is a time-dependent complex coefficient and $\chi_1(x, t), \chi_2(y, t)$ are time-dependent basis functions called single particle functions (SPFs), which can be e.g. solutions of harmonic oscillator, Legendre rotator etc. This equation does not determine the single-particle functions uniquely, since it is always possible to multiply one SPF by an arbitrary factor and divide another SPF by the same factor without changing the total wavefunction. Moreover, the introduction of the $a(t)$ coefficient gives the same amount of arbitrariness to all basis functions. To ensure unique equations of motion, the constraint that the SPFs remain normalised at all times is introduced

$$\langle\chi_1|\frac{\partial}{\partial t}\chi_1\rangle = \langle\chi_2|\frac{\partial}{\partial t}\chi_2\rangle = 0 \tag{2.120}$$

Application of the Dirac-Frenkel variational principle

$$\langle\delta\mathrm{X}|\,\hat{H} - i\frac{\partial}{\partial t}\,|\mathrm{X}\rangle = 0 \tag{2.121}$$

results in a set of coupled one-dimensional equations of motion for $a(t)$, $\chi_1(x, t)$ and $\chi_2(y, t)$, i.e. the time evolution of the wavefunction.

Despite being conceptually simple, the performance of TDH is often very poor. This seems surprising if we make a parallel with electronic structure calculations, where the mono-configurational SCF method describes quite well the lower electronic state of molecules. The difference is that the potentials in nuclear dynamics provide strong coupling between the modes, which is completely missed by the TDH method.

In order to recover the missing correlation, a multiconfigurational form of TDH was formulated (MCTDH), in which the wavefunction is a linear combination of Hartree products

$$\begin{aligned} \mathrm{X}(q_1, \dots, q_f, t) &= \mathrm{X}(Q_1, \dots, Q_p, t) \\ &= \sum_{j_1=1}^{n_1} \cdots \sum_{j_p=1}^{n_p} A_{j_1 \dots j_p}(t) \prod_{k=1}^{f} \chi_{j_k}^{(k)}(Q_k, t) \end{aligned} \tag{2.122}$$

where $A_{j_1 \dots j_f}$ are the MCTDH expansion coefficients. Equation (2.122) is a linear combination of products over $p$ sets of orthonormal time-dependent SPFs $\{\chi^{(k)}\}$. There is one set of SPFs for each degree of freedom $p$, which is a composite coordinate of one or more nuclear coordinates

$$Q_k = (q_a, q_b, \dots) \tag{2.123}$$

Thus, the basis functions are $d$-dimensional, where $d$ is the number of combined nuclear coordinates that are treated as one 'particle' (usually $d$ = 1,2 or 3). If the number of SPFs per mode is reduced to one, equation (2.122) reduces to the TDH wavefunction. On the other hand, as the SPFs number is increased, the propagation of the wavefunction becomes more accurate, converging towards the numerically exact one (but increasing also the computational cost). As all possible configurations from the set of SPFs are used in the Hartree products, the method is unfortunately also plagued by exponential scaling ($\sim\ n^p$ where $n$ is the dimension of the SPF basis and $p$ the number of 'particles'). However, the base of the exponential is substantially smaller compared with the standard QD (because the number of physically important SPFs is usually small) and the number of particles $p$ is often smaller than the total number of nuclear degrees of freedom due to contraction (equation (2.123)), allowing MCTDH to treat larger systems.

As in the case of the TDH approximation, the MCTDH wavefunction representation is not unique, as one may linearly transform the SPFs and the expansion coefficients while still representing the same wavefunction. A uniquely-defined propagation is obtained by imposing the constraint that the initially orthonormal SPFs remain orthonormal for all times.

Using this multiconfigurational wavefunction ansatz, a variational solution to the TDSE is provided by a coupled set of equations of motion for the expansion coefficients $A_{j_1 \dots j_p}(t)$ and for the SPFs $\chi_{j_k}^{(k)}(Q_k, t)$. A full mathematical derivation of the MCTDH equations of motion is beyond the scope of this thesis, however, it is illuminating to know that the time derivative of the SPFs is orthogonal to the space spanned by the functions: thus, any change spans new basis functions. If the basis set were complete, the orthogonal space would be null, and the SPFs would be time independent (i.e. the equations of motion would be identical to the standard method). On the other hand, if the SPFs do not provide a complete basis set, then they change in time so as to provide the best possible basis for the description of the evolving wavepacket.

The possibility to contract the degrees of freedom in particle SPFs (equation (2.123)) is a strategy to substantially reduce the number of configurations, allowing to treat larger systems. However, a balance needs to be found between the gain in the configuration number and the cost of propagating combined-mode SPFs, which scales exponentially with $d$[28]. In MCTDH, the time-dependent contracted SPFs are represented by combinations of time-independent Hartree products with time-dependent coefficients. An improved and systematic strategy is then to represent each contracted particle mode by an MCTDH-type ansatz. This leads to the multi-layer MCTDH (ML-MCTDH) ansatz[30], where the hierarchy is started by expanding the overall wavefunction X in first-layer SPFs $\chi_{j_{k_1}}^{[1](k_1)}$

$$\mathrm{X}(t) = \sum_J A_J^{[1]} \prod_{k_1=1}^{f^{[1]}} \chi_{j_{k_1}}^{[1](k_1)} \tag{2.124}$$

which are in turn expanded in second-layer SPFs

$$\chi_{j_{k_1}}^{[1](k_1)} = \sum_J A_{j,J}^{[2](k_1)} \prod_{k_2=1}^{f_{k_1}^{[2]}} \chi_{j_{k_2}}^{[2](k_1,k_2)} \tag{2.125}$$

and the procedure can be re-iterated for an M-layer representation. The SPFs of the final layer are eventually represented in a primitive, time-independent basis. The equations of motion for the multi-layer approach involve a hierarchy of differential equations for the coefficients, which must be solved from the bottom layer. The multilayer construction of the wavefunction does not impose any additional limitations, and any Hamiltonian that can be treated via the MCTDH approach can equally be handled with the ML-MCTDH theory. The only additional complexity relies in its implementation, which is however compensated by the advantages of treating larger systems.

The main drawback of (ML-)MCTDH is that it is efficient only if the Hamiltonian can be written as a sum of products of one-dimensional operators. The kinetic energy operator usually satisfies product form, while the potential generally does not, but in many cases it can be well approximated with functions of the correct form. In cases where this is not possible, and the PESs show a more complex topology, the standard method must be applied.

### 2.2.3 Trajectory based approaches: mixed quantum/classical dynamics

In the simulation of many photoinduced processes, quantum effects like tunnelling or interference are negligible, and the energetic spacing between the nuclear quantum levels is sufficiently small compared to the kinetic energy to allow a classical propagation of the nuclei. This has the major advantage to remove the exponential complexity, allowing to simulate the dynamics of large systems that could not be modelled with QD. Moreover, all properties can computed locally at a single geometry, removing the non-locality imposed by the form of the kinetic operator in QD. This approximation is at the base of mixed quantum-classical methods[31], in which the nuclei are propagated classically on a QM electronic potential. The force acting on the nuclei is given by the PES gradient with respect to the nuclear coordinates. However, when more than one electronic state comes to play a role in the process (which is always the case of photoinduced processes), a question is posed about how to treat the nonadiabatic events. The surface hopping (SH) algorithm[32] is a popular approach to solve this problem, and will be briefly described in the following.

The basic assumption of SH is that, during non-adiabatic dynamics, the nuclei move under the influence of a single QM potential in a classical way, whereas the electrons are subject to non-adiabatic effects. As a consequence, in the course of the dynamics the population can distribute over several states (coherence) and can actually be completely transferred to a different electronic state. The classical nuclear dynamics takes notion of this non classical event by an instantaneous switch (*hop*) to the new electronic state (whose potential will following drive the dynamics). This stratagem opposes SH to the Ehrenfest approach, in which the nuclei always follow a trajectory under the influence of an averaged gradient, that is weighted by the population in each state and does not require a hopping mechanism. Figure 2.6 shows a schematic comparison between the wavepacket propagation in QD and the trajectory SH approach. In QD, the quantum treatment of the nuclei allows to reproduce the splitting between electronic states within a single simulation: as the wavepacket reaches the crossing region, population splits between the states, and the two parts of the wavepacket continue to evolve on different states at the same time. On the other hand, in a trajectory approach, the nuclei follow a well-defined path on a single PES, which is stochastically allowed to hop to the lower state near the crossing. In order to recover the quantum behaviour, many trajectories need to be simulated, and the results averaged.

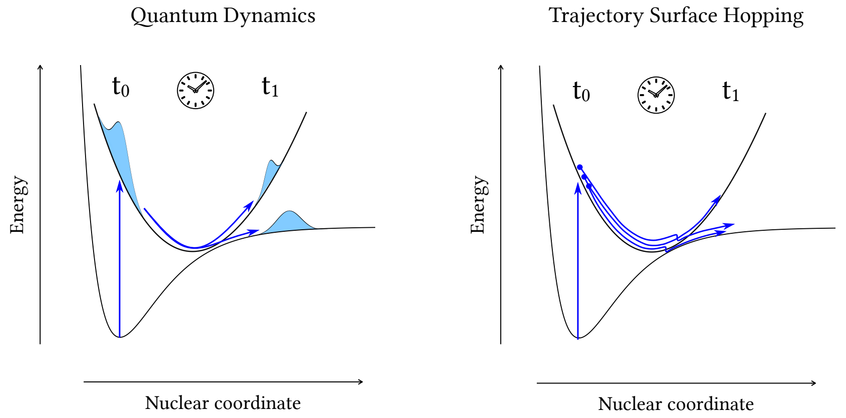
Quantum Dynamics

Trajectory Surface Hopping

**Figure 2.6:** Comparison between wavepacket QD (left) and SH trajectories (right). In QD, the wavepacket splits in two parts at the crossing. In SH, some trajectories hop to the lower state nearby the crossing, while some others do not and remain in the initial state.

In trajectory surface hopping (TSH) the nuclei are propagated according to Newton's equation of motion

$$-\frac{\partial E}{\partial \mathbf{R}_A} = m_A \frac{\partial^2 \mathbf{R}_A}{\partial t^2} \tag{2.126}$$

where $\mathbf{R}_A$ and $m_A$ are the position and mass of nucleus $A$, while $E$ is the electronic energy. The electronic wavefunction $\Psi_{\text{el}}(t)$ is expressed as a linear combination of electronic eigenstates

$$|\Psi_{\text{el}}(t)\rangle = \sum_i c_i(t)\,|\varphi_i(\mathbf{r};\mathbf{R}(t))\rangle \tag{2.127}$$

with time-dependent coefficients. The basis states are also time-dependent, because the electronic eigenstates parametrically depend on the nuclear coordinates, which change in time. In turn, the evolution of the nuclear trajectory also depends on the PES gradient, and thus on $\Psi_{\mathrm{el}}(t)$.

Among all the electronic eigenstates, only the gradient of the *active* state (i.e. the PES on which the trajectory is localised) determines the gradient leading the nuclear motion. The active state is stochastically determined at each time step through the SH algorithm. In order to conserve the total energy, the kinetic energy is adjusted whenever a hop takes place by modifying the velocity vector in a way that compensates for the potential energy gap. At the end of all simulations, the fraction of trajectories with active state $i$ at a specific time is equal to the electronic population of that state. The simulation procedure is composed of the following steps:

1. Calculate the new positions of the nuclei;
2. Compute electronic quantities: energies, gradients, couplings;
3. Propagate the electronic wavefunction from point $n-1$ to $n$ to obtain the new electronic coefficients $c_i(t)$;
4. Evaluate the hopping probability and stochastically decide whether to change state or not;
5. Obtain forces for the (new) active state;
6. Restart from step 1.

The update of the electronic coefficients (step 3) requires the output quantities of the nuclear and electronic calculations (steps 1 and 2) and determines the hopping probability (step 4). The time evolution of the electronic coefficients vector $\mathbf{c}$ is obtained inserting the electronic wavefunction (2.127) into the TDSE

$$\frac{\partial}{\partial t}\mathbf{c} = -\left[\frac{i}{\hbar}\mathbf{H} + \mathbf{K}\right]\mathbf{c} \tag{2.128}$$

with

$$H_{ij} = \langle\varphi_i|\,\hat{H}\,|\varphi_j\rangle \tag{2.129}$$

and

$$K_{ij} = \langle\varphi_i|\,\frac{\partial}{\partial t}\,|\varphi_j\rangle = \frac{\partial\mathbf{R}}{\partial t}\cdot\langle\varphi_i|\,\frac{\partial}{\partial\mathbf{R}}\,|\varphi_j\rangle = \mathbf{v}\cdot\langle\varphi_i|\,\nabla_{\mathbf{R}}\,|\varphi_j\rangle \tag{2.130}$$

where $\mathbf{v}$ is the nuclear velocity and $\langle\varphi_i|\,\nabla_{\mathbf{R}}\,|\varphi_j\rangle$ the NAC between the $\varphi_i$ and $\varphi_j$ electronic states. Given the updated $\mathbf{c}$ vector and an active state $\varphi_i$, the hopping probability for all other $\varphi_j$ states can be computed in different ways[33], and the stochastic hopping event is determined by comparison between the probabilities and a random number $r$ between 0 and 1. A schematic representation is given in Figure 2.7: each $\varphi_j \neq \varphi_i$ state defines an interval of the $[0,1]$ range whose width is equal to the relative hopping probability, and a hop to state $\varphi_j$ takes place if $r$ falls in the $j$-th interval.

One of the main problems that the TSH approach had to face is that, if no corrections are introduced, the electronic populations are propagated with too much coherence. For example, the coherence created near a CI (i.e non-zero coefficients for

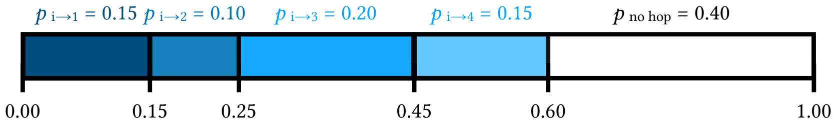

**Figure 2.7:** Graphic representation of the stochastic hopping algorithm for a five-state simulation: each state is assigned an interval in the $[0, 1]$ range whose width is equal to the relative hopping probability. A random number between 0 and 1 is then generated, and hopping to another state (or not) is decided by comparison with the probability intervals.

more than one state) would survive forever, even in regions far away from crossings and where the coupling is small. This happens because all the electronic amplitudes follow the gradient of the active state (while in an exact QD each wavepacket follows its electronic state), and can lead to artefacts like excited-state amplitudes overcoming huge barriers. To fix this, a decoherence correction algorithm can be applied, that over time collapses or decreases the amplitudes of the non-active states so that, far away from crossing regions, every trajectory eventually recovers a wavefunction on a single electronic state. Several decoherence schemes exist: simple suppression of the excited state amplitudes below a certain NAC threshold[34], exponential damping in time[35, 36], or even more sophisticated schemes (see reference [33]).

The TSH technique is surely more approximated that the QD methods described in previous sections as it neglects a number of quantum effects. Nevertheless, it has shown to work for the simulation of many excited states processes, and is still one of the most used simulation techniques. Its main advantage relies in the classical approximation for the nuclei, that allows to treat large systems with hundreds of atoms, as long as the electronic Schrödinger equation can be approximately solved. Additionally, the independent trajectories make the surface hopping approach computationally efficient.

### 2.2.4 Adiabatic and diabatic representations

In section 2.1 we have shown that the eigenstates of the full molecular hamiltonian (i.e. the *adiabatic* states) are coupled by the nuclear kinetic energy operator $\hat{T}_N$ (see equation (2.16)). The resulting NAC coupling is usually small, and its neglect is the justification for the famous Born-Oppenheimer approximation. However, in regions of avoided crossings between the PESs, the adiabatic states may change their character dramatically, leading to high NAC values (i.e. BO approximation fails). When running a non adiabatic dynamics, adiabatic PESs and NACs can be difficult to deal with, due to the cusp shape of the potentials at crossings and the local, spiky nature of the NACs. Therefore, other choices of basis may prove more convenient to obtain smoother potentials and couplings.

In a *diabatic* basis, the nuclear kinetic energy operator is diagonal, and the molecular states are coupled via the potential operator (i.e. the coupling turns to a scalar), which is often easier do deal with. The comparison between adiabatic and diabatic representations is schematised in Figure 2.8. The diabatic potentials are often easier to approximate with low order Taylor polynomials, and the scalar diabatic couplings are typically easier to determine and handle. At any time along a dynamics, the real solutions of the Hamiltonian can be retrieved by applying the back-transformation

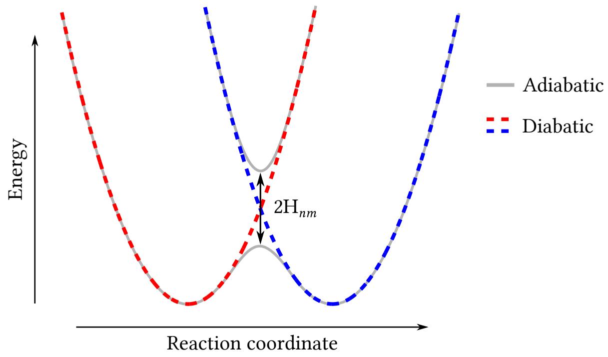

**Figure 2.8:** Adiabatic and diabatic representations: the avoided crossing between adiabatic states (grey curves) becomes a real crossing between the diabatic states (red and blue curves), with diabatic coupling $H_{nm}$ proportional to the splitting between the adiabatic states. Away from the crossing, the coupling is small and the two representations coincide.

which gives the original adiabatic states.

The transformation which diagonalises the kinetic operator is not unique, and an infinite number of possible diabatic representations exist. The choice of the most convenient diabatic states depends on the problem under consideration, so as to preserve the states properties of interest (e.g. electronic state character, dipole moment etc.).

## References

[1] P. Hohenberg and W. Kohn, "Inhomogeneous Electron Gas," *Physical Review*, vol. 136, B864–B871, 3B **1964**.

[2] J. B. Foresman, M. Head-Gordon, J. A. Pople, and M. J. Frisch, "Toward a systematic molecular orbital theory for excited states," *The Journal of Physical Chemistry*, vol. 96 (1), pp. 135–149, **1992**.

[3] J. A. Pople, R. Seeger, and R. Krishnan, "Variational configuration interaction methods and comparison with perturbation theory," *International Journal of Quantum Chemistry*, vol. 12 (S11), pp. 149–163, **2009**.

[4] B. O. Roos and K. P. Lawley, "Ab initio methods in quantum chemistry II," *Advances in Chemical Physics*, vol. 69, pp. 399–446, **1987**.

[5] J. Olsen, B. O. Roos, P. Jorgensen, and H. J. A. Jensen, "Determinant based configuration interaction algorithms for complete and restricted configuration interaction spaces," *The Journal of Chemical Physics*, vol. 89 (4), pp. 2185–2192, **1988**.

[6] D. Ma, G. Li Manni, J. Olsen, and L. Gagliardi, "Second-Order Perturbation Theory for Generalized Active Space Self-Consistent-Field Wave Functions," *Journal of Chemical Theory and Computation*, vol. 12 (7), pp. 3208–3213, **2016**.

[7] J. Ivanic, "Direct configuration interaction and multiconfigurational self-consistent-field method for multiple active spaces with variable occupations. I. Method," *The Journal of Chemical Physics*, vol. 119 (18), pp. 9364–9376, **2003**.

[8] P. G. Szalay, T. Müller, G. Gidofalvi, H. Lischka, and R. Shepard, "Multiconfiguration Self-Consistent Field and Multireference Configuration Interaction Methods and Applications," *Chemical Reviews*, vol. 112 (1), pp. 108–181, **2012**.

[9] K. Andersson, P. A. Malmqvist, B. O. Roos, A. J. Sadlej, and K. Wolinski, "Second-order perturbation theory with a CASSCF reference function," vol. 94 (14), pp. 5483–5488, **1990**.

[10] G. Li Manni, S. D. Smart, and A. Alavi, "Combining the Complete Active Space Self-Consistent Field Method and the Full Configuration Interaction Quantum Monte Carlo within a Super-CI Framework, with Application to Challenging Metal-Porphyrins," *Journal of Chemical Theory and Computation*, vol. 12 (3), pp. 1245–1258, **2016**.

[11] G. H. Booth, A. J. W. Thom, and A. Alavi, "Fermion Monte Carlo without fixed nodes: A game of life, death, and annihilation in Slater determinant space," *The Journal of Chemical Physics*, vol. 131 (5), p. 054 106, **2009**.

[12] D. Cleland, G. H. Booth, and A. Alavi, "Communications: Survival of the fittest: Accelerating convergence in full configuration-interaction quantum Monte Carlo," *The Journal of Chemical Physics*, vol. 132 (4), p. 041 103, **2010**.

[13] D. M. Cleland, G. H. Booth, and A. Alavi, "A study of electron affinities using the initiator approach to full configuration interaction quantum Monte Carlo," *The Journal of Chemical Physics*, vol. 134 (2), p. 024 112, **2011**.

[14] C. Overy, G. H. Booth, N. S. Blunt, J. J. Shepherd, D. Cleland, and A. Alavi, "Unbiased reduced density matrices and electronic properties from full configuration interaction quantum Monte Carlo," *The Journal of Chemical Physics*, vol. 141 (24), p. 244 117, **2014**.

[15] R. E. Thomas, Q. Sun, A. Alavi, and G. H. Booth, "Stochastic Multiconfigurational Self-Consistent Field Theory," *Journal of Chemical Theory and Computation*, vol. 11 (11), pp. 5316–5325, **2015**.

[16] D. Zgid and M. Nooijen, "The density matrix renormalization group self-consistent field method: Orbital optimization with the density matrix renormalization group method in the active space," *The Journal of Chemical Physics*, vol. 128 (14), p. 144 116, **2008**.

[17] D. Ghosh, J. Hachmann, T. Yanai, and G. K.-L. Chan, "Orbital optimization in the density matrix renormalization group, with applications to polyenes and β-carotene," *The Journal of Chemical Physics*, vol. 128 (14), p. 144 117, **2008**.

[18] E. Maradzike, M. Hapka, K. Pernal, and A. E. DePrince, "Reduced Density Matrix-Driven Complete Active Space Self-Consistent Field Corrected for Dynamic Correlation from the Adiabatic Connection," *Journal of Chemical Theory and Computation*, vol. 16 (7), pp. 4351–4360, **2020**.

[19] S. Reiter, D. Keefer, and R. de Vivie-Riedle, "Quantum Chemistry and Dynamics of Excited States," in, L. González and R. Lindh, Eds. Wiley, **2020**, ch. Exact Quantum Dynamics (Wave Packets) in Reduced Dimensionality, pp. 355–381.

[20] V. Sauri, L. Serrano-Andrés, A. R. M. Shahi, L. Gagliardi, S. Vancoillie, and K. Pierloot, “Multiconfigurational Second-Order Perturbation Theory Restricted Active Space (RASPT2) Method for Electronic Excited States: A Benchmark Study,” vol. 7 (1), pp. 153–168, **2011**.

[21] C. Bloch, “Sur la théorie des perturbations des états liés,” *Nuclear Physics*, vol. 6, pp. 329–347, **1958**.

[22] J. Finley, P.-Å. Malmqvist, B. O. Roos, and L. Serrano-Andrés, “The multi-state CASPT2 method,” *Chemical Physics Letters*, vol. 288 (2), pp. 299–306, **1998**.

[23] A. A. Granovsky, “Extended multi-configuration quasi-degenerate perturbation theory: The new approach to multi-state multi-reference perturbation theory,” *The Journal of Chemical Physics*, vol. 134 (21), p. 214 113, **2011**.

[24] T. Shiozaki, W. Győrffy, P. Celani, and H.-J. Werner, “Communication: Extended multi-state complete active space second-order perturbation theory: Energy and nuclear gradients,” *The Journal of Chemical Physics*, vol. 135 (8), p. 081 106, **2011**.

[25] S. Battaglia and R. Lindh, “Extended Dynamically Weighted CASPT2: The Best of Two Worlds,” *Journal of Chemical Theory and Computation*, vol. 16 (3), pp. 1555–1567, **2020**.

[26] H. D. Meyer, U. Manthe, and L. S. Cederbaum, “The multi-configurational time-dependent Hartree approach,” *Chemical Physics Letters*, vol. 165 (1), pp. 73–78, **1990**.

[27] U. Manthe, H. Meyer, and L. S. Cederbaum, “Wave-packet dynamics within the multiconfiguration Hartree framework: General aspects and application to NOCl,” *The Journal of Chemical Physics*, vol. 97 (5), pp. 3199–3213, **1992**.

[28] M. H. Beck, A. Jäckle, G. A. Worth, and H. D. Meyer, “The multiconfiguration time-dependent Hartree (MCTDH) method: A highly efficient algorithm for propagating wavepackets,” *Physics Reports*, vol. 324 (1), pp. 1–105, **2000**.

[29] A. D. McLachlan, “A variational solution of the time-dependent Schrodinger equation,” *Molecular Physics*, vol. 8 (1), pp. 39–44, **1964**.

[30] H. Wang and M. Thoss, “Multilayer formulation of the multiconfiguration time-dependent Hartree theory,” *The Journal of Chemical Physics*, vol. 119 (3), pp. 1289–1299, **2003**.

[31] J. C. Tully, “Mixed quantum–classical dynamics,” *Faraday Discussions*, vol. 110, pp. 407–419, **1998**.

[32] J. C. Tully and R. K. Preston, “Trajectory Surface Hopping Approach to Nonadiabatic Molecular Collisions: The Reaction of H+ with D2,” *The Journal of Chemical Physics*, vol. 55 (2), pp. 562–572, **1971**.

[33] S. Mai, P. Marquetand, and L. González, “Quantum Chemistry and Dynamics of Excited States,” in, L. González and R. Lindh, Eds. Wiley, **2020**, ch. Surface Hopping Molecular Dynamics, pp. 499–530.

[34] B. J. Schwartz and P. J. Rossky, “Aqueous solvation dynamics with a quantum mechanical Solute: Computer simulation studies of the photoexcited hydrated electron,” *The Journal of Chemical Physics*, vol. 101 (8), pp. 6902–6916, **1994**.

[35] G. Granucci and M. Persico, “Critical appraisal of the fewest switches algorithm for surface hopping,” *The Journal of Chemical Physics*, vol. 126 (13), p. 134 114, **2007**.

[36] G. Granucci, M. Persico, and A. Zoccante, “Including quantum decoherence in surface hopping,” *The Journal of Chemical Physics*, vol. 133 (13), p. 134 111, **2010**.

# Chapter 3

# Parameterisation protocols

In this chapter, we present some computational protocols for the parameterisation of the electronic Hamiltonian for subsequent dynamics simulations based on multiconfigurational wavefunction-based methods. The procedures are fully portable and can be applied to many systems whose photobehaviour requires a detailed and accurate dynamical study. Once the degrees of freedom have been defined, the general steps of the parameterisation protocol include:

1. Coordinate representation
2. Selection of level of theory
3. PESs and wavefunctions calculations
4. Non adiabatic couplings (NACs) and transition dipole moments (TDMs) calculations from wavefunctions
    4.1 Transition densities (TRDs) calculations from wavefunctions (optional)
5. NACs and TDMs sign-correction according to wf overlaps
    5.1 TRDs sign-correction according to WF overlaps (optional)

## 3.1 Coordinate representation

Depending on the photochemical problem, the coordinates to be included in the model range from few to many tens of modes. Their number is mostly determined by the complexity of the photophysical/photochemical deactivation path and by the level of accuracy with which one intends to reproduce the real mechanism. These parameters affect the choice of the type of simulation to be performed: classical molecular dynamics with ad-hoc force fields allows to include all the internal coordinates, but only some of them can be parameterised to describe motion away from equilibrium geometries, while all remaining degrees of freedom will suffer from the use of harmonic approximation (i.e. only regions of the PESs close to the equilibrium structure will be correctly described). Semiclassical simulations with pre-computed PESs can in principle handle all degrees of freedom, whose number is however limited by the computational effort required by the preliminary energy computations (making on-the-fly semiclasscial dynamics more practical). Concerning the number of coordinates in QD simulations, it is strongly dependent on the wavepacket propagation technique: “traditional” QD (i.e. expanding the nuclear wavefunction in a time-independent basis) in a diabatic or adiabatic representation can only handle few coordinates, while newer implementations relying on time-dependent basis functions like MCTDH[1] and its multilayer extension (ML-MCTDH)[2] allow for the simulation of many degrees of freedom, provided that the PES can be approximated with simple analytical functions.

The selection of the appropriate degrees of freedom depends on the photophysics/photochemistry of the problem under investigation. Upon photoexcitation, the electronic density is perturbed instantaneously (with respect to the time scale of the nuclear vibrations). As a consequence, nuclear motion is then started by the necessity of the nuclei to adapt to the perturbation. Since different electronic states have different electronic structure, such nuclear motions are state-specific. In a one-dimensional harmonic potential representation, this can be depicted by displaced harmonic potentials (Figure 3.1). The adaptation of the nuclei to the electronic structure results in a horizontal displacement. The PESs gradient points towards the respective minimum (local or global). The system might get trapped there upon energy dissipation (Figure 3.1 (a)), in which case there is no ultrafast photochemistry. Under suitable conditions PES can cross in a CI (Figure 3.1 (b)). As noted earlier, this promotes ultrafast non adiabatic transfer between surfaces, that can occur on a sub-1 ps time scale, i.e. before energy dissipation and equilibration in the ES can set in.

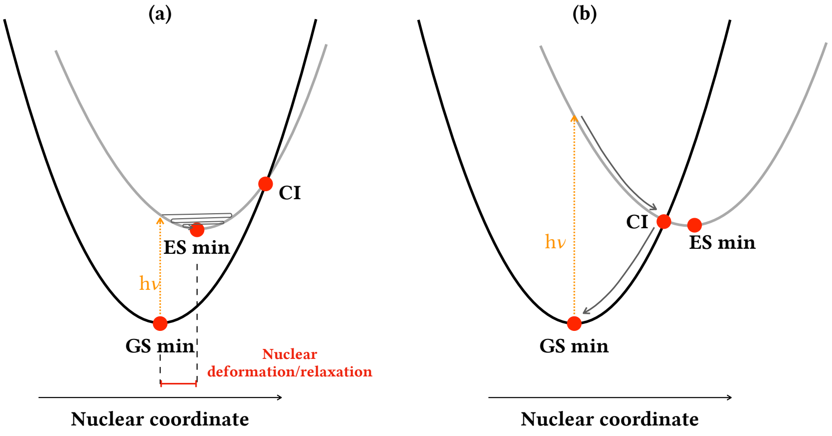

**Figure 3.1:** Schematic representation of the photophysical/photochemical processes following photoexcitation in a one-dimensional displaced harmonic potentials model.

In the most general scenario, the deformations that lead from the Frank-Condon (FC) point to the ES minimum are different from the ones that lead to the CI, thus requiring energy redistribution (facilitated through coupling between kinetic terms in the Hamiltonian). As a consequence, the FC point (the doorway into the ES) as well as minima and CI (the doorways out of an ES) represent critical structures that need to be considered when deriving reactive coordinates. These modes are known as *tuning modes* as they affect the relative positions of the PES. Sometimes one has to explicitly consider also *coupling modes* which give rise to strong wavefunction couplings and promote non adiabatic transfer.

After the selection of the coordinates for the parameterisation, it is important to define their representation in terms of molecular displacements, that is answering to the questions “which is(are) the reference geometry(geometries)?”, “how do we generate molecular displacements along each coordinate starting from our reference(s)?”. The relevant structures that one wishes to describe are usually those of the reactant (ground state minimum) and photoproduct, but also all those key geometries that are found along the MEP describing the photoinduced process, such as excited state minima, transition states and most accessible CIs between the states included in the model. If the reactive coordinates are well identified, it is typically possible to take one of these optimised geometries as a reference and reach all the others by displacing along the chosen degrees of freedom. In this way, the reference geometry will be fully-optimised, while all the other key structures will be approximated but still well described. As reference geometry, it is advisable to choose the one which needs more accuracy in the description due to its importance in the dynamics (e.g. the most accessible conical intersection, while ground state minima are usually visited only at the beginning and end of the propagation and suffer less from approximations) or the one which best trades with all the others in terms of the non-scanned coordinates, so that it will give a fair description of all of them. This “rigid scan” strategy was successfully applied to the azobenzene and pyrene molecules (see Chapters 4 and 5). For the generation of the grid structures, it is generally easier to work with internal coordinates rather than cartesian ones, since the reaction path is often more easily expressed in terms of few of the former. In the cases where the photochemically relevant degrees of freedom are described by simple internal coordinates (e.g. azobenzene), it is possible to generate structures by editing the proper values in the Z-matrix of the reference geometry. Instead, when using normal modes (e.g. pyrene) many tools are available to displace the reference structure along normal coordinates (we used the ones provided by the FCclasses code[3]).

However, there are systems for which the deactivation mechanism cannot be approximated with the rigid scan of few degrees of freedom, but rather it is a complex mixture of coordinates which are often delocalised on the whole molecule. Such cases need a more complex treatment, an example of which is the retinal chromophore inside the rhodopsin protein (whose photoisomerization triggers the process of vision) that is extensively detailed in Chapter 6.

## 3.2 Selection of level of theory

The selection of the level of theory is the fundamental starting step to obtain accurate data. Benchmark studies are required to properly select the best electronic structure method to apply both at the equilibrium structure(s) and at very distorted geometries. Indeed, the parameterisation procedure for dynamics simulations must include not only structures nearby the FC region, CIs and/or MEP connecting them, but also very distorted geometries far from equilibrium, in regions that might be explored by the wavepacket/trajectory due to momentum conservation.

Among wavefunction-based multiconfigurational methods, we have chosen CASSCF/CASPT2 for our protocol, which allow to correctly describe on an equal footing electronic states with different nature (e.g. singly and doubly excited states). Moreover, with a grid mesh of the proper size, it is possible to keep track of the orbital transformations along the scan and identify the desired states in all grid points. The main parameters that need to be optimised in a CASSCF/CASPT2 calculation are the number of states included, the active space size and composition and the type of perturbative correction (see Section 2.1.7), which must be chosen after a deep analysis of their effect on the electronic structure in different regions of the PESs.

Concerning the states to include, their number is determined by studying the photochemistry of the system: upon interaction with light, only excited states showing a non-vanishing TDM with the ground state $\langle\varphi_{\mathrm{GS}}|\,\mathbf{r}\,|\varphi_{\mathrm{ES}}\rangle$ can be populated (among those falling in the energy window of the excitation pulse). Such states are often called *bright states*, and each of them is a potential doorway out of the GS, as it can be populated by light in a realistic experiment. Thus, the number of relevant states depends on the experimental excitation wavelength to simulate. The relevant bright state(s) as well as all states below and around them can be involved in the photochemical/photophysical processes that follow excitation (i.e. they might acquire population from the bright state). Besides these, higher lying states that get stabilised along the reactive coordinates might also be included, since they can interact or even cross with the selected states in some regions, making it necessary to include more roots to keep track of the original states. An additional point to take care of is the possible discrepancy between CASSCF and CASPT2 state order, that often makes it necessary to include high-lying CASSCF states that are much stabilised by subsequent CASPT2 correction. For all these reasons, it is advisable to perform some preliminary tests across the grid with a higher number of roots before choosing the number of CASSCF/CASPT2 states.

When possible, a uniform level of theory across the grid is preferred. However, there are cases in which the best compromise between computational cost and accuracy forces to reduce the active space and/or change the type of perturbative correction in certain grid areas. As an example, in our study on the azobenzene molecule (Chapter 4) the use of a big active space limited the possibility to apply MS-RASPT2 in all the points. In this case, we assessed the accuracy of SS- and MS-CASPT2 correction along several scans of all reactive coordinates, and found out that the state energies obtained with both methods were identical in the regions where the two states included in the model were significantly far from each other. On the other hand, where the two states approached, MS-RASPT2 was needed to obtain smooth and physically meaningful PESs. As a consequence, the two methods were successfully combined in the parameterisation. A more complicated example is represented by the Pyrene molecule, whose complex electronic structure required the combination of different perturbative correction as well as active space sizes (Chapter 5). In this case, the computational effort is strongly determined by the need to include several excited states in the description: indeed, the rigidity of the aromatic system does not allow for huge deformations, but the lowest excited states are so close in energy that slight alterations the active space composition, number of states in the SA or even a simple reduction of the symmetry of the system leads to changes in the energy ordering of the states. The high symmetry of pyrene in its ground state equilibrium structure reduces significantly the computational cost and at the same time it also limits the interaction between close-lying states belonging to different irreducible representations. Unfortunately, some of the modes that we have included in the model reduce the symmetry of the system, allowing for new inter-state interactions and increasing the computational cost. Moreover, in such delicate situations the use of MS- or XMS-RASPT2 is mandatory to have a good description of the electronic states, therefore we had to reduce the active space size along the symmetry-breaking coordinates, excluding some virtual orbitals.

In any case, the level of theory must be accurately selected (and tuned, when the computational cost is too high to afford expensive calculations across all the grid) in order to deal between computational time and accuracy of the description. As a rule of thumb, to reduce the cost of CASSCF calculations, it is possible to use its restricted version (RASSCF) putting all the orbitals which are doubly-occupied in the ground state configuration in RAS1 and all virtual orbitals in RAS3, leaving RAS2 empty and allowing for maximum four holes/electrons in RAS1/RAS3, respectively. This strategy was benchmarked by previous studies[4] and proved to give results as accurate as "traditional" schemes after perturbative correction. Concerning the PT2 correction, different flavours are implemented in MOLCAS[5]: SS-CASPT2 is cheaper and typically performs well in cases where the reference CASSCF states are well separated in energy and no not mix. On the other hand, regions of degeneracy or quasi-degeneracy between electronic states are better described by multistate procedures, either MS-, XMS- or the newer dynamically weighted DWMS-CASPT2[6]. Despite this general trends, a preliminary investigation of the electronic structure changes along each selected degree of freedom is always necessary to find the best compromise between accuracy and computational cost.

## 3.3 Grid construction: PESs and wavefunctions calculations

With the grid structures in hand, and once the level of theory has been defined, the electronic state energies and wavefunctions can be calculated in all the points. This is the most straightforward part of the parameterisation protocol, but still requires care and attention to avoid errors and rough approximations that will bring about wrong dynamics simulations. Indeed, it is important to asses the range and step for each of the reactive coordinates before moving on. All state minima and the accessible CIs along the path should be far from the grid edges, which must therefore be properly enlarged to avoid that the wavepacket or trajectory goes out of the border. Moreover, a smaller step is advisable close to crossing points, in order to better describe the NAC spikes in regions where the PESs approach.

To obtain smoothly-varying orbitals across the scan, which avoid discontinuities in the wavefunctions and energies, it is advisable to scan the PESs starting from a reference geometry, taking every time the starting orbitals from the output of the closest point as initial guess. In the presence of more than one reference geometry (e.g. *trans* and *cis* isomers of azobenzene, see Chapter 4), the region of the PESs in which grid points derived from different references are joined can show discontinuities, which need to be addresses by, e.g., fitting functions to obtain smooth surfaces.

The obtained PESs are also an important assessment of the selected coordinates: if one of the photochemically relevant structures is not caught by the scan, it is possible that the reactive coordinates were not properly selected or represented and should be revised.

## 3.4 Calculations of properties along the grid: NACs and TDMs

Using the CASSCF/CASPT2 wavefunctions, it is possible to calculate several interstate couplings such as transition dipole moments (TDMs) and NACs, which are needed to simulate the state transitions during the dynamics. The TDM between two states is expressed in cartesian coordinates and its calculation is quite simple, while the NAC calculation can be more complicated since analytical CASPT2 NACs are not available, and will be discussed in detail below.

### 3.4.1 Numerical NACs and gradients in internal coordinates

In the cases when analytical NACs are not available, their components can be computed numerically by making small displacements along every degree of freedom and computing the wavefunction overlap with the reference point using finite differences[7]:

$$\mathrm{NAC}_{ij,R} = \frac{\left(\langle\Psi_i(R)|\Psi_j(R+\mathrm{d}R)\rangle - \langle\Psi_i(R)|\Psi_j(R-\mathrm{d}R)\rangle\right) + \left(\langle\Psi_j(R)|\Psi_i(R+\mathrm{d}R)\rangle - \langle\Psi_j(R)|\Psi_i(R-\mathrm{d}R)\rangle\right)}{4\mathrm{d}R} \tag{3.1}$$

where $i$ and $j$ label electronic states, and $R$ is the nuclear coordinate of interest. Even if the numerical calculation is highly parallelizable (since all displacements are generated independently), obtaining the cartesian NAC for medium/big systems is still demanding, since the number of cores needed to speed up the calculation increases quickly with the number of atoms. Indeed, the calculation of one cartesian NAC requires 1 single-point calculation at the reference geometry plus the calculation of energies and wavefunctions for the displacement of each atom $n$ along $\pm x_n$, $\pm y_n$ and $\pm z_n$, resulting in $1 + 6N_{\text{atoms}}$ calculations. A first approximation to reduce the computational expense is the neglect of the NAC components fore some atoms (e.g. hydrogens) that prove to be negligible after some benchmarking calculations. However, in many cases, one is not interested in the NAC vector itself (expressed in 3N coordinates), but rather in its projection along a coordinate of interest. It is the case of QD performed in a reduced space, where the NAC components orthogonal to the chosen degrees of freedom are discarded. In such cases, the direct calculation of the NAC in terms of the desired coordinate(s), would significantly diminish the computational cost without introducing any further approximation to the dynamics, reducing the calculation to a single point for the reference geometry plus only two displacements (± direction) for each reactive coordinate. As an example, for the study of the azobenzene photoisomerization along the C—N=N—C dihedral and the two C—N=N/N=N—C angles, the cartesian NAC calculation would require $1 + 24 \times 6 = 145$ single point calculations; instead, for a direct NAC calculation along the reactive coordinates they are only $1 + 3 \times 2 = 7$. In the case one needs to map the NAC for a significant number of geometries, the computational time with the latter scheme would be dramatically reduced. However, this this goes at the expenses of accuracy in reproducing the coupling: if an important coupling mode internal is excluded from the model, the interstate coupling will consequently be reduced. Therefore, the above simplification is only effective in an appropriate coordinate model.

We have implemented the use of external displacements in the numerical CASSCF/CASPT2 NAC and gradient calculation in the software COBRAMM[7–9], developed by or group. This was done by defining a new calculation type called "`nac`" which is equivalent to one step of a MD (with Tully's surface hopping algorithm) in which the energies, gradients and NACs are computed and printed out. In contrast to a standard MD calculation, however, the numerical routines were edited to handle an arbitrary number of coordinates, and to read the relative displacements from external files (provided by the user together with the input files). Below, the procedure for calculating numerical NACs with MOLCAS[5] through COBRAMM is outlined, assuming that the positive and negative cartesian displacements along the desired coordinates are available. More details about the generation of correct cartesian displacements are given in Appendix A.

### Input files

The required input files for a COBRAMM calculation and the keywords are described in the COBRAMM wiki page[9]. For a NAC calculation, the basic input files are the same as for a molecular dynamics simulation without initial velocity:

- `cobram.command` input file;
- molecular structure in AMBER crd format `real.crd`;
- QM/MM layers definition in `real_layers.xyz` format[9] (if `real.crd` is missing, the molecular structure as well is read from `real_layers.xyz`).

In the case of a QM/MM calculation, additional files for the MM AMBER[10] calculation are needed. These are

- AMBER "topology file" `real.top` holding the MM parameters of the whole system (QM+MM parts);
- AMBER "topology file" `model-H.top` holding the MM parameters for the high layer only.

In addition to this standard COBRAMM files, the user should provide $2n$ more input files, where $n$ is the number of coordinates. They must be named `dq1.xyz`, `dq2.xyz`, ..., dq$n$`.xyz` and consecutive numbers should be used for displacements relative to the same reactive coordinates (i.e. `dq1.xyz` and `dq2.xyz` must refer to coordinate one and so on). Below is reported the `command` section of the COBRAMM input file for a numerical NAC calculation:

```
!command
1 nac
10 1
14 0
15 1
51 6
85 6
86 1000
210 3
?command
```

Table 3.1 contains the explanation for the keys/keywords

**Table 3.1:** COBRAMM keys/keywords and corresponding value and meaning for a numerical NAC calculation with external displacements

| Key | Keyword | Value | Meaning |
|---|---|---|---|
| 1 | `type` | `nac` | calculation type: numerical NAC with external displacements |
| 10 | `distype` | `1` | displace in ± direction for numerical computations (default) |
| 14 | `nacs` | `0` | compute NACs numerically using WF overlap |
| 15 | `savnum` | `1` | save output of single points during numerics |
| 51 | `qm-type` | `6` | QM calculation type (6 = MOLCAS) |
| 85 | `surhop` | `6` | activate surface hopping using use Tully FSSH with Persico decoherence (required to activate NAC calculation) |
| 86 | `ediff` | `1000` | energy threshold (kcal/mol) to activate surface hopping (required high value to compute NAC independent of energy gap) |
| 210 | not defined yet | `3` | number of reactive coordinates for numerical calculations |

### Output

The gradients and NACs components along the user-defined coordinates are printed out in the output file `cobramm.log` at the end of the parallel numerics section. The example below shows a numerical NACs calculation involving three electronic states along three reactive coordinates (six displacements). All the available NACs are printed, while the gradient is reported only for the state of interest.

```
GRADIENT ALONG COMPUTED COORDINATES:

!!! Parallel computation with external coordinates !!!!
If less then 3*n coordinates are used, the missing ones to fit
cartesian format will be set equal to 0.0 for printout
 -0.013255889133   0.028076026103   0.005449466915

COMPUTED NACs:
NAC between  states 1-2
  0.098685464299  -0.272135201665  -0.039918747494
NAC between  states 3-2
  0.205292976033   0.119425242138  -0.014651858616
NAC between  states 1-3
  0.145999198727   0.068389275208  -0.011274120479
```

## 3.5 Sign correction

Even if the wavefunction coefficients vary smoothly between consecutive grid points, its phase is arbitrarily changing, which reflects in random sign changes in NACs and TDMs. In order to fix this, it is possible to calculate wavefunction overlaps between consecutive points and propagate the sign correction starting from a reference geometry, as schematised in Figure 3.2 The first step of the procedure is the path definition: all grid points must be connected in a smart way, in order to minimise the number of wavefunction overlaps required. We have made use of a simple script that, given the grid points as input, connects them all according to nearest neighbour criterion, without passing through each point more than once.

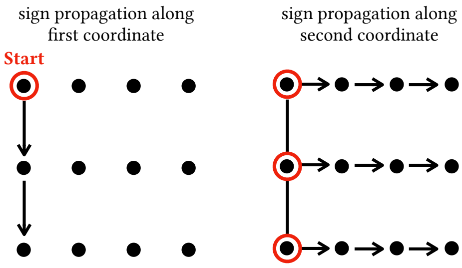

**Figure 3.2:** Schematic representation of sign correction procedure: all TDM and NAC signs are corrected with respect to a reference starting geometry from which the sign is propagated.

Once the paths have been defined, the wavefunction overlaps $\langle\Psi_i(\mathrm{r})|\Psi_i(\mathrm{r}+1)\rangle$ and $\langle\Psi_j(\mathrm{r})|\Psi_j(\mathrm{r}+1)\rangle$ are calculated (e.g. through MOLCAS RASSI routine), where $i$ and $j$ denote the two adiabatic states for which the coupling was calculated. Their signs determine wether the coupling sign at point r + 1 is coherent with that at point r or its sign is to be changed: if $\langle\Psi_i(\mathrm{r})|\Psi_i(\mathrm{r}+1)\rangle$ and $\langle\Psi_j(\mathrm{r})|\Psi_j(\mathrm{r}+1)\rangle$ are both positive (negative), the wavefunctions of both states have kept (changed) their sign from point r to point r + 1 and the NAC or TDM sign is already coherent. On the other hand, if only one of the two states has changed its wavefunction sign with respect to point r, the sign of the $ij$ coupling (either NAC or TDM) has to be changed. Since the sign has to be coherent on the whole grid, the decision to change the sign at a particular point is also connected to the memory of the sign correction at the previous points, for which the path connecting all points (defined above) is needed.

Figure 3.3 shows the effect of sign correction for the BLA component of the $S_1/S_0$ NAC and for the $y$ component of the TDM along a C11=C12 torsional scan for rhodopsin (see chapter 6 for coordinate definitions): before the sign correction, the NAC and TDM experience random sign changes which get fixed after the sign correction, retaining only the expected sign inversion at the CI.

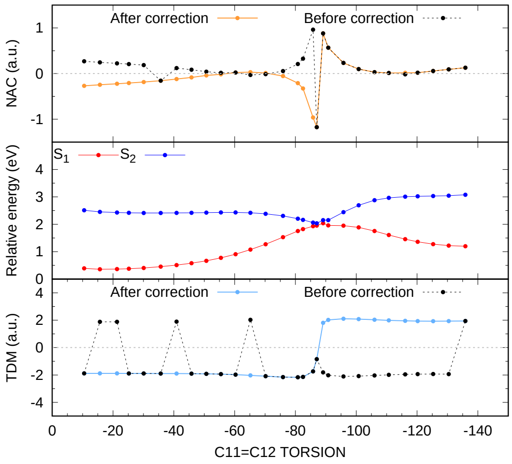

**Figure 3.3:** $S_1/S_0$ NAC (BLA component, top panel) and TDM ($y$ component, lower panel) along a C11=C12 torsional scan for rhodopsin (see chapter 6) before and after sign correction. In the central panel are represented the corresponding $S_1$ and $S_0$ PESs.

## References

[1] M. Beck, A. Jäckle, G. Worth, and H.-D. Meyer, "The multiconfiguration time-dependent Hartree (MCTDH) method: A highly efficient algorithm for propagating wavepackets," vol. 324 (1), pp. 1–105, **2000**.

[2] H. Wang and M. Thoss, "Multilayer formulation of the multiconfiguration time-dependent Hartree theory," vol. 119 (3), pp. 1289–1299, **2003**.

[3] F. Santoro, *FC classes: A Fortran 77 code*, Visit http://village.ipcf.cnr.it, **2020**.

[4] V. Sauri, L. Serrano-Andrés, A. R. M. Shahi, L. Gagliardi, S. Vancoillie, and K. Pierloot, "Multiconfigurational Second-Order Perturbation Theory Restricted Active Space (RASPT2) Method for Electronic Excited States: A Benchmark Study," vol. 7 (1), pp. 153–168, **2011**.

[5] I. Fdez. Galván, M. Vacher, A. Alavi, C. Angeli, F. Aquilante, J. Autschbach, J. J. Bao, S. I. Bokarev, N. A. Bogdanov, R. K. Carlson, L. F. Chibotaru, J. Creutzberg, N. Dattani, M. G. Delcey, S. S. Dong, A. Dreuw, L. Freitag, L. M. Frutos, L. Gagliardi, F. Gendron, A. Giussani, L. González, G. Grell, M. Guo, C. E. Hoyer, M. Johansson, S. Keller, S. Knecht, G. Kovačević, E. Källman, G. Li Manni, M. Lundberg, Y. Ma, S. Mai, J. P. Malhado, P. Å. Malmqvist, P. Marquetand, S. A. Mewes, J. Norell, M. Olivucci, M. Oppel, Q. M. Phung, K. Pierloot, F. Plasser, M. Reiher, A. M. Sand, I. Schapiro, P. Sharma, C. J. Stein, L. K. Sørensen, D. G. Truhlar, M. Ugandi, L. Ungur, A. Valentini, S. Vancoillie, V. Veryazov, O. Weser, T. A. Wesołowski, P.-O. Widmark, S. Wouters, A. Zech, J. P. Zobel, and R. Lindh, "OpenMolcas: From Source Code to Insight," *Journal of Chemical Theory and Computation*, vol. 15 (11), pp. 5925–5964, **2019**.

[6] S. Battaglia and R. Lindh, "Extended Dynamically Weighted CASPT2: The Best of Two Worlds," vol. 16 (3), pp. 1555–1567, **2020**.

[7] O. Weingart, A. Nenov, P. Altoè, I. Rivalta, J. Segarra-Martí, I. Dokukina, and M. Garavelli, "COBRAMM 2.0 — A software interface for tailoring molecular electronic structure calculations and running nanoscale (QM/MM) simulations," *Journal of Molecular Modeling*, vol. 24 (9), p. 271, **2018**.

[8] P. Altoè, M. Stenta, A. Bottoni, and M. Garavelli, "A tunable QM/MM approach to chemical reactivity, structure and physico-chemical properties prediction," *Theoretical Chemistry Accounts*, vol. 118 (1), pp. 219–240, **2007**.

[9] Cobramm on GitLab, available at: `https://gitlab.com/cobrammgroup/cobramm/-/wikis/home`.

[10] D. Case, I. Ben-Shalom, S. Brozell, D. Cerutti, T. Cheatham, V. Cruzeiro, T. Darden, R. Duke, D. Ghoreishi, M. Gilson, H. Gohlke, A. Goetz, D. Greene, R. Harris, N. Homeyer, Y. Huang, S. Izadi, A. Kovalenko, T. Kurtzman, T. Lee, S. LeGrand, P. Li, C. Lin, J. Liu, T. Luchko, R. Luo, D. Mermelstein, K. Merz, Y. Miao, G. Monard, C. Nguyen, H. Nguyen, I. Omelyan, A. Onufriev, F. Pan, R. Qi, D. Roe, A. Roitberg, C. Sagui, S. Schott-Verdugo, J. Shen, C. Simmerling, J. Smith, R. Salomon- Ferrer, J. Swails, R. Walker, J. Wang, H. Wei, R. Wolf, X. Wu, L. Xiao, D. York, and P. Kollman, *AMBER18*, **2018**.

# Chapter 4

# Azobenzene

## 4.1 Introduction

Azobenzene is an aryl azo compound made up of two phenyl rings connected by an azo group. Due to the two possible configurations of the −N=N− double bond, both *cis*- and *trans*-azobenzene isomers exist (Figure 4.1). The interconversion between the two isomers is thermally allowed only in the *cis* ⟶ *trans* direction, due to the grater thermodynamical stability of the *trans* isomer. On the other hand, a bidirectional *trans* ⇌ *cis* interconversion is photochemically allowed, that was first observed by Hartley in 1937[1]. The possibility to switch the molecular conformation between *trans* and *cis*, together with other favourable properties such as the reversibility of the photoisomerization process, the stability of both isomers and the photoactivity even under unfavourable or constrained conditions[2], make azobenzene the perfect candidate for application in light-powered nanomachines[3, 4], actuators[5, 6] and in general in materials with photomodulable properties[7–13]. A deep mechanistic understanding of the photochemistry of azobenzene opens further chemical design opportunities to increase switching efficiencies (and thereby material functionality) or to tailor azobenzene derivates for the specific surrounding they are incorporated in.

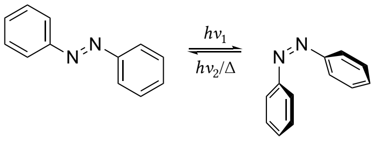

**Figure 4.1:** Azobenzene *trans* ⇌ *cis* interconversion

The UV-Vis spectrum of *trans*-azobenzene (Figure 4.2) shows a weak band in the visible region near 440 nm, which is associated with the symmetry-forbidden $S_0 \longrightarrow S_1$ transition (n$\pi^*$ nature), while the strong UV band around 320 nm is associated with the symmetry-allowed $\pi\pi^*$ transition populating the bright $S_2$ state. The same bands are observed also in the spectrum of *cis*-azobenzene, even though with a different relative intensity (see Figure 4.2) due to the non-planar structure of the *cis* isomer, which is mitigating the symmetry selection rules. The most challenging aspect of the photoisomerization of azobenzene (both *trans* ⟶ *cis* and *cis* ⟶ *trans*) is the quantum yield dependence on the excitation wavelength, which contradicts Kasha-Vavilov rule[14]. Indeed, in inert solvents such as *n*-hexane the experimental quantum yields are about 11% and 25% in the *trans* case and 27% and 56% in the *cis* case starting from $S_2$ or $S_1$, respectively[15]. In other solvents, the quantum yields show a similar trend[16]. This suggests that different reaction mechanism could take place starting from the $n\pi^*$ (Vis irradiation) or $\pi\pi^*$ state (UV irradiation).

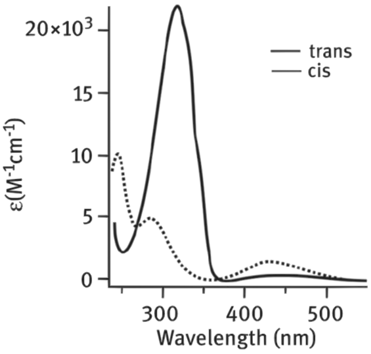

**Figure 4.2:** Azobenzene UV-Vis absorption spectrum in ethanol. From reference[17].

Over the years, theoretical chemists and physicists have tried to give an explanation of this behaviour and to unveil the reaction mechanism. Indeed, two reaction coordinates can be identified for the *trans* ⇌ *cis* interconversion: pure torsion around the N=N bond or pure in-plane inversion of one C–N=N angle (see Figure 4.3), and the relevance of each of these pathways when exciting $S_1$ or $S_2$ has been debated for over eighty years. Early theoretical studies by Bortolus et al.[15] reported an energetically favourable inversion path, while a high barrier was found along the C–N=N–C torsion. This was supported by evidence from the Raman experiments by Fujino[18], who found that the N=N retains a double bond nature also in the excited state, that was not compatible with the expected $\pi$-bond breaking along torsion. However, starting around the year 2000, the application of accurate multiconfigurational methods to

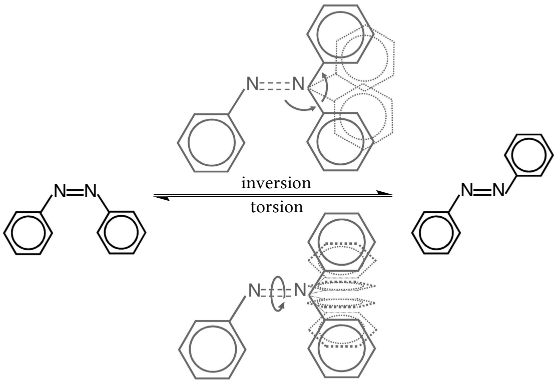

**Figure 4.3:** Possible isomerization mechanisms in azobenzene: C–N=N inversion (top) and C–N=N–C torsion (bottom).

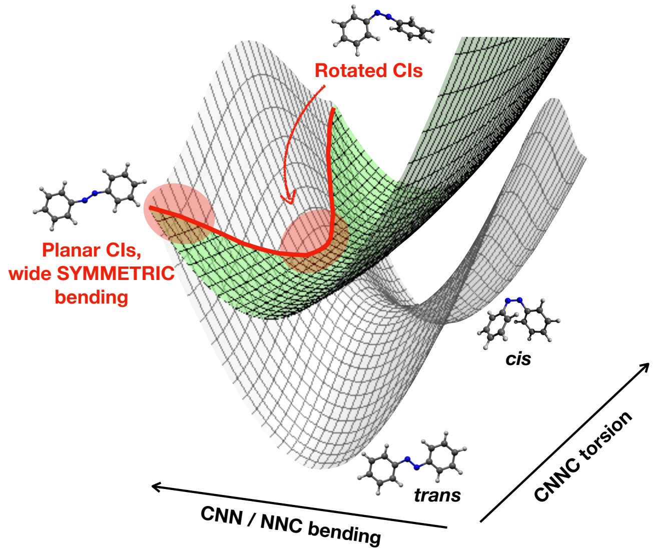

**Figure 4.4:** Sketch of the $S_0$ and $S_1$ PESs of azobenzene along the torsion and symmetric bending coordinates. The crossing seam (red line) extends from planar, high-energy structures to fully rotated structures, which represent the most accessible part of the CI seam.

the study of the PESs of azobenzene questioned the hypothesis of the inversion pathway. CASSCF potential energy surfaces by Ishikawa et al.[19] turned out to be quite flat along the torsion coordinate, along which a $S_1/S_0$ CI was found, that was identified as the preferred deactivation channel. Further applications of CASPT2/CASSCF[20–23], TD-DFT[24] and semiempirical methods[25] all supported the C−N=N−C torsion as the preferred path, although with an important role of the oscillations in the C−N=N/N=N−C bending angles to reach the crossing region. In addition, a more favorable torsional gradient on the *cis*-side was able to explain the higher *cis* ⟶ *trans* quantum yield. In the same years, a study by Taketsugu and coworkers[26] demonstrated through CASPT2 frequencies that the N=N stretching frequency is insensitive to the reaction mechanism, thus making the torsional path compatible with Fujino's experiments. The general consensus at present is represented by the so-called "bending-assisted torsion", in which the $S_1 \longrightarrow S_0$ decays does not take place through a unique crossing point along torsion, but rather a wide crossing region is present, spanning large portions of the torsion and bending coordinates[14, 21–25] (Figure 4.4). The latter, however, does not represent a productive deactivation channel, since the C−N=N/N=N−C oscillations are found to be symmetric, while the inversion hypothesis would require the inversion of only one of the two angles. If the bending oscillations are wide enough, the crossing region is reached much before 90° torsion, reducing the isomerization quantum yield. This is more likely to happen in the case of *trans*-azobenzene, because on the *cis* side the torsional gradient is steeper. Moreover, the quantum yield reduction upon $S_2$ excitation (−50%) is also ascribed to the wider and faster symmetric bending oscillations associated with promotion to this higher-lying state.

The experimental *trans* ⟶ *cis* deactivation time constants obtained by transient absorption (TA)[27–31], time-resolved photoelectron spectroscopy (TRPES)[32] and jet-cooled multiphoton ionization[33] are 0.34, 3.0, and 12 ps (after n$\pi^*$ excitation[29]), with an additional faster component of about 170 fs when starting from the $\pi\pi^*$ state [30, 32, 33]. For the *cis* ⟶ *trans* process, the experimental time constants are 0.1, 0.9 and 5.6 ps, independent of the excitation[29, 30]. Although they were at first assigned to the inversion process[27, 28], these time constants are more congruent with a fast movement out of the Frank-Condon region, followed by a large-amplitude motion on the $S_1$ PES, ascribable to the slow torsional coordinate. The ultrafast component recorded when *trans*-azobenzene is excited to $S_2$ is assigned to a $S_2 \longrightarrow S_1$ decay which takes place in the femtosecond regime, after which the excited state processes are the same as after n$\pi^*$ excitation, even though with a different relative amplitude due to the different starting point on the $S_1$ PES (outside the Franck-Condon region)[30].

We have produced an extended mapping of PESs, TDM and NAC of $S_0$ and $S_1$ (n$\pi^*$) of azobenzene in the 3D space spanned by C−N=N−C torsion and the two C−N=N bending angles at an unprecedented level of accuracy (SS- and MS-RASPT2/RASSCF, using a full $\pi/\pi^*$ active space plus the two non-bonding n orbitals[34]) with the aim of producing a wide and solid database that allows to simulate on the same basis the excited state dynamics of azobenzene (on the isomerizing $S_1$ state) with several methods, from classical MD with tailored force fields to purely quantum dynamics, thus allowing for direct comparison between the results of the different approaches. Indeed, excited state dynamic simulations are fundamental to understand what happens after the n$\pi^*$ or $\pi\pi^*$ states are populated, as well as to compare the calculated quantum yields with the experimental ones to validate the model picture itself. The obtained PESs show that the selected degrees of freedom are sufficient to accurately locate the crossing points where the non adiabatic decay takes place. The accuracy of the PESs was first validated with semi-classical dynamics in the reduced space of the three torsional and bending coordinates[34], whose results are in good agreement with past simulations[2, 25, 35]. Subsequently, in collaboration with the group of Professor Shaul Mukamel of the University of California, Irvine, we have simulated the photoisomerization (in both directions) by means of quantum dynamics (QD) simulations on the adiabatic PESs[36, 37], enriching our database with state and transition electron densities, that were used to simulate various kinds of time-resolved experiments: X-ray diffraction patterns during the isomerization resolved in time[36], and frequency[38] or coupled with resonant infrared field to enhance coherence signatures[39], electron diffraction patterns along the photodynamics[40] and also the effect of using entangled two-photon absorption on the quantum yield[37]. We have also started to investigate the effects of substitution on the azobenzene photoisomerization mechanism, focusing on the *push-pull* derivatives, which are of interest for in vivo applications. The results of our preliminary study alredy gave promising results, that we published in reference[41].

The following section 4.2 gives an introduction to the simulation of time-dependent diffraction signals, that we have applied to the QD of azobenzene. Section 4.3 includes the technical details of the calculations. The results concerning the PESs and interstate couplings of azobenzene are presented in sections 4.4.1 and 4.4.2, while the dynamics simulations and the simulated transient signals are discussed in sections 4.4.3 and 4.4.4. Eventually, section 4.5 is entirely dedicated to *push-pull* azobenzene derivatives.

## 4.2 Time-resolved x-ray and electron diffraction

X-ray diffraction (XRD) allows for the structural determination of compounds based on diffraction patterns. It is a widely used technique for crystals, but the possibility to perform transient experiments opens a doorway to monitor the molecular structure during the photochemistry, including signatures specific to conical intersections during non adiabatic events. Diffraction signals reveal the momentum transfer experienced by an incident photon through interference with one or more scatterers. They depend on the charge density $\sigma(\mathbf{q})$ of the sample, where $\mathbf{q} = \mathbf{k}_s - \mathbf{k}_p$ is the momentum difference between the incident $\mathbf{k}_p$ and scattered $\mathbf{k}_s$ wavevectors. Diffraction signals can be recorded either with photon or electron beams. While photons scatter off the electronic charge density of the sample, electrons scatter off the total (nuclear + electronic) charge density. Traditionally, stationary X-ray diffraction is used to determine the structure of crystalline matter. A momentum-space image, provided by the scattered photons, is recorded, allowing for the reconstruction of the real-space crystal structure. The XRD signal, expressed in terms of the electron densities of individual molecules in a sample, is given by the sum of one-molecule ($S_1(\mathbf{q}, t)$) and two-molecule ($S_2(\mathbf{q}, t)$) terms[42]:

$$S_1(\mathbf{q}, t) = N \int \mathrm{d}t \left|E_p(t - T)\right|^2 \langle\hat{\sigma}(-\mathbf{q}, t)\hat{\sigma}(\mathbf{q}, t)\rangle \tag{4.1}$$

$$S_2(\mathbf{q}, t) = F(\mathbf{q}) \int \mathrm{d}t \left|E_p(t - T)\right|^2 \left|\langle\hat{\sigma}(\mathbf{q}, t)\rangle\right|^2 \tag{4.2}$$

Here, $N$ is the number of active molecules, and $T$ is the the central time of the X-ray probe pulse envelope $E_p(t - T)$. $F(\mathbf{q})$ is the structure factor which encodes the long-range, intermolecular structure of the sample. In crystals, $F(\mathbf{q})$ is sharply peaked at the Bragg points which are directly related to reciprocal lattice vectors. At these Bragg peaks, contributions from ordered multiple scatterers coherently add up in phase and the $S_2(\mathbf{q}, t)$ signal scales as $N^2$. Away from the Bragg peaks, these terms have essentially a random relative phase, and the signal is negligible. In contrast, $S_1(\mathbf{q}, t)$ scales linearly with the number of molecules in the sample $N$, and does not depend on the structure factor. As a consequence, diffraction in crystals is usually dominated by the 2-molecule (or more generally 2-scatterer) coherent response that is responsible for the formation of Bragg peaks. Instead, for single molecule diffraction or diffraction in the absence of order, $S_1(\mathbf{q}, t)$ dominates and a continuous pattern is observed in momentum space.

The temporal resolution in X-ray diffraction, as obtained by formulas (4.1) and (4.2), are only possible due to the advent of free-electron X-ray light sources[43, 44] providing sub-femtosecond pulse durations, also available from tabletop setups (e.g. through high harmonic generation[45] or laser-driven plasma sources[46]). Another game-changing ingredient provided by such light sources is peak brilliancy: the high number of photons in the beam allows for a significant reduction of the sample size, while still achieving the necessary ratio of scattered photons per object to record diffraction patterns. Structure determination of nanocrystals[47, 48], aligned gas-phase molecular samples[49], and macromolecular structures[50, 51] were reported. Attempts toward imaging single molecules at free-electron lasers were made[52], although some challenges remain. Time-resolved X-ray (or electron) diffraction movies

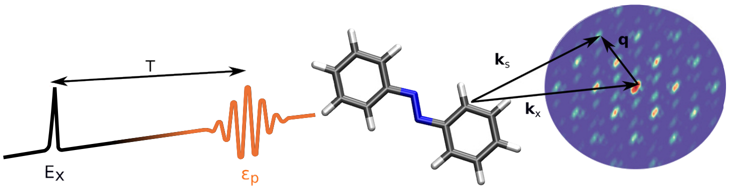

**Figure 4.5:** Ultrafast X-ray diffraction scheme: a pump pulse $\epsilon_p$ excites the molecules in the sample, then, a time-delayed X-ray probe pulse with envelope $E_x$ images the molecular structure in momentum space by elastic and inelastic photon scattering. $\mathbf{q} = \mathbf{k}_s - \mathbf{k}_x$ is the momentum difference between the incident $\mathbf{k}_x$ and scattered $\mathbf{k}_s$ wavevectors. From reference[39].

can monitor the electronic (or nuclear + electronic) charge density evolution during a chemical process[53–65]. A schematic representation of an ultrafast X-ray diffraction experiment is given in Figure 4.5.

Diffraction from matter in non stationary states, such as molecules undergoing a chemical transformation, involves physical processes that go beyond elastic scattering from instantaneous snapshots of the electronic ground state density. This is especially true for excited molecules, being in a time-evolving superposition of many-body states: in such cases, inelastic scattering from different electronic states[42, 66, 67], as well as electronic and vibrational coherences[42, 68–70] contribute to the signal. The latter, which are created when the molecular system corresponds to a linear superposition of different electronic and/or vibrational eigenstates, are non stationary and evolve in time as damped oscillations with a frequency corresponding to the energy difference between the involved eigenstates. They are of particular interest because their detection could allow for the direct imaging of conical intersections (where they are created by the bifurcation of the wavepacket between two electronic states). Unfortunately, coherences only persist for a short time before dephasing, and are generally much weaker than other contributions to the signals, therefore, they are hard to detect.

Recently, a lot of effort has been put on the simulation of transient diffraction signals[42, 67, 71] as a powerful tool to disentangle the different contributions to the total signal and get insight into the reaction mechanism (and, in particular, to the non adiabatic events). After the creation of an excited state wavepacket by an optical pump pulse and during the excited state dynamics, photons from an incident X-ray probe pulse are scattered from the molecular electron density $\hat{\sigma}(\mathbf{q})$, which is the Fourier transform of the real-space density $\hat{\sigma}(\mathbf{r})$ (we denote the real space electronic and nuclear coordinates $\mathbf{r}$ and $\mathbf{R}$, respectively). The total time-dependent wavefunction $\Psi(\mathbf{r}, \mathbf{R}, t)$ is expanded in the adiabatic basis

$$\Psi(\mathbf{r}, \mathbf{R}, t) = \sum_i c_i(t)\chi_i(\mathbf{R}, t)\varphi_i(\mathbf{r}; \mathbf{R}) \tag{4.3}$$

where $\chi_i(\mathbf{R}, t)$ is the normalised nuclear wave packet in the adiabatic electronic state $\varphi_i(\mathbf{r}; \mathbf{R})$ and $c_i(t)$ is the electronic state amplitude. Equation (4.3) is an exact representation which does not invoke the adiabatic approximation and can be similarly formulated in, e.g. a diabatic basis. Although $\hat{\sigma}(\mathbf{q})$ is a single-body electron operator, it depends on the nuclear configuration as well. Therefore, it remains an operator in the nuclear space after taking its matrix elements in the electronic subspace, i.e.

$\langle\varphi_i|\,\hat{\sigma}(\mathbf{q},\mathbf{R})\,|\varphi_j\rangle = \hat{\sigma}_{ij}(\mathbf{q},\mathbf{R})$.

The one-molecule time-resolved X-ray diffraction (TXRD) signal of a sample with $N$ noninteracting molecules is defined as the integrated rate of photon number change during the scattering process and is given by[42]

$$S_1(\mathbf{q},T) \propto N \int dt \left|E_p(t-T)\right|^2 \tilde{S}_1(\mathbf{q},t) \tag{4.4}$$

where $\tilde{S}_1(\mathbf{q},t)$ is the time-dependent molecular response. For a two-electronic-state model (with ground state $g$ and excited state $e$) $\tilde{S}_1(\mathbf{q},t)$ reads

$$\begin{aligned}\tilde{S}_1(\mathbf{q},t) &= \rho_{gg}(t)\,\langle\chi_g(t)|\,\hat{\sigma}^{\dagger}_{gg}\hat{\sigma}_{gg}\,|\chi_g(t)\rangle\\ &+ \rho_{ee}(t)\,\langle\chi_e(t)|\,\hat{\sigma}^{\dagger}_{ee}\hat{\sigma}_{ee}\,|\chi_e(t)\rangle\\ &+ \rho_{gg}(t)\,\langle\chi_g(t)|\,\hat{\sigma}^{\dagger}_{ge}\hat{\sigma}_{eg}\,|\chi_g(t)\rangle\\ &+ \rho_{ee}(t)\,\langle\chi_e(t)|\,\hat{\sigma}^{\dagger}_{eg}\hat{\sigma}_{ge}\,|\chi_e(t)\rangle\\ &+ 2\mathscr{R}\,\big[\,\rho_{eg}(t)\,\langle\chi_e(t)|\,\hat{\sigma}^{\dagger}_{ee}\hat{\sigma}_{eg}\,|\chi_g(t)\rangle\\ &+ \rho_{eg}(t)\,\langle\chi_e(t)|\,\hat{\sigma}^{\dagger}_{eg}\hat{\sigma}_{gg}\,|\chi_g(t)\rangle\,\big]\end{aligned} \tag{4.5}$$

where $\rho_{gg}(t)$ and $\rho_{ee}(t)$ are the electronic state populations and $\rho_{eg}(t)$ is the coherence magnitude. Matrix elements $\hat{\sigma}_{gg}$ and $\hat{\sigma}_{ee}$ are the ordinary electronic charge densities involving the electrons of the molecule. On the other hand, $\hat{\sigma}_{eg}$ and $\hat{\sigma}_{ge}$ represent transition charge densities that only account for orbitals involved in a particular electronic transition. As such, they are more sensitive to charge migration between the ground and valence excited states, that typically only involve one or few electrons. An equivalent result is obtained for ultrafast electron diffraction (UED)[71], with additional terms arising from nuclear and mixed electron-nuclear scattering.

The various contribution to the signal are conveniently represented by loop diagrams (Figure 4.6), that show the time evolution of the *bra* and *ket* of the molecular many-body wavefunction and the perturbative interactions with the incoming X-ray or electron beam. In a loop diagram, each field interaction is represented by an arrow, which either points to the right (photon annihilation and excitation of the molecule) or to the left (photon creation and de–excitation of the molecule). Free evolution periods on the left branch indicate forward propagation in real time, and on the right branch to backward propagation, respectively. For complete loop diagram rules see reference[72].

The first two terms in equation (4.5), corresponding to Figure 4.6 (i) and (ii), respectively, are the elastic contributions from the ground and excited states, whereas terms (iii) and (iv) represent inelastic Stokes (Figure 4.6 (iii)) and anti-Stokes (Figure 4.6 (iv)) processes. Finally, the last two terms (Figure 4.6 (v) and (vi)) represent mixed elastic/inelastic processes, which scatter off vibronic coherences. They contain the nuclear wave packet of the two different states in bra and ket, and their amplitude is given by the coherence magnitude $\rho_{eg}(t)$. The mixed elastic/inelastic processes involve an elastic scattering from $\hat{\sigma}_{gg}$ or $\hat{\sigma}_{ee}$ and an inelastic one from $\hat{\sigma}_{ge}$ or $\hat{\sigma}_{eg}$. The two scattered photon amplitudes, therefore, have frequencies centred around $\omega_X$ and $\omega_X \pm \omega_{eg}$ , where $\omega_X$ is the incoming X-ray frequency and $\omega_{eg}$ is the transition frequency between states $e$ and $g$. In order to generate a signal, a population must be

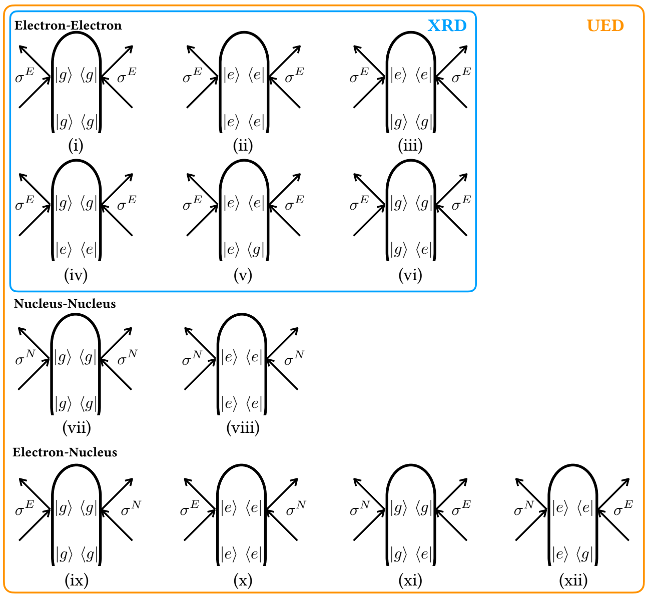

**Figure 4.6:** Loop diagrams for one-molecule XRD and UED expanded in electronic eigenstates for a two-state model. XRD is given by diagrams (i)–(vi), while all diagrams contribute to UED. The total XRD signal is the sum of electronic elastic ((i) and (ii)), inelastic electronic Stokes and anti-Stokes ((iii) and (iv)), and mixed electronic elastic/inelastic terms ((v) and (vi)). UED has additional contributions from nuclear elastic ((vii) and (viii)), mixed nuclear/electronic elastic ((ix) and (x)), and mixed nuclear/electronic elastic/inelastic ((xi) and (xii)) scattering. From reference[71].

created on the detector, which is possible only if these two amplitudes have a frequency within the detector bandwidth. The vibronic coherences, therefore, can be observed only by a broadband detector with a bandwidth larger than $\omega_{eg}$, which is usually the case for XRD detectors.

There are a few important points to note. First, as can be seen from equation (4.5), scattering does not simply occur from charge densities but from expectation values over products of charge density operators $\langle\sigma^\dagger\sigma\rangle$ (in the limit of impulsive diffraction, where both interactions occur at the same time). This means that the real-space molecular structure may not be simply reconstructed from the inverse Fourier transform of the diffraction pattern, an issue that is related to the well-known "phase problem" in diffraction. An extensive literature exists that solves this problem, e.g. by oversampling[73] or by anomalous diffraction[74]. However, phase retrieval for structure reconstruction is still scarce in femtosecond X-ray diffraction studies, as this is a difficult task with many technical subtleties and pitfalls. The second point to note is that equation (4.5) is exact and contains all contributions to the signal. Its use requires to explicitly calculate $\hat{\sigma}(\mathbf{q}, \mathbf{R})$ across the nuclear space, which can be a demanding task. In most experimental circumstances, the majority of the molecular charge can be definitively assigned to particular atoms, and only few electrons participate in chemical bonds. This inspires the commonly used independent atom approximation, where the total density of the molecule $\alpha$ is constructed by assigning form factors $f_a$ to each atom a and summing over them:

$$\sigma_\alpha(\mathbf{q}) = \sum_a \left|f_a(\mathbf{q})\right| e^{i\mathbf{q}\mathbf{R}_a} \tag{4.6}$$

This approximation may be useful in describing elastic scattering or population dynamics but misses the coherence term, which is the most relevant one for tracking non adiabatic events.

## 4.3 Computational details

An accurate simulation of TXRD signals requires electronic PESs, non adiabatic couplings, transition dipoles and charge densities as well as a nuclear quantum dynamics propagation scheme. All the simulations of the non adiabatic dynamics of azobenzene involved a preliminary study of PESs and other relevant quantities, followed by dynamics simulations of the photoisomerization process. The mapping of the state energies and couplings represents the core of the parameterisation protocol that we aim to describe with this thesis, and will be described in detail below. On the other hand, only the most significant details of the dynamics (that were performed in collaboration with other research groups) will be described. Further technical details of the various propagation schemes can be found in the corresponding published works.

### 4.3.1 Ab initio calculations

The PESs of both ground and first excited states of azobenzene were mapped along three internal coordinates: the C−N=N−C dihedral and the two C−N=N angles. RASSCF was applied for all calculations, using a 16 orbitals/18 electrons active space that includes all $\pi$ and $\pi^*$ orbitals as well as the two non-bonding n orbitals (Figures 4.7 and 4.8), employing the ANO-L-VDZP basis set[75]. The $\pi$ and n orbitals were put in RAS1, while the $\pi^*$ orbitals in RAS3, allowing for a maximum of four holes in RAS1 and four electrons in RAS3. The shorthand notation to describe this distribution among active spaces is RASSCF(4,9|0,0|4,7), where the RAS subspaces are divided by pipes, and for each subspace the couple of numbers $n$, $m$ indicates the maximum number $n$ of holes (for RAS1) or electrons (for RAS3) and the number of active orbitals $m$.

In all cases, the RASSCF calculation was followed by a RASPT2 correction, either at the Single State (SS) or at the Multi State (MS) level, using an imaginary shift of 0.2 a.u. and setting the IPEA shift to zero. The quality of the results was assessed by checking the reference wavefunction weight after the perturbation correction, which was always around 60%. The two lowest singlet states (ground and n$\pi^*$ states) were included in the state averaging (SA) procedure in all points of the grid (SA-2-RASSCF), except for a small region close to the *trans* FC point, where the $\pi\pi^*$ state was also mapped. Indeed, the latter is the third state ($S_2$) close to the *trans* minimum, but it exhibits pronounced energetic destabilisation for values of the C−N=N−C torsion away from 180° or symmetric bending above 120°. As a consequence, a large number of states would have to be included in the SA-RASSCF calculations to keep track of this particular state along the scan, resulting in a high computational cost. Moreover, recent results published by our group[14] show that, after $\pi\pi^*$ excitation, the molecule retains a planar structure and exhibits wide and fast symmetric bending oscillations,

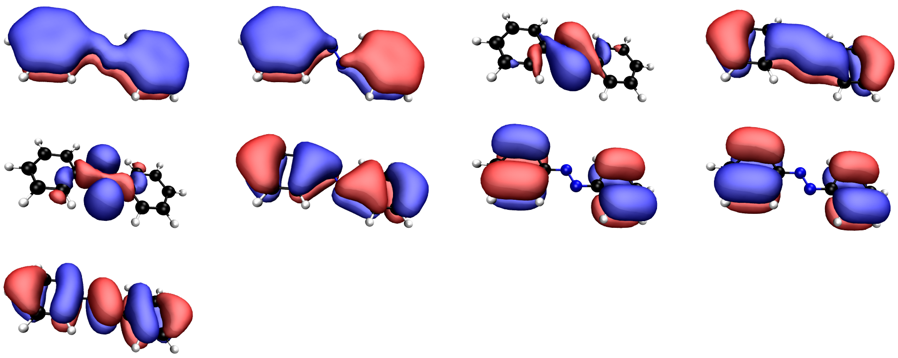

(a) RAS1 orbitals

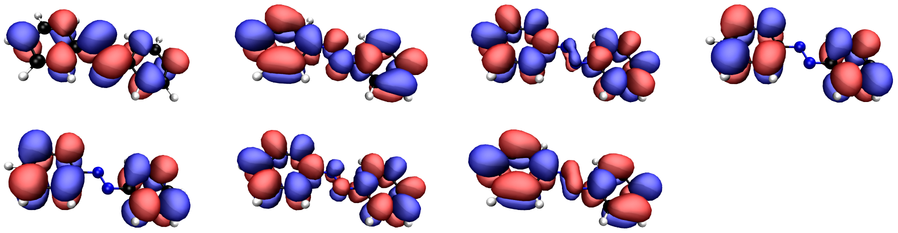

(b) RAS3 orbitals

**Figure 4.7:** Active space orbitals of *trans*-azobenzene (SA-2-RASSCF(4,9|0,0|4,7)/ANO-L-VDZP).

that immediately lead towards a planar $S_2/S_1$ CI found at $\mathrm{C{-}N{=}N} = \mathrm{N{=}N{-}C} = 105^\circ$. It is therefore reasonable to think that, for the study of the reaction mechanism starting from the $\pi\pi^*$ state, it should be sufficient to map the surface of $S_2$ only close to $\mathrm{C{-}N{=}N{-}C} = 180^\circ$ and for small values of the two $\mathrm{C{-}N{=}N}$ angles (i.e. in a region that goes from the FC point up to the $S_2/S_1$ CI). All the energy computations have been performed with the MOLCAS8[76] quantum chemistry program, applying Cholesky decomposition.

The selected torsional and bending coordinates were scanned starting from the MP2/ANO-L-VDZP ground-state-optimized structures of both *trans* and *cis*-azobenzene isolated isomers in gas phase (Figure 4.9). All remaining degrees of freedom were kept frozen at their ground state minimum value. The results of the two rigid scans (i.e. starting from *trans* or *cis* ground state equilibrium structure) were eventually merged keeping the structure which gave the lowest $S_1$ energy for each point of the 3D grid.

*Trans*-azobenzene has a $C_{2\mathrm{h}}$ symmetry in its minimum, but the $\sigma_\mathrm{h}$ plane is removed by torsion around the $\mathrm{C{-}N{=}N{-}C}$ dihedral, reducing the symmetry to $C_2$. On the other hand, *cis*-azobenzene already belongs to the $C_2$ point group at its $S_0$ minimum. For both isomers, the $C_2$ axis is preserved under symmetric bending, while it is removed by asymmetric bending deformations, resulting in a $C_1$ structure. As a consequence, the structures of 3D scan characterised by identical $\mathrm{C{-}N{=}N}/\mathrm{N{=}N{-}C}$ bending angles have $C_2$ symmetry, while all other geometries have $C_1$ symmetry. For consistency, all calculations were performed without symmetry.

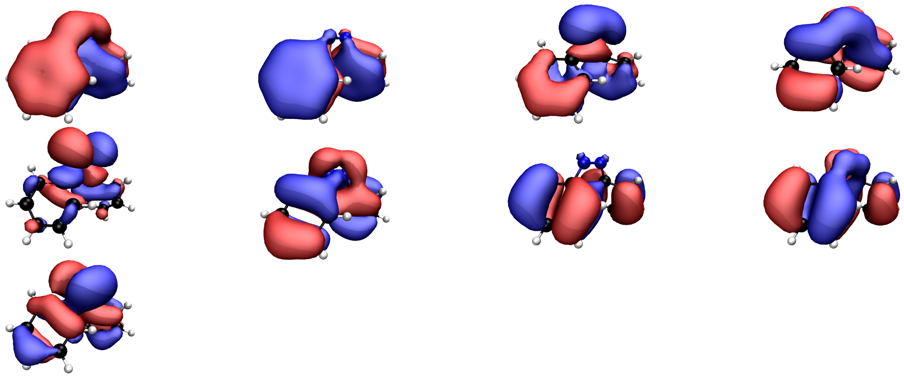

(a) RAS1 orbitals

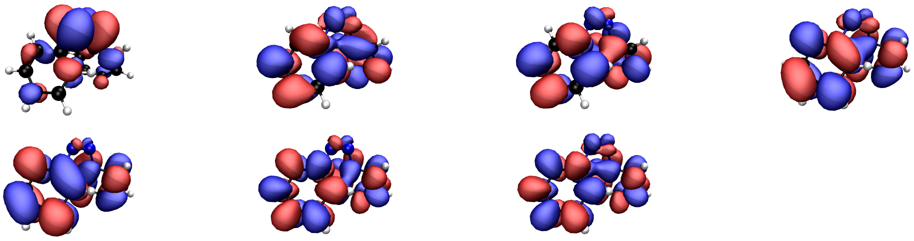

(b) RAS3 orbitals

**Figure 4.8:** Active space orbitals of *cis*-azobenzene (SA-2-RASSCF(4,9|0,0|4,7)/ANO-L-VDZP).

We first made a 2D scan of C−N=N−C torsion and C−N=N/N=N−C symmetric bending. The C−N=N−C dihedral was mapped between 0° and 180°, with a step of 10°, that was reduced to 4° in the twisted region where the PESs get closed (i.e. between 82° and 110°). Symmetric C−N=N/N=N−C bending was mapped between 100° and 180° with a step of 2°. Then, for selected values of the CNNC dihedral (namely 180°, 150°, 120°, 106°, 102°, 98°, 94°, 90°, 86°, 82°, 60°, 30°, 10°) we additionally scanned the two C−N=N bending angles independently, using the same range and step as before, giving rise to roughly 22000 points in the global 3D surface.

Concerning the type of perturbative correction, benchmarking showed that the SS- and MS-RASPT2 methods are equivalent when $S_0$ and $S_1$ are well separated in energy (i.e. C−N=N−C < 82° or C−N=N−C > 106°, see Figure 4.10 (a)), therefore, the cheaper SS-RASPT2 correction was applied in such cases. On the other hand, the state mixing when 82° ≤ C−N=N−C ≤ 106° causes the SS-RASPT2 PESs to show double or triple crossings (see Figure 4.10 (b)), which disappear after MS-RASPT2 correction. The SS-RASPT2 crossings are not accompanied by a sudden change in the state nature, as expected in a real crossing point, but rather the two wavefunctions show a multiconfigurational nature. This is a consequence of the strong wavefunction mixing at the RASSCF level in this region, that is not properly fixed by the SS-RASPT2 correction. In these cases, MS-RASPT2 was applied, which gives a more balanced description and is able to resolve the CASSCF wavefunction mixing. The electronic states densities as well as the $S_0 \longrightarrow S_1$ TDM and transition densities were calculated across all the grid through the MOLCAS &RASSI routine, making use of RASSCF or

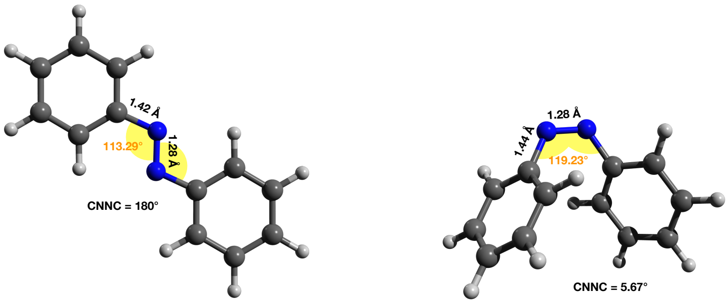

(a) *trans*-azobenzene (b) *cis*-azobenzene

**Figure 4.9:** MP2/ANO-L-VDZP optimised structures of *trans* and *cis*-azobenzene.

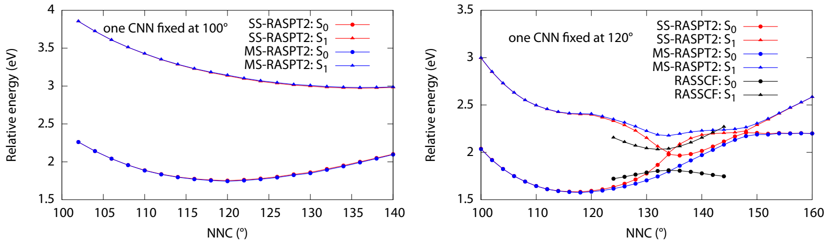

(a) C—N═N—C = 60° (b) C—N═N—C = 90°

**Figure 4.10:** Comparison between SS- and MS-RASPT2 corrections far from the twisted region (a) and at 90° torsion (b). From reference[34].

MS-RASPT2 wavefunctions for the points in which SS- or MS-RASPT2 was applied, respectively. The one-electron (transition) densities $\sigma_{ij}(\mathbf{r},\mathbf{R})$ were rotated from the molecular to the atomic orbital basis $\{\phi_r(\mathbf{r},\mathbf{R})\}$ and Fourier transformed according to the formula

$$\sigma_{ij}(\mathbf{q},\mathbf{R}) = \int \mathrm{d}\mathbf{r}e^{-i\mathbf{q}\mathbf{r}} \sum_{rs} P^{ij}_{rs}(\mathbf{R})\phi^*_r(\mathbf{r},\mathbf{R})\phi_s(\mathbf{r},\mathbf{R}) \tag{4.7}$$

The sign of TDMs and electronic densities were corrected according to the procedure described in Section 3.5.

The same level of theory of the rigid scans (MS-2-RASPT2/SA-2-RASSCF(4,9|0,0|4,7)/ANO-L-VDZP) was used for a fully relaxed geometry optimisation of the first excited state (n$\pi^*$) and for a $S_1/S_0$ CI optimisation, both performed without imposing any symmetry.

Besides the PESs and TDMs, we also mapped the $S_1/S_0$ NAC at MS-RASPT2 level for the points of our 3D grid where 82° ≤ C—N═N—C ≤ 106° and the energy gap $\Delta E_{S_1-S_0}$ was lower than 0.3 eV. A computation of the full numerical cartesian NAC would require 144 single-point calculations for each geometry in the case of azobenzene. However, from a preliminary analysis of the full NAC vector at some test geometries, we noticed that only the cartesian components that refer to the four central C—N═N—C atoms adopt significant values (see the supporting information of reference[34]). Given this result, we first approximated the NAC calculating only its components in the subspace of the four central atoms (24 single-point calculations per geometry). This data was used for the semiclassical dynamics published in reference[34]. Following collaboration with the Mukamel's group for the QD simulations required either a wider and/or a denser NAC mapping in the bidimensional subspaces of the QD dynamics. For the *cis* ⟶ *trans* simulation, that was run in the subspace of C−N=N−C dihedral and one C−N=N angle (keeping the other fixed at 116°), we have mapped the NAC at C−N=N−C = 82°, 86°, 90°, 91°, 92°, 93°, 94°, 95°, 96°, 97°, 98°, 102° and 106° between C−N=N = 126° and 156° (with a step of 1°). For the *trans* ⟶ *cis* simulation, that was run in the subspace of C−N=N−C dihedral and symmetric C−N=N/N=N−C bending, the NAC was mapped for 80° ≤ C−N=N−C ≤ 110° (step 2° everywhere except between 96° and 102°, where a step of 1° was used), and symmetric bending between 110° and 156° (step 1°). By the time of the *trans* ⟶ *cis* simulation, we had developed the machinery for numerical NAC calculations in internal coordinates described in Section 3.4.1. For the case of three reactive coordinates, this reduces the number of single point calculations required for each NAC up to 6. Therefore, for the corresponding NACs we employed this protocol. All NACs used for QD were sign-corrected according to the protocol described in Section 3.5. Minima and CI optimisations with numerical RASPT2 gradients as well as numerical NAC calculations were performed using the suite COBRAMM[77–79] interfaced with MOLCAS[76] and with an integrated scheme for obtaining numerical gradients and NACs.

### 4.3.2 Dynamics simulations

The propagation of trajectories or wavepackets for dynamics simulations requires smooth potentials. For this reason, we fitted the obtained PESs with a combination of the first 6 terms of the cosine Fourier series for the CNNC dihedral, and the first 6 terms of the power series expansion for the CNN and NNC angles, obtaining satisfactory results. Details of the fitting procedure and functions can be found in the Supporting Information of reference[34].

#### Semiclassical dynamics

A simple semiclassical dynamics in the subspace of the scanned coordinates was used to asses the accuracy of the 3D PESs, in a collaboration with the group of Professor Claudio Zannoni of our department (details in reference[34]). We propagated the nuclei classically on the fitted PESs, while all the remaining degrees of freedom were effectively frozen by setting the corresponding force field constant to artificially high values. Electrostatic charges and Lennard-Jones coefficients were set to zero as well. We ran 200 10 ps NVE simulations of a single *trans*-azobenzene molecule in vacuum at 300 K with a timestep of 0.1 fs. The simulations were started in n$\pi^*$ state, sampling the 3D phase space from a Wigner distribution in the reduced coordinate space around the ground state *trans* minimum at 300 K. Whenever the classical trajectory on the excited state entered a region where the NAC was mapped, it was allowed to instantaneously hop to the ground state according to Tully's fewest switches probability[80]. After the non adiabatic event, the force field felt by the molecule was changed from that of $S_1$ to that of $S_0$ until the end of the simulation, without allowing for back hopping. The use of only three non-frozen degrees of freedom reduces significantly the modules of the atomic velocities with respect to a fully unconstrained simulation. This implies a smaller decay probability, due to the presence of a dot product between NAC and velocity in its formula. For this reason, we compared our average velocity of the four central C, N, N, C atoms ($\bar{v}_R$) with that of a Wigner sampling in the full coordinate space ($\bar{v}_F$), finding a $\bar{v}_R/\bar{v}_F$ ratio of 4.5 that was applied to our velocities as scaling factor. All MD simulations were performed with an in-house-modified version of the Molecular Dynamics software NAMD[81], interfaced with the COBRAMM code[77–79] for the calculation of the hopping probability.

### Quantum dynamics

The QD of both *trans* ⟶ *cis* and *cis* ⟶ *trans* processes in gas phase was simulated in a series of collaborations with the group of Professor Shaul Mukamel of the University of California, Irvine. The high level of accuracy, together with the additional computational cost for the simulation of transient signals along the propagation, required the reduction of the number of coordinates to two. Therefore, we have simulated the *cis* ⟶ *trans* dynamics in the subspace of C−N=N−C torsion and one of the two C−N=N angles, keeping the other fixed at 116°. This choice allows to accurately describe the lowest part of the $S_1/S_0$ crossing seam (driving the non adiabatic event), while the regions of the PESs which are less involved in the decay (e.g. FC regions) are still reasonably well described. Instead, for the *trans* ⟶ *cis* conversion, we used as coordinates the C−N=N−C dihedral and the symmetric C−N=N/N=N−C bending, in order to correctly describe also the symmetric bending CIs which are more accessible on the *trans* side (see section 4.4).

Exact QD simulations in the reduced-dimensional space of two reactive coordinates were performed by solving the time-dependent Schrödinger equation (4.8):

$$i\hbar\frac{\partial}{\partial t}\Psi = \hat{H}\Psi = \left[\hat{T}_q + \hat{V} - \hat{\mu}\varepsilon(t)\right]\Psi \tag{4.8}$$

where the $\hat{\mu}\varepsilon(t)$ is needed to simulate an explicit pump pulse. The nuclear wave function $\chi(\mathbf{R}, t)$ was obtained by propagating the $S_0$ ground state vibrational wave function $\chi(\mathbf{R}, t_0)$ with a Chebychev propagator[82] using a time step of 0.05 fs. The kinetic energy operator $\hat{T}_q$ in equation (4.8) is set up according to the G-Matrix formalism[83, 84] in 2 reactive coordinates. More technical details about the propagation can be found in references[36, 38, 39] (*cis* ⟶ *trans* simulation) and [37] (*trans* ⟶ *cis* simulation).

## 4.4 Results and discussion

### 4.4.1 Potential energy surfaces

Figure 4.11 shows selected cuts of the 3D PESs, while Table 4.1 collects details about minima, saddle points and relevant CIs. In the two ground state minima, the vertical excitation to $S_1$ is found to be 2.66 eV (466 nm) for the *trans* and 2.78 eV (445 nm) for the *cis* isomer, while for $S_2$ only the *trans* excitation energy is available, which is 3.86 eV (321 nm). These values are in good agreement with the experimental ones[85], with a small underestimation in the case of the $n\pi^*$ state, possibly due to the neglect of solvation effects.

**Table 4.1:** Structures and energies* of $S_0$, $S_1$ and $S_2$ at significant points (minima, saddle points, relevant CIs) obtained with the rigid scan (in the space of C−N=N−C torsion and C−N=N/N=N−C bending) and with unconstrained optimisations (more structures in reference[34]; * *a*=SS-RASPT2, *b*=MS-RASPT2)

| | CNNC (°) | CNN (°) | NNC (°) | $E_{S_0}$ (eV) | $E_{S_1}$ (eV) | $E_{S_2}$ (eV) |
|---|---|---|---|---|---|---|
| $S_0$ *trans* min | 180 | 112-114 | 112-114 | $0.00^a$ | $2.66^a$ | $3.86^a$ |
| $S_0$ *cis* min | 0 | 120 | 120 | $0.37^a$ | $3.15^a$ | - |
| $S_0$ TS | 90 | 118 | 118 | $1.57^a$ | $2.14^a$ | - |
| $S_2$ min | 180 | 108-110 | 108-110 | $0.11^a$ | $2.99^a$ | $3.84^a$ |
| $S_1/S_0$ CI-bend1 | 180 | 150 | 150 | $3.04^a$ | $3.08^a$ | - |
| $S_1/S_0$ CI-bend2 | 0 | 156 | 156 | $3.22^a$ | $3.24^a$ | - |
| T102-$S_0$ min | 102 | 116 | 116 | $1.51^b$ | $2.13^b$ | - |
| T102-$S_1$ min | 102 | 120 | 122 | $1.55^b$ | $2.15^b$ | - |
| T94-$S_0$ min | 94 | 116 | 116 | $1.54^b$ | $2.42^b$ | - |
| T94-$S_1$ min | 94 | 116 | 132 | $1.74^b$ | $2.16^b$ | - |
| T82-$S_0$ min | 82 | 116 | 116 | $1.45^b$ | $2.42^b$ | - |
| T82-$S_1$ min | 82 | 116 | 134 | $1.70^b$ | $2.17^b$ | - |
| T98-$S_1/S_0$ CI | 98 | 116 | 146 | $2.12^b$ | $2.22^b$ | - |
| T94-$S_1/S_0$ CI | 94 | 114 | 146 | $2.16^b$ | $2.19^b$ | - |
| T90-$S_1/S_0$ CI | 90 | 114 | 146 | $2.13^b$ | $2.20^b$ | - |
| opt-$S_1$ min | 96 | 115 | 145 | $1.98^b$ | $1.98^b$ | - |
| opt-$S_1/S_0$ CI | 95 | 115 | 146 | $1.98^b$ | $1.99^b$ | - |

Figure 4.12 shows the gradients along C−N=N−C torsion and C−N=N symmetric bending near the *trans* and *cis* FC points. The ground state is destabilised along the torsion coordinate, and a barrier is separating the two minima (see Figure 4.11 (a) and (c)) with a saddle point ($S_0$ TS in Table 4.1) standing 1.57 eV above the *trans* minimum and 1.20 eV above the *cis* minimum. On the other hand, the $n\pi^*$ state PES along torsion is extremely flat, with a small but favourable gradient pointing towards twisted geometries (Figure 4.12 (a) and (c)). $S_1$ does not display any torsional barrier within our grid points, neither starting from the *trans* nor starting from the *cis* isomer. Although it is possible that we may overlook the presence of a torsional saddle point due to the lack of full geometry relaxation, the topology of the $n\pi^*$ PES suggests that (if it exists) the barrier should be extremely low, in agreement with past computational studies[14, 21, 86] and photoelectron spectroscopy[33]. Despite being quite flat in all the grid points, the torsional $S_1$ gradient is a bit more negative at the *cis* FC point, where the torsion is expected to be activated faster than in the *trans* case. In contrast, torsion is not favoured after excitation to $S_2$, whose minimum exhibits a planar structure ($S_2$ min in Table 4.1).

The excited state gradients are much more pronounced along the symmetric bending coordinate, especially at the *trans* FC point (Figure 4.12 (b) and (d)). Here, both $S_1$ and $S_2$ minima (relative to symmetric bending) are displaced with respect to the FC point, even though in opposite directions: the gradient on $S_1$ points towards an opening of the two C−N=N angles, while on $S_2$ they tend to reduce. Moreover, close to the $S_2$ minimum, the PESs of the $n\pi^*$ and $\pi\pi^*$ states approach and almost cross at C−N=N = N=N−C = 100°. Due to the rigidity of our scan, we do not observe a real degeneracy point, but still our results agree very well with those of a fully-

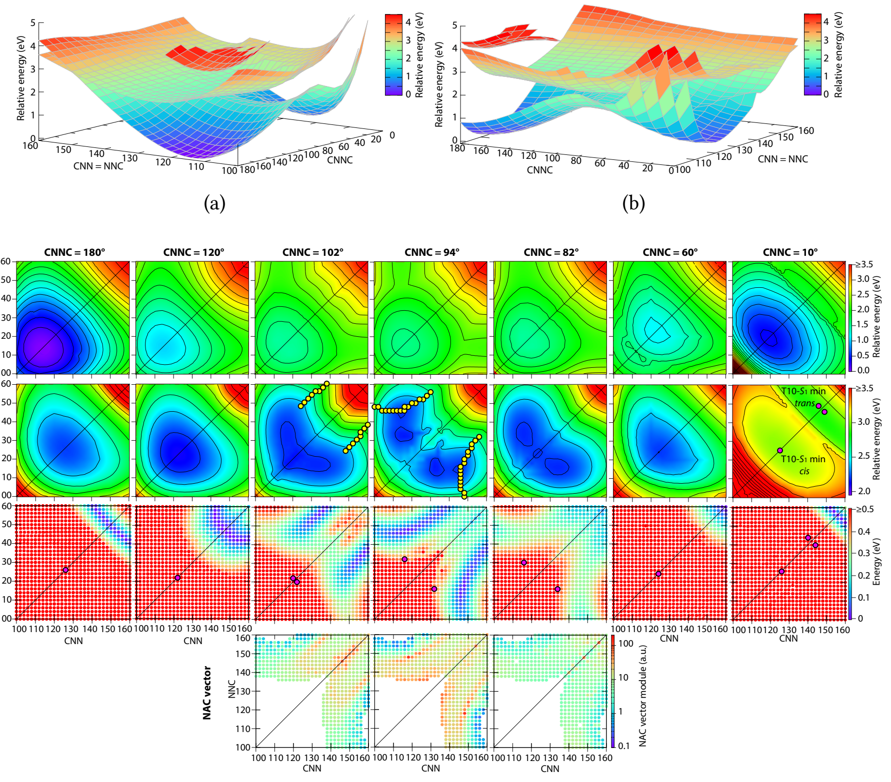

(a)

(b)

(c)

**Figure 4.11:** Side views ((a), (b)) of the PESs in the space of C−N=N−C torsion and symmetric C−N=N bending; top views (c) of $S_0$ and $S_1$ PESs (isolines every 0.1 eV) and energy gap $E_{S_1-S_0}$ in the space of C−N=N and N=N−C bending angles for fixed torsional values of 180°, 120°, 102°, 94°, 82°, 60° and 10° (the diagonal connects symmetric structures). The yellow dots label the CIs whose energy is lower than the FC point, the purple dots indicate $S_1$ minima. For 102°, 94° and 82° torsion the NAC vector module (in atomic units) is also displayed, for the points where $E_{S_1-S_0} \leqslant 0.3$ eV. From reference[34].

relaxed $S_2/S_1$ CI optimisation performed at a similar level of theory[14], that found a planar crossing at C−N=N = N=N−C = 105°. Our results indicate that, after $\pi\pi^*$ excitation, the main molecular deformations should be along symmetric bending, to reach the planar $S_2$ minimum ($S_2$ min in Table 4.1). Symmetric bending oscillations are likely to cause a very fast decay to $S_1$ through the close-lying $S_2/S_1$ CI around C−N=N = N=N−C = 100°, starting the dynamics on $S_1$ in a region with a steep symmetric bending gradient. This view is in perfect agreement with the most recent studies on the $\pi\pi^*$ state deactivation mechanism[14]. Symmetric bending is favoured on $S_1$ also at the *cis* FC point, even though the wider C−N=N values of the *cis* isomer reduce the excited state gradient with respect to the *trans* case (see Figure 4.12 (d)).

As introduced in section 4.3.1, the *trans* and *cis* $S_0$ minima both show a symmetric structure. On the ground state, desymmetrization of the two C−N=N angles is never favoured, as testified by the diagonal position of the minima in the $S_0$ PESs

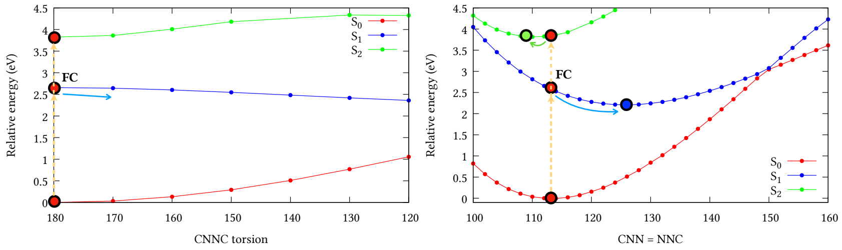

(a) C—N=N = N=N—C = 112° (b) C—N=N—C = 180°

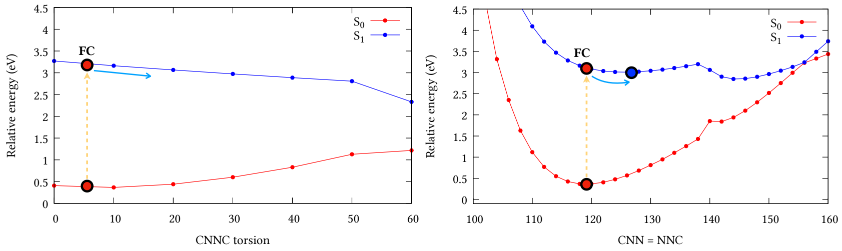

(c) C—N=N = N=N—C = 118° (d) C—N=N—C = 10°

**Figure 4.12:** Initial gradients on the *trans* side ((a),(b)) and on the *cis* side* ((c),(d)) along C—N=N—C torsion ((a),(c)) and symmetric C—N=N bending ((b),(d)). Coloured spots label the ground state minima (red, FC points) and excited state minima relative to the represented coordinate (blue: $S_1$; green: $S_2$). Excited state gradients pointing away from the FC point are represented with coloured arrows. (* discontinuities in the PESs on the *cis* side are caused by merging the two rigid scans and are smoothed by the fitting, see section 4.3.1)

of Figure 4.11 (c). In contrast, $S_1$ shows a different trend: far from twisted geometries (i.e. for C—N=N—C > 106° or C—N=N—C < 82°), the desymmetrization of the two C—N=N angles is not favoured even on the excited state. On the other hand, for 82° ≤ C—N=N—C ≤ 106° the $n\pi^*$ PES shows two off-diagonal minima (see Figure 4.11), even though the stabilisation brought by the asymmetric deformation is not large (~0.2 eV lower than the closest symmetric structures). Indeed, the $n\pi^*$ surface in our reduced space is extremely flat, and it is difficult to locate the absolute $S_1$ minimum in the 3D grid, since for 30° ≤ C—N=N—C ≤ 150° all the local minima are almost isoenergetic, or their energy difference falls below the RASPT2 error (see T102-$S_1$ min, T94-$S_1$ min and T82-$S_1$ min structures reported in table 4.1). However, our results clearly indicate that the absolute $S_1$ minimum will have a twisted geometry, with C—N=N—C close to 90°, and asymmetric C—N=N angles.

Our scans allow to reconstruct the excited state MEP after $n\pi^*$ excitation, which is represented in Figure 4.13. On the *trans* side, starting from FC point ($E_{S_1}$ = 2.66 eV), the MEP initially follows the symmetric bending gradient leading to an opening of both C—N=N angles, then it deviates along C—N=N—C torsion. The initial gradient along bending is due to the significant difference in the C—N=N/N=N—C values between the FC point and the $n\pi^*$ minimum (see Table 4.1) and it is responsible for most of the $n\pi^*$ stabilisation, while the points of the MEP that connect the planar structures and the twisted $S_1$ minimum are almost isoenergetic. In contrast, on the *cis* side, the difference in symmetric bending between the FC point and the $S_1$ minimum is small,

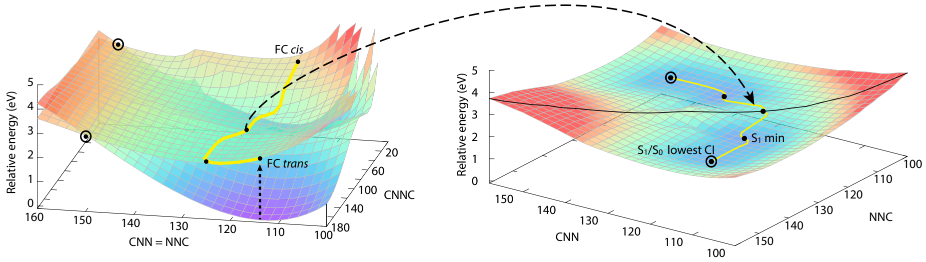

**Figure 4.13:** Excited state MEP after n$\pi^*$ excitation of *trans* or *cis*-azobenzene (yellow line). The MEP initially follows symmetric bending and torsion (left panel), then, once the twisted region is reached, the two C−N=N angles desymmetrise (right panel). Black spots label local and global state minima (•) or $S_1/S_0$ CIs (⊙)

and the MEP is mainly torsional and characterised by a steeper C−N=N−C gradient, since the *cis* FC point ($E_{S_1} = 3.15$ eV) is higher in energy compared to the *trans* one. For both *trans* and *cis*, once the MEP reaches C−N=N−C ≃ 90°, the n$\pi^*$ gradient leads towards the almost isoenergetic asymmetric $S_1$ minima and $S_1/S_0$ CIs.

The third row of Figure 4.11 (c) shows the $S_1$-$S_0$ energy gap. Far from 90° torsion, the crossing seam (blue/violet region) includes only high in energy structures (~ 3 eV) characterised by wide bending angles, with the shape of a straight line perpendicular to the diagonal (i.e. C−N=N + N=N−C constant around 300°). This is probably because opening one of the two angles increases the repulsion with the respective nitrogen lone pair, requiring a reduction of the other C−N=N to compensate and preserve degeneracy. The two structures $S_1/S_0$ CI-bend1 and $S_1/S_0$ CI-bend2 (Table 4.1) are sloped CIs (see Figure 4.12 (b) and (d)) and their presence had already been reported[14, 21, 22]. $S_1/S_0$ CI-bend1 on the *trans* side is difficult to reach at room temperature with direct n$\pi^*$ excitation, since it lies significantly higher in energy than the *trans* FC point. Moreover, the excited state gradient points in the opposite direction. According to reference [14], this crossing point becomes accessible via excitation to the $\pi\pi^*$ state, and it is responsible for the violation of Kasha's rule, as explained above. In contrast, on the *cis* side the FC point and $S_1/S_0$ CI-bend2 are nearly isoenergetic, but here the favourable $S_1$ gradient along C−N=N−C torsion is likely to drive most of the molecules away from this region before $S_1/S_0$ CI-bend2 is reached.

On the other hand, in the twisted region (82° ⩽ C−N=N−C ⩽ 102°) the crossing seam is wider and includes only asymmetric structures, which is a common feature of many conjugated compounds[87]. Indeed, the lowest-energy CIs of the grid are found between 90° and 98° torsion: we find three isoenergetic crossing points around 2.2 eV, which are asymmetric and characterised by similar bending values (T98- , T94- and T90-$S_1/S_0$ CI in Table 4.1). Although these results are coming from a rigid scan, they perfectly match those of some fully-unconstrained CASPT2 optimisations[21, 22], both in terms of energy and geometry. It is important to stress the fact that the surface of the n$\pi^*$ state in this region is so flat that the lowest points of the seam are almost isoenergetic with the $S_1$ asymmetric minima (see Table 4.1), and the path connecting them is practically barrierless.

To sum up, out PESs clearly indicate that the $S_1/S_0$ states are crossing for an extended range of geometries, which together form a wide crossing seam. Far from twisted geometries (i.e. close to the *trans* and *cis* FC regions) it includes high-energy and wide-bending geometries, which are not easily accessible after direct n$\pi^*$ excitation. Decay through such CIs is not likely to lead to isomerization, since the C−N=N−C value is always too close to that of the starting isomer, and the symmetric value of the two C−N=N angles prevents the inversion route as well. On the other hand, as C−N=N−C torsion proceeds, the crossing seam lowers in energy and shift towards asymmetric C−N=N/N=N−C structures, which represent the most accessible and productive deactivation channels, lying more or less halfway between *trans* and *cis*.

## 4.4.2 Unconstrained optimizations

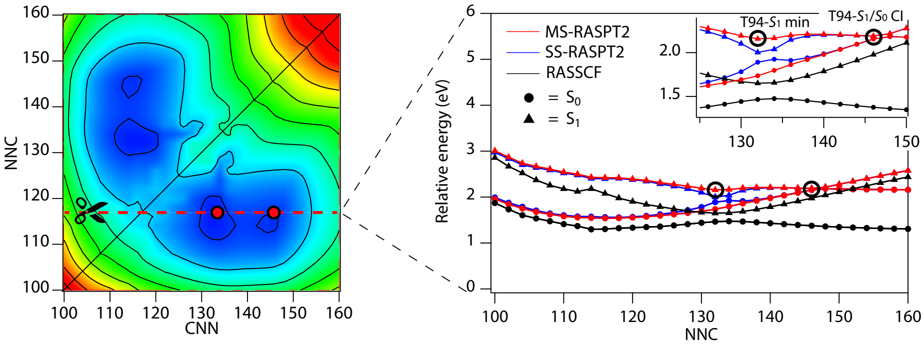

**Figure 4.14:** Cut through the PESs along one C−N=N angle for C−N=N−C fixed at 94° and the other C−N=N fixed at 116°. This cut shows both T94-$S_1$ min and the lowest crossing point T94-$S_1$/$S_0$ CI. From reference[34]

Figure 4.14 shows a cross-section of the RASSCF, SS-RASPT2 and MS-RASPT2 potential energy surfaces at 94° torsion including the two structures T94-$S_1$ min and T94-$S_1$/$S_0$ CI (see geometrical parameters and state energies in Table 4.1 and structures in Figure 4.15 (a) and (b)), which can be identified as the absolute $S_1$ minimum and the lowest $S_1$/$S_0$ CI from our rigid scan, respectively. Both structures are local minima on the excited state, separated just by a very small barrier. T94-$S_1$ min almost corresponds to a degeneracy point at RASSCF level ($\Delta E^{\mathrm{RASSCF}}_{S_1-S_0} = 0.18$ eV) and at SS-RASPT2 level ($\Delta E^{\mathrm{SS\text{-}RASPT2}}_{S_1-S_0} = 0.11$ eV). However, after MS-RASPT2 correction, the two states split ($\Delta E^{\mathrm{MS\text{-}RASPT2}}_{S_1-S_0} = 0.42$ eV). On the other hand, at T94-$S_1$/$S_0$ CI, the RASSCF states are well separated in energy, and the SS- and MS-RASPT2 results are similar, resulting in a crossing point in both cases ($\Delta E^{\mathrm{SS\text{-}RASPT2}}_{S_1-S_0} = \Delta E^{\mathrm{MS\text{-}RASPT2}}_{S_1-S_0} = 0.03$ eV). It is therefore probable that T94-$S_1$ min is an artefact of the RASPT2 correction, that suffers from the heavy wavefunction mixing at RASSCF level. To assess our results, we performed a geometry optimisation on the n$\pi^*$ state and a $S_1$/$S_0$ conical intersection optimisation, employing the same level of theory of the rigid scan for twisted geometries (MS-2-RASPT2/SA-2-RASSCF(4,9|0,0|4,7)/ANO-L-VDZP), both without constraints and without symmetry. Figure 4.15 (c) and (d) show the resulting optimised structures, while the relative energies are reported in the lower part of Table 4.1. The two optimised structures are almost identical, showing that the fully relaxed excited state minimum coincides with the lowest energy $S_1$/$S_0$ CI. Comparing this structure

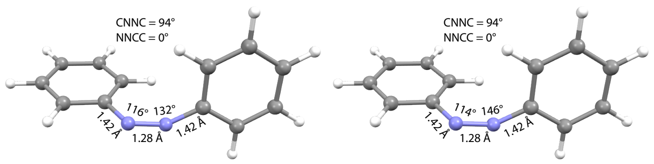

(a) T94-$S_1$ min (b) T94-$S_1/S_0$ CI

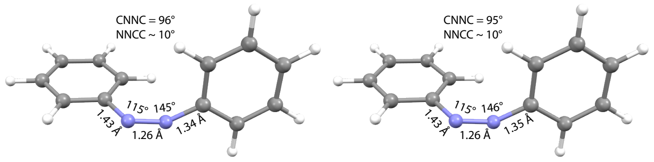

(c) optimised $S_1$ minimum (d) optimised $S_1/S_0$ CI

**Figure 4.15:** Structures of the $S_1$ asymmetric minimum (a) and $S_1/S_0$ lowest-energy CI (b) from the rigid scan; optimised $S_1$ minimum (c) and $S_1/S_0$ CI (d). From reference[34].

to the FC geometries, the most significant differences are found along the C−N=N−C torsion and C−N=N/N=N−C bending values, confirming that these coordinates are the most relevant ones both for the $n\pi^*$ relaxation and to reach the $S_1/S_0$ crossing seam. It is remarkable that the structure is asymmetric, and that the rigid scan predicts very well the values of the C−N=N−C dihedral and C−N=N angles. In addition, the relative energy of the optimised CI is only 0.2 eV lower than that of the CIs from the rigid scan, which means that other internal coordinates are only of secondary importance.

In reference[34] we have compared our optimised CI with some literature results[21, 22] obtained at a similar level of theory (but with smaller active spaces), whose energy was recomputed at our level of theory. Even though the scenario from both references is in good agreement with our results, only one of the reported CIs is a real crossing point also at our level of theory, demonstrating how strongly the electronic structure calculations are affected by the composition of the active space. The effect of the active space size is also visible in the absolute energy of the states (reported in reference[34]), which are considerably different from the original values.

### 4.4.3 Semiclassical dynamics simulations

The accuracy of our PESs, was assessed with semiclassical dynamics simulation of the *trans* ⟶ *cis* photoisomerization at 300 K in the subspace of the three mapped coordinates. For the simulation of the non adiabatic event we computed the $S_1/S_0$ NAC vector in the subspace of the central CNNC atoms between 82° and 102° torsion as described in Section 4.3.1. The NAC modules for C−N=N−C = 82°, 94° and 102° are reported in the lowest part of Figure 4.11. As expected, the largest magnitudes are found at 94° torsion, where the two PESs are closer in energy. Moreover, the fact that the highest NAC modules are found for asymmetric bending geometries (i.e. close to the crossing seam) confirms the importance of desymmetrization for coupling the two states. Figure 4.16 shows the average values of the C−N=N−C dihedral and C−N=N

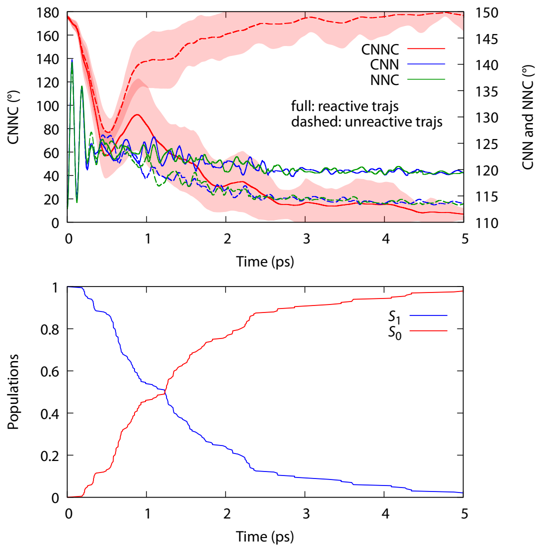

**Figure 4.16:** Average values of the C−N=N−C dihedral and C−N=N angles along the bunch of trajectories (top) and $S_1$ and $S_0$ populations as a function of time (bottom). From reference[34].

angles along the bunch of trajectories as well as the $S_1$ population as a function of time. On average, the C−N=N−C dihedral takes about 0.4 ps to reach 90°. During this time, we observe clear coherent oscillations (i.e. 2-3 periods) of C−N=N/N=N−C bending, with large amplitude. It is also worth noting that the combined effect of the flatness of the $S_1$ PES along the C−N=N−C torsion coordinate and the initial inertia of the system, lead the molecule to C−N=N−C values up to 40° already in this short period of time. As soon as the trajectory approaches 90° torsion, the two C−N=N angles desymmetrize, since the $n\pi^*$ PES in this region is characterised by asymmetric minima. Furthermore, the oscillation amplitude of the C−N=N angles decreases, due to an energy transfer from the bending to the torsional mode.

Table 4.2 shows the obtained excited state lifetime ($\tau_{n\pi^*}$) and photoisomerization quantum yield ($\Phi_{t \longrightarrow c}$), compared with literature data. The obtained $\Phi_{t \longrightarrow c}$ is 0.44, which is in good agreement with the results of past simulations[2, 88]. On the other hand, the resulting $S_1$ lifetime is almost three times larger than literature data[2, 88]. Indeed, even if the time required to reach twisted geometries is perfectly in line with past simulations[25], the average decay time is longer, resulting a $\tau_{n\pi^*}$ of 1.5 ps. This is a consequence of two main approximations: first of all, the molecule is allowed to decay only in the $82° \leq$ C−N=N−C $\leq 102°$ window, where we have mapped the NAC. Secondly, the PES of the excited state was calculated with a rigid scan starting from the *trans* ground state minimum, thus the $S_1$-$S_0$ energy gap is overestimated, with the effect of reducing the hopping probability. In addition, even though the frozen degrees of freedom are not fundamental for the description of the photoprocess, they can act as a thermal bath, influencing the molecular motion and the atomic velocities in a way that goes beyond the simple scaling factor that we have introduced in the calculation of the decay probability (see Section 4.3.2).

**Table 4.2:** *Trans* ⟶ *cis* photoisomerization quantum yield ($\Phi_{t\rightarrow c}$) and excited state lifetime of the n$\pi^*$ state ($\tau_{n\pi^*}$) from our simulations and from literature data. ($^{(a)}$ = extrapolated from ref[88]. FMS = Full Multiple Spawning; TSH = Tully Surface Hopping; MD = Molecular Dynamics).

| | $\Phi_{t\rightarrow c}$ | $\tau_{n\pi^*}$ (ps) |
|---|---|---|
| This work, 300 K | 0.44 | 1.5 |
| FMS[88], 298 K | 0.46 | $0.4^{(a)}$ |
| TSH[88], 298 K | 0.33 | $0.3^{(a)}$ |
| MD[2], 300 K | 0.52 | 0.44 |

### 4.4.4 Quantum dynamics: simulation of transient signals

After validation provided by comparison with fully optimised structures and semiclassical dynamics[34], our model was employed for the simulation of transient diffraction and spectroscopic signals during QD (of both *trans* ⟶ *cis* and *cis* ⟶ *trans* processes). Indeed, the produced PESs and state couplings constitute a rich and solid database that can be employed for the simulation of several transient experiments during the *trans* ⇌ *cis* photoswitching process, with particular interest in the non adiabatic event. The limited number of degrees of freedom can produce some artefacts in the QD due to the lack of internal vibrational energy redistribution. Such effects can be mitigated by wavepacket absorption at specific geometries (i.e. photoproduct $S_0$ minima). This has negligible effects on the time required for the wavepacket to reach the CI and primary photoproduct formation, as well as on the wavepacket distribution around the CI (which determine the appearance of coherence signals). However, this affects the population distribution in the long time range, thus impeding a one-to-one comparison with quantum yields from other dynamics simulations.

#### *cis*⟶ *trans* photoisomerization

A QD simulation of the *cis* ⟶ *trans* photoisomerization was performed in the subspace of the C−N=N−C dihedral and one of the two C−N=N bending angles, keeping the other fixed at 116°. This choice is supported by the fact that, on the *cis* side, the torsional gradient is much steeper than on the *trans* side, and quickly drives the molecules away from the FC point, with much less pronounced symmetric bending oscillations compared to *trans*-azobenzene photoexcitation. Indeed, the non reactive part of the crossing seam (which is reached mainly through symmetric opening of the two C−N=N angles) is less visited after the excitation of the *cis* isomer, and the final *cis* ⟶ *trans* quantum yield is consequently higher. For this reason, a good description of the deactivation mechanism can be achieved through the use of the C−N=N−C dihedral and one C−N=N angle only. The selected 2D cut of the PESs includes a good approximation of both $S_0$ minima, which are reproduced with slightly asymmetric C−N=N/N=N−C angles of 116°/112° and 116°/118° (instead of symmetric 112° and 118° for *trans* and *cis* isomer, respectively). On the other hand, the lowest $S_1/S_0$ CI from the rigid scan is perfectly reproduced. The obtained 2D PESs are shown in Figure 4.17 (A). For the simulation of the non adiabatic event, the cartesian NACs calculated in the subspace of the four central atoms were projected in the 2D subspace of the dynamics and sign-corrected, as shown in Figure 4.18. Both NAC components show a

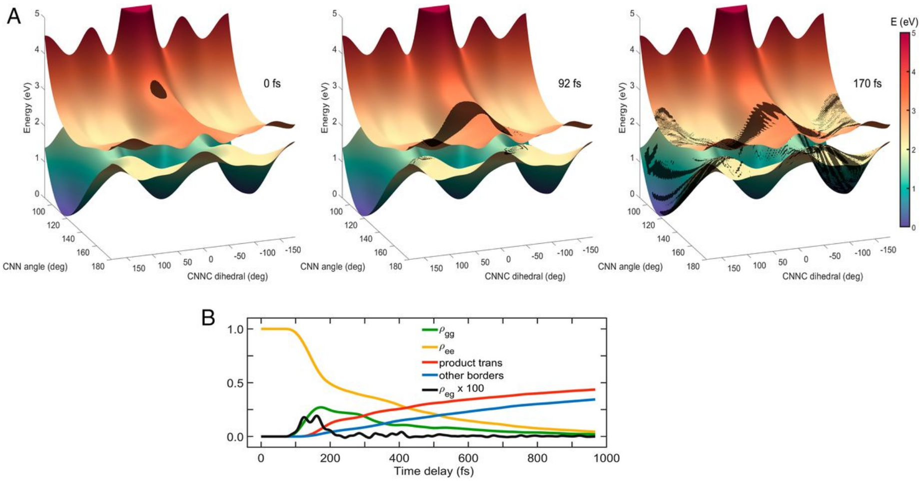

**Figure 4.17:** (A) PESs and nuclear wave packet snapshots during *cis* ⟶ *trans* photoisomerization in the two-dimensional nuclear space. (B) Electronic state populations and coherence magnitude during the process: the nuclear wave packet relaxes from $S_1$ (yellow) to $S_0$ (green). The amount that has reached the trans geometry is drawn in red, while parts of the wave packet exiting the nuclear grid at elsewhere are depicted in blue. From reference[36].

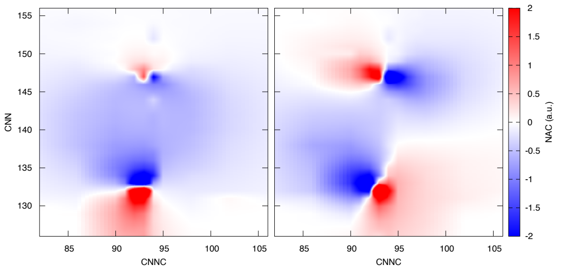

**Figure 4.18:** NAC components along C−N=N−C torsion (left) and C−N=N bending (right) for the 2D cut of the PESs in which one of the two angles is kept fixed at 116°

peak and a sign inversion at C−N=N−C = 94°, C−N=N = 116°, N=N−C = 146°, which corresponds to the $S_1/S_0$ CI. The same trend is also observed at C−N=N−C = 94°, C−N=N = 116°, N=N−C = 132°, which is not a real crossing, but corresponds to the $S_1$ minimum from the rigid scan: here the two states approach due to the minimum in the $S_1$ PES and the wavefunctions mix heavily due to the presence of a real crossing at RASSCF level (see Section 4.4.2) which is not completely resolved by RASPT2, therefore, high NAC values are expected as well.

Assuming impulsive excitation, the wave packet starts in $S_1$ at the *cis* geometry (Figure 4.17A, left) and is initially localised in both nuclear degrees of freedom. Within the first few femtoseconds, it evolves to higher C−N=N angles and starts to spread along the C−N=N−C torsion. Around 90 fs, it reaches the crossing region and starts to relax to $S_0$(Figure 4.17 (A), middle). Around 170 fs, the first significant parts of the wave packet have reached the *trans* geometry (Figure 4.17 (A), right). After reaching the product minimum, the wave packet is artificially absorbed at C−N=N−C = ± 180°, completing the photochemical reaction. In reality, most of the nuclear wave packet will be trapped there by, e.g., vibrational relaxation to other modes not contained in our Hamiltonian and that we can in this way mimic, at the price of neglecting back-evolution to the CI. As can be seen in Figure 4.17 (B), the product yield represented by the red line emerges slightly before 200 fs and accumulates thereafter. Some parts of the wave packet exit the nuclear grid at C−N=N ≥ 180° as a consequence of the flatness of the C−N=N coordinate at rotated geometries, a process that is not further captured by our Hamiltonian and thus acts as a loss channel (blue line in Figure 4.17 (B)).

This wavepacket dynamics, together with the electronic densities that we have computed across the grid, were used to simulate the transient diffraction patterns through equation (4.1), during the first 300 fs (i.e. the period of the primary CI dynamics) with particular interest in the coherence signal. A detailed analysis of the results is given in reference[36]. Isolating the coherence term could provide a real space image of CIs, and thus direct insight into the determining event of molecular photochemistry. The simulations that we have presented in reference[36] refer to the ideal case of an azobenzene molecule oriented as in Figure 4.19 (A) with the $x$ axis perpendicular to the molecular plane of the *trans* geometry, the $y$ axis going through both carbon rings (and the azo unit), and the $z$ axis going only through one carbon ring. For a randomly oriented molecular sample, rotational averaging of the presented data must be performed (as we subsequently did in reference[39]), that makes the diffraction patterns look not as clean but still exhibiting the key features.

Figure 4.19 (B) shows the state and transition electron densities at a geometry that is in the vicinity of the $S_1/S_0$ CI. The state densities $\hat{\sigma}_{gg}(\mathbf{r})$ and $\hat{\sigma}_{ee}(\mathbf{r})$ look very similar, with a total of 96 electrons contributing. The transition density $\hat{\sigma}_{eg}(\mathbf{r})$ is much smaller, with only one electron contributing. It is mainly located around the nitrogen atoms, reflecting the $n\pi^*$ character of the excitation. The difference in the number of electrons gives one reason why elastic scattering usually dominates the inelastic contributions. Furthermore, since the terms of the time dependent molecular response (equation (4.5)) consist of products of $\hat{\sigma}(\mathbf{q}, \mathbf{R})$ operators, this relative strength gets further amplified. In smaller and/or lighter molecules, where fewer electrons contribute to the elastic scattering, the relative strength of inelastic and mixed contributions will be larger.

Figure 4.20 shows the two-dimensional diffraction patterns of the total signal in the $\mathbf{q}_{xy}$, $\mathbf{q}_{xz}$, and $\mathbf{q}_{yz}$ planes, together with the diffraction patterns of pure *cis* and *trans* geometries (i.e. without considering the nuclear wave packet) which serve as references. The transformation from *cis* to *trans* is clearly visible going from 0 fs to 170 fs, where significant parts of the wave packet have reached the *trans* product minimum. This shows how TXRD can monitor the photoisomerization in real time.

The complete three-dimensional diffraction pattern at 170 fs is shown in in Figure 4.21, dissected into the different contributions to time-dependent molecular response $\tilde{S}_1(\mathbf{q}, t)$ (the two coherence terms presented in equation (4.5) are referred to as a unique term (v) in Figure 4.21). The dominant term is elastic scattering from the excited state (ii), since $\rho_{ee}$ is larger than $\rho_{gg}$ and $\rho_{eg}$ at 170 fs (see Figure 4.17 (B)). Ground state elastic scattering (i) is weaker, although well visible. The relative magnitude of ground and excited state elastic contributions in a real experiment would depend on the excitation fraction (i.e. how much population is transferred from $S_0$ to $S_1$). The inelastic scattering components (terms (iii) and (iv) in Figure 4.21) are around three orders

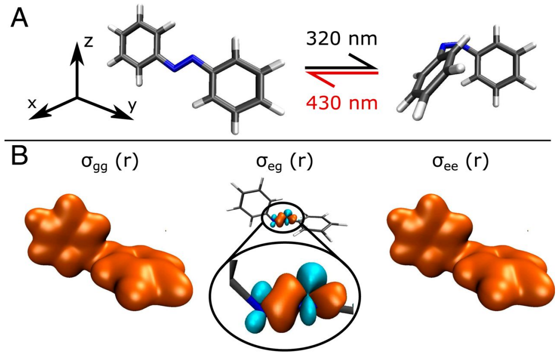

**Figure 4.19:** (A) Isomerization scheme with *trans* (left) and *cis* (right) geometries. (B) Real-space electronic densities at C−N=N−C = 92°, C−N=N/N=N−C = 116°/140°, with the ground state (96 electrons; reft), the transition (1 electron; middle), and the excited state (96 electrons; right) density. From reference[36].

of magnitude weaker than their elastic counterparts. This can be attributed to their scattering from the product of two transition density operators, each being around 100 times smaller than the state densities (1 electron versus 96 electrons). Scattering from the vibronic coherence (v) is 2000 times weaker than the total signal and equally strong as the inelastic scattering terms. In contrast to all other terms, the coherence scattering exhibits negative (blue) as well as positive (red) contributions and a pronounced dynamic behaviour. Some two-dimensional snapshots of the coherence term are depicted in Figure 4.22. The signal emerges at 90 fs, where a vibronic coherence builds up due to state crossing. It is initially localised at the CI, visible through the wave packet overlap in the two states (Figure 4.17A, middle), then it spreads along the C−N=N angle as well. This coherence term is a unique signature of a non adiabatic event. Ideally, one would like to isolate this feature from the total diffraction signal to record a **q**-space movie of the CI dynamics. However, it is significantly weaker and masked by the elastic scattering. The situation improves when going to higher momentum transfer, since the transition densities $\hat{\sigma}_{eg}$ (involving few electrons) are usually more confined in real space than the diagonal state densities (involving all the electrons in the molecule, compare Figure 4.19), and thus have a wider spread in **q**. However, going to these momentum transfer amplitudes requires pulse energies between 30 and 40 keV. Currently, up to 25 keV are possible using superconducting accelerators at the European X-ray Free Electron Laser in Hamburg and the Stanford Linear Coherent Light Source[43]. Another tool that may be used to retrieve the coherence term is frequency-resolved detection: by frequency-dispersing the scattered photons, inelastic (Stokes and anti-Stokes) contributions can be measured separately at different frequencies. On the other hand, the coherence term can only be recorded by detecting both photons with a broadband detector, as discussed in section 4.2. Separation of the coherence term could be achieved by measuring the total signal with a broadband detector and subsequently subtracting the purely elastic and purely inelastic events measured in a separate experiment with a frequency-resolved detection (although frequency-resolved measurement to single out the coherence term can be more easily performed in the two-molecule diffraction signal, which is not the case of our simulations). Other possibilities entail stochastic covariance-based measure-

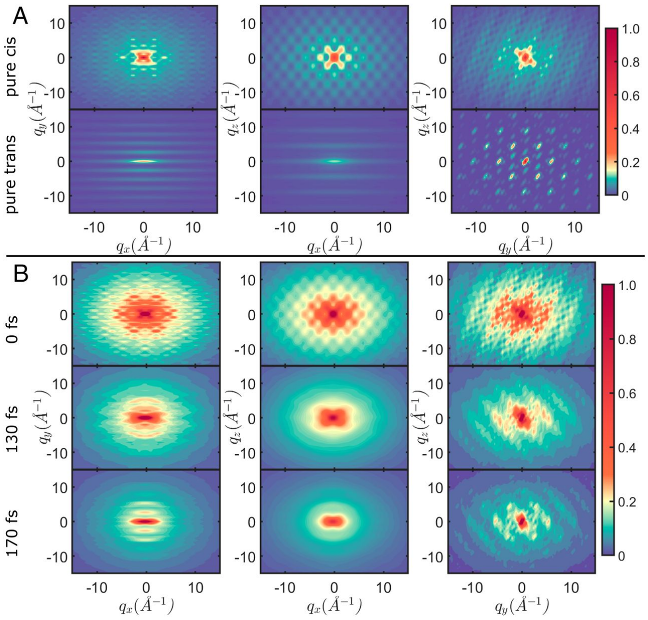

**Figure 4.20:** Two-dimensional diffraction patterns of the total signal in the $\mathbf{q}_{xy}$, $\mathbf{q}_{xz}$, and $\mathbf{q}_{yz}$ planes, while integrating over the respective other direction. The molecular axes are defined in Figure 4.19. (A) Scattering from the pure *cis* (top) and *trans* (bottom) geometry (as a reference). (B) Diffraction patterns at 0, 130, and 170 fs during the dynamics. The complete movie is provided as electronic supplement to reference[36].

ments[89, 90] or using entangled photons[91]. In reference[38] the use of covariance X-ray diffraction signals was simulated for powder diffraction off randomly oriented nanocrystals of azobenzene employing data from this *cis* ⟶ *trans* simulation, and using covariance-based analysis to recover the joint spectral and temporal resolutions needed for CI detection and hidden by the stochasticity of the pulses.

Our ultimate goal is to record movies of CI dynamics in real space. As mentioned above, the inverse Fourier transform of the diffraction image does not yield the real-space image. It yields the Patterson function[92], which shows correlations between atomic positions or interatomic distances rather than the full real-space molecular geometry. Additionally, for a correct inversion of the diffraction pattern, the phases of the photons that are lost upon measurement need to be recovered[73]. Nevertheless, we can perform a naive inverse Fourier transform of the coherence term and compare it to the real-space image that we have access to through simulations (although not experimentally observable and not given by the Patterson function). This is shown in Figure 4.23 (b) together with the coherence term (a) and the real-space picture of the transition density (c-f), which we have calculated by $\langle\chi_e(t)|\,\hat{\sigma}_{ge}(\mathbf{r},\mathbf{R})\,|\chi_g(t)\rangle$, i.e. the expectation value of the real-space transition density across the nuclear space. The temporal oscillation pattern is preserved after the Fourier transform. This is also visible in the complete three-dimensional snapshots of $\langle\chi_e(t)|\,\hat{\sigma}_{ge}(\mathbf{r},\mathbf{R})\,|\chi_g(t)\rangle$ on the right of Figure 4.23. Thus, by imaging the diffraction pattern of the vibronic coherence, fundamental information about the CI itself can be retrieved.

The direct imaging of the charge density at CI by isolating the coherence term in

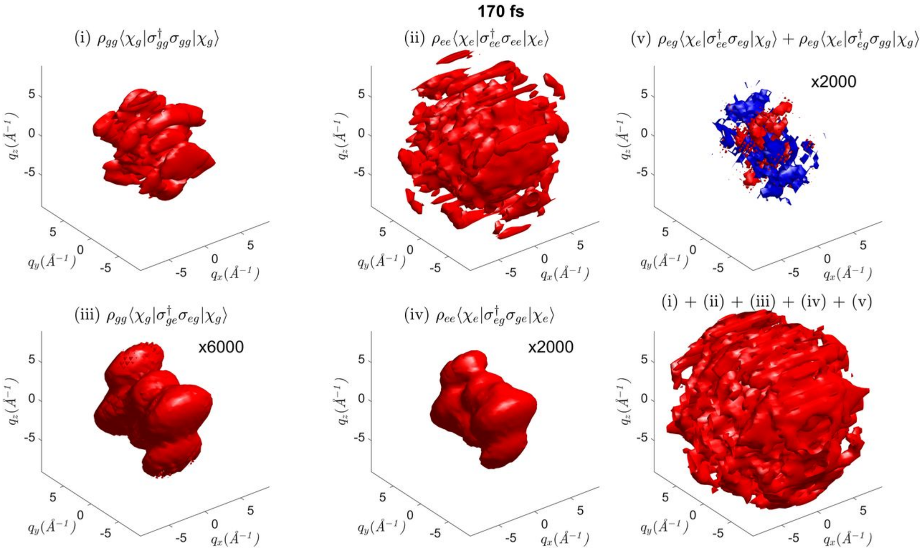

**Figure 4.21:** Contributions to the complete **q**-space X-ray diffraction pattern at 170 fs. (i) elastic scattering from $S_0$; (ii) elastic scattering from $S_1$; (iii) inelastic scattering from $S_0$, scaled by a factor of 6000; (iv) inelastic scattering from $S_1$, scaled by a factor of 2000; (v) mixed elastic/inelastic scattering from vibronic coherences, scaled by a factor of 2000. In contrast to the other terms, positive (red) and negative (blue) contributions are present. Bottom right: total signal. The complete movie is provided as electronic supplement to reference[36].

diffraction patterns is an intriguing possibility. Unfortunately, as showed above, this contribution is difficult to obtain experimentally, and the coherence signal is typically buried under stronger elastic contributions. In reference[39] we show that it would be possible to significantly enhance the coherence signal when an infrared (IR) laser field resonant with the electronic transition in the CI region is employed. By slightly shifting around populations between the excited states the coherence is significantly enhanced, while leaving the natural photochemistry virtually intact (i.e. noninvasive amplification). The optimal pulse for coherence signal amplification was found employing optimal control theory (OCT)[93, 94], in which laser pulses are shaped to prepare a targeted quantum state at a desired time.

A simulation of the *cis* ⟶ *trans* photoisomerization in the same two-dimensional nuclear subspace was performed, initially placing the wavepacket in the *cis* minimum of $S_0$. Upon electronic excitation by a pump optical pulse, the wavepacket is mostly located in $S_1$, thanks to a nonvanishing transition dipole moment between the two states. As in the previous case, X-ray diffraction signals were simulated along the dynamics, this time employing an additional IR field at the same time delay as the X-ray probe pulse. The IR pulse amplifies the signals differentially by introducing a resonance at the small energy gap in the vicinity of the CI. Small amounts of population in this region are shifted around between the two electronic states, enhancing the wavepacket overlap and thus the coherence. In our simulations, the IR field is included in the propagation of $\chi(t)$, and thus the signal expression remains the same of equation (4.5). In principles, there are three groups of signals that can potentially be maximised at desired times by application of OCT. The first is related to the ground-

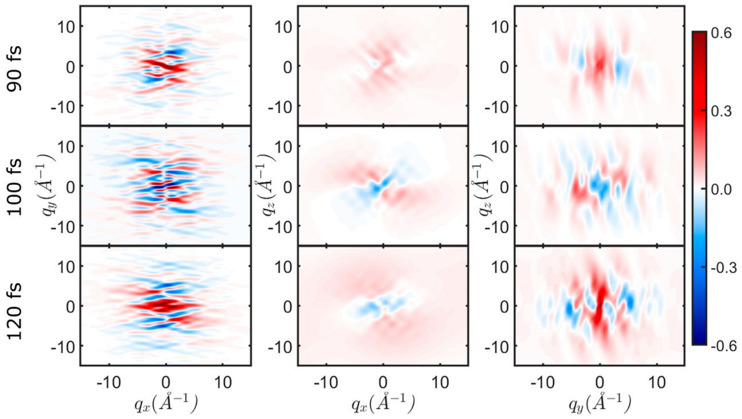

**Figure 4.22:** Two-dimensional diffraction patterns of the coherence contribution in the $\mathbf{q}_{xy}$, $\mathbf{q}_{xz}$, and $\mathbf{q}_{yz}$ planes, while integrating over the respective other direction. The complete movie is provided as electronic supplement to reference[36].

state population and is trivially enhanced by removing the optical pump $\epsilon_p$, leaving azobenzene in the electronic ground state. The second group is associated with the excited-state population. Amplification of this signal means shaping $\epsilon_p$ to achieve maximum population transfer from $S_0$ to $S_1$, potentially enabling direct excited-state structure determination. The third group is the most interesting and involves the coherences. For the latter, the OCT optimisation algorithm converges to an additional field directly centred around 105 fs with an almost Gaussian envelope and a frequency range in the IR regime. The effect is shown in Figure 4.24: the almost vanishing coherence $\rho_{eg}$ at 105 fs without the IR field is greatly enhanced. Importantly, as can be seen from the population dynamics (and especially the product yield) in 4.24 (B), the photochemical reaction remains intact. This ensures that the photochemical process is observed in its natural form, without modifying it during the observation. The required IR field is smooth, meaning that the proposed scheme is thus readily feasible and does not require an elaborate pulse shaping. The effect of IR amplification on the diffraction signal is quantitatively appreciable: being well below $10^{-3}$ in the absence of the IR field, and thus much weaker than other contributions and probably not detectable, the coherence term is amplified by at least 1 order of magnitude when the IR field is employed, reaching 1% relative strength at high $\mathbf{q}$ and precisely at the time of the CI passage.

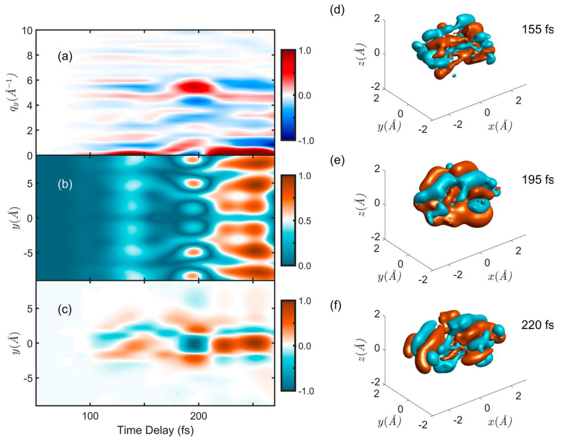

**Figure 4.23:** (a) Mixed elastic/inelastic scattering from the vibronic coherence along $\mathbf{q}_y$; (b) absolute value of the inverse Fourier transform of (a); (c) real-space picture of the transition density $\langle\chi_e(t)|\,\hat{\sigma}_{ge}(\mathbf{r},\mathbf{R})\,|\chi_g(t)\rangle$ along the $y$ molecular axis, integrated over the nuclear space $\mathbf{R}$; (d–f) snapshots of the real space transition density at 155, 195, and 220 fs. The complete movie is provided as electronic supplement to reference[36].

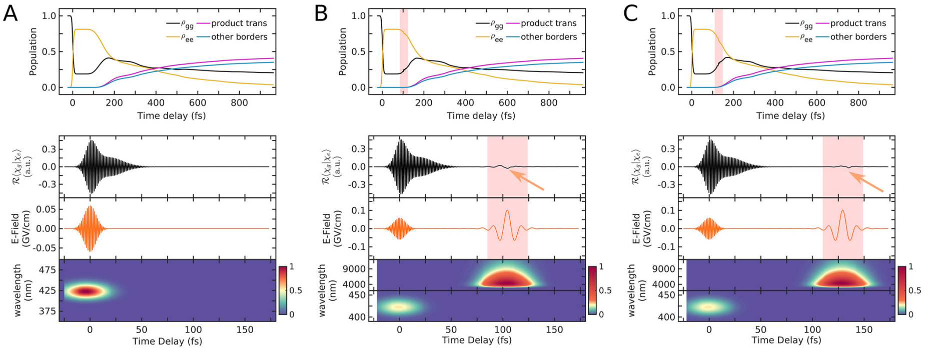

**Figure 4.24:** Population dynamics (top), coherence magnitudes (black), laser pulses (orange), and spectrograms (bottom) using only a visible field (A) or with additional IR field at 105 fs (B) or 130 fs (C) delay. The red shaded area in B and C indicates the time where the IR field is active. From reference [39].

### *trans*⟶ *cis* photoisomerization

For the QD simulation of the *trans* ⟶ *cis* photoisomerization, we have used a different bidimensional cut of our PESs compared to the previous case. It spans the C−N=N−C dihedral and symmetric C−N=N/N=N−C bending. Indeed, in contrast with the *cis* case, the torsional gradient in the *trans* FC region is less steep, and our PESs, as well as many semiclassical dynamics simulations[2, 14, 34, 35, 88], clearly indicate that the molecule experiences wide symmetric bending oscillations, before momentum is transferred to the torsional coordinate. These oscillations allow to reach the higher-energy part of the $S_1/S_0$ crossing seam, which is characterised by wide symmetric C−N=N/N=N−C angles and planar (or only slightly rotated) structures. Deactivation through this CIs (which was much less important starting the isomerization on the *cis* side) is responsible for the lower quantum yield of the *trans* ⟶ *cis* process, since the $S_1 \longrightarrow S_0$ decay takes place too early along the torsion coordinate, leading back to the *trans* photoreactant. The bidimensional $S_0$ and $S_1$ PESs are shown in the left part of Figure 4.25, with the productive and unproductive paths drown as magenta and black arrows, respectively. The selected 2D subspace includes the *trans* and *cis* $S_0$ minima, while it misses an accurate representation of the lowest energy CIs, which are reached through desymmetrization of the C−N=N/N=N−C angles, as shown in sections 4.4.1 and 4.4.2. Still, the two states come very close around 100°-95° torsion, in an avoided crossing region that exhibits high NAC values, allowing for $S_1 \longrightarrow S_0$ decay, even though less efficient than that through a real crossing. Therefore, this subspace represents a good compromise between the necessity to reproduce both deactivation pathways (productive torsional-driven and unproductive symmetric bending-driven) while being able to reproduce transient X-ray signals, whose computational cost does not allow to use more than two coordinates.

The $S_1/S_0$ NACs were mapped between C−N=N−C = 80° and 110° and symmetric C−N=N bending from 126° to 156° directly in internal coordinates (as described in section 3.4.1). Instead, for the higher part of the crossing seam (i.e. from C−N=N−C = 180° up to 110°), the calculated profile at C−N=N−C = 180° (Figure 4.26) was replicated until C−N=N−C = 110°, shifting the NAC peak to match the CI at each torsional value. This choice is justified by the fact that all these CIs do not show wavefunction mixing close to them, but rather a clean swap of the state nature is observed between adjacent points. As a consequence, the sharply peaked NAC profile shown in Figure 4.26 can be applied in all cases, saving computational time. A complete map of the NACs is shown in the right part of Figure 4.25.

We have simulated the *trans* ⟶ *cis* photoisomerization triggered by classical two-photon absorption (CTPA) and entangled two-photon absorption (ETPA). CTPA is a nonlinear process in which two photons are absorbed simultaneously by the same molecule, and involves a “virtual state” with energy corresponding roughly to the half of the energy of the final allowed state. The simultaneous nature of CTPA implies that this process depends quadratically on the light intensity, and is related to the probability that two photons are localised in the same restricted space at the same time. In practice, this phenomenon is only commonly observed at the very high photon flux in the focus of a laser beam, allowing for high spatial resolution of the excitation[95]. The use of IR-NIR light makes TPA well suited for biological applications, as tissues are relatively transparent at such wavelengths. Moreover, in centrosymmetric molecules (like *trans*-azobenzene) one- and two-photon allowed transitions are mutually exclu-

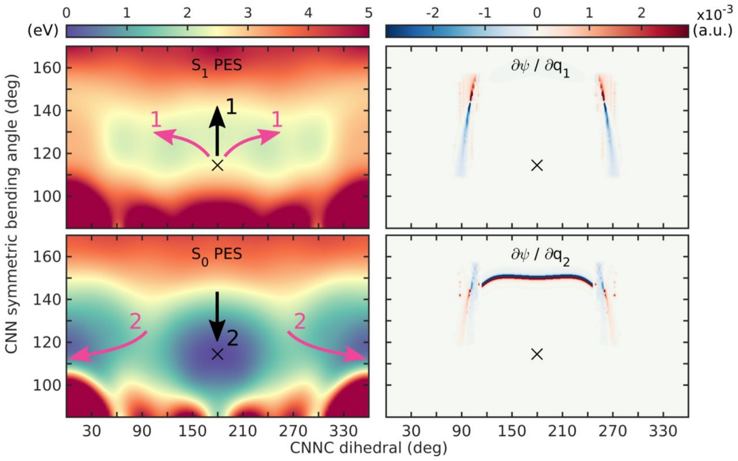

**Figure 4.25:** Left: $S_1$ (top) and $S_0$ (bottom) PESs in the two-dimensional nuclear space used for the *trans* ⟶ *cis* QD simulation. The *trans* minimum is marked with a black cross. The reactive pathway is marked in magenta: (1) breaking the molecular plane and wave packet evolution to the reactive crossing region and (2) continuing the C—N=N—C torsional motion after relaxation to $S_0$, thus completing the photochemical reaction. The nonreactive pathway is marked in black: (1) keeping the planar symmetry and relaxing via the nonreactive CIs and (2) evolving back to the *trans* minimum in $S_0$. Right: $S_1/S_0$ NAC components along the two selected coordinates ($q_1$ = torsion; $q_2$ = symmetric bending). From reference[37].

sive, therefore the optically dark $n\pi^*$ excitation is much more efficient through TPA, as demonstrated repeatedly in experiments[96–98].

In ETPA, quantum light (i.e. with entangled photons, created by e.g. parametric down conversion[99] or biexciton decay[100, 101]) is used as incident beam. A clear signature of entanglement is that, at low photon fluxes, ETPA scales linearly rather than quadratically with the pump intensity[102, 103], indicating that the two photons effectively act as a single particle. Entanglement of the incident photons can lead to quantum pathway selection: in resonant processes, the matter actively participates and gets entangled with the photons, making it possible to control the pathway of matter by varying the degree of entanglement, thereby improving the resolution of nonlinear spectroscopic techniques[104].

ETPA excitation is schematised in Figure 4.27: a pump pulse creates an entangled photon pair, known as signal and idler, through interaction with a second-order nonlinear crystal. The photon pair then brings the azobenzene molecule to the $n\pi^*$ state by two-photon absorption, launching the photoisomerization process. The effects of quantum light were studied varying the entanglement time $T_e$, which defines the difference between the arrival times of the signal and idler photons. The entangled light excitation process was simulated using the protocol detailed in reference[105]. The initial quantum light excitation process is relatively short (tens of fs) compared with the isomerization dynamics (1 ps) so that they can be separately considered.

For the CTPA simulation, two uncorrelated classical Gaussian laser pulses with bandwidth resembling the signal and idler photons for a given joint spectral amplitude were used. Such pulses exhibit a power spectrum resembling the quantum light and allow for comparison with ETPA simulations and assessment of the entanglement

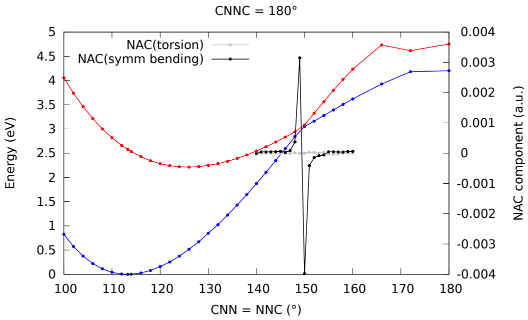

**Figure 4.26:** NAC torsion and symmetric bending components along a C$-$N$=$N symmetric bending scan for C$-$N$=$N$-$C torsion fixed at 180°.

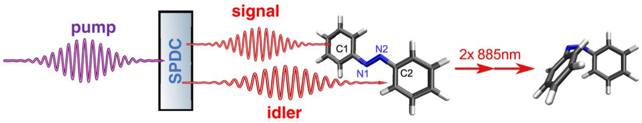

**Figure 4.27:** Azobenzene *trans* ⟶ *cis* photoisomerization initiated by entangled two-photon absorption. The combined energy of the two photons matches the $S_0 \longrightarrow S_1$ transition at the *trans* geometry. From reference[37].

effects.

Figure 4.28 shows the nuclear wave packets on the $S_1$ surface excited by an entangled photon pair with different entanglement times. The variation of the nuclear wave packet shape over $T_e$ is periodic with period ~ 3 fs, and the wave packets excited by entangled photons with $T_e = 3$ and 6 fs are more delocalised compared to $T_e = 1$ or 4 fs. This is due to the fact that the expression for the transition amplitude between vibronic states when using entangled photons strongly depends on $T_e$ (see details in reference[37]), which then results in a dependence of the created nuclear wave packet on the entanglement time. In contrast, no variation is observed in the wavepackets created by CTPA, which all resemble the $T_e = 1$ fs snapshot in Figure 4.28 (see reference[37] for a complete comparison and discussion of all wavepackets).

Figure 4.29 shows the wavepacket evolution upon excitation with two non entangled NIR photons. Within 20 fs, the wave packet starts to evolve to higher C$-$N$=$N values while retaining the planar symmetry; at 68 fs, it has bounced back to the FC, while small parts have relaxed to $S_0$ through the non productive CI seam. During the second symmetric bending oscillation, the planar symmetry starts to break, and the wave packet spreads along C$-$N$=$N$-$C as well. This is already visible at 117 fs and becomes more pronounced at 165 fs (Figure 4.29 top-right and bottom-left panels). Already at 165 fs, considerable parts of the wave packet have reached the productive part of the CI seam at rotated geometries, and start to relax to $S_0$. At later times, the wave packet broadly spreads along C$-$N$=$N$-$C in $S_1$. On the other hand, on $S_0$, major parts of the wave packet have reached the *cis* minimum, thus completing the photoisomerization. Once this minimum is reached, the nuclear wave packet was absorbed with a Butterworth filter operation[106]. In reality, vibrational relaxation to other modes will redistribute the kinetic energy, thus preventing major parts of

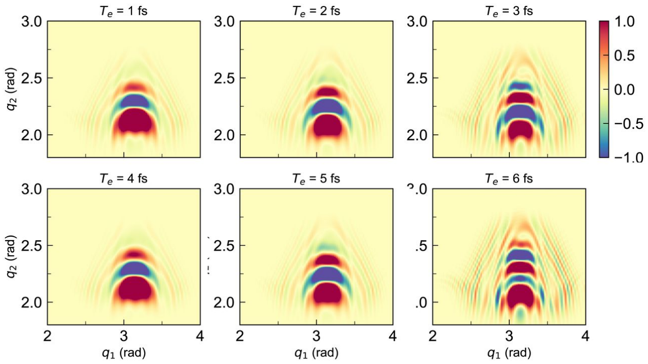

**Figure 4.28:** Entangled two-photon excited nuclear wave packets in the $S_1$ surface at $t = 20$ fs varying the entanglement time $T_e$ as indicated. From reference[37].

the wave packet from continuing along the dihedral bending and crossing the 2 eV barrier in the ground state back to the *trans* minimum or even evolving back to $S_1$ through the CIs. This vibrational relaxation is not captured by our two-dimensional Hamiltonian, and absorbing the wave packet in the product minimum prevents these artefacts. After 900 fs, the product yield amounts to 44%, with 13% population still remaining in $S_1$ and 7% in $S_0$. The rest of the wavepacket exits the numerical grid in the symmetric bending direction, as a consequence of the lack of momentum transfer to other modes, that would dampen this wide oscillations. The ETPA simulations look similar to CTPA in terms of wavepacket motions in the 2D subspace, but with a different relative weight of the quantum pathways, as expected because of the difference in the initial wavepackets varying $T_e$. In contrast to their classical counterparts, which do not show any significant $T_e$ dependance, the entanglement time does affect the isomerization yield, varying from 47% for $T_e = 3$ fs to 41% for $T_e = 9$ fs. Photon entanglement is thus able to add a control knob for photochemistry not available by classical light sources.

The comparison of the state populations upon variation of $T_e$ gives insight into the influence of the photon entanglement on the process kinetics. In order to investigate deeper the entanglement effect, we evaluated its influence on the transition state of the photochemistry, i.e. the conical intersection. For this we have computed the TRUECARS signal (transient redistribution of ultrafast electronic coherence in attosecond Raman signals), which probes the vibronic coherences exactly around the CI[107, 108]. It is a spectroscopic technique that gives information about the energies of the states in the vibronic coherence associated with the CI. In TRUECARS, a broadband (500 as) and narrowband (3 fs) X-ray pulses induce an off-resonant stimulated Raman process between two electronic states, and the signal is given by the time-integrated rate of change of photon numbers in the broadband pulse field. TRUECARS is a sensitive probe of CIs as its signal only exists if there is an electronic coherence. Figure 4.30 shows the TRUECARS signals and frequency-resolved optical gating (FROG) spectrogram (which allows to retrieve the precise pulse intensity and phase vs. time) obtained in CTPA and ETPA simulations with $T_e = 1$ and 3 fs. In all cases, the coherence signal is non vanishing already at 20 fs, as tails of the wave packet have already reached the planar CIs through symmetric bending. It gets stronger dur-

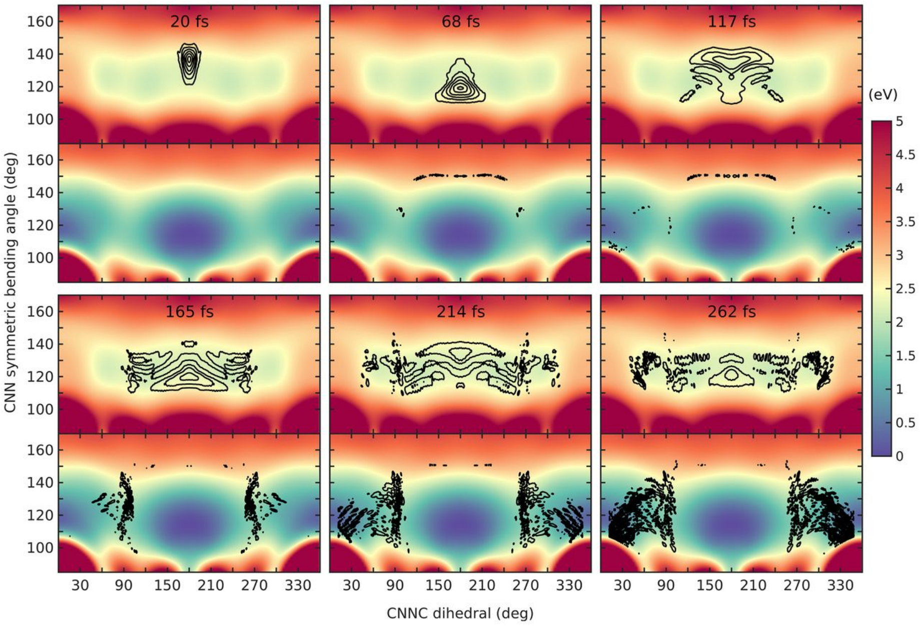

**Figure 4.29:** Snapshots of the nuclear wavepacket evolution on the $S_1$ (top of each panel) and $S_0$ (bottom of each panel) PESs after classical two-photon absorption (starting wave packet at 20 fs is created by a classical pulse whose bandwidth mimics an entanglement time $T_e = 1$ fs). From reference[37].

ing the dynamics, when the reactive CI is reached by other parts of the wave packet and persists throughout the propagation. In the dynamics started by CTPA, neither the kinetics or product yield, nor the coherence structure associated with the CI is changing. In contrast, for wavepackets prepared by ETPA, the photon entanglement effect is visible in both TRUECARS signal and spectrogram. This is illustrated in Figure 4.30, where the spectrograms for ETPA with $T_e = 1$ fs and $T_e = 3$ fs are significantly different. The vibronic coherence around the CI, and thus the transition state of the isomerization, is thus strongly modulated by quantum light.

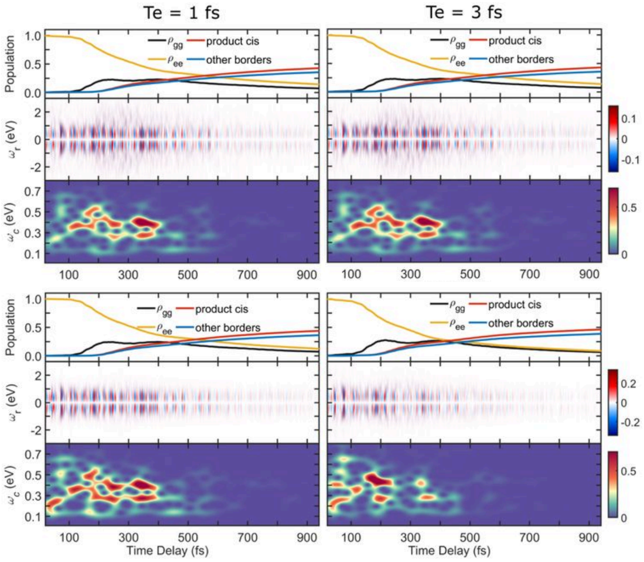

**Figure 4.30:** Photoisomerization dynamics following CTPA (top panels) and ETPA (bottom panels) for starting wave packets corresponding to $T_e = 1$ and 3 fs. For each panel, top shows population dynamics with the ground and exited state populations as well as product yield and the cumulative amount of population that has been absorbed at the symmetric bending grid borders; middle shows TRUECARS signal; bottom shows spectrogram of the TRUECARS signal, revealing the vibronic coherence distribution. From reference[37].

## 4.5 *Push-pull* azobenzene derivatives

Among the fields of application azobenzene and its derivatives, photobiology and photopharmacology have attracted much interest in recent years[97, 98, 109–113]. The incorporation of photoswitchable compounds in the membrane proteins of cells or in drugs allows for optical remote control of, e.g., cell receptors and channels[97, 114], cancer chemotherapy[115, 116], neurology[117] and antibiotic treatments[118].

Already in the late 1960s, azobenzene was applied to the photocontrol of enzymes and ion channels[119, 120]. Targeted protein modification with azobenzenes has now led to many more in-vivo applications[97, 109]. The main advantages of this simple photoswitch are the large change in geometry and dipole moment upon photoisomerization. Traditionally, *trans* ⟶ *cis* conversion is achieved with UV-light irradiation, whereas the reverse *cis* ⟶ *trans* process can occur via either thermal relaxation or visible-light irradiation. For applications in vivo, however, photoswitching in the Vis-NIR window is desirable to enable effective tissue penetration without the need for fiber optics. By contrast, UV light can damage cells, it is nonselectively absorbed by many chromophores, and is quickly attenuated in tissues. Even though progresses were made thanks to two-photon absorption[121, 122] and upconverting nanoparticles[123], there are still practical and technological limitations for these strategies, that make it desirable to find photoswitches that undergo single photon isomerization with Vis-NIR light under physiological conditions (i.e. in aqueous solutions at neutral pH). To this aim, a way to lower the gap and therefore red-shift the absorption peaks of azobenzene is to introduce electron-donating and/or electron-withdrawing groups in *ortho* or *para* position with respect to the N=N, in order to tune the HOMO-LUMO gap. One of the most important classes of azobenzene derivatives is represented by the so-called *push-pull* azobenzenes (Figure 4.31), in which one ring is functionalised with an electron-donating substituent, while the other one bears an electron-withdrawing group. In such compounds, the simultaneous destabilisation of the last occupied $\pi$ orbital (HOMO) by the electron-donor substituent, and stabilisation of the $\pi^*$ (LUMO) by the electron-withdrawing substituent, results in a red-shift of the $\pi\pi^*$ absorption in the 400-600 nm region[85, 124–130].

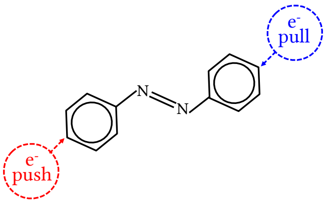

**Figure 4.31:** Schematic representation of a general *push-pull* azobenzene

The presence of the substituents polarises the molecule, causing solvatochromism, and concomitantly destabilises the *cis* isomer, resulting in faster thermal relaxation rates[130]. These two effects, which accompany the red-shift of the $\pi\pi^*$ band, become more pronounced with the strength of the donor/acceptor substituents, therefore, *Push-pull* azobenzene derivatives belong to the class of T-type switches[110], for which one isomer is thermally unstable and typically reverts to the thermodynamically stable form within milliseconds to few minutes. Although this type of compound is usually not addressable in both directions with light, the high rate of thermal back-isomerization allows reversion of the switch by simply stopping the irradiation.

In a work published in reference[41], we have demonstrated how *push-pull* substitution can induce spectral tuning towards the visible range but also improve the photoisomerization efficiency of azobenzene-based photoswitches. We have compared the behaviour of parent azobenzene (from here on, AB) with two different *push-pull* substituted systems with increasing electron-donating/withdrawing strength: 4-methoxy-4'-cyanoazobenzene (NC-AB-OMe) and 4-(4-Nitrophenylazo)aniline ($O_2N$-AB-$NH_2$, also known as Disperse Orange 3 or DO3), which are depicted in Figure 4.32. The comparison is made by means of time-dependent density functional theory (TD-DFT) semiclassical dynamics simulations (RASPT2-validated at crossing points) accounting for multireference dynamically correlated energies.

Although being only a preliminary study, our results already allow to identify the control knobs of productive (i.e. photoisomerization) vs non-productive (i.e. aborted photoisomerization) radiationless decays, thus paving the way to a rational design of AB derivatives with tuneable spectral properties and increased photoisomerization efficiency.

### 4.5.1 Computational details

For each of the three considered systems, we generated 40 *trans* and 40 *cis* initial conditions sampling from a Wigner distribution at 300 K using gas-phase B3LYP/6-31G* normal modes and frequencies (obtained at the corresponding *trans* and *cis* ground

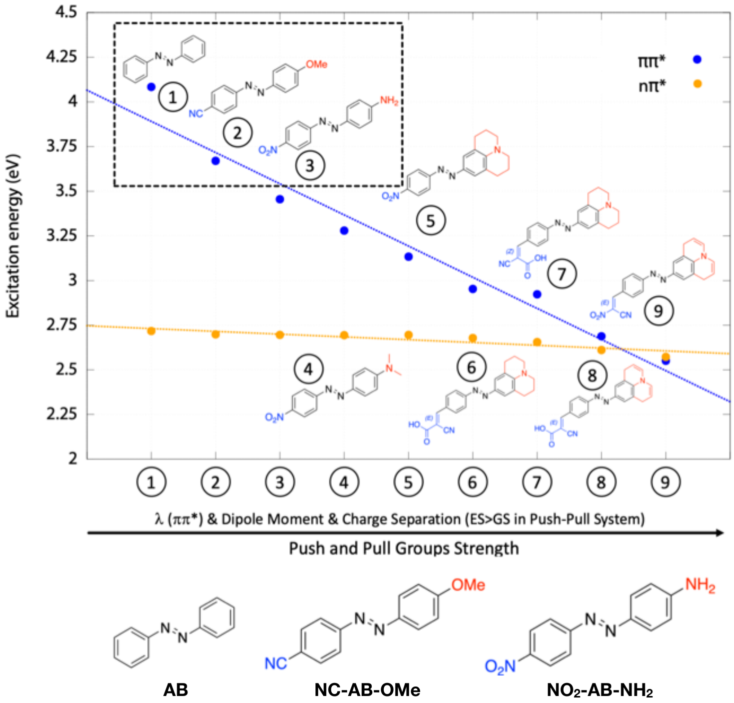

**Figure 4.32:** Selected AB-systems (bottom) considering an ensemble of 8 *push-pull* derivatives: correlation between strength of *push-pull* substituents and the lowest $n\pi^*/\pi\pi^*$ vertical excitation energies (yellow/blue lines respectively). From reference[41].

state equilibrium structures) through an interface with a stand-alone script part of the quantum MD program JADE[131]. High frequency modes (> 2000 cm$^{-1}$, i.e. C−H stretching) were excluded from the sampling. For each frame, we ran semiclassical dynamics in vacuum starting from the lowest $\pi\pi^*$ bright state (usually $S_2$) propagating the nuclei classically for 1500 fs on the TD-DFT/CAM-B3LYP/6-31G* PESs, using a timestep of 1 fs. Non adiabatic events were treated with a simplified hopping scheme based on the energy gap, changing the electronic state anytime it was lower than 3 kcal/mol. Back hopping was always allowed between excites states (ESs), while it was not permitted after decay to the ground state (GS). For the *trans*-AB parent system, we run 40 additional dynamics simulations from the $n\pi^*$ state ($S_1$), using the same starting frames as for the $\pi\pi^*$ dynamics, in order to see the possible differences in the photoisomerization mechanism.

As an assessment of the TD-DFT results, we performed CAM-B3LYP/6-31G*/TD-DFT and SS-8-RASPT2/SA-8-RASSCF/ANO-L-VDZP single point calculations at each GS minimum and at the $S_1/S_0$ decay points of the *trans* ⟶ *cis* 0 K TD-DFT dynamics simulations (i.e. started at the GS minimum without initial velocity) initiated in the $\pi\pi^*$ state. The RASPT2/RASSCF/ANO-L-VDZP protocol was already validated in our previous work on azobenzene[34], and served here as reference. Different active space dimensions were employed for the three systems: the (RAS1|RAS2|RAS3) structure was (4,9|0,0|4,7) for *trans*- and *cis*-AB, (2,9|10,8|2,6) for *trans*-NC-AB-OMe, (2,6|10,9|2,4) for *cis*-NC-AB-OMe, (2,9|10,6|2,5) for *trans*-$O_2N$-AB-$NH_2$ and (2,9|10,7|2,4) for *cis*-$O_2N$-

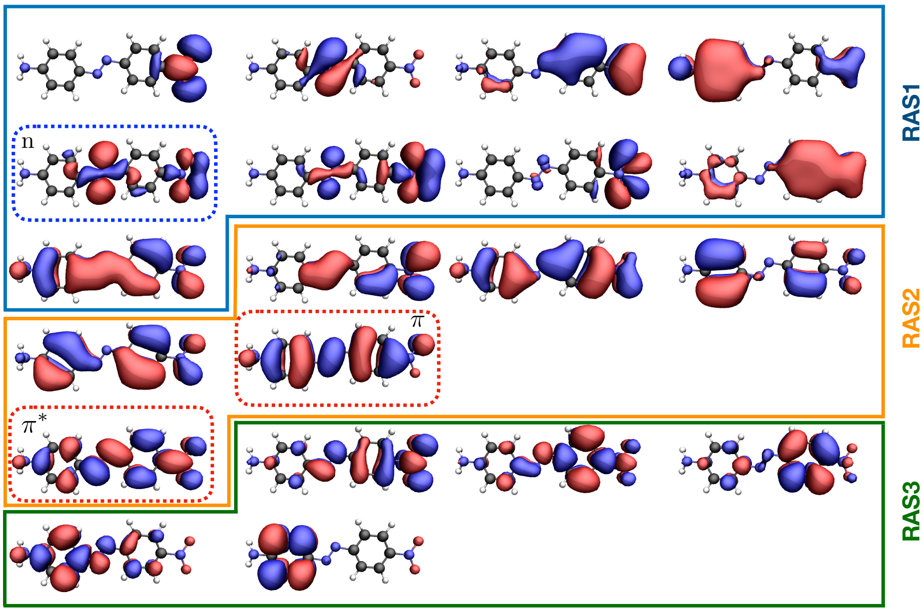

**Figure 4.33:** Active space orbitals for *trans*-$O_2N$-AB-$NH_2$. Corresponding orbitals were used for the *cis* isomer, changing the (RAS1|RAS2|RAS3) distribution as indicated in the text.

AB-$NH_2$ . The differences in the number of active space orbitals and/or orbital distribution between the corresponding *trans* and *cis* isomers are due to the high computational cost of the RASPT2/RASSCF calculations for the *push-pull* systems, that made sometimes necessary to exclude some low-contributing orbitals and/or change the distribution between RAS subspaces. The RASSCF active space orbitals for the parent system are those depicted in Figures 4.7 and 4.8, while those of the *trans-push-pull* systems are shown in Figures 4.33 and 4.34. The quantitative accuracy of the employed method is supported by the good agreement between the experimental and computed vertical energies (reported in Tables 4.3 and 4.5). This also validates the prediction for the absorption values ($\pi\pi^*$ and $n\pi^*$) which are not available in the literature, in particular for the *push-pull cis*-conformers, which are thermally unstable and, therefore, difficult to isolate and characterise. Validation of the decay points was necessary because TD-DFT fails to produce correctly-shaped PESs in the region surrounding intersections between ESs and the GS. The good matching between the high level multi reference RASPT2 method and the single reference TD-DFT (Table 4.3) enforces the reliability of the latter method. Nevertheless, we limited the analysis to the ES dynamics until the $S_1 \longrightarrow S_0$ decay, since the fate of the trajectory on the ground state could not be reliably predicted.

All the dynamics simulations and the TD-DFT calculations were performed using the suite COBRAMM[77–79] interfaced with the software GAUSSIAN[132] for the energy calculations, while the RASSCF/RASPT2 calculations were performed using the OpenMolcas[133] quantum chemistry program.

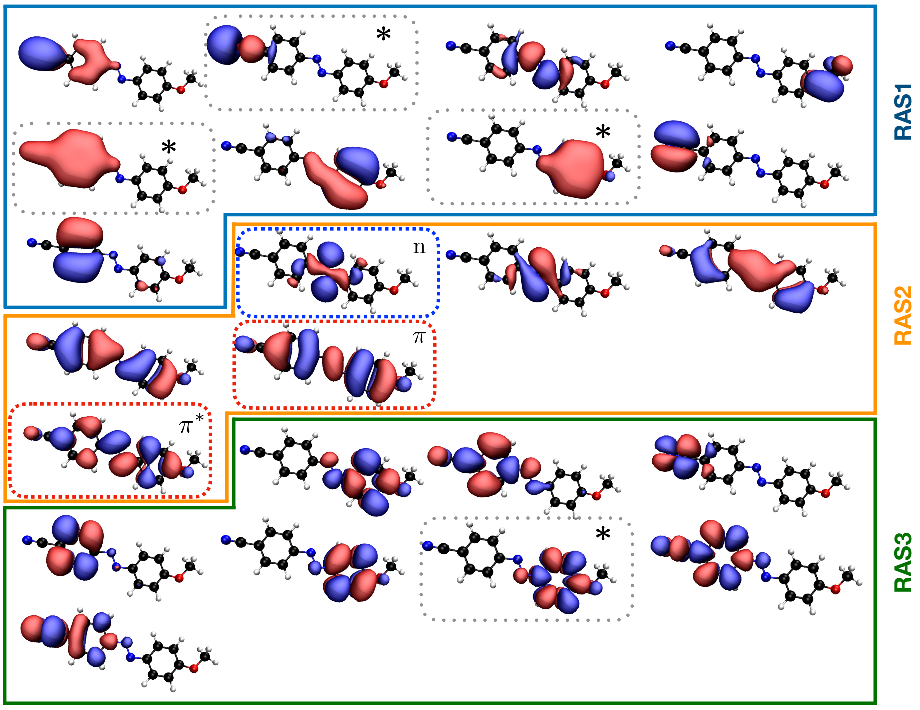

**Figure 4.34:** Active space orbitals for *trans*-NC-AB-OMe. Corresponding orbitals were used for the *cis* isomer, excluding those marked with an asterisk and changing the (RAS1|RAS2|RAS3) distribution as indicated in the text.

### 4.5.2 Results and discussion

The NC-AB-OMe and $O_2N$-AB-$NH_2$ derivatives were selected after a preliminary study (at the CAM-B3LYP/6-31G* level) of eight systems with increasing push-pull strength: Figure 4.32 shows how the substituents stabilise the $\pi\pi^*$ state, leaving roughly unchanged the dark $n\pi^*$. Increasing the *push-pull* strength reduces the $\pi\pi^*$-$n\pi^*$ gap, until inversion of the energy order. Due to their small size, the selected systems are good candidates to make accurate predictions about AB-*push-pull* derivatives. The *push-pull* character is higher for $O_2N$-AB-$NH_2$, due to the stronger electron donating/withdrawing substituents, compared to NC-AB-OMe (see Figure 4.32).

Increasing the strength of the *push-pull* substituents also affects the charge distribution on the two phenyl rings and, consequently, the molecular dipole moment. The calculated ground state dipole moments are 0.074/0.071 D and 0.115/0.106 D *trans*/*cis* NC-AB-OMe and $O_2N$-AB-$NH_2$, respectively. The charge separation is even more pronounced on the $\pi\pi^*$ state, resulting in 0.162/0.247 D and 0.241/0.327 D dipole moments for *trans*/*cis* NC-AB-OMe and $O_2N$-AB-$NH_2$, respectively (the complete charge distributions are reported in the supporting information of reference[41]). The larger dipole moment of the *cis* conformers could be referred to the non-planar geometry that hinders the orbital delocalisation, leading to a larger charge separation between the two halves.

Our results show that the *push-pull* derivatives behave dynamically different, compared to the parent system, when they are excited to the bright $\pi\pi^*$ state. Because

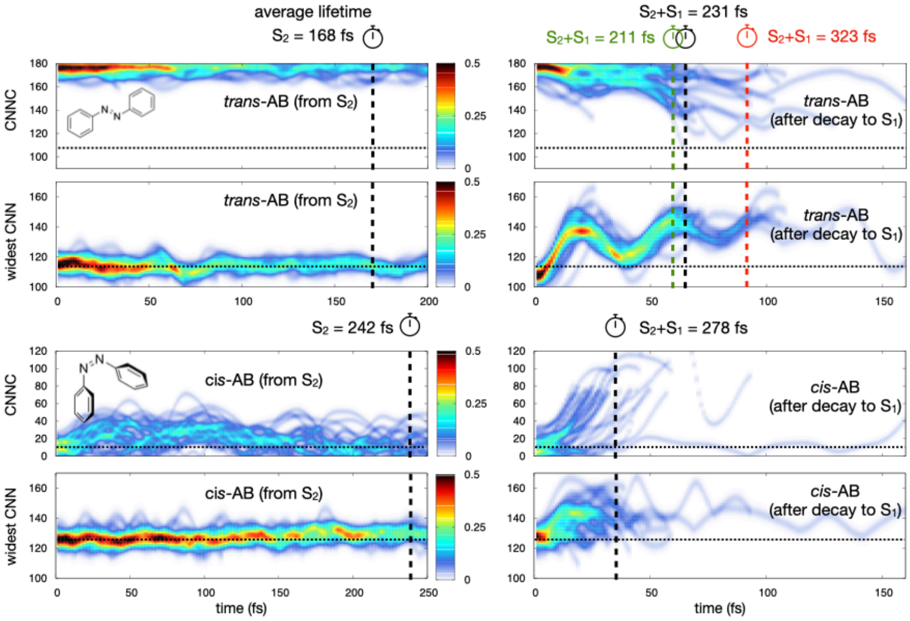

**Figure 4.35:** Normalised distribution of the C−N=N−C torsional value and widest C−N=N bending value over time for the *trans*- (top) and *cis*-AB (bottom) dynamics (40 trajectories for each panel) on $S_2$ (left panels) and on $S_1$ (right panels) until decay to $S_0$. The colour scale refers to the normalised density of trajectories. Vertical dashed lines: excited state lifetimes averaged over all trajectories (black) and over torsional (red) or bending paths (green). Horizontal dotted lines: FC value of the relative coordinate. *Push-pull* systems show similar oscillations, although with different timescales dictated by the different lifetimes (see reference[41]).

photoexcited *trans* and *cis* isomers lead to quite different paths, they are analysed separately.

### *Trans*-AB derivatives

Table 4.3 shows the vertical excitation energies for the *trans*-systems at the FC points and at the $S_1/S_0$ decay point of the 0 K TD-DFT $\pi\pi^*$ dynamics simulations, while the data from the dynamics simulations are shown in Figure 4.35 and Table 4.4. In the three *trans*-systems, during the initial dynamics leading to the $S_2 \longrightarrow S_1$ decay, the C−N=N−C dihedral remains close to 180°, while both C−N=N bending angles close and then oscillate around a value that is a bit smaller than in the FC geometry (see Figure 4.35), in agreement with recent AB $\pi\pi^*$ dynamics[14]. The most significant effect of *push-pull* substitution is a drastically shorter $\pi\pi^*$ lifetime with respect to the parent compound, where $S_2$ is living two times longer than in the substituted *trans*-systems (168 fs for AB against 70 and 86 fs for NC-AB-OMe and $O_2N$-AB-$NH_2$, respectively, see Table 4.4).

On the other hand, in the subsequent dynamics on the $n\pi^*$ state, momentum is transferred to the torsional motion, which is accompanied by wide bending oscillations, which are clearly visible in Figure 4.35. The resulting $S_1 \longrightarrow S_0$ hopping geometries includes planar to fully rotated C−N=N−C values. This is in agreement with

**Table 4.3:** *Trans*-systems: gas-phase vertical excitation energies at the $S_0$ minimum (experimental, TD-DFT and RASPT2/RASSCF) and at the $S_1/S_0$ decay point of the 0 K TD-DFT $\pi\pi^*$ dynamics simulations. (*a*) in 2-methyltetrahydrofuran at 77 K.

| | | $S_0$ *trans*-min | | | | | | $S_0/S_1$ decay | |
|---|---|---|---|---|---|---|---|---|---|
| | | Exp. value | | TD-DFT | | RASPT2 | | TD-DFT | RASPT2 |
| | | (nm) | (eV) | (nm) | (eV) | (nm) | (eV) | (eV) | (eV) |
| AB | $S_0$ | - | 0.00 | - | 0.00 | - | 0.00 | 3.17 | 3.74 |
| | $S_1$ | 440[134] | 2.82 | 456 | 2.72 | 478 | 2.59 | 3.25 | 3.80 |
| | $S_2$ | 301[134] | 4.12 | 304 | 4.08 | 322 | 3.85 | - | - |
| NC-AB-OMe | $S_0$ | - | 0.00 | - | 0.00 | - | 0.00 | 2.78 | 3.24 |
| | $S_1$ | $460^{(a)}$[135] | 2.70 | 459 | 2.70 | 509 | 2.44 | 2.90 | 3.29 |
| | $S_2$ | $380^{(a)}$[135] | 3.26 | 338 | 3.67 | 343 | 3.62 | - | - |
| $O_2N$-AB-$NH_2$ | $S_0$ | - | 0.00 | - | 0.00 | - | 0.00 | 2.72 | 3.20 |
| | $S_1$ | 442[136] | 2.81 | 4.60 | 2.70 | 453 | 2.74 | 2.78 | 3.31 |
| | $S_2$ | 353[136] | 3.51 | 3.59 | 3.46 | 414 | 2.99 | - | - |

the shape and extension of the $S_1/S_0$ crossing seam that we have documented in reference[34], covering both bending and torsional modes, where the fully (~ 90°) rotated structures are the lowest in energy, but also higher-energy, less rotated structures could be accessible through the bending mode, provided that enough kinetic energy is available in the dynamics. Based on the characteristics of the $S_1/S_0$ seam, we have grouped the trajectories in two different sets, labelled "torsional" and "bending" paths, based on the C−N=N−C torsional value at the $S_1/S_0$ hop: the former group includes trajectories decaying on $S_0$ at C−N=N−C < 135° (half between 180° and 90°), while the latter includes trajectories which, to a great extent, preserve the planarity of AB until decaying to $S_0$ (C−N=N−C > 135°). Most trajectories for all the three *trans*-systems follow the bending path (82.5/65/65% for AB/NC-AB-OMe/$O_2N$-AB-$NH_2$ respectively, see Table 4.4), but none of them reaches bending values ascribable to an inversion-driven isomerization process. Moreover, the bending motions are mainly symmetric, and even a hypothetical concerted bending mechanism would lead back to the reagent. Consequently, on the basis of the large number of dynamics, we conclude that the only productive process follows the torsion mechanism in all the considered AB derivatives. However, since our analysis is limited to the excited state dynamics until decay to the ground state, the number of torsional paths populated for each system is only an upper bound estimate of the $\pi\pi^*$ quantum yields: we obtained 17.5%, 35% and 35% for *trans*-AB, NC-AB-OMe and $O_2N$-AB-$NH_2$, respectively, envisaging a larger quantum yield in the *push-pull* systems than in the parent AB (see Table 4.4). The correlation between the number of "torsional" trajectories and the quantum yield is further supported by the results of our $n\pi^*$ *trans*-AB dynamics: for this state, previous semiclassical dynamics by Granucci and Persico[35] employing a semiempirical Hamiltonian reported values for the quantum yields of 15% and 33% starting from the $\pi\pi^*$ and $n\pi^*$ state, respectively, which is perfectly in line with the amount of torsional trajectories obtained in each case from our simulations (17.5% and 32.4%, see Table 4.4). Remarkably, the ratio between the torsional paths populated when initiating the dynamics either in the $\pi\pi^*$ or in the $n\pi^*$ state (17.5/32.4 = 0.5) well matches the experimental $\pi\pi^*$ and $n\pi^*$ yield ratio (11/25 = 0.44 in *n*-hexane[15]).

**Table 4.4:** *Trans*-systems dynamics. Relative amount, average excited state lifetime $\tau$ and geometrical parameters of the decay geometries (torsional path: CNNC < 135° , bending path: 135° < CNNC < 180° at the $S_1 \longrightarrow S_0$ decay). The average values refer to the set of trajectories belonging to the torsional or bending path.

| | | Relative amount (%) | $\tau_{S_2}$ (fs) | $\tau_{S_2+S_1}$ (fs) | $S_2 \longrightarrow S_1$ hop | | $S_1 \longrightarrow S_0$ hop | |
|---|---|---|---|---|---|---|---|---|
| | | | | | CNNC (°) | CNN-NNC (°) | CNNC (°) | CNN-NNC (°) |
| AB from $\pi\pi^*$ | tors. path | 17.5 | 235 | 323 | 173 | 108-105 | 126 | 145-141 |
| | bend. path | 82.5 | 153 | 211 | 175 | 108-104 | 157 | 149-142 |
| | all | | 168 | 231 | 175 | 108-105 | 140 | 151-142 |
| AB from $n\pi^*$ | tors. path | 32.4 | - | 270 | - | - | 119 | 139-134 |
| | bend path | 67.6 | - | 62 | - | - | 156 | 147-141 |
| | all | | - | 130 | - | - | 144 | 144-139 |
| NC-AB-OMe | tors. path | 35.0 | 75 | 386 | 177 | 108-111 | 122 | 130-136 |
| | bend. path | 65.0 | 67 | 138 | 176 | 107-110 | 161 | 147-142 |
| | all | | 70 | 225 | 177 | 111-107 | 147 | 143-137 |
| $O_2N$-AB-$NH_2$ | tors. path | 35.0 | 87 | 300 | 173 | 114-110 | 123 | 131-138 |
| | bend. path | 65.0 | 85 | 180 | 173 | 110-113 | 158 | 144-139 |
| | all | | 86 | 227 | 173 | 113-110 | 145 | 142-136 |
| Experiment[32] | | | 170 | 420 | | | | |

Figure 4.36 shows the $S_2/S_1$ (red) and the $S_1/S_0$ (dark blue) hopping points distribution, along the bending/torsional coordinates, for the $\pi\pi^*$ trajectories of the three different systems. Interestingly, for the *push-pull* systems, the distribution obtained starting from the bright $\pi\pi^*$ resembles that of *trans*-AB starting from the $n\pi^*$ state (light blue points in Figure 4.36 panel (a)), for which a larger isomerization productivity is experimentally documented. This further suggests that the *push-pull* derivatives excited to $\pi\pi^*$ behave exactly as the $n\pi^*$ of AB, envisaging a higher photoisomerization efficiency. In contrast, the $S_1/S_0$ decay points for *trans*-AB when excited to $S_2$ are mostly concentrated in the bending region, and the productive torsional path is much less populated. It is thus apparent that, by calibrating the strength of *push-pull* substituents, one could red-shift the absorption maximum of the bright $\pi\pi^*$ state and concurrently increase the photoisomerization efficiency, two main achievements in the design of photoactive AB-based systems.

Concerning the lifetimes, we see a nice agreement with the experiments: time-resolved photoelectron spectroscopy[32] yields two decay time constants for *trans*-AB: the shorter one (170 fs) is perfectly matching our *trans*-AB $S_1/S_0$ average decay time value of 168 fs; the longer one (420 fs) is close to the computed $S_2 + S_1$ average decay time of 323 fs of the slower torsional paths (see Table Table 4.4). Even though the original work documented in reference[32] attributed the longer experimental lifetime to two higher-lying $\pi\pi^*$ states ($S_3$-$S_4$), the low oscillator strength reported for them in the literature[22, 32] suggests that population of $S_2$ is by far more probable, and that the 420 fs time constant could instead be associated to the $S_2 + S_1$ deactivation following the C−N=N−C torsional motion towards the twisted $S_1/S_0$ CIs. This hypothesis was already proposed by Granucci et al.[35], and it is also supported by following theoretical[2, 88, 137] and experimental[30] works reporting a $S_1$ lifetime of about 0.4 ps. The shorter $\pi\pi^*$ lifetime in *push-pull* systems is accompanied by a longer $n\pi^*$ lifetime after $S_2 \longrightarrow S_1$ decay, whose values (155 fs, 141 fs and 63 fs for

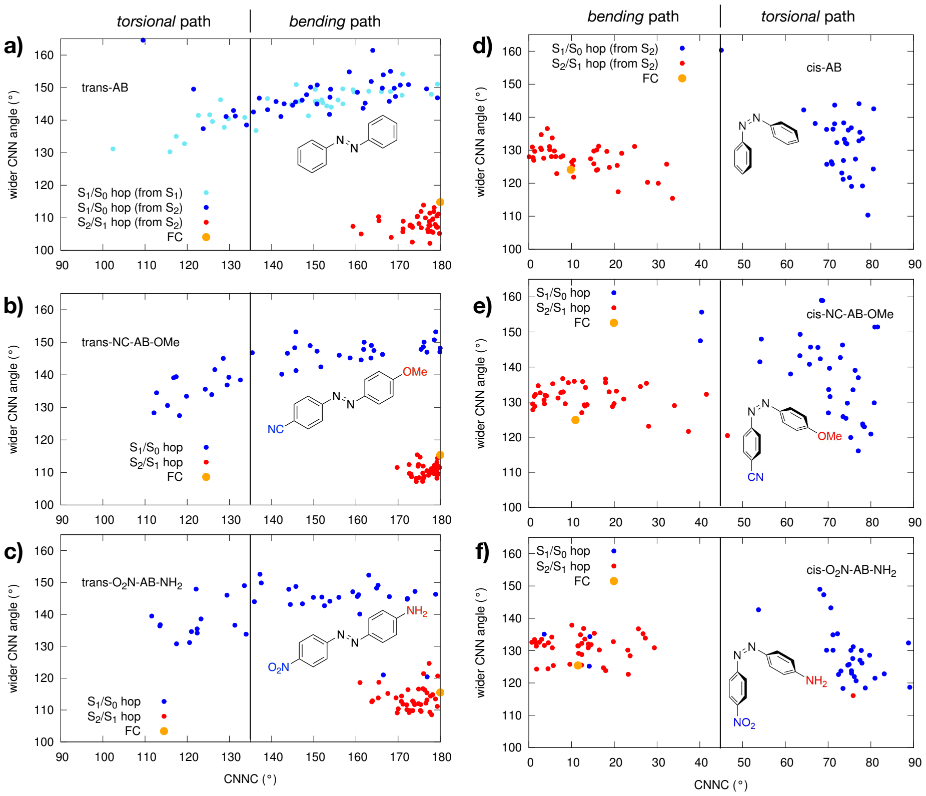

**Figure 4.36:** Projection of all the decay geometries in the torsion/bending space for the *trans* (left) and *cis* (right) dynamics. Red points = $S_2/S_1$, blue points = $S_1/S_0$ hopping points distribution populated along the $\pi\pi^*$ ($S_2$) dynamics of the three systems. Light blue points in panel (a), correspond to $S_1/S_0$ hopping points populated by the 40 trajectories starting from the *trans*-AB $n\pi^*$ ($S_1$) state. The vertical line in each panel defines the torsional and the bending regions (i.e. half way between 180° and 90° for the *trans* isomers and between 0° and 90° for the *cis*). From reference[41].

NC-AB-OMe, $O_2N$-AB-$NH_2$ and AB, respectively) are close to that of the $n\pi^*$ state of the parent AB when it is directly excited (130 fs), once again showing the similarity between the dynamics of the $\pi\pi^*$ state of the *push-pull* and the $n\pi^*$ state of AB. In the parent compound, the $S_1$ average lifetime for the torsional paths is about three times longer than in the bending paths, due to the longer time required by internal vibrational energy redistribution from the bending to the torsional mode. This is in line with the recently published AB $\pi\pi^*$ CASPT2 dynamics[14] indicating that the productive C−N=N−C torsional mechanism is slower than the unproductive route characterised by symmetric bending modes.

To explain the opposite trend in the $S_2$ and $S_1$ lifetimes observed in *push-pull* ABs as compared to the parent compound, we proposed a simple model, which rationalises entirely the observed differences. Because the *push-pull* substituents stabilise the bright state, while keeping the $n\pi^*$ energy unaffected, we imagine a simple shift of the $\pi\pi^*$ PES, as shown in Figure 4.37. By lowering the $\pi\pi^*$ state, the crossing with $n\pi^*$ becomes more accessible (i.e. lower activation energy), thus leading to the

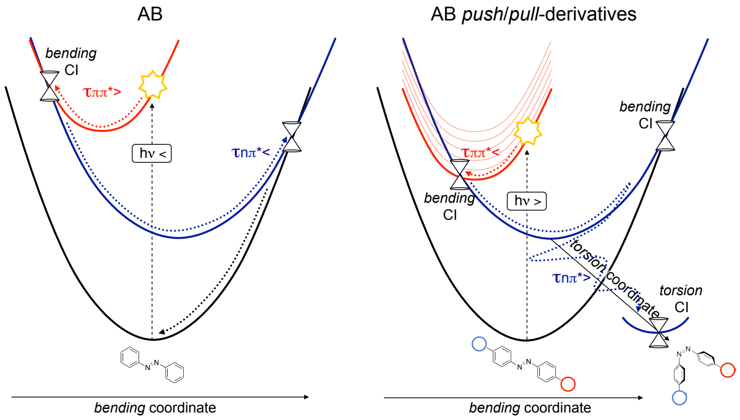

**Figure 4.37:** *Push-pull* substitution effect. From reference[41].

a shorter $S_2$ lifetime for the *push-pull* derivatives. Additionally, less energy becomes available along the initially populated bending modes after $S_2 \longrightarrow S_1$ decay to access the higher part of the $S_1/S_0$ crossing region at planar structures (C−N=N−C ≈ 180°). Eventually, vibrational energy redistribution takes place, triggering population of the n$\pi^*$ (torsional) minimum energy path and initiating the slower, but more productive, torsional motion leading to rotated $S_1/S_0$ CI structures.

### *Cis*-AB derivatives

The effect of *push-pull* substitution on the linear absorption spectrum of *cis*-isomers is again a red-shift of the $\pi\pi^*$ intense band according to the electron-donating/withdrawing strength of the substituents, while the n$\pi^*$ state energy is roughly unchanged (see Table 4.5). The main difference with respect to the *trans*-conformers is that, except for few outliers, more than 99% of the 120 cis-dynamics is attributed to the torsional decay mechanism (C−N=N−C > 45°, see Table 4.6 and CI distribution in Figure 4.36). This is in line with the larger experimental quantum yield observed in *cis*-AB (0.27 vs 0.11 of *trans*-AB[15]). Moreover, torsion is activated already on $S_2$ (reaching torsion values up to 50°, see Figure 4.36), and becomes notably larger on $S_1$, due to the non-planar FC starting structure. The earlier activation of the torsional motion, compared to their *trans* analogues, disadvantages the early decay to the n$\pi^*$ state through the bending funnel, resulting in a longer $S_2$ lifetime, in agreement with previous dynamics simulations of AB from the $\pi\pi^*$ state[137]. The bending motions are more asymmetric than in the *trans*-systems (see values at the decay points in Table 4.6) with larger bendings in the fragment bearing the electron donor group (-OMe or -$NH_2$). However, none of the *cis*-dynamics reaches bending angles close to 180°, once again ruling out the inversion path hypothesis. Like in the *trans*-systems, the $S_2$ lifetime is shortening with the increasing *push-pull* strength. Instead, the n$\pi^*$ lifetime after $S_2 \longrightarrow S_1$ decay in the *cis*-isomers is not affected by the *push-pull* substituents, because the steeper gradient along the torsional coordinate drives the system straight to the rotated $S_1/S_0$ rotated CIs. These differences in the $S_1$ PES topology (compared to the flat *trans*-n$\pi^*$ surface) correlate with a grater torsional momentum, inevitably leading to an increased photoisomerization yield. That said, the $S_2/S_1$ and $S_1/S_0$ CIs distribution in

**Table 4.5:** *Cis*-systems. Gas-phase vertical excitation energies at the $S_0$ minimum (experimental, TD-DFT and RASPT2/RASSCF).

| | | $S_0$ *trans*-min | | | | | |
|---|---|---|---|---|---|---|---|
| | | Exp. value (nm) | Exp. value (eV) | TD-DFT (nm) | TD-DFT (eV) | RASPT2 (nm) | RASPT2 (eV) |
| AB | $S_0$ | - | 0.00 | - | 0.00 | - | 0.00 |
| | $S_1$ | 425[134] | 2.92 | 464 | 2.67 | 450 | 2.75 |
| | $S_2$ | 265[134] | 4.68 | 265 | 4.68 | 302 | 4.11 |
| NC-AB-OMe | $S_0$ | - | 0.00 | - | 0.00 | - | 0.00 |
| | $S_1$ | - | - | 472 | 2.62 | 474 | 2.62 |
| | $S_2$ | - | - | 288 | 4.30 | 322 | 3.85 |
| $O_2N$-AB-$NH_2$ | $S_0$ | - | 0.00 | - | 0.00 | - | 0.00 |
| | $S_1$ | - | - | 472 | 2.62 | 506 | 2.45 |
| | $S_2$ | - | - | 313 | 3.96 | 348 | 3.56 |

**Table 4.6:** *Cis*-systems dynamics. Average excited state lifetime and geometrical parameters of the decay geometries (>99% trajectories assignable to torsional path, defined as CNNC > 45° at the $S_1 \longrightarrow S_0$ decay). (*a*) in ethanol at room temperature.

| | $\tau_{S_2}$ (fs) | $\tau_{S_2+S_1}$ (fs) | $S_2 \longrightarrow S_1$ hop CNNC (°) | $S_2 \longrightarrow S_1$ hop CNN-NNC (°) | $S_1 \longrightarrow S_0$ hop CNNC (°) | $S_1 \longrightarrow S_0$ hop CNN-NNC (°) |
|---|---|---|---|---|---|---|
| AB | 242 | 278 | 12 | 127-113 | 79 | 132-111 |
| NC-AB-OMe | 181 | 221 | 14 | 131-112 | 74 | 138-115 |
| $O_2N$-AB-$NH_2$ | 118 | 144 | 14 | 131-120 | 75 | 128-115 |
| Experiment[30] | | 0.2E03$^{(a)}$ | | | | |

Figure 4.36, shows that the parent and the *push-pull* AB-derivatives behave similarly, thus suggesting a smaller effect of *push-pull* substitution on the photoisomerization yield, compared to the *trans* analogues.

## 4.6 Conclusions

In the previous sections, the potential energy surfaces and other relevant quantities for the modelling of the n$\pi^*$ photoisomerization of azobenzene were described in detail. The reactive coordinates are identified with the C−N=N−C torsion and C−N=N/N=N−C bending, that were mapped in an extended 3D subspace, producing a database of unprecedented accuracy (RASPT2/RASSCF with a 18-electrons-in-16-orbitals active space)[34]. Despite the rigid scan procedure, the selected coordinates suffice to correctly describe all the relevant structures along the isomerization path, especially the $S_1/S_0$ CIs, which are funnelling the nonradiative decay. We found a wide $S_1/S_0$ crossing seam, that extends from planar to fully-rotated structures. The former are found at higher energy and can be reached from *trans* or *cis* FC point only with some extra kinetic energy which is available e.g. when the n$\pi^*$ state is populated by internal conversion from the higher-lying $\pi\pi^*$. In particular, kinetic energy along symmetric C−N=N/N=N−C bending is required for this deactivation path. On the other hand, the lower and most accessible part of the crossing seam is composed of rotated structures (110° > C−N=N−C > 80°) characterised by asymmetric C−N=N/N=N−C angles, and is responsible for the photoisomerization.

Our data served as solid and accurate base for semiclassical[34] and quantum dynamics simulations[36, 37, 39], all confirming the torsional mechanism as productive deactivation channel, while paths ascribable to the historically debated C−N=N inversion mechanism were never detected. The semiclassical dynamics gave a photoisomerization quantum yield which is in line with results from previous, more accurate dynamics simulations[2, 88], and served as an assessment of our PESs.

Following validation, the QD simulation of *trans* $\rightleftharpoons$ *cis* photochemical conversion in some selected 2D subspaces served as case study for the simulation of transient X-ray diffraction signals during the ultrafast process, thanks to collaboration with the group of professor Shaul Mukamel of the University of California, Irvine. These pioneering results predict that it would be possible, overcoming the experimental hurdles which are still present, to track the isomerization dynamics with transient diffraction experiments, and in particular to obtain a real-space movie of the molecule undergoing the CI dynamics, which is a very intriguing possibility. Moreover, the promising application of quantum light (i.e. with entangled photons) to trigger the photoisomerization of azobenzene was investigated, and our results show that the degree of entanglement in two-photon absorption could serve as a parameter to control the quantum pathways.

Besides all this fascinating simulations, we also investigated the potential of azobenzene for biological applications in photopharmacology and photobiology, requiring a Vis-NIR absorption for in vivo applications. To this aim, we have shown that azobenzene *push-pull* derivatives (which are known to show Vis-NIR $\pi\pi^*$ absorption) are also likely to show a higher *trans* $\longrightarrow$ *cis* quantum yield compared to pure azobenzene[41]. This result, that comes out from TD-DFT semiclassical dynamics simulations, is attributed to the different effect of the *push-pull* substituents on the $\pi\pi^*$ and $n\pi^*$ electronic states: the former is much stabilised by the presence of the electron donating/withdrawing groups, while the latter is almost unaffected by the substituents. As a result, the $S_2/S_1$ CI is lowered in energy and much more accessible compared to the parent azobenzene, reflecting in a very short $S_2$ lifetime and in a grater activation of the torsional mode (due to the lower kinetic energy available after $\pi\pi^*$ excitation). Favouring the productive torsional motion is expected to increase the quantum yield.

All the presented result prove that this simple chromophore, despite being the subject of a plethora of scientific studies since the beginning of the XX century[1], is still able to provide us with new insight into its nonadiabatic dynamics and, more in general, into the phenomenon of photoswitching. On one side, the wide knowledge on azobenzene and the simplicity of the reactive coordinates make it a textbook example which perfectly suits the simulation of new transient diffraction and spectroscopic techniques. On the other hand, the possibility to functionalise azobenzene in several different ways (and, therefore, to influence the photoisomerization mechanism) paves the way to many different applications and makes this molecule a never ending source of new possible studies.

# References

[1] G. S. Hartley, "The Cis-form of Azobenzene," *Nature*, vol. 140 (3537), pp. 281–281, **1937**.

[2] G. Tiberio, L. Muccioli, R. Berardi, and C. Zannoni, "How Does the Trans-Cis Photoisomerization of Azobenzene Take Place in Organic Solvents?" *ChemPhysChem*, vol. 11 (5), pp. 1018–1028, **2010**.

[3] M. Baroncini, G. Ragazzon, S. Silvi, M. Venturi, and A. Credi, "The eternal youth of azobenzene: New photoactive molecular and supramolecular devices," *Pure and Applied Chemistry*, vol. 87 (6), pp. 537–545, **2015**.

[4] H. Koshima, N. Ojima, and H. Uchimoto, "Mechanical Motion of Azobenzene Crystals upon Photoirradiation," *Journal of the American Chemical Society*, vol. 131 (20), pp. 6890–6891, **2009**.

[5] T. Guin, M. J. Settle, B. A. Kowalski, A. D. Auguste, R. V. Beblo, G. W. Reich, and T. J. White, "Layered liquid crystal elastomer actuators," *Nature Communications*, vol. 9 (1), p. 2531, **2018**.

[6] Y. Shang, J. Wang, T. Ikeda, and L. Jiang, "Bio-inspired liquid crystal actuator materials," *Journal of Materials Chemistry C*, vol. 7, pp. 3413–3428, 12 **2019**.

[7] C. Tonnelé, A. Pershin, S. M. Gali, A. Lherbier, J.-C. Charlier, F. Castet, L. Muccioli, and D. Beljonne, "Atomistic simulations of charge transport in photoswitchable organic-graphene hybrids," *Journal of Physics: Materials*, vol. 2 (3), p. 035 001, **2019**.

[8] J. Fregoni, G. Granucci, E. Coccia, M. Persico, and S. Corni, "Manipulating azobenzene photoisomerization through strong light-molecule coupling," *Nature Communications*, vol. 9 (1), p. 4688, **2018**.

[9] A. Natansohn and P. Rochon, "Photoinduced Motions in Azobenzene-Based Amorphous Polymers: Possible Photonic Devices," *Advanced Materials*, vol. 11 (16), pp. 1387–1391, **1999**.

[10] Y. Cao, S. Dong, S. Liu, Z. Liu, and X. Guo, "Toward Functional Molecular Devices Based on Graphene–Molecule Junctions," *Angewandte Chemie, International Edition*, vol. 52 (14), pp. 3906–3910, **2013**.

[11] L. Meng, N. Xin, C. Hu, J. Wang, B. Gui, J. Shi, C. Wang, C. Shen, G. Zhang, H. Guo, S. Meng, and X. Guo, "Side-group chemical gating via reversible optical and electric control in a single molecule transistor," *Nature Communications*, vol. 10 (1), p. 1450, **2019**.

[12] A. Emoto, E. Uchida, and T. Fukuda, "Optical and Physical Applications of Photocontrollable Materials: Azobenzene-Containing and Liquid Crystalline Polymers," *Polymers*, vol. 4 (1), pp. 150–186, **2012**.

[13] J. M. Mativetsky, G. Pace, M. Elbing, M. A. Rampi, M. Mayor, and P. Samorì, "Azobenzenes as Light-Controlled Molecular Electronic Switches in Nanoscale Metal–Molecule–Metal Junctions," *Journal of the Americal Chemical Society*, vol. 130 (29), pp. 9192–9193, **2008**.

[14] A. Nenov, R. Borrego-Varillas, A. Oriana, L. Ganzer, F. Segatta, I. Conti, J. Segarra-Marti, J. Omachi, M. Dapor, S. Taioli, C. Manzoni, S. Mukamel, G. Cerullo, and M. Garavelli, "UV-Light-Induced Vibrational Coherences: The Key to Understand Kasha Rule Violation in trans-Azobenzene," *Journal of Physical Chemistry Letters*, vol. 9 (7), pp. 1534–1541, **2018**.

[15] P. Bortolus and S. Monti, "Cis-trans photoisomerization of azobenzene. Solvent and triplet donors effects," *The Journal of Physical Chemistry*, vol. 83 (6), pp. 648–652, **1979**.

[16] H. Rau, "Further evidence for rotation in the $\pi,\pi^*$ and inversion in the $n,\pi^*$ photoisomerization of azobenzenes," *Journal of Photochemistry*, vol. 26 (2), pp. 221–225, **1984**.

[17] A. A. Beharry and G. A. Woolley, "Azobenzene photoswitches for biomolecules," *Chemical Society Reviews*, vol. 40, pp. 4422–4437, 8 **2011**.

[18] T. Fujino and T. Tahara, "Picosecond Time-Resolved Raman Study of trans-Azobenzene," *The Journal of Physical Chemistry A*, vol. 104 (18), pp. 4203–4210, **2000**.

[19] T. Ishikawa, T. Noro, and T. Shoda, "Theoretical study on the photoisomerization of azobenzene," *The Journal of Chemical Physics*, vol. 115 (16), pp. 7503–7512, **2001**.

[20] L. Gagliardi, G. Orlandi, F. Bernardi, A. Cembran, and M. Garavelli, "A theoretical study of the lowest electronic states of azobenzene: The role of torsion coordinate in the cis–trans photoisomerization," *Theoretical Chemistry Accounts*, vol. 111 (2), pp. 363–372, **2004**.

[21] J. Casellas, M. J. Bearpark, and M. Reguero, "Excited-State Decay in the Photoisomerisation of Azobenzene: A New Balance Between Mechanisms.," *ChemPhysChem*, vol. 17 (19), pp. 3068–3079, **2016**.

[22] I. Conti, M. Garavelli, and G. Orlandi, "The Different Photoisomerization Efficiency of Azobenzene in the Lowest $n\pi^*$ and $\pi\pi^*$ Singlets: The Role of a Phantom State," *Journal of the American Chemical Society*, vol. 130 (15), pp. 5216–5230, **2008**.

[23] Y. Ootani, K. Satoh, A. Nakayama, T. Noro, and T. Taketsugu, "Ab initio molecular dynamics simulation of photoisomerization in azobenzene in the $n\pi*$ state," *The Journal of Chemical Physics*, vol. 131 (19), p. 194 306, **2009**.

[24] S. Yuan, Y. Dou, W. Wu, Y. Hu, and J. Zhao, "Why Does trans-Azobenzene Have a Smaller Isomerization Yield for $\pi\pi^*$ Excitation Than for $n\pi^*$ Excitation?" *The Journal of Physical Chemistry A*, vol. 112 (51), pp. 13 326–13 334, **2008**.

[25] C. Ciminelli, G. Granucci, and M. Persico, "The Photoisomerization Mechanism of Azobenzene: A Semiclassical Simulation of Nonadiabatic Dynamics.," *Chemistry - A European Journal*, vol. 10 (9), pp. 2327–2341, **2004**.

[26] Y. Harabuchi, M. Ishii, A. Nakayama, T. Noro, and T. Taketsugu, "A multireference perturbation study of the NN stretching frequency of trans-azobenzene in $n\pi^*$ excitation and an implication for the photoisomerization mechanism," *The Journal of Chemical Physics*, vol. 138 (6), p. 064 305, **2013**.

[27] T. Nägele, R. Hoche, W. Zinth, and J. Wachtveitl, "Femtosecond photoisomerization of cis-azobenzene," *Chemical Physics Letters*, vol. 272 (5), pp. 489–495, **1997**.

[28] I. Lednev, T. Ye, P. Matousek, M. Towrie, P. Foggi, F. Neuwahl, S. Umapathy, R. Hester, and J. Moore, "Femtosecond time-resolved UV-visible absorption spectroscopy of trans-azobenzene: Dependence on excitation wavelength," *Chemical Physics Letters*, vol. 290 (1), pp. 68–74, **1998**.

[29] H. Satzger, S. Spörlein, C. Root, J. Wachtveitl, W. Zinth, and P. Gilch, "Fluorescence spectra of trans- and cis-azobenzene – emission from the Franck–Condon state," *Chemical Physics Letters*, vol. 372 (1), pp. 216–223, **2003**.

[30] H. Satzger, C. Root, and M. Braun, "Excited-State Dynamics of trans- and cis-Azobenzene after UV Excitation in the $\pi\pi^*$ Band," *The Journal of Physical Chemistry A*, vol. 108 (30), pp. 6265–6271, **2004**.

[31] M. Quick, A. L. Dobryakov, M. Gerecke, C. Richter, F. Berndt, I. N. Ioffe, A. A. Granovsky, R. Mahrwald, N. P. Ernsting, and S. A. Kovalenko, "Photoisomerization Dynamics and Pathways of trans- and cis-Azobenzene in Solution from Broadband Femtosecond Spectroscopies and Calculations," *The Journal of Physical Chemistry B*, vol. 118 (29), pp. 8756–8771, **2014**.

[32] T. Schultz, J. Quenneville, B. Levine, A. Toniolo, T. J. Martínez, S. Lochbrunner, M. Schmitt, J. P. Shaffer, M. Z. Zgierski, and A. Stolow, "Mechanism and Dynamics of Azobenzene Photoisomerization," *Journal of the American Chemical Society*, vol. 125 (27), pp. 8098–8099, **2003**.

[33] E. M. M. Tan, S. Amirjalayer, S. Smolarek, A. Vdovin, F. Zerbetto, and W. J. Buma, "Fast photodynamics of azobenzene probed by scanning excited-state potential energy surfaces using slow spectroscopy," *Nature Communications*, vol. 6 (1), p. 5860, **2015**.

[34] F. Aleotti, L. Soprani, A. Nenov, R. Berardi, A. Arcioni, C. Zannoni, and M. Garavelli, "Multidimensional Potential Energy Surfaces Resolved at the RASPT2 Level for Accurate Photoinduced Isomerization Dynamics of Azobenzene," *Journal of Chemical Theory and Computation*, vol. 15 (12), pp. 6813–6823, **2019**.

[35] G. Granucci and M. Persico, "Excited state dynamics with the direct trajectory surface hopping method: Azobenzene and its derivatives as a case study," vol. 117 (5), pp. 1131–1143, **2007**.

[36] D. Keefer, F. Aleotti, J. R. Rouxel, F. Segatta, B. Gu, A. Nenov, M. Garavelli, and S. Mukamel, "Imaging conical intersection dynamics during azobenzene photoisomerization by ultrafast X-ray diffraction," *Proceedings of the National Academy of Sciences*, vol. 118 (3), **2021**.

[37] B. Gu, D. Keefer, F. Aleotti, A. Nenov, M. Garavelli, and S. Mukamel, "Photoisomerization transition state manipulation by entangled two-photon absorption," *Proceedings of the National Academy of Sciences*, vol. 118 (47), **2021**.

[38] S. M. Cavaletto, D. Keefer, J. R. Rouxel, F. Aleotti, F. Segatta, M. Garavelli, and S. Mukamel, "Unveiling the spatial distribution of molecular coherences at conical intersections by covariance X-ray diffraction signals," *Proceedings of the National Academy of Sciences*, vol. 118 (22), **2021**.

[39] D. Keefer, J. R. Rouxel, F. Aleotti, F. Segatta, M. Garavelli, and S. Mukamel, "Diffractive Imaging of Conical Intersections Amplified by Resonant Infrared Fields," *Journal of the American Chemical Society*, vol. 143 (34), pp. 13 806–13 815, **2021**.

[40] J. Rouxel, D. Keefer, F. Aleotti, A. Nenov, M. Garavelli, and S. Mukamel, "Coupled electronic and nuclear motions during azobenzene photoisomerization monitored by ultrafast electron diffraction," Submitted to the Journal of Chemical Theory and Computation.

[41] F. Aleotti, A. Nenov, L. Salvigni, M. Bonfanti, M. M. El-Tahawy, A. Giunchi, M. Gentile, C. Spallacci, A. Ventimiglia, G. Cirillo, L. Montali, S. Scurti, M. Garavelli, and I. Conti, "Spectral Tuning and Photoisomerization Efficiency in Push–Pull Azobenzenes: Designing Principles," *The Journal of Physical Chemistry A*, vol. 124 (46), pp. 9513–9523, **2020**.

[42] K. Bennett, M. Kowalewski, J. R. Rouxel, and S. Mukamel, "Monitoring molecular nonadiabatic dynamics with femtosecond X-ray diffraction," *Proceedings of the National Academy of Sciences*, vol. 115 (26), pp. 6538–6547, **2018**.

[43] L. Young, K. Ueda, M. Gühr, P. H. Bucksbaum, M. Simon, S. Mukamel, N. Rohringer, K. C. Prince, C. Masciovecchio, M. Meyer, A. Rudenko, D. Rolles, C. Bostedt, M. Fuchs, D. A. Reis, R. Santra, H. Kapteyn, M. Murnane, H. Ibrahim, F. Légaré, M. Vrakking, M. Isinger, D. Kroon, M. Gisselbrecht, A. L'Huillier, H. J. Wörner, and S. R. Leone, "Roadmap of ultrafast x-ray atomic and molecular physics," *Journal of Physics B: Atomic, Molecular and Optical Physics*, vol. 51 (3), p. 032 003, **2018**.

[44] E. A. Seddon, J. A. Clarke, D. J. Dunning, C. Masciovecchio, C. J. Milne, F. Parmigiani, D. Rugg, J. C. H. Spence, N. R. Thompson, K. Ueda, S. M. Vinko, J. S. Wark, and W. Wurth, "Short-wavelength free-electron laser sources and science: A review," *Reports on Progress in Physics*, vol. 80 (11), p. 115 901, **2017**.

[45] T. Popmintchev, M.-C. Chen, P. Arpin, M. M. Murnane, and H. C. Kapteyn, "The attosecond nonlinear optics of bright coherent X-ray generation," vol. 4 (12), pp. 822–832, **2010**.

[46] F. Zamponi, Z. Ansari, M. Woerner, and T. Elsaesser, "Femtosecond powder diffraction with a laser-driven hard X-ray source," vol. 18 (2), pp. 947–961, **2010**.

[47] H. N. Chapman, P. Fromme, A. Barty, T. A. White, R. A. Kirian, A. Aquila, M. S. Hunter, J. Schulz, D. P. DePonte, U. Weierstall, R. B. Doak, F. R. N. C. Maia, A. V. Martin, I. Schlichting, L. Lomb, N. Coppola, R. L. Shoeman, S. W. Epp, R. Hartmann, D. Rolles, A. Rudenko, L. Foucar, N. Kimmel, G. Weidenspointner, P. Holl, M. Liang, M. Barthelmess, C. Caleman, S. Boutet, M. J. Bogan, J. Krzywinski, C. Bostedt, S. Bajt, L. Gumprecht, B. Rudek, B. Erk, C. Schmidt, A. Hömke, C. Reich, D. Pietschner, L. Strüder, G. Hauser, H. Gorke, J. Ullrich, S. Herrmann, G. Schaller, F. Schopper, H. Soltau, K.-U. Kühnel, M. Messerschmidt, J. D. Bozek, S. P. Hau-Riege, M. Frank, C. Y. Hampton, R. G. Sierra, D. Starodub, G. J. Williams, J. Hajdu, N. Timneanu, M. M. Seibert, J. Andreasson, A. Rocker, O. Jönsson, M. Svenda, S. Stern, K. Nass, R. Andritschke, C.-D. Schröter, F. Krasniqi, M. Bott, K. E. Schmidt, X. Wang, I. Grotjohann, J. M. Holton, T. R. M.

Barends, R. Neutze, S. Marchesini, R. Fromme, S. Schorb, D. Rupp, M. Adolph, T. Gorkhover, I. Andersson, H. Hirsemann, G. Potdevin, H. Graafsma, B. Nilsson, and J. C. H. Spence, "Femtosecond X-ray protein nanocrystallography," *Nature*, vol. 470 (7332), pp. 73–77, **2011**.

[48] P. Fromme and J. C. H. Spence, "Femtosecond nanocrystallography using X-ray lasers for membrane protein structure determination," *Current Opinion in Structural Biology*, vol. 21 (4), pp. 509–516, **2011**.

[49] J. Küpper, S. Stern, L. Holmegaard, F. Filsinger, A. Rouzée, A. Rudenko, P. Johnsson, A. V. Martin, M. Adolph, A. Aquila, S. š. Bajt, A. Barty, C. Bostedt, J. Bozek, C. Caleman, R. Coffee, N. Coppola, T. Delmas, S. Epp, B. Erk, L. Foucar, T. Gorkhover, L. Gumprecht, A. Hartmann, R. Hartmann, G. Hauser, P. Holl, A. Hömke, N. Kimmel, F. Krasniqi, K.-U. Kühnel, J. Maurer, M. Messerschmidt, R. Moshammer, C. Reich, B. Rudek, R. Santra, I. Schlichting, C. Schmidt, S. Schorb, J. Schulz, H. Soltau, J. C. H. Spence, D. Starodub, L. Strüder, J. Thøgersen, M. J. J. Vrakking, G. Weidenspointner, T. A. White, C. Wunderer, G. Meijer, J. Ullrich, H. Stapelfeldt, D. Rolles, and H. N. Chapman, "X-Ray Diffraction from Isolated and Strongly Aligned Gas-Phase Molecules with a Free-Electron Laser," *Physical Review Letters*, vol. 112, p. 083 002, 8 **2014**.

[50] H. N. Chapman, "X-Ray Free-Electron Lasers for the Structure and Dynamics of Macromolecules," *Annual Review of Biochemistry*, vol. 88 (1), pp. 35–58, **2019**.

[51] T. Gorkhover, M. Adolph, D. Rupp, S. Schorb, S. W. Epp, B. Erk, L. Foucar, R. Hartmann, N. Kimmel, K.-U. Kühnel, D. Rolles, B. Rudek, A. Rudenko, R. Andritschke, A. Aquila, J. D. Bozek, N. Coppola, T. Erke, F. Filsinger, H. Gorke, H. Graafsma, L. Gumprecht, G. Hauser, S. Herrmann, H. Hirsemann, A. Hömke, P. Holl, C. Kaiser, F. Krasniqi, J.-H. Meyer, M. Matysek, M. Messerschmidt, D. Miessner, B. Nilsson, D. Pietschner, G. Potdevin, C. Reich, G. Schaller, C. Schmidt, F. Schopper, C. D. Schröter, J. Schulz, H. Soltau, G. Weidenspointner, I. Schlichting, L. Strüder, J. Ullrich, T. Möller, and C. Bostedt, "Nanoplasma Dynamics of Single Large Xenon Clusters Irradiated with Superintense X-Ray Pulses from the Linac Coherent Light Source Free-Electron Laser," *Physical Review Letters*, vol. 108, p. 245 005, 24 **2012**.

[52] K. Ayyer, G. Geloni, V. Kocharyan, E. Saldin, S. Serkez, O. Yefanov, and I. Zagorodnov, "Perspectives for imaging single protein molecules with the present design of the European XFEL," *Structural Dynamics*, vol. 2 (4), p. 041 702, **2015**.

[53] M. Woerner, F. Zamponi, Z. Ansari, J. Dreyer, B. Freyer, M. Prémont-Schwarz, and T. Elsaesser, "Concerted electron and proton transfer in ionic crystals mapped by femtosecond x-ray powder diffraction," *The Journal of Chemical Physics*, vol. 133 (6), p. 064 509, **2010**.

[54] M. J. J. Vrakking and T. Elsaesser, "X-rays inspire electron movies," *Nature Photonics*, vol. 6 (10), pp. 645–647, **2012**.

[55] T. Elsaesser and M. Woerner, "Perspective: Structural dynamics in condensed matter mapped by femtosecond x-ray diffraction," *The Journal of Chemical Physics*, vol. 140 (2), p. 020 901, **2014**.

[56] R. J. D. Miller, “Femtosecond crystallography with ultrabright electrons and x-rays: Capturing chemistry in action,” *Science*, vol. 343 (6175), pp. 1108–1116, **2014**.

[57] J. M. Glownia, A. Natan, J. P. Cryan, R. Hartsock, M. Kozina, M. P. Minitti, S. Nelson, J. Robinson, T. Sato, T. van Driel, G. Welch, C. Weninger, D. Zhu, and P. H. Bucksbaum, “Self-Referenced Coherent Diffraction X-Ray Movie of ångstrom- and Femtosecond-Scale Atomic Motion,” *Physics Review Letters*, vol. 117, p. 153 003, 15 **2016**.

[58] C. Hauf, S. A.-A. Hernandez, M. Holtz, M. Woerner, and T. Elsaesser, “Soft-mode driven polarity reversal in ferroelectrics mapped by ultrafast x-ray diffraction,” *Structural Dynamics*, vol. 5 (2), p. 024 501, **2018**.

[59] G. N. Kovacs, J.-P. Colletier, M. L. Grünbein, Y. Yang, T. Stensitzki, A. Batyuk, S. Carbajo, R. B. Doak, D. Ehrenberg, L. Foucar, R. Gasper, A. Gorel, M. Hilpert, M. Kloos, J. E. Koglin, J. Reinstein, C. M. Roome, R. Schlesinger, M. Seaberg, R. L. Shoeman, M. Stricker, S. Boutet, S. Haacke, J. Heberle, K. Heyne, T. Domratcheva, T. R. M. Barends, and I. Schlichting, “Three-dimensional view of ultrafast dynamics in photoexcited bacteriorhodopsin,” *Nature Communications*, vol. 10 (1), **2019**.

[60] R. J. D. Miller, O. Paré-Labrosse, A. Sarracini, and J. E. Besaw, “Three-dimensional view of ultrafast dynamics in photoexcited bacteriorhodopsin in the multiphoton regime and biological relevance,” *Nature Communications*, vol. 11 (1), **2020**.

[61] J. C. Williamson, J. Cao, H. Ihee, H. Frey, and A. H. Zewail, “Clocking transient chemical changes by ultrafast electron diffraction,” *Nature*, vol. 386 (6621), pp. 159–162, **1997**.

[62] G. Sciaini and D. R. J. Miller, “Femtosecond electron diffraction: Heralding the era of atomically resolved dynamics,” *Reports on Progress in Physics*, vol. 74 (9), p. 096 101, **2011**.

[63] M. Gao, C. Lu, H. Jean-Ruel, L. C. Liu, A. Marx, K. Onda, S.-y. Koshihara, Y. Nakano, X. Shao, T. Hiramatsu, G. Saito, H. Yamochi, R. R. Cooney, G. Moriena, G. Sciaini, and R. J. D. Miller, “Mapping molecular motions leading to charge delocalization with ultrabright electrons,” *Nature*, vol. 496 (7445), pp. 343–346, **2013**.

[64] T. J. A. Wolf, D. M. Sanchez, J. Yang, R. M. Parrish, J. P. F. Nunes, M. Centurion, R. Coffee, J. P. Cryan, M. Gühr, K. Hegazy, A. Kirrander, R. K. Li, J. Ruddock, X. Shen, T. Vecchione, S. P. Weathersby, P. M. Weber, K. Wilkin, H. Yong, Q. Zheng, X. J. Wang, M. P. Minitti, and T. J. Martínez, “The photochemical ring-opening of 1, 3-cyclohexadiene imaged by ultrafast electron diffraction,” *Nature Chemistry*, vol. 11 (6), pp. 504–509, **2019**.

[65] J. Yang, X. Zhu, J. P. F. Nunes, J. K. Yu, R. M. Parrish, T. J. A. Wolf, M. Centurion, M. Gühr, R. Li, Y. Liu, B. Moore, M. Niebuhr, S. Park, X. Shen, S. Weathersby, T. Weinacht, T. J. Martinez, and X. Wang, “Simultaneous observation of nuclear and electronic dynamics by ultrafast electron diffraction,” *Science*, vol. 368 (6493), pp. 885–889, **2020**.

[66] J. Cao and K. R. Wilson, “Ultrafast X-ray Diffraction Theory,” *The Journal of Physical Chemistry A*, vol. 102 (47), pp. 9523–9530, **1998**.

[67] G. Dixit, O. Vendrell, and R. Santra, “Imaging electronic quantum motion with light,” *Proceedings of the National Academy of Sciences*, vol. 109 (29), pp. 11 636–11 640, **2012**.

[68] M. Simmermacher, N. E. Henriksen, K. B. Møller, A. Moreno Carrascosa, and A. Kirrander, “Electronic Coherence in Ultrafast X-Ray Scattering from Molecular Wave Packets,” *Physical Review Letters*, vol. 122, p. 073 003, 7 **2019**.

[69] B. Stankus, H. Yong, N. Zotev, J. M. Ruddock, D. Bellshaw, T. J. Lane, M. Liang, S. Boutet, S. Carbajo, J. S. Robinson, W. Du, N. Goff, Y. Chang, J. E. Koglin, M. P. Minitti, A. Kirrander, and P. M. Weber, “Ultrafast X-ray scattering reveals vibrational coherence following Rydberg excitation,” *Nature Chemistry*, vol. 11 (8), pp. 716–721, **2019**.

[70] G. Hermann, V. Pohl, G. Dixit, and J. C. Tremblay, “Probing Electronic Fluxes via Time-Resolved X-Ray Scattering,” *Physics Reviiew Lett*, vol. 124, p. 013 002, 1 **2020**.

[71] J. R. Rouxel, D. Keefer, and S. Mukamel, “Signatures of electronic and nuclear coherences in ultrafast molecular x-ray and electron diffraction,” *Structural Dynamics*, vol. 8 (1), p. 014 101, **2021**.

[72] S. Mukamel and S. Rahav, “Chapter 6 - Ultrafast Nonlinear Optical Signals Viewed from the Molecule’s Perspective: Kramers–Heisenberg Transition-Amplitudes versus Susceptibilities,” in *Advances in Atomic, Molecular, and Optical Physics*, ser. Advances In Atomic, Molecular, and Optical Physics, E. Arimondo, P. R. Berman, and C. C. Lin, Eds., vol. 59, Academic Press, **2010**, pp. 223–263.

[73] J. Miao, P. Charalambous, J. Kirz, and D. Sayre, “Extending the methodology of X-ray crystallography to allow imaging of micrometre-sized non-crystalline specimens,” *Nature*, vol. 400 (6742), pp. 342–344, **1999**.

[74] S.-K. Son, H. N. Chapman, and R. Santra, “Multiwavelength Anomalous Diffraction at High X-Ray Intensity,” *Physical Review Letters*, vol. 107, p. 218 102, 21 **2011**.

[75] P.-O. Widmark, P.-Å. Malmqvist, and B. O. Roos, “Density matrix averaged atomic natural orbital (ANO) basis sets for correlated molecular wave functions,” *Theoretica chimica acta*, vol. 77 (5), pp. 291–306, **1990**.

[76] F. Aquilante, J. Autschbach, R. K. Carlson, L. F. Chibotaru, M. G. Delcey, L. De Vico, I. Fdez. Galván, N. Ferré, L. M. Frutos, L. Gagliardi, M. Garavelli, A. Giussani, C. E. Hoyer, G. Li Manni, H. Lischka, D. Ma, P. Å. Malmqvist, T. Müller, A. Nenov, M. Olivucci, T. B. Pedersen, D. Peng, F. Plasser, B. Pritchard, M. Reiher, I. Rivalta, I. Schapiro, J. Segarra-Martí, M. Stenrup, D. G. Truhlar, L. Ungur, A. Valentini, S. Vancoillie, V. Veryazov, V. P. Vysotskiy, O. Weingart, F. Zapata, and R. Lindh, “Molcas 8: New capabilities for multiconfigurational quantum chemical calculations across the periodic table,” *Journal of Computational Chemistry*, vol. 37 (5), pp. 506–541, **2016**.

[77] O. Weingart, A. Nenov, P. Altoè, I. Rivalta, J. Segarra-Martí, I. Dokukina, and M. Garavelli, "COBRAMM 2.0 - A software interface for tailoring molecular electronic structure calculations and running nanoscale (QM/MM) simulations," vol. 24 (9), p. 271, **2018**.

[78] P. Altoè, M. Stenta, A. Bottoni, and M. Garavelli, "A tunable QM/MM approach to chemical reactivity, structure and physico-chemical properties prediction," vol. 118 (1), pp. 219–240, **2007**.

[79] Cobramm on GitLab, available at: `https://gitlab.com/cobrammgroup/cobramm/-/wikis/home`.

[80] J. C. Tully, "Molecular dynamics with electronic transitions," *The Journal of Chemical Physics*, vol. 93 (2), pp. 1061–1071, **1990**.

[81] J. C. Phillips, R. Braun, W. Wang, J. Gumbart, E. Tajkhorshid, E. Villa, C. Chipot, R. D. Skeel, L. Kalé, and K. Schulten, "Scalable molecular dynamics with NAMD," *Journal of Computational Chemistry*, vol. 26 (16), pp. 1781–1802, **2005**.

[82] H. Tal-Ezer and R. Kosloff, "An accurate and efficient scheme for propagating the time dependent Schrödinger equation," *The Journal of Chemical Physics*, vol. 81 (9), pp. 3967–3971, **1984**.

[83] P. H. Berens and K. R. Wilson, "Molecular dynamics and spectra. I. Diatomic rotation and vibration," *The Journal of Chemical Physics*, vol. 74 (9), pp. 4872–4882, **1981**.

[84] S. Thallmair, M. K. Roos, and R. de Vivie-Riedle, "Design of specially adapted reactive coordinates to economically compute potential and kinetic energy operators including geometry relaxation," *The Journal of Chemical Physics*, vol. 144 (23), p. 234 104, **2016**.

[85] V. Marturano, V. Ambrogi, N. A. G. Bandeira, B. Tylkowski, M. Giamberini, and P. Cerruti, "Modeling of Azobenzene-Based Compounds," *Physical Sciences Reviews*, vol. 2 (11), **2017**.

[86] T. Cusati, G. Granucci, E. Martínez-Núñez, F. Martini, M. Persico, and S. Vázquez, "Semiempirical Hamiltonian for Simulation of Azobenzene Photochemistry," *The Journal of Physical Chemistry A*, vol. 116 (1), pp. 98–110, **2012**.

[87] A. Nenov and R. de Vivie-Riedle, "Geometrical and substituent effects in conical intersections: Linking chemical structure and photoreactivity in polyenes," *The Journal of Chemical Physics*, vol. 135 (3), p. 034 304, **2011**.

[88] A. Toniolo, C. Ciminelli, M. Persico, and T. J. Martínez, "Simulation of the photodynamics of azobenzene on its first excited state: Comparison of full multiple spawning and surface hopping treatments," *The Journal of Chemical Physics*, vol. 123 (23), p. 234 308, **2005**.

[89] J. O. Tollerud, G. Sparapassi, A. Montanaro, S. Asban, F. Glerean, F. Giusti, A. Marciniak, G. Kourousias, F. Billè, F. Cilento, S. Mukamel, and D. Fausti, "Femtosecond covariance spectroscopy," *Proceedings of the National Academy of Sciences*, vol. 116 (12), pp. 5383–5386, **2019**.

[90] L. Ye, J. R. Rouxel, D. Cho, and S. Mukamel, "Imaging electron-density fluctuations by multidimensional x-ray photon-coincidence diffraction," *Proceedings of the National Academy of Sciences*, vol. 116 (2), pp. 395–400, **2019**.

[91] S. Asban, K. E. Dorfman, and S. Mukamel, “Quantum phase-sensitive diffraction and imaging using entangled photons,” *Proceedings of the National Academy of Sciences*, vol. 116 (24), pp. 11 673–11 678, **2019**.

[92] A. L. Patterson, “A Direct Method for the Determination of the Components of Interatomic Distances in Crystals,” *Zeitschrift für Kristallographie - Crystalline Materials*, vol. 90 (1-6), pp. 517–542, **1935**.

[93] R. S. Judson and H. Rabitz, “Teaching lasers to control molecules,” *Physical Review Letters*, vol. 68, pp. 1500–1503, 10 **1992**.

[94] H. Rabitz, R. de Vivie-Riedle, M. Motzkus, and K. Kompa, “Whither the Future of Controlling Quantum Phenomena?” *Science*, vol. 288 (5467), pp. 824–828, **2000**.

[95] W. Denk, J. H. Strickler, and W. Watt Webb, “Two-Photon Laser Scanning Fluorescence Microscopy,” *Science*, vol. 248 (4951), pp. 73–76, **1990**.

[96] G. Bort, T. Gallavardin, D. Ogden, and P. I. Dalko, “From One-Photon to Two-Photon Probes: “Caged” Compounds, Actuators, and Photoswitches,” *Angewandte Chemie International Edition*, vol. 52 (17), pp. 4526–4537, **2013**.

[97] G. Cabré, A. Garrido-Charles, M. Moreno, M. Bosch, M. Porta-de-la-Riva, M. Krieg, M. Gascón-Moya, N. Camarero, R. Gelabert, J. M. Lluch, F. Busqué, J. Hernando, P. Gorostiza, and R. Alibés, “Rationally designed azobenzene photoswitches for efficient two-photon neuronal excitation,” *Nature Communications*, vol. 10 (1), **2019**.

[98] M. Dudek, N. Tarnowicz-Staniak, M. Deiana, Z. Pokładek, M. Samoć, and K. Matczyszyn, “Two-photon absorption and two-photon-induced isomerization of azobenzene compounds,” *RSC Advances*, vol. 10, pp. 40 489–40 507, 66 **2020**.

[99] L. Mandel and E. Wolf, *Optical coherence and quantum optics.* Cambridge university press, **1995**.

[100] O. Benson, C. Santori, M. Pelton, and Y. Yamamoto, “Regulated and Entangled Photons from a Single Quantum Dot,” *Physical Review Letters*, vol. 84, pp. 2513–2516, 11 **2000**.

[101] H. J. Kimble, M. Dagenais, and L. Mandel, “Photon Antibunching in Resonance Fluorescence,” *Physical Review Letters*, vol. 39, pp. 691–695, 11 **1977**.

[102] J. Javanainen and P. L. Gould, “Linear intensity dependence of a two-photon transition rate,” *Physical Review A*, vol. 41, pp. 5088–5091, 9 **1990**.

[103] O. Varnavski and T. Goodson, “Two-Photon Fluorescence Microscopy at Extremely Low Excitation Intensity: The Power of Quantum Correlations,” *Journal of the American Chemical Society*, vol. 142 (30), pp. 12 966–12 975, **2020**.

[104] O. Roslyak, C. A. Marx, and S. Mukamel, “Nonlinear spectroscopy with entangled photons: Manipulating quantum pathways of matter,” *Physical Review A*, vol. 79, p. 033 832, 3 **2009**.

[105] B. Gu, D. Keefer, and S. Mukamel, “Wavepacket control and simulation protocol for entangled two-photon-absorption of molecules,” Submitted on September, 11 2021 [arXiv:2109.05146].

[106] S. Butterworth, "On the theory of filter amplifiers," *Exp. Wirel. Wirel. Eng.*, vol. 7, pp. 536–541, **1930**.

[107] D. Keefer, V. M. Freixas, H. Song, S. Tretiak, S. Fernandez-Alberti, and S. Mukamel, "Monitoring molecular vibronic coherences in a bichromophoric molecule by ultrafast X-ray spectroscopy," *Chemical Science*, vol. 12, pp. 5286–5294, 14 **2021**.

[108] D. Keefer, T. Schnappinger, R. de Vivie-Riedle, and S. Mukamel, "Visualizing conical intersection passages via vibronic coherence maps generated by stimulated ultrafast X-ray Raman signals," *Proceedings of the National Academy of Sciences*, vol. 117 (39), pp. 24 069–24 075, **2020**.

[109] M. Dong, A. Babalhavaeji, S. Samanta, A. A. Beharry, and G. A. Woolley, "Red-Shifting Azobenzene Photoswitches for in Vivo Use," *Accounts of Chemical Research*, vol. 48 (10), pp. 2662–2670, **2015**.

[110] D. Bléger and S. Hecht, "Visible-Light-Activated Molecular Switches," *Angewandte Chemie International Edition*, vol. 54 (39), pp. 11 338–11 349, **2015**.

[111] M. J. Hansen, M. M. Lerch, W. Szymanski, and B. L. Feringa, "Direct and Versatile Synthesis of Red-Shifted Azobenzenes," *Angewandte Chemie International Edition*, vol. 55 (43), pp. 13 514–13 518, **2016**.

[112] M. Dong, A. Babalhavaeji, C. V. Collins, K. Jarrah, O. Sadovski, Q. Dai, and G. A. Woolley, "Near-Infrared Photoswitching of Azobenzenes under Physiological Conditions," *Journal of the American Chemical Society*, vol. 139 (38), pp. 13 483–13 486, **2017**.

[113] M. Wegener, M. J. Hansen, A. J. M. Driessen, W. Szymanski, and B. L. Feringa, "Photocontrol of Antibacterial Activity: Shifting from UV to Red Light Activation," *Journal of the American Chemical Society*, vol. 139 (49), pp. 17 979–17 986, **2017**.

[114] P. Gorostiza and E. Y. Isacoff, "Optical Switches for Remote and Noninvasive Control of Cell Signaling," *Science*, vol. 322 (5900), pp. 395–399, **2008**.

[115] M. J. Hansen, W. A. Velema, G. de Bruin, H. S. Overkleeft, W. Szymanski, and B. L. Feringa, "Proteasome inhibitors with photocontrolled activity," *ChemBioChem*, vol. 15 (14), pp. 2053–2057, **2014**.

[116] M. Borowiak, W. Nahaboo, M. Reynders, K. Nekolla, P. Jalinot, J. Hasserodt, M. Rehberg, M. Delattre, S. Zahler, A. Vollmar, D. Trauner, and O. Thorn-Seshold, "Photoswitchable Inhibitors of Microtubule Dynamics Optically Control Mitosis and Cell Death," *Cell*, vol. 162 (2), pp. 403–411, **2015**.

[117] M. Volgraf, P. Gorostiza, R. Numano, R. H. Kramer, E. Y. Isacoff, and D. Trauner, "Allosteric control of an ionotropic glutamate receptor with an optical switch," *Nature Chemical Biology*, vol. 2 (1), pp. 47–52, **2005**.

[118] W. A. Velema, J. P. van der Berg, M. J. Hansen, W. Szymanski, A. J. M. Driessen, and B. L. Feringa, "Optical control of antibacterial activity," *Nature Chemistry*, vol. 5 (11), pp. 924–928, **2013**.

[119] H. Kaufman, S. M. Vratsanos, and B. F. Erlanger, "Photoregulation of an Enzymic Process by Means of a Light-Sensitive Ligand," *Science*, vol. 162 (3861), pp. 1487–1489, **1968**.

[120] E. Bartels, N. H. Wassermann, and B. F. Erlanger, “Photochromic Activators of the Acetylcholine Receptor,” *Proceedings of the National Academy of Sciences*, vol. 68 (8), pp. 1820–1823, **1971**.

[121] M. Gascón-Moya, A. Pejoan, M. Izquierdo-Serra, S. Pittolo, G. Cabré, J. Hernando, R. Alibés, P. Gorostiza, and F. Busqué, “An Optimized Glutamate Receptor Photoswitch with Sensitized Azobenzene Isomerization,” *The Journal of Organic Chemistry*, vol. 80 (20), pp. 9915–9925, **2015**.

[122] M. Izquierdo-Serra, M. Gascón-Moya, J. J. Hirtz, S. Pittolo, K. E. Poskanzer, È. Ferrer, R. Alibés, F. Busqué, R. Yuste, J. Hernando, and P. Gorostiza, “Two-Photon Neuronal and Astrocytic Stimulation with Azobenzene-Based Photoswitches,” *Journal of the American Chemical Society*, vol. 136 (24), pp. 8693–8701, **2014**.

[123] N. Desai, “Challenges in Development of Nanoparticle-Based Therapeutics,” *The AAPS Journal*, vol. 14 (2), pp. 282–295, **2012**.

[124] H. M. D. Bandara and S. C. Burdette, “Photoisomerization in different classes of azobenzene,” *Chemical Society Reviews*, vol. 41, pp. 1809–1825, 5 **2012**.

[125] C. R. Crecca and A. E. Roitberg, “Theoretical Study of the Isomerization Mechanism of Azobenzene and Disubstituted Azobenzene Derivatives,” *The Journal of Physical Chemistry A*, vol. 110 (26), pp. 8188–8203, **2006**.

[126] S. Yamada, J. Bessho, H. Nakasato, and O. Tsutsumi, “Color tuning donor–acceptor-type azobenzene dyes by controlling the molecular geometry of the donor moiety,” *Dyes and Pigments*, vol. 150, pp. 89–96, **2018**.

[127] P. Krawczyk, “DFT study of linear and nonlinear optical properties of donor-acceptor substituted stilbenes, azobenzenes and benzilideneanilines,” *Journal of Molecular Modeling*, vol. 16 (4), pp. 659–668, **2009**.

[128] A. A. Blevins and G. J. Blanchard, “Effect of Positional Substitution on the Optical Response of Symmetrically Disubstituted Azobenzene Derivatives,” *The Journal of Physical Chemistry B*, vol. 108 (16), pp. 4962–4968, **2004**.

[129] L. Antonov, K. Kamada, K. Ohta, and F. S. Kamounah, “A systematic femtosecond study on the two-photon absorbing D-π-A molecules–π-bridge nitrogen insertion and strength of the donor and acceptor groups,” *Physical Chemistry Chemical Physics*, vol. 5, pp. 1193–1197, 6 **2003**.

[130] J. García-Amorós and D. Velasco, “Recent advances towards azobenzene-based light-driven real-time information-transmitting materials,” *Beilstein journal of organic chemistry*, vol. 8 (1), pp. 1003–1017, **2012**.

[131] L. Du and Z. Lan, “An On-the-Fly Surface-Hopping Program JADE for Nonadiabatic Molecular Dynamics of Polyatomic Systems: Implementation and Applications,” *Journal of Chemical Theory and Computation*, vol. 11 (4), pp. 1360–1374, **2015**.

[132] M. J. Frisch, G. W. Trucks, H. B. Schlegel, G. E. Scuseria, M. A. Robb, J. R. Cheeseman, G. Scalmani, V. Barone, G. A. Petersson, H. Nakatsuji, X. Li, M. Caricato, A. V. Marenich, J. Bloino, B. G. Janesko, R. Gomperts, B. Mennucci, H. P. Hratchian, J. V. Ortiz, A. F. Izmaylov, J. L. Sonnenberg, D. Williams-Young, F. Ding, F. Lipparini, F. Egidi, J. Goings, B. Peng, A. Petrone, T. Henderson, D. Ranasinghe, V. G. Zakrzewski, J. Gao, N. Rega, G. Zheng, W. Liang, M. Hada, M. Ehara, K. Toyota, R. Fukuda, J. Hasegawa, M. Ishida, T. Nakajima, Y. Honda, O. Kitao, H. Nakai, T. Vreven, K. Throssell, J. A. Montgomery Jr., J. E. Peralta, F. Ogliaro, M. J. Bearpark, J. J. Heyd, E. N. Brothers, K. N. Kudin, V. N. Staroverov, T. A. Keith, R. Kobayashi, J. Normand, K. Raghavachari, A. P. Rendell, J. C. Burant, S. S. Iyengar, J. Tomasi, M. Cossi, J. M. Millam, M. Klene, C. Adamo, R. Cammi, J. W. Ochterski, R. L. Martin, K. Morokuma, O. Farkas, J. B. Foresman, and D. J. Fox, *Gaussian˜16 Revision C.01*, Gaussian Inc. Wallingford CT, **2016**.

[133] I. Fdez. Galván, M. Vacher, A. Alavi, C. Angeli, F. Aquilante, J. Autschbach, J. J. Bao, S. I. Bokarev, N. A. Bogdanov, R. K. Carlson, L. F. Chibotaru, J. Creutzberg, N. Dattani, M. G. Delcey, S. S. Dong, A. Dreuw, L. Freitag, L. M. Frutos, L. Gagliardi, F. Gendron, A. Giussani, L. González, G. Grell, M. Guo, C. E. Hoyer, M. Johansson, S. Keller, S. Knecht, G. Kovačević, E. Källman, G. Li Manni, M. Lundberg, Y. Ma, S. Mai, J. P. Malhado, P. Å. Malmqvist, P. Marquetand, S. A. Mewes, J. Norell, M. Olivucci, M. Oppel, Q. M. Phung, K. Pierloot, F. Plasser, M. Reiher, A. M. Sand, I. Schapiro, P. Sharma, C. J. Stein, L. K. Sørensen, D. G. Truhlar, M. Ugandi, L. Ungur, A. Valentini, S. Vancoillie, V. Veryazov, O. Weser, T. A. Wesołowski, P.-O. Widmark, S. Wouters, A. Zech, J. P. Zobel, and R. Lindh, "OpenMolcas: From Source Code to Insight," *Journal of Chemical Theory and Computation*, vol. 15 (11), pp. 5925–5964, **2019**.

[134] J.-Å. Andersson, R. Petterson, and L. Tegnér, "Flash photolysis experiments in the vapour phase at elevated temperatures I: Spectra of azobenzene and the kinetics of its thermal cis-trans isomerization," *Journal of Photochemistry*, vol. 20 (1), pp. 17–32, **1982**.

[135] C. Zhao, H. Horiuchi, T. Hoshi, M. Hasegawa, M. Kobayashi, and H. Hiratsuka, "Observation of the Radical Anion Intermediates in the Photolyses of 4-Cyano- and 4-Nitro-azobenzene in MTHF at 77 K," *Chemistry Letters*, vol. 32 (2), pp. 124–125, **2003**.

[136] G. Rodionova, I. Krutovskaya, Y. G. Tuchin, A. Rodionov, and V. Karpov, "Electronic spectra and structure of several azo dyes in various states of aggregation," *Journal of Applied Spectroscopy*, vol. 34 (4), pp. 434–438, **1981**.

[137] V. Cantatore, G. Granucci, and M. Persico, "Simulation of the $\pi \longrightarrow \pi*$ photodynamics of azobenzene: Decoherence and solvent effects," *Computational and Theoretical Chemistry*, vol. 1040-1041, pp. 126–135, **2014**.

# Chapter 5

# Pyrene

## 5.1 Introduction

As discussed in section 2.2, the QD simulation of molecules allows to simulate ultrafast photoinduced processes with unparalleled accuracy, gaining insight into the fundamental mechanisms and allowing to predict also quantum effects. When the problem under investigation cannot be reduced to few fundamental coordinates, the MCTDH method is by far the reference for multidimensional QD. It is extremely effective, especially if the coupled PESs have some simple functional form, like a low-order Taylor expansion in normal coordinates. Hamiltonians that use these simplified PESs are often referred to as model vibronic coupling Hamiltonians[1, 2]. They use a diabatic representation and quadratic expansions for the diagonal and off-diagonal PESs. If no other approximation is invoked, the above definition describes what is known as quadratic vibronic coupling (QVC) Hamiltonian. Further assumption that all diagonal PESs share the same normal modes and frequencies (usually taken all equal to the ones of the ground state), and that off-diagonal terms are linear functions of the coordinates, lead to the so-called linear vibronic coupling (LVC) model. LVC is the simplest Hamiltonian that can describe CIs and intersection seams. Despite the "model" attribute, these Hamiltonians can be adopted for accurate descriptions of realistic problems, especially if the investigated molecules are rigid and/or the timescale of interest is very short (~ 100 fs). In the last decade they have been employed in the study of fast intersystem crossings in metal-organic complexes[3–6], $\pi\pi^*/n\pi^*$ decays in nucleobases[7–11], to couple QD simulations with an explicit description of the environment[9, 12] and to clarify the main features of a non adiabatic dynamics around a CI[1, 2]. It became increasingly evident that the QD results can be drastically dependent on the parameters of the vibronic Hamiltonians, especially if the investigated system is characterised by several coupled quasi-degenerate states[10, 11]. These findings highlight the necessity to work out effective protocols to parametrise model Hamiltonians with electronic structure methods as accurate as possible. Recently, a method based on a maximum-overlap diabatisation to parametrise LVC Hamiltonians with time-dependent DFT (TD-DFT) calculations has been proposed[10], which is very effective also for several excited states (10-20) and molecules with many degrees of freedom (100)[13]. However, dealing with excited states of different nature including charge-transfer and double-excited states, challenges TD-DFT, and for such problems wavefunction-based multiconfigurational methods (CASSCF/CASPT2) have proven to be more robust, provided that the active space is properly selected. Therefore, a parameterisation protocol for an LVC Hamiltonian based on the CASSCF/CASPT2 protocol would open the way for the study of systems presenting an intricate electronic structure. In a collaboration with the group of Doctor Fabrizio Santoro of the ICCOM institute of the National Research Council (CNR) of Pisa, we have developed the first parameterisation protocol for an LVC Hamiltonian based on (X)MS-RASPT2/RASSCF calculations, that we have presented in reference[14]. The ideal candidate to assess our protocol is a small, rigid molecule, with a significant (but not too high) number of degrees of freedom whose PESs can be well approximated with coupled harmonic potentials, and that shows an interesting photophysics requiring RASSCF/RASPT2 for the description. The pyrene molecule, which is introduced below, perfectly satisfies such requirements.

Pyrene is the smallest peri-fused polycyclic aromatic hydrocarbon, composed of four fused benzene rings (Figure 5.1) forming a planar, highly symmetric structure ($D_{2h}$ group). Despite having 16 $\pi$ electrons, and thus not following the Hückel's $4n+2$ rule, it is aromatic[15]. Its name comes from the Greek word $\pi\upsilon\rho$ - $\pi\upsilon\rho\acute{o}\varsigma$ (fire), because it is obtained during the combustion of organic compounds and pyrolytic processes. Since its discover in 1837 in the residue of the distillation of coal tar, this small molecule has been the subject of tremendous investigation.

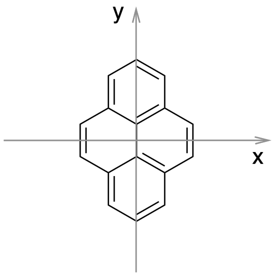

**Figure 5.1:** Pyrene structure, lying in the $xy$ plane. This orientation is considered for further state symmetry assignments.

Pyrene was initially used in the synthetic dye industry. Later, in 1955, Förster and Kasper reported the first observation of intermolecular excimers in a pyrene solution[16], whose fluorescence bands were clearly distinguishable from those of the monomer. In time, the possibility to form excimers exploiting concentration, and the unique photophysical properties like long-lived excited states, high fluorescence quantum yield[17] and sensitivity to environmental changes[18], made pyrene one of the most popular molecular probes for the study of e.g. water-soluble polymers[19], surfactant micelles[20] and structural properties of macromolecular systems like proteins and peptides[21–23], but also DNA recognition[24–26] and investigation of lipid membranes[27, 28]. In addition to the photophysical properties, the small and rigid chemical structure of pyrene and its derivatives make these compounds the most commonly studied family of guest molecules to mimic host-guest interactions in catalytic enzymes[29]. Recently, there has also been an increased interest in the use of pyrene as organic semiconductor for application in materials science and organic electron-

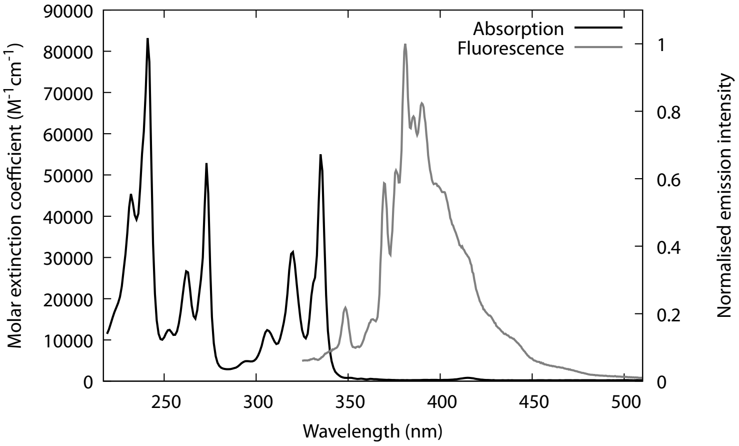

**Figure 5.2:** Pyrene absorption and fluorescence spectra in cyclohexane[31].

ics[30].

Figure 5.2 shows the UV-Vis absorption and fluorescence spectra of pyrene in cyclohexane[31]. The absorption spectrum displays an intense band peaking at 334 nm (3.7 eV), with well-resolved vibronic replicas at 319 nm (3.9 eV) and 306 nm (4.1 eV), followed by a second band peaking at 274 nm (4.5 eV) with a well visible replica at 262 nm (4.7 eV). The lower absorption band is associated to the second excited state, of $B_{2u}$ symmetry ($S_2$ or $1B_{2u}$), while the first excited state belongs to the $B_{3u}$ irreducible representation and is optically dark ($S_1$ or $1B_{3u}$). The second bright state, originating the second band, is the fifth excited state according to state-of-the-art RASPT2 calculations[14] and also belongs to the $B_{3u}$ group ($S_5$ or $2B_{3u}$). Several characteristics of pyrene require the adoption of multiconfigurational methods, like the presence of a state with a high contribution from a double excitation[14] and the difficulty of many TD-DFT functionals in reproducing the relative order of the lowest-energy states[32–34]. After excitation, the photoinduced dynamics of pyrene is characterised by ultrafast internal conversion (IC) to the lowest dark $S_1$ state. While the IC process from the first bright excited state ($S_2$) has been studied in detail both experimentally[35–38] and theoretically[39, 40] the IC process from the second excited state has been addressed only recently with transient absorption, bidimensional and photoelectron spectroscopy[38, 41, 42]. Thanks to the unprecedented time-resolution (down to 6 fs), transient spectroscopy has allowed to resolve quantum beatings due to the motion of the vibrational wavepacket in the excited state. Still, the picture of the IC mechanism from the second bright state ($S_5$) is incomplete. Picchiotti et al.[41] and Noble et al. [42] have recognised the involvement of intermediate dark states but their role in the IC is not well understood yet.

We have studied the decay dynamics of pyrene excited to either $S_2$ or $S_5$, adopting our new protocol to develop LVC Hamiltonians that fully accounts for the couplings of the lowest seven excited states and include all the 49 active nuclear coordinates. The reliability of LVC PES was assessed by recomputing energies at relevant points of the dynamics, like minima and energy-accessible CIs. Moreover, we have investigated in depth the dependence of the QD results on different parameterisations of the Hamiltonian obtained with different active spaces, and different implementations of the perturbative corrections. A parameterisation of an LVC Hamiltonian is, actually, a much more stringent test of the stability of the computational protocol than the computation of the vertical excitations and/or of the numerical gradients, and based on our results we can enunciate few recommendations for future studies.

## 5.2 The Linear Vibronic Coupling model

We consider a $n$ dimensional diabatic basis of nuclear coordinates $\{d_i\}$, and the following expression of the Hamiltonian

$$\hat{H} = \sum_i \left(\hat{K} + V_{ii}^{\text{dia}}(\mathbf{q})\right) |d_i\rangle \langle d_i| + \sum_{i,j>i} V_{ij}^{\text{dia}}(\mathbf{q})\Big( |d_i\rangle \langle d_j| + |d_j\rangle \langle d_i| \Big) \tag{5.1}$$

where $\mathbf{q}$ is the column vector of the ground state dimensionless normal coordinates. According to the LVC model the kinetic ($\hat{K}$) and potential ($\hat{V}$) terms have the following form:

$$\hat{K} = \frac{1}{2}\mathbf{p}^T\Omega\mathbf{p} \tag{5.2}$$

$$V_{ii}^{\text{dia}}(\mathbf{q}) = E_i^0 + \boldsymbol{\lambda}_{ii}^T\mathbf{q} + \frac{1}{2}\mathbf{q}^T\Omega\mathbf{q}, \tag{5.3}$$

$$V_{ij}^{\text{dia}}(\mathbf{q}) = \boldsymbol{\lambda}_{ij}^T\mathbf{q}. \tag{5.4}$$

where $\Omega$ is the diagonal matrix of the GS normal-modes frequencies, $\mathbf{p}$ is the vector of the conjugated momenta and $T$ indicates the standard transpose operation for matrices. Therefore, the diagonal terms of the potential energy $V_{ii}^{\text{dia}}(\mathbf{q})$ are described in the harmonic approximation and they share the same frequencies as the GS. The linear terms in the Hamiltonian represent the diabatic energy gradients $\boldsymbol{\lambda}_{ii}$ and the inter-state diabatic couplings $\boldsymbol{\lambda}_{ij}$ $(i \neq j)$.

The LVC Hamiltonian is parametrized by defining each diabatic state $|d_i\rangle$ to be coincident with an adiabatic reference state $|a_i\rangle$ at a reference geometry ($S_0$ minimum in our case). At displaced geometries, diabatic states are defined so to remain as similar as possible to the reference states $|\boldsymbol{a}(\mathbf{0})\rangle$. This idea was already proposed by Cimiraglia et al.[43] for CI wavefunctions, and then extended to TD-DFT[10, 44]. More precisely, we follow the derivation presented in ref.[10] and for each displaced geometry $\mathbf{0} + \Delta_\alpha$ (since now on $\Delta_\alpha$), we compute the adiabatic states $|\boldsymbol{a}(\Delta_\alpha)\rangle$ and the matrix $\mathrm{S}(\Delta_\alpha)$ of their overlaps with $|\boldsymbol{a}(\mathbf{0})\rangle$

$$S_{ij}(\Delta_\alpha) = \langle a_i(\mathbf{0})|a_j(\Delta_\alpha)\rangle \tag{5.5}$$

The transformation matrix $\mathbf{D}$ that defines the diabatic states at $\Delta_\alpha$,

$$|\mathbf{d}\rangle = |\boldsymbol{a}(\Delta_\alpha)\rangle\, \mathbf{D}(\Delta_\alpha), \tag{5.6}$$

is then obtained as

$$\mathbf{D} = \mathrm{S}^T(\mathrm{S}\mathrm{S}^T)^{-\frac{1}{2}}. \tag{5.7}$$

where for brevity the dependence on $\Delta_\alpha$ is not explicitly reported. In Eq. 5.7 a Löwdin orthogonalization is used to account for the fact that the set of the computed adiabatic states at the displaced geometries is finite and therefore not complete.

At each displaced geometry the computed adiabatic energies form a diagonal matrix $\mathbf{V}^{\mathrm{ad}}(\Delta_\alpha)$ and the diabatic potential terms are simply:

$$\mathbf{V}^{\mathrm{dia}}(\Delta_\alpha) = \mathbf{D}^T(\Delta_\alpha)\mathbf{V}^{\mathrm{ad}}(\Delta_\alpha)\mathbf{D}(\Delta_\alpha) \tag{5.8}$$

Therefore, the gradients $\lambda_{ii}$ and couplings parameters $\lambda_{ij}$ can be obtained from numerical differentiation with respect to each $q_\alpha$:

$$\lambda_{ij}(\alpha) = \frac{\partial \mathbf{V}^{\mathrm{dia}}_{ij}(\mathbf{q})}{\partial q_\alpha} \simeq \frac{\mathbf{V}^{\mathrm{dia}}_{ij}(\Delta_\alpha) - \mathbf{V}^{\mathrm{dia}}_{ij}(-\Delta_\alpha)}{2\Delta_\alpha} \tag{5.9}$$

In the following, the normal coordinates $\mathbf{q}$ and frequencies $\boldsymbol{\Omega}$ were obtained at the MP2/ANO-L-VDZP level, whereas the energies $E_i^{\mathrm{ad}}(\Delta_\alpha)$ of the adiabatic states at each displaced geometry and their overlap S with the wave functions at the reference geometry were obtained at the RASSCF/RASPT2/ANO-L-VDZP level (see below).

The vibronic wavefuction is defined in terms of the diabatic basis as

$$|\Psi(\mathbf{q},t)\rangle = \sum_i |d_i\rangle\,|\Psi_i(\mathbf{q},t)\rangle \tag{5.10}$$

and the time evolution is computed by solving the TDSE (2.1). In the following, we will investigate the time evolution of the population of the diabatic states:

$$P_i(t) = \langle\Psi_i(\mathbf{q},t)|\Psi_i(\mathbf{q},t)\rangle \tag{5.11}$$

## 5.3 Computational details

### 5.3.1 Parameterisation

Pyrene is a highly symmetric molecule ($D_{2h}$ point group) with 26 atoms and 72 normal modes. For the parameterisation of the LVC Hamiltonian, we have identified our diabatic states with the lowest seven excited adiabatic states at the $S_0$ equilibrium geometry, belonging to four different irreducible representations: two $A_g$ states, two $B_{3u}$ states, one $B_{2u}$ and three $B_{1g}$ states. Then, we have displaced the atoms along each normal coordinate (obtained at MP2/ANO-L-VDZP level) both in positive and in negative direction and calculated two main quantities: excitation energies and wavefunction overlaps $\langle S_i^{\mathrm{ref}}|S_j^{\mathrm{displ}}\rangle$ between all the eigenstates at the displaced and reference geometry (see Supplementary Material of reference[14]). These data were then used to parametrise the LVC Hamiltonian according to equations 5.7-5.9. We note that, while energy gradients are non vanishing only along symmetry conserving ($A_g$) modes, interstate couplings exist also along modes belonging to $B_{1g}$, $B_{2u}$ and $B_{3u}$ irreducible representations, which decrease the symmetry of the system as indicated in Table 5.1. The remaining 23 modes do not couple the electronic states of interest and were excluded from the model. Previous studies employing parameterisation of the LVC Hamiltonian from TD-DFT indicate that a shift $\Delta$=0.1 in dimensionless coordinates guarantees accurate and robust results[10, 45]. Since diabatic states are built so to preserve their electronic character at all geometries, in the following they will be labelled with the $D_{2h}$ symmetry labels of the corresponding adiabatic states at the $S_0$ minimum. In contrast, adiabatic states will be given the usual nomenclature $S_x$ with $x$=1,2,...,7 in order of increasing energy. It is important to remark that

**Table 5.1:** Coupling of the reference states along symmetry-breaking modes. Forbidden interactions in $\mathrm{D_{2h}}$ symmetry are possible between states falling in the same irreducible representation of the lower point groups.

| $\mathrm{D_{2h}}$ **irr. repr. of modes** | **Point group at displaced geometries** | **Classification of** $\mathrm{D_{2h}}$ **states into new irreducible repr.** | |
|---|---|---|---|
| $\mathrm{B_{3u}}$ | $\mathrm{C_{2v}}$ | $\mathrm{A_1}$: $\mathrm{1A_g}$, $\mathrm{1B_{3u}}$, $\mathrm{2A_g}$, $\mathrm{2B_{3u}}$ | $\mathrm{B_1}$: $\mathrm{1B_{2u}}$, $\mathrm{1B_{1g}}$, $\mathrm{2B_{1g}}$, $\mathrm{3B_{1g}}$ |
| $\mathrm{B_{2u}}$ | $\mathrm{C_{2v}}$ | $\mathrm{A_1}$: $\mathrm{1A_g}$, $\mathrm{1B_{2u}}$, $\mathrm{2A_g}$ | $\mathrm{B_2}$: $\mathrm{1B_{3u}}$, $\mathrm{1B_{1g}}$, $\mathrm{2B_{3u}}$, $\mathrm{2B_{1g}}$, $\mathrm{3B_{1g}}$ |
| $\mathrm{B_{1g}}$ | $\mathrm{C_{2h}}$ | $\mathrm{A_g}$: $\mathrm{1A_g}$, $\mathrm{2A_g}$, $\mathrm{1B_{1g}}$, $\mathrm{2B_{1g}}$, $\mathrm{3B_{1g}}$ | $\mathrm{B_u}$: $\mathrm{1B_{3u}}$, $\mathrm{1B_{2u}}$, $\mathrm{2B_{3u}}$ |

different diabatisation techniques are actually possible[46]: a strategy based on a one-shot computation of energy, gradients and nonadiabatic coupling vectors with multireference CIS and CISD methods has been recently presented and implemented in SHARC code[5]; "energy-based" methods, which rely only on energies and not on wavefunctions, are also very attractive, and their simplicity makes them well suited for application also in combination with accurate and time-consuming electronic-structure methods like CASSCF[47], extended multi-configuration quasi-degenerate perturbation theory[48], and equation-of-motion coupled-cluster with singles and doubles[49]. However, their implementation is very straightforward only when each mode can only couple two states[48]. The method we have applied is computationally demanding but fully general. Moreover, being based on wavefunction overlaps, it allows a direct and detailed control of the electronic character of the diabatic PESs. Electronic structure calculations with $\mathrm{D_{2h}}$ and with reduced symmetry were performed at the RASPT2/RASSCF/ANO-L-VDZP level of theory. The calculations encompass the lowest 8 roots of pyrene which, due to the use of symmetry, fall in different irreducible representations. Three active spaces were used: a minimal one consisting of the frontier 8 $\pi$ and 8 $\pi^*$ orbitals (full-$\pi$), with up to quadruple excitations i.e. RAS(4,8|0,0|4,8), as well as two extended active spaces encompassing four and eight extra-valence virtual orbitals of $\pi^*$ character with a higher angular quantum number, i.e. RAS(4,8|0,0|4,12) and RAS(4,8|0,0|4,16), respectively. The RASSCF scheme in which all molecular orbitals are put in RAS1 and RAS3 (leaving RAS2 empty) has been benchmarked previously[50] and has already shown to give accurate results for pyrene[41]. We note that the extra-valence orbitals, despite bearing some resemblance to Rydberg orbitals, are not suitable for describing Rydberg states (not present among the states below 5 eV). Their only role is to capture more dynamic correlation at the RASSCF level which has been shown to significantly improve the agreement with experimental data[51–53]. Figure 5.3 shows the active orbitals.

In all calculations, on top of the RASSCF results, we have applied a perturbative corrections of either SS-, MS- or XMS-RASPT2 type, always using an imaginary shift of 0.2 a u and setting the IPEA shift to zero. For a more compact notation, each calculation will be labelled SS($n$:$m$), MS($n$:$m$) or XMS($n$:$m$) depending on the type of perturbative correction, where $n$ and $m$ refer to the number of orbitals in RAS1 and RAS3, respectively. For calculations with $\mathrm{D_{2h}}$ symmetry (at the reference geometry and along $\mathrm{A_g}$ modes), we rely on SS(8:16) energies which are virtually identical to MS results since the states are energetically separated, with the only exception of the three close lying $\mathrm{B_{1g}}$ states, for which also MS(8:16) and XMS(8:16) energies were

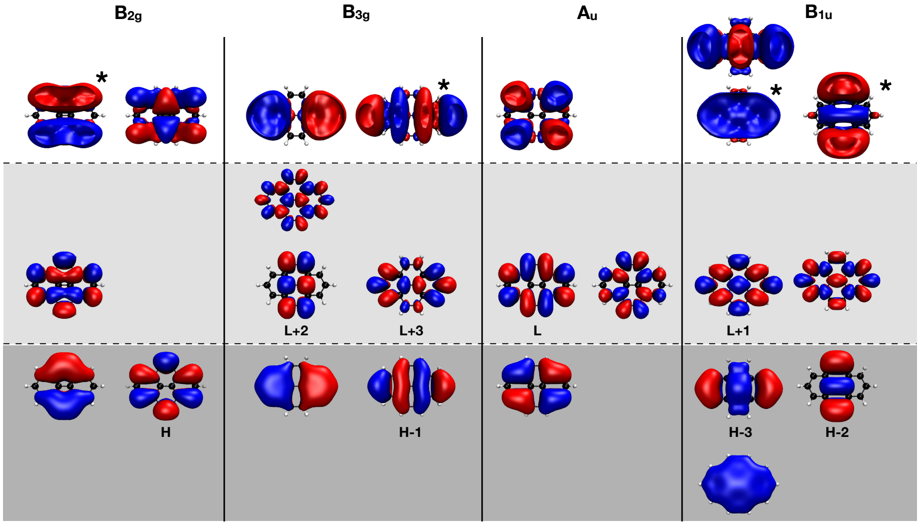

**Figure 5.3:** Active orbitals for pyrene in $D_{2h}$ symmetry, for each irreducible representation (top label). Representations $A_g$, $B_{1g}$, $B_{2u}$ and $B_{3u}$ have no active orbitals. Bottom row (dark grey): $\pi$ orbitals (RAS1), middle row (light grey) $\pi^*$ orbitals (RAS3), top row (white): virtual orbitals with higher angular momentum (RAS3). The orbitals marked with $*$ were excluded from the MS(8:12) and XMS(8:12) calculations. From reference[14].

evaluated. The SS(8:16) energies at the reference geometry were used as a uniform reference. For calculations with lower symmetry we rely on (X)MS-RASPT2 energies and wavefunctons with reduced active space (i.e. (X)MS(8:12)) due to the interaction of near-degenerate states (forbidden at $D_{2h}$ symmetry) and the increase of computational effort. To allow for consistency, the change of energy along symmetry-reducing modes, evaluated at the (X)MS(8:12) level, was added to the reference SS(8:16) energies. The only exception are $A_1$ states at geometries with $C_{2v}$ symmetry obtained by displacing along $B_{3u}$ modes, which were computed at the (X)MS(8:16) level as smaller active spaces were found to give nonphysically large interstate couplings. Overlaps were computed with the perturbatively modified wavefunctions, obtained either at the (X)MS(8:12) or (X)MS(8:16) level. Further details on the calculations of the overlaps are given the Supplementary Material of reference[14]. All the QM computations were performed with OpenMolcas[54, 55] applying Cholesky decomposition.

### 5.3.2 Quantum dynamics simulations

ML-MCTDH wavepacket propagations were performed with the Quantics package[56, 57]. The seven lowest energy excited states and the 49 (out of 72) normal coordinates with the appropriate symmetry to have non-vanishing couplings were included for all the LVC parametrised diabatic PESs. The dimension of the primitive basis set, the number of single particle functions and the structure of the ML-MCTDH trees are shown the Supplementary Material of reference[14] for each type of calculation, together with some convergence tests. A variable mean field scheme with a fifth-order Runge-Kutta integrator of $10^{-7}$ accuracy threshold was used, and the wavepackets were propagated for a total time of 2 ps. All the QD simulations were performed by the group of Doctor Fabrizio Santoro.

## 5.4 Results and discussion

### 5.4.1 Energies and gradients

The lowest seven excited states of pyrene belong to four irreducible representations of the $D_{2h}$ group (see Table 5.2). We identify two optically bright states ($1B_{2u}$ with dominant configuration H(OMO)⟶L(UMO) and $2B_{3u}$ with dominant configurations H-1⟶L + H⟶L+1) as well as several dark states. Importantly, the lowest excited state $S_1$ is optically dark and, thus, responsible for the characteristic fluorescence of pyrene of hundreds of nanoseconds[58, 59]. The presence of a doubly excited state of $A_g$ symmetry in the vicinity of the second bright state evidences the need of multiconfigurational methods.

The vertical excitation energies at the reference geometry, obtained at different levels of theory, are reported in Table 5.2. The full-$\pi$ (8:8) active space shows both quantitative and qualitative differences with respect to the stronger correlated (8:12) and (8:16) active spaces. Indeed, while the energies of states such as $2A_g$, $1B_{1g}$ and $1B_{3u}$ are already converged with respect to the active space size, the remaining states (in particular both bright states $1B_{2u}$ and $2B_{3u}$), exhibit strong dependence on the active space size, being red-shifted by 0.2-0.3 eV at the SS(8:8) level with respect to SS(8:16). As a consequence of the unbalanced description, the energy order of the states changes as a function of the active space, with profound consequences for the QD simulations. The trend in the (8:8)-(8:12)-(8:16) sequence evidences that energies are not fully converged even with the largest active space but they show an asymptotic behaviour. Accordingly, comparison with the experimental gas-phase data[60–62] shows that the computed transition energies of the bright states are underestimated. The SS(8:16) set provides closest agreement, thus implicitly supporting the predicted state order.

Concerning the type of perturbative correction, SS-RASPT2 is the best choice with $D_{2h}$ symmetry where states of the same irreducible representation are far apart in energy and do not mix. Only in the case of the $B_{1g}$ states, (X)MS-RASPT2 energies were considered due to the proximity of the electronic states. Indeed, the three methods predict energies which deviate by up to 0.16 eV. XMS-RASPT2, whose use is advocated for near-degenerate and strongly interacting electronic states[63], is found to deviate only marginally from the SS-RASPT2 results. Eventually, considering the computational cost and the small error, SS(8:16) was used to calculate the energies along symmetry-conserving normal modes.

At the $S_0$ equilibrium geometry, all the excited states show a gradient only along the totally symmetric $A_g$ modes. With the numerical gradients at hand, within the displaced harmonic oscillator approximation, we can predict the structures of the minima of the adiabatic states and the reorganisation energies $\lambda$ (see Supplementary Material of reference[14]), which are reported in Table 5.3. Interestingly, we obtain small reorganisation energies (up to ~0.3 eV), which reflect the rigidity of the pyrene molecule and justify the harmonic approximation underlying the LVC model. The predicted structures and reorganisation energies are in a very good agreement with results from explicit optimisations at the SS-RASPT2/RASSCF(4,8|0,0|4,8)/ANO-L-VDZP level[41]

**Table 5.2:** Vertical excitation energies and TDM module at the reference geometry for the first seven excited states of pyrene at different levels of theory. State labels refer to the irreducible representations of the $D_{2h}$ point group. In the third column are reported the most relevant configuration state functions (CFSs) describing each state (see Figure 5.3 for the involved orbitals). The last column reports the experimental adiabatic transition energies in gas phase[60, 61] for bright states or of two-photon absorption experiments in apolar solvent[62] for dark states. The (8:16) active space results are all reported relative to the SS(8:16) ground state value.

| State | Label | CSFs | TDM | Energy (eV) | | | | | $\Delta E_{0\text{-}0}$ (eV) |
|---|---|---|---|---|---|---|---|---|---|
| | | | (Debye) | SS(8:8) | SS(8:12) | SS(8:16) | MS(8:16) | XMS(8:16) | |
| $S_0$ | $1A_g$ | GS | - | 0.00 | 0.00 | 0.00 | - | - | - |
| $S_1$ | $1B_{3u}$ | H→L+1<br>H-1→L | 0.00 | 3.23 | 3.22 | 3.23 | - | - | 3.36[61] |
| $S_2$ | $1B_{2u}$ | H→L | 1.83 | 3.55 | 3.69 | 3.75 | - | - | 3.84[60] |
| $S_3$ | $1B_{1g}$ | H→L+2 | 0.00 | 4.11 | 4.13 | 4.16 | 4.00 | 4.10 | 4.12[62] |
| $S_4$ | $2A_g$ | $(H\rightarrow L)^2$ | 0.00 | 4.30 | 4.35 | 4.32 | - | - | 4.29[62] |
| $S_5$ | $2B_{3u}$ | H→L+1<br>H-1→L | 1.73 | 4.18 | 4.35 | 4.43 | - | - | 4.66[60] |
| $S_6$ | $2B_{1g}$ | H-2→L<br>H→L+2 | 0.00 | 4.28 | 4.46 | 4.56 | 4.64 | 4.48 | 4.54[62] |
| $S_7$ | $3B_{1g}$ | H-3→L<br>H→L+3 | 0.00 | 4.73 | 4.77 | 4.82 | 4.89 | 4.85 | 4.94[62] |

(i.e. SS(8:8), Table 5.3) [1]. Taking into consideration the reorganisation energies resolves the apparent disagreement between experiment and theory regarding the the energetic order of $2B_{3u}$ ($S_5$) and $2B_{1g}$ ($S_6$): two-photon absorption experiments put the $2B_{1g}$ state (4.54 eV) below the second bright state $2B_{3u}$ (4.66 eV) at the respective excited minimum, however, when the reorganisation energies are considered, the state order is inverted in the Franck Condon point, in agreement with our calculations.

### 5.4.2 Interstate couplings: wavefunction overlaps

Vibronic coupling between the considered diabatic states is observed both along totally symmetric $A_g$ modes, and along the symmetry-decreasing modes belonging to the $B_{3u}$, $B_{2u}$ and $B_{1g}$ irreducible representations. As noted earlier, in $D_{2h}$ symmetry electronic states of the same irreducible representation are energetically well separated, which results in a weak interaction. On the other hand, displacement along symmetry-lowering modes allows for interactions that were forbidden in $D_{2h}$ symmetry: this is particularly evident in the case of the first bright state $S_2$, which is the only $B_{2u}$ state in $D_{2h}$ symmetry and otherwise would never be depopulated. Changing the symmetry results in variable grouping of the states in irreducible representations of lower point groups. This requires a different state averaging along each of the three symmetry-decreasing sets of normal modes, which affects both the RASSCF and RASPT2 results, in particular in the case of XMS-RASPT2 which relies on an average Fock operator. Moreover, the presence of close lying states requires the use of the more expensive (X)MS-RASPT2 corrections. Because of this, the level of theory of

---

[1] In the cases were the RASPT2 minimum was not reported in the literature or had been obtained with a different state-averaging (i.e. for states $S_3$, $S_4$ and $S_6$), we have done the SS(8:8) optimisation.

**Table 5.3:** Reorganisation energies for the adiabatic excited states of pyrene obtained through SS-RASPT2/RASSCF(4,8|0,0|4,8)/ANO-L-VDZP optimisation[41] ($\lambda_{\mathrm{OPT}}$) and with the LVC model ($\lambda_{\mathrm{LVC}}$). Details about the calculation of reorganisation energies can be found in the Supplementary Material of reference[14]. The root mean square deviation (RMSD) between the two cartesian structures for each state are reported in the last column.

| State | $\lambda_{\mathrm{OPT}}$ (eV) | $\lambda_{\mathrm{LVC}}$ (eV) | RMSD |
|---|---|---|---|
| $S_1$ | 0.08 | 0.09 | 0.005 |
| $S_2$ | 0.10 | 0.10 | 0.005 |
| $S_3$ | 0.19 | 0.16 | 0.004 |
| $S_4$ | 0.26 | 0.18 | 0.012 |
| $S_5$ | 0.05 | 0.06 | 0.005 |
| $S_6$ | 0.22 | 0.24 | 0.010 |

the wavefunction overlap calculations must be accurately selected for each irreducible representation of each point group, in order to balance between computational cost and accuracy of the description.

To assess the reliability of the reduced symmetry calculations in reproducing the electronic structure (with respect to $D_{2h}$ calculations), the vertical excitation energies at the reference geometry were computed with each of the lower symmetries. Figure 5.4 shows the deviation of the adiabatic energies at the (X)MS(8:12) and (X)MS(8:16) levels from the reference $D_{2h}$-SS(8:16) values when the symmetry is reduced. The agreement with the reference values is generally good, with XMS- being more accurate than MS-RASPT2, which tends to overestimate the energy splitting and wavefunction mixing in case of strongly interacting states. Comparing the two active spaces, it is evident how the energies are sensitive to the degree of electronic correlation, with the (8:16) results being more faithful to the reference energies than the (8:12) ones, both for MS- and XMS-RASPT2. Thus, it is obvious that the best choice would be to calculate all the wavefunction overlaps necessary for the LVC parameterisation using the larger active space, however, this would be computationally very demanding. To balance between computational cost and accuracy of the description, we have computed the wavefunction overlaps at the (X)MS(8:12) level, except for critical situations (i.e. strongly interacting states) discussed in the following, for which we have used (X)MS(8:16).

For each group of symmetry-reducing modes we identified a pair of close lying states requiring particular attention in order to make sure that the various levels of theory preserve the reference state order and energy gaps: $S_4/S_5$ along $B_{3u}$ modes ($\Delta E^{D_{2h}}_{SS(8:16)} = 0.11$ eV), $S_5/S_6$ along $B_{2u}$ modes ($\Delta E^{D_{2h}}_{SS(8:16)} = 0.13$ eV) and $S_3/S_4$ along $B_{1g}$ modes ($\Delta E^{D_{2h}}_{SS(8:16)} = 0.16$ eV). Table 5.4 shows the average, maximum and minimum wavefunction overlap (absolute value) for each critical couple of states. For $S_6$-$S_5$ (along $B_{2u}$ modes) and $S_4$-$S_3$ (along $B_{1g}$ modes), the (8:12) energy splitting is always overestimated with respect to the reference one, and the wavefunction overlaps are consequently small. Even though, from the theoretical point of view, the overestimation of the energy gap is conceptually as wrong as its underestimation, from the practical point of view a larger energy gap (which results in a smaller diabatic coupling in the final Hamiltonian) is not as dramatic as a too small energy gap, since artificially large diabatic couplings can make the QD calculations much more problematic. On

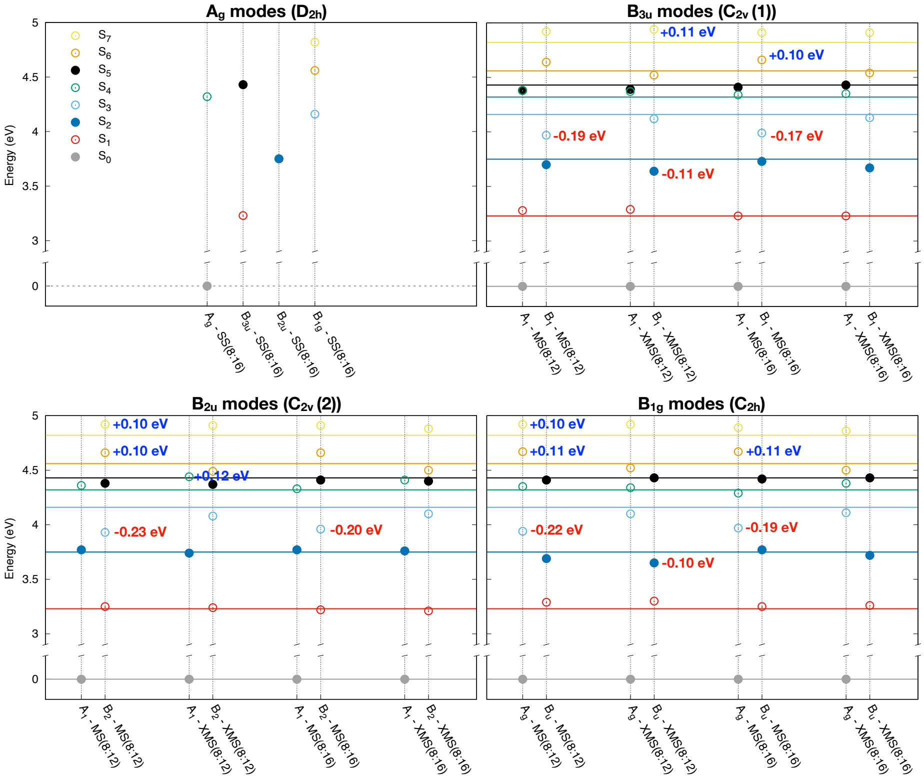

**Figure 5.4:** Vertical excitation energies at the reference geometry calculated with the reduced symmetries of the $B_{3u}$, $B_{2u}$ and $B_{1g}$ modes. In the top left panel are reported the reference $D_{2h}$-SS(8:16) energies. Full circles = $S_0$ and bright states; empty circles = dark states. Vertical dotted lines connect states of the same irreducible representation for each point group and level of theory. The horizontal full lines set the reference $D_{2h}$-SS(8:16) energies. Positive and negative deviations from reference larger than 0.10 eV in absolute value are reported in blue and red, respectively, close to the corresponding state. Edited from reference[14].

the contrary, the case of $S_4$-$S_5$ states along $B_{3u}$ modes (i.e. $A_1$ representation, see Figure 5.4) is more critical: (X)MS(8:12) reduce the energy gap until near-degeneracy of the two states, producing an unphysically high wavefunction overlap (and diabatic coupling, see Supplementary Material of reference[14] for the correlation between accuracy of the $\Delta E$ and wavefunction mixing). Table 5.4 shows that, at MS(8:12) level, they are perfectly degenerate, resulting in an average wavefunction overlap of about 0.40. On the other hand, increasing the active space, the energy gap increases, getting closer to the reference $D_{2h}$-SS(8:16) value, and the $S_5$-$S_4$ mixing is significantly reduced (0.012 at MS(8:16) and 0.006 at XMS(8:16) level).

In conclusion, the (X)MS(8:12) wavefunction overlaps represent a fair compromise between computational time and accuracy, except for the states of $A_1$ representation along $B_{3u}$ modes (which reduce the symmetry to $C_{2v}$), for which the bigger active space is needed to avoid artificially high $S_5/S_4$ overlaps. For comparison of the resulting QD, we have produced three sets of data for the LVC parameterisation: one in which all the overlaps were computed at XMS(8:12) level, and two sets in which the

**Table 5.4:** Energy gap and wavefunction overlaps along symmetry reducing modes (average, minimum and maximum absolute values) between states $S_5$-$S_4$ (top), $S_6$-$S_5$ (middle) and $S_4$-$S_3$ (bottom) calculated with different symmetry and level of theory.

| | **Modes** | **Symm.** | **Level of theory** | **ΔE (eV)** | **Deviation from ref. ΔE (eV)** | $\langle S_i^{ref} \vert S_j^{displ} \rangle$ | | |
|---|---|---|---|---|---|---|---|---|
| | | | | | | average | min | max |
| $S_5$-$S_4$ | $B_{3u}$ | $C_{2v}(1)$ | MS(8:12) | 0.00 | −0.11 | 0.395 | 0.137 | 0.613 |
| | | | MS(8:16) | 0.09 | −0.02 | 0.012 | 0.001 | 0.044 |
| | | | XMS(8:12) | 0.01 | −0.10 | 0.080 | 0.001 | 0.262 |
| | | | XMS(8:16) | 0.09 | −0.02 | 0.006 | 8e-05 | 0.020 |
| $S_6$-$S_5$ | $B_{2u}$ | $C_{2v}(2)$ | MS(8:12) | 0.27 | 0.14 | 0.025 | 3e-04 | 0.070 |
| | | | XMS(8:12) | 0.13 | 0.00 | 0.029 | 0.001 | 0.112 |
| $S_4$-$S_3$ | $B_{1g}$ | $C_{2h}$ | MS(8:12) | 0.41 | 0.25 | 0.030 | 0.005 | 0.090 |
| | | | XMS(8:12) | 0.25 | 0.09 | 0.010 | 0.001 | 0.033 |

$B_{3u}$-$A_1$ states were computed with the bigger active space (i.e. MS(8:16) or XMS(8:16)).

### 5.4.3 Accuracy of the LVC model

The three different parameterisations of the LVC Hamiltonian will be named from now on $LVC_{MS(16)}$, $LVC_{XMS(12)}$ and $LVC_{XMS(16)}$ depending on the highest level of theory employed for the computation of the wavefunction overlaps (MS(8:16), XMS(8:12) or XMS(8:16), respectively). Figure 5.5 shows the $LVC_{MS(16)}$ diabatic PESs along $A_g$ collective coordinates leading from the $S_0$ minimum to each LVC diabatic state minimum, as well as the energies of the corresponding adiabatic states (recomputed at $D_{2h}$-SS(8:16) level). The comparison shows that LVC PESs are remarkably accurate, especially for the lower energy states. Some inaccuracies arise for $3B_{1g}$ and $2B_{3u}$ along the coordinate connecting the $S_0$ and the $1B_{1g}$ minima (Figure 5.5, middle left panel). This is connected with the degeneracy, at distorted geometries, with a higher lying "intruder" state at RASSCF level, that is influencing the CASPT2 correction. We emphasise that, upon (X)MS-CASPT2 correction, the "intruder" states blue-shift above 5 eV, which evidences that their involvement at the RASSCF level is merely an artefact of the unbalanced description of the electronic states when dynamic correlation is not considered.

The performance of our LVC parameterisation was further assessed by recalculating the SS(8:16) energies of the $LVC_{MS(16)}$ diabatic states minima (see Supplementary Material of reference[14]). LVC and RASPT2 energies are extremely similar, with the largest differences for a state in its own minimum being only 0.04 eV, and also the energies of the other (out-of-minimum) states are in very good agreement.

With the LVC model it is also possible to analytically locate the lowest energy crossing of pairs of diabatic states in $D_{2h}$ symmetry. Notice that, since off-diagonal couplings among states of the same irreducible representation are possible, diabatic and adiabatic LVC states do not coincide and, therefore ,these crossings do not correspond, rigorously speaking, to CIs between adiabatic states. However, we already showed that mixings between states of the same symmetry are minimal when the $D_{2h}$ point group is applied (due to large energy separation between states falling into the same irreducible representation). Table 5.5 reports the $LVC_{MS(16)}$ and SS(8:16) energies of all states at crossings with energies lower than 4.5 eV (i.e. accessible from $S_5$, whose vertical excitation energy is 4.43 eV). For the considered crossings, the agree-

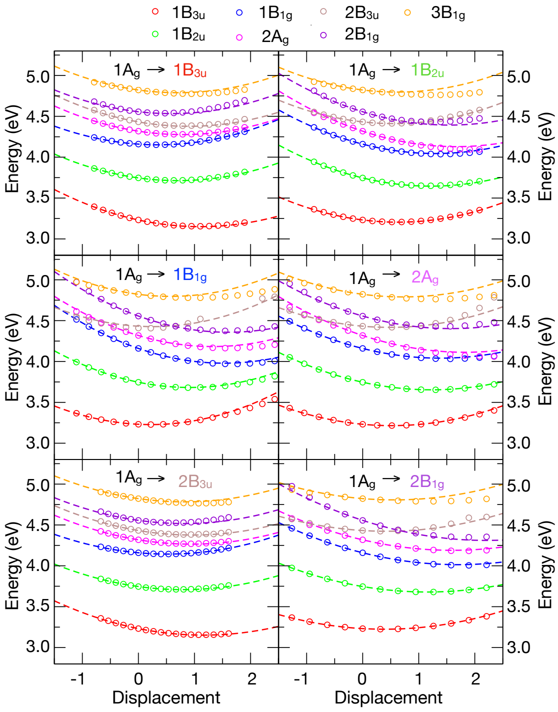

**Figure 5.5:** Scans of the $\text{LVC}_{\text{MS}(16)}$ diabatic potential energy surfaces (dashed lines) along collective $A_g$ coordinates connecting the $1A_g$ equilibrium geometry with the minima of the LVC diabatic states. The corresponding adiabatic energies recomputed at the SS(8:16) level are shown as circles. Although the SS(8:16) states are adiabatic, they are distinguished by symmetry, which explains the observed crossings and justifies the similarity, for each symmetry, between diabatic and adiabatic energies. From reference[14].

ment is remarkably good: RASPT2 confirms that these structures correspond to points of quasi-degeneracy, and in most of the cases also the LVC absolute energy is correct up to few hundredths of eV. In particular, LVC correctly predicts that the $1B_{1g}/2B_{3u}$ crossing (i.e. $S_3/S_5$) actually corresponds to a quasi-triple CI involving also the $2A_g$ state ($S_4$), and reproduces the absolute energies up to 0.02 eV. A further quasi-triple CI involving the $1B_{3u}$, $1B_{2u}$ and $1B_{1g}$ states (i.e. $S_1/S_2/S_3$, proposed previously based on orbital analysis and CI search[41]) is also confirmed. In this case, however, LVC overestimates the energy by ~0.1-0.15 eV. For diabatic crossings at higher energy (see Supplementary Material of reference[14]), LVC predictions are still rather reliable but, as expected, differences with respect to RASPT2 energies increase. Interestingly, LVC correctly predicts that at $1B_{3u}/2A_g$ crossing, four states are found in <0.17 eV (i.e. also $1B_{2u}$ and $1B_{1g}$, see Supplementary material of reference[14]) suggesting that a quasi-fourfold CI might exist in the proximity of that structure.

### 5.4.4 Dynamics simulations

Figure 5.6 shows the time evolution of the electronic populations up to 2 ps after the initial photo-excitation to either the first ($1B_{2u}$) or the second ($2B_{3u}$) bright state according to the $\text{LVC}_{\text{MS}(16)}$ and $\text{LVC}_{\text{XMS}(16)}$ parameterisations. $\text{LVC}_{\text{XMS}(12)}$ yields a

**Table 5.5:** Diabatic (LVC$_{MS(16)}$) and adiabatic (RASPT2, SS(8:16)) energies (eV) of pyrene at a number of crossing points between LVC diabatic states. Bold characters highlight states that are quasi-degenerate.

| **Crossing** | **Method** | **States** | | | | | | |
|---|---|---|---|---|---|---|---|---|
| | | $S_1$ ($1B_{3u}$) | $S_2$ ($1B_{2u}$) | $S_3$ ($1B_{1g}$) | $S_4$ ($2A_g$) | $S_5$ ($2B_{3u}$) | $S_6$ ($2B_{1g}$) | $S_7$ ($3B_{1g}$) |
| $1B_{3u}/1B_{2u}$ | LVC | **4.20** | **4.20** | 4.42 | 4.53 | 5.37 | 4.76 | 5.64 |
| | RASPT2 | **4.16** | **4.16** | 4.37 | 4.37 | 5.72 | 5.07 | 5.07 |
| $1B_{3u}/1B_{1g}$ | LVC | **4.43** | **4.46** | **4.43** | 4.81 | 5.57 | 4.84 | 5.73 |
| | RASPT2 | **4.27** | **4.29** | **4.33** | 4.60 | 5.71 | 4.81 | 5.41 |
| $1B_{2u}/1B_{1g}$ | LVC | 4.04 | **4.25** | **4.25** | 4.68 | 5.18 | 4.68 | 5.37 |
| | RASPT2 | 3.88 | **4.12** | **4.18** | 4.56 | 5.57 | 4.63 | 5.14 |
| $1B_{1g}/2B_{3u}$ | LVC | 3.20 | 3.89 | **4.45** | **4.50** | **4.45** | 4.80 | 4.91 |
| | RASPT2 | 3.21 | 3.89 | **4.47** | **4.49** | **4.46** | 4.88 | 4.96 |
| $2A_g/2B_{3u}$ | LVC | 3.17 | 3.80 | 4.27 | **4.40** | **4.40** | 4.64 | 4.83 |
| | RASPT2 | 3.17 | 3.80 | 4.27 | **4.39** | **4.40** | 4.65 | 4.82 |
| $2B_{3u}/2B_{1g}$ | LVC | 3.19 | 3.67 | 4.06 | 4.20 | **4.40** | **4.40** | 4.79 |
| | RASPT2 | 3.19 | 3.68 | 4.06 | 4.20 | **4.41** | **4.42** | 4.75 |

very different dynamics from both excited states due to wrong couplings ascribable to the smaller active space, and will not be further discussed here (see Supplementary Material of reference [14] for more details). On the other hand, LVC$_{MS(16)}$ and LVC$_{XMS(16)}$ Hamiltonians deliver similar predictions: $1B_{2u}$ ($S_2$) decays essentially on the lowest state $1B_{3u}$ ($S_1$) while, after an initial excitation to $2B_{3u}$ ($S_5$) we observe a fast (< 20 fs) rise of a transient population of some intermediate states, followed by a only slightly slower population of the first bright state $1B_{2u}$ which reaches its maximum population (~ 0.5) in 100 fs and then slowly decays toward $1B_{3u}$. The intermediate population of $1B_{2u}$ is consistent with the two-step interpretation of Borrego-Varillas et al. who reported transient signatures of $1B_{2u}$ when pumping the second bright state[38]. Moreover, the delayed decay to the lowest excited state (on a 0.5 ps time scale) observed after excitation to $2B_{3u}$ agrees with experimental time constants reported in the literature[38, 41, 42].

A closer analysis highlights some differences between the two Hamiltonians: after excitation to $2B_{3u}$($S_5$), the initial decay (~10 fs) according to LVC$_{MS(16)}$ is towards $2B_{1g}$ ($S_6$) and $2A_g$ ($S_4$), while using LVC$_{XMS(16)}$ it decays towards $2B_{1g}$ ($S_6$), $1B_{1g}$ ($S_3$) and directly to $1B_{2u}$ ($S_2$). These differences can be attributed to the corresponding coupling patterns reported in Table 5.6. Indeed, the couplings of the $2B_{3u}$ state with $1B_{1g}$ and $1B_{2u}$ are remarkably larger according to LVC$_{XMS(16)}$. On the contrary, the coupling of $2B_{3u}$ with $2A_g$ is larger according to LVC$_{MS(16)}$. The latter also predicts a much larger coupling of the higher-energy state $2B_{1g}$ with $2A_g$ which explains why, despite its energy, $2B_{1g}$ gains some transient population which reaches slightly larger values compared to LVC$_{XMS(16)}$.

After excitation to $1B_{2u}$ ($S_2$) the decay to $1B_{3u}$ ($S_1$) is faster according to LVC$_{MS(16)}$ than according to LVC$_{XMS(16)}$. Thereby, the LVC$_{MS(16)}$ dynamics agrees better with experiments, uniformly assigning a sub-100 fs time constant to the $S_2 \longrightarrow S_1$ IC. This difference is partially ascribable to the larger $1B_{2u}/1B_{3u}$ coupling in LVC$_{MS(16)}$ (norm: 0.042 eV) than in LVC$_{XMS(16)}$ (norm: 0.030 eV, see Table 5.6), but further motivations

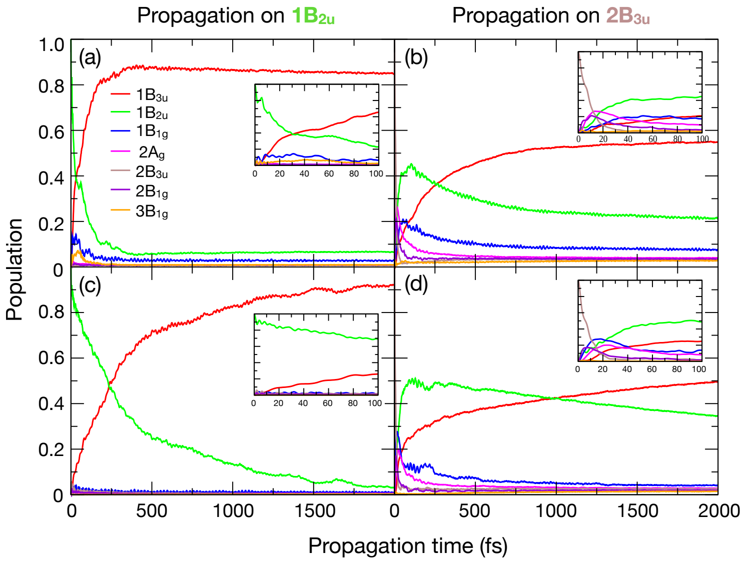

**Figure 5.6:** Dynamics of the populations of the diabatic electronic states obtained exciting the wavepacket on $1B_{2u}$(left) or $2B_{3u}$(right) states for the $LVC_{MS(16)}$ ((a), (b)) and $LVC_{XMS(16)}$ ((c), (d)) parameterisations. The insets highlight the dynamics in the first 100 fs. From reference[14].

can be found in the population distribution. The populations in Figure 5.6 suggests that, after photoexcitation to $1B_{2u}$, the dynamics is quite simple, being essentially characterised by a progressive (approximatively mono-exponential) flow of population to the lowest-energy $1B_{3u}$ dark state. This is not surprising if we consider that, at the FC point, the third state ($1B_{1g}$) is ~ 0.5 eV above $1B_{2u}$. However, Table 5.6 shows that $1B_{1g}$ is strongly coupled to both $1B_{2u}$ and $1B_{3u}$ states, with coupling values much larger than the direct $1B_{1g}/1B_{2u}$ coupling. A small transient population on $1B_{1g}$ is actually seen in Figure 5.6 for $LVC_{MS(16)}$ (which shows larger couplings than $LVC_{XMS(16)}$). In order to investigate in greater detail the impact of the $1B_{1g}$ state on the $S_2 \longrightarrow S_1$ population transfer, we have run some dynamics with reduced models (i.e. excluding some electronic states) using the $LVC_{MS(16)}$ Hamiltonian: a 2-state model "$1B_{2u}$+$1B_{3u}$", a 3-state model "$1B_{2u}$+$1B_{3u}$+$1B_{1g}$", and a 6-state model obtained including all states except $1B_{1g}$. Figure 5.7 shows the comparison of the reduced models with the full 7-states model in terms of population dynamics. Differences are striking: according to the 2-state model, the population transfer is much slower, smaller in amplitude and shows large oscillations. Including also $1B_{1g}$, the population transfer becomes much faster (even more than in the 7-states model) and irreversible, without any significant quantum beating. Despite the significant impact of the $1B_{1g}$ state, also higher-lying states play a role. This is shown considering the 6-state model in which $1B_{1g}$ is removed: here, the predicted population flow from $1B_{2u}$ to $1B_{3u}$ is similar to that of the complete 7-state model. Actually, in the long-time limit, $1B_{3u}$ reaches even a higher population, although the transfer is slower in the first 500 fs. To sum up, the existence of $1B_{1g}$ has a dramatic impact on the $1B_{2u} \longrightarrow 1B_{3u}$ transfer, much larger than what one could predict looking at the small transient population it acquires. Its main role is to provide an alternative (and very effective) coupling channel

**Table 5.6:** Norm of the diabatic coupling vectors for MS(8:16) and XMS(8:16) parameterisations. Differences between the two parameterisations having a remarkable impact on the population dynamics are highlighted.

| State | MS(8:16) | | | | | | |
|---|---|---|---|---|---|---|---|
| | $1B_{3u}$ | $1B_{2u}$ | $1B_{1g}$ | $2A_g$ | $2B_{3u}$ | $2B_{1g}$ | $3B_{1g}$ |
| $1B_{3u}$ | 0.159 | | | | | | |
| $1B_{2u}$ | **0.043** | 0.184 | | | | | |
| $1B_{1g}$ | **0.199** | **0.196** | 0.257 | | | | |
| $2A_g$ | 0.108 | 0.116 | 0.049 | 0.257 | | | |
| $2B_{3u}$ | 0.108 | **0.124** | **0.027** | **0.054** | 0.126 | | |
| $2B_{1g}$ | 0.087 | 0.096 | 0.037 | **0.235** | 0.152 | 0.266 | |
| $3B_{1g}$ | 0.175 | 0.238 | 0.042 | 0.089 | 0.077 | 0.073 | 0.143 |
| | XMS(8:16) | | | | | | |
| | $1B_{3u}$ | $1B_{2u}$ | $1B_{1g}$ | $2A_g$ | $2B_{3u}$ | $2B_{1g}$ | $3B_{1g}$ |
| $1B_{3u}$ | 0.159 | | | | | | |
| $1B_{2u}$ | **0.030** | 0.184 | | | | | |
| $1B_{1g}$ | **0.111** | **0.096** | 0.257 | | | | |
| $2A_g$ | 0.105 | 0.043 | 0.058 | 0.256 | | | |
| $2B_{3u}$ | 0.072 | **0.176** | **0.096** | **0.028** | 0.126 | | |
| $2B_{1g}$ | 0.056 | 0.126 | 0.059 | **0.109** | 0.146 | 0.267 | |
| $3B_{1g}$ | 0.105 | 0.028 | 0.089 | 0.093 | 0.046 | 0.037 | 0.142 |

between the two lowest states. On the short-time scale, the effect of $1B_{1g}$ is partially contrasted by the higher-energy states which slow down the rise of the population of $1B_{3u}$. On the long-time scale, however, according to the 7-state model $1B_{1g}$ maintains a weak population (~ 3 %). If such state is not included in the calculation, this small population flows to $1B_{3u}$ making the yield of this state even larger (6-state model). The effect of the $1B_{1g}$ and higher-energy states is expected to be similar also with the XMS(8:16) parameterisation, even though less pronounced due to the smaller couplings. Therefore, the faster $1B_{2u} \longrightarrow 1B_{3u}$ decay predicted by $LVC_{MS(16)}$ with respect to $LVC_{XMS(16)}$, is not only due to the larger direct coupling (as discussed above) but also to the larger couplings of both states with $1B_{1g}$.

Figure 5.8 plots the diabatic LVC PES at the average position of the wavepacket as a function of time according to the $LVC_{MS(16)}$ Hamiltonian (adiabatic energies as well as results for $LVC_{XMS(16)}$ are very similar and can be found in the Supplementary Material of reference[14]). $S_1$ and $S_2$ are well separated in energy at all times, and rather distant from two pairs of close-lying states, namely $S_3$-$S_4$, and $S_5$-$S_6$. Interestingly, these data indicate that the average position of the wavepacket does not encounter conical intersections. This finding, together with the smooth changes of the electronic populations, suggest the dynamics is not best described by a ballistic movement of the wavepacket toward a CI. On the contrary, we observe a gradual transfer, because vibrational states of the upper electronic states are embedded in (and coupled to) a dense manifold of vibrational states of the lower-energy electronic states. Actually, the possible occurrence of fast population transfer in QD even in cases where CIs are inaccessible has been recently discussed in literature[64]. While this mechanism could be anticipated for the excitation to $1B_{2u}$, since the initial potential energy of the wavepacket is 3.75 eV (see Table 5.2) and the lowest $1B_{1g}/1B_{2u}$ crossing is at ~4.2 eV (see Table 5.5), it is noteworthy that the same picture applies also for an initial ex-

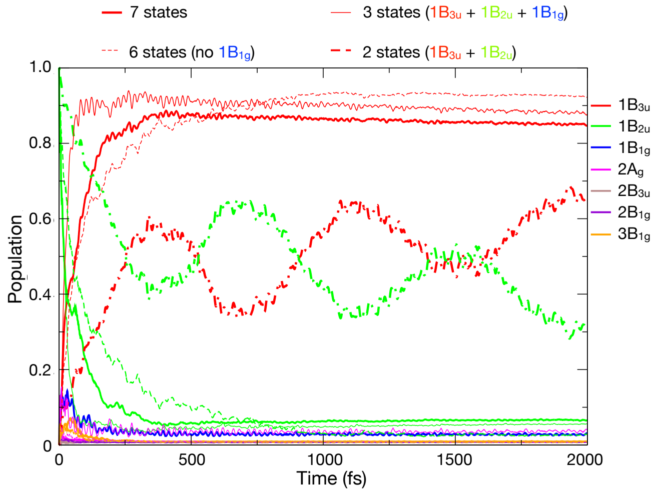

**Figure 5.7:** Dynamics of the populations of the diabatic electronic states after an excitation on $1B_{2u}$. Comparison of the results obtained with the complete 7-states model and with some of reduced-dimensionality models in which some electronic states are removed from the $LVC_{MS(16)}$ Hamiltonian. From reference[14].

citation to $2B_{3u}$, although in this case several crossings between diabatic states are accessible, including the (quasi) triple-crossings $1B_{3u}/1B_{2u}/1B_{1g}$ and $1B_{1g}/2A_g/2B_{3u}$.

Concerning the nuclear dynamics, both starting from $1B_{2u}$ and from $2B_{3u}$ (and with both Hamiltonians) the dynamics is dominated by the oscillations of four modes (Figure 5.9): two CC stretchings with frequencies 1456 $cm^{-1}$ (mode 52) and 1669 $cm^{-1}$ (mode 62) and two lower frequency modes corresponding to a breathing mode with frequency 593 $cm^{-1}$ (mode 17) and to an in-plane elongation along the long molecular axis with frequency of 406 $cm^{-1}$ (mode 8). These modes agree with Raman signatures of $1B_{2u}$ and $2B_{3u}$states[65, 66] and their involvement is consistent with the analysis of excited state vibrational coherences resolved recently in transient absorption spectra with a 6 fs time-resolution[41].

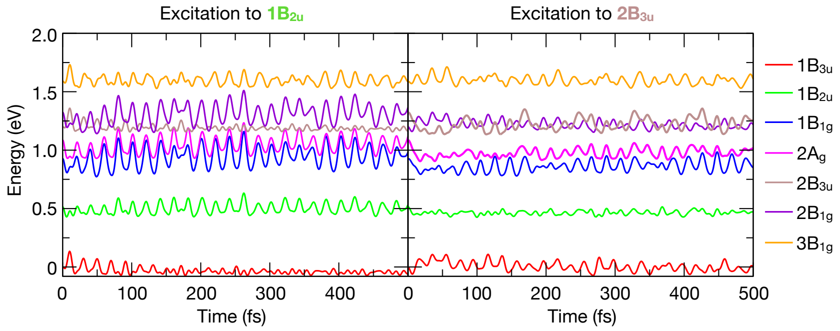

**Figure 5.8:** Diabatic LVC potential energies at the average position of the wavepacket obtained for an initial photoexcitation to $1B_{2u}$(left) or $2B_{3u}$(right) with the $LVC_{MS(16)}$ Hamiltonian. From reference[14].

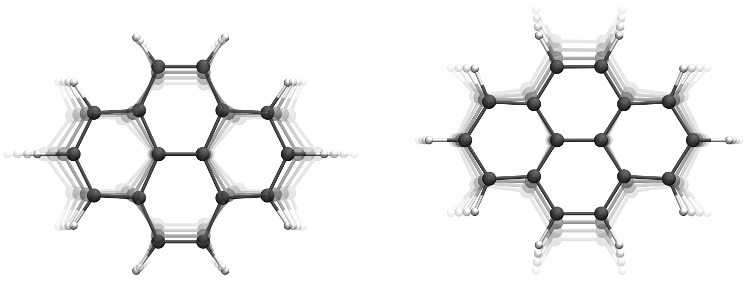

(a) mode 8 (406 cm$^{-1}$) (b) mode 17 (593 cm$^{-1}$)

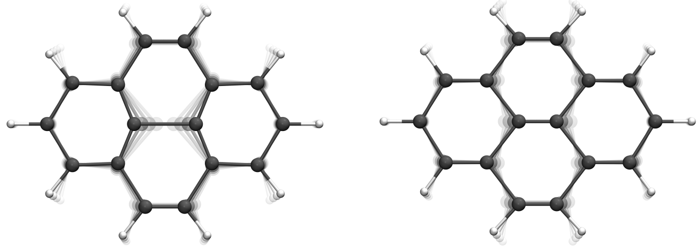

(c) mode 52 (1456 cm$^{-1}$) (d) mode 62 (1669 cm$^{-1}$)

**Figure 5.9:** Normal modes showing the widest oscillations in the QD of pyrene.

## 5.5 Simulation of transient absorption spectra

The parameterisation based on RASPT2/RASSCF makes also our LVC Hamiltonian suitable for the simulation of transient absorption spectra based on the MCTDH population dynamics. Indeed, states reached by the absorption of the probe have an increased probability to show a significant double-excited character[67], for which our electronic structure methods are best suited.

Among the possible experimental techniques for the study of ultrafast electronic dynamics, pump-probe spectroscopy is probably the simplest and most used. In a pump-probe experiment, an intense laser pulse (pump) is used to excite the sample, generating a non-equilibrium state. Then, a second (and less intense) beam called "probe" is used to monitor the evolution of the system induced by the change in electronic state after a certain time. Measuring the changes in the optical constants (e.g. absorbance/transmittance) as a function of the time delay between the arrival of pump and probe pulses yields information about the relaxation of electronic states in the sample. The probe pulse may induce a transition between the time-evolving electronic states populated by the pump and a higher lying states, in which case the signal is called an excited state absorption (ESA), or it could stimulate the population back to the ground state, in which case the signal is a stimulated emission (SE). Moreover, if the ground state absorption spectrum is in the same spectral range as the probe wavelengths, the depletion of the ground state population induced by the pump causes a transparency of the sample, resulting in a positive signal which is called ground state bleach (GSB).

For the simulation of the transient spectra upon excitation of either $S_2$ (or $S_5$), we

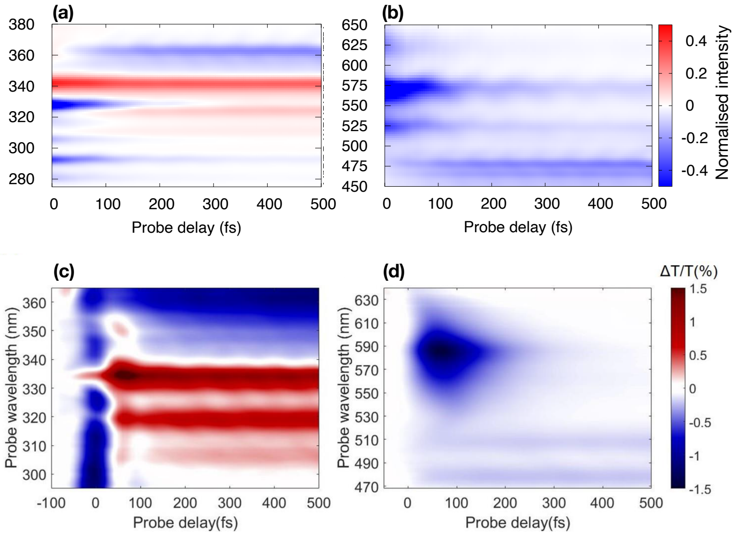

**Figure 5.10:** Experimental ((b),(c) from reference[38]) and simulated ((a),(b) using $\mathrm{LVC}_{\mathrm{MS}(16)}$ population dynamics) pyrene transient absorption maps after $S_2$ excitation (i.e. pump pulse centred at 340 nm), and probing in the UV ((a), (c)) and visible ((b), (d)) range.

have calculated all the possible transitions (energies and dipole moments) from $S_1$ and $S_2$ (or all the $S_1$-$S_6$ states) towards final states lying in the 250-650 nm probe window (5.0-1.9 eV). This choice allows to compare our results with the recent pump-probe experiments by Borrego-Varrillas et. al[38]. All calculations were performed at the same reference geometry used for the MCTDH parameterisation, at the SS(8:16) level of theory and applying the $D_{2h}$ symmetry. The produced QM data were processed via the iSPECTRON code[69], and the pump-probe spectra simulated with SPECTRON [68], with in-house modifications to allow the use of external population dynamics (i.e. ML-MCTDH populations) instead of using a predefined rate-equation model. The transient spectra obtained by focusing the pump pulse onto the $S_0 \longrightarrow S_2$ absorption were simulated including only $S_1$ and $S_2$ in the first-excitation manifold (i.e. the manifold of states that can be populated after the interaction with the pump pulse), since only these two states have a significant population in the MCTDH dynamics (see Figure 5.6, left). On the other hand, for the simulation of the transient spectrum upon $S_5$ excitation, such manifold of low-lying relevant states was extended, including all states below $S_6$ (included).

Figure 5.10 shows the simulated ((a),(b), using $\mathrm{LVC}_{\mathrm{MS}(16)}$ population dynamics) and experimental ((b),(c)) pump-probe maps obtained pumping $S_2$ and probing in two different energy windows. Focusing on the UV-probe experimental spectrum (Figure 5.10 (c)), the strong, short-lived signal around time zero in the experimental UV-probe spectrum is assigned to the solvent response and is due to two-photon-absorption of overlapping pump and probe pulses[38]. The strong positive peak at 334 nm, with well-resolved vibronic replicas at 320 and 306 nm, corresponds to GSB of the $S_0 \longrightarrow S_2$ transition. At longer wavelengths (360–370 nm), and at later times, the experimental spectrum shows a strong ESA band, assigned to a transition from the $S_1$ state. Indeed, $S_1$ is not formed instantaneously, but rather grows on the 200 fs timescale. The

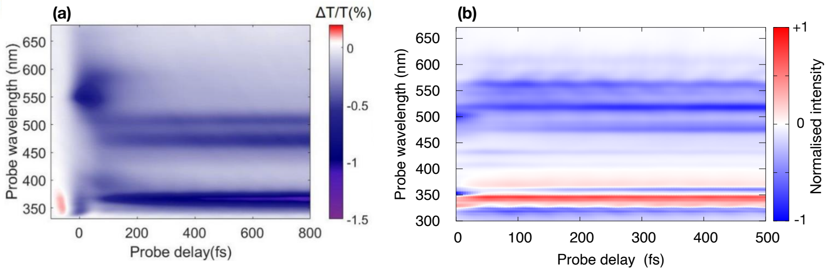

**Figure 5.11:** Experimental ((a), from reference[38]) and simulated ((b), using $\mathrm{LVC}_{\mathrm{MS}(16)}$ population dynamics) pyrene transient absorption maps after $S_5$ excitation (i.e. pump pulse centred at 270 nm), and probing in the visible range.

simulated transient absorption map in the UV range (Figure 5.10 (a)) reproduces well the experimental ground state bleaching and $S_1$ ESA signal at 360 nm. At early times, however, the $S_0 \longrightarrow S_2$ photobleach is partially covered by a negative signal peaking around 325 nm, which is not experimentally recorded. This ESA signal arises from an excitation from $S_2$ towards a higher state of $A_g$ symmetry lying 3.81 eV above $S_2$. This transition energy, considered together with the $S_0 \longrightarrow S_2$ excitation (3.75 eV), reaches the ionisation limit of pyrene which is experimentally determined at 7.42 eV[70]. This could explain the absence of this signal in the experimental spectrum: states lying close to the dissociation limit live very shortly, and the corresponding ESA signal is consequently broadened in the energy domain. Therefore, in a real experiment this signal could be broad enough for the peak to be covered by the ground state bleaching signal. In our simulation, a selective lifetime broadening for the signals above dissociation limit is missing, and the corresponding ESA can show intense and sharper peaks. Improvements of the SPECTRON/iSPECTRON codes to allow this type of broadening are currently under development.

In the visible range (Figure 5.10 (b)) the simulations predict two ESA bands: a weaker one at 525 nm and a stronger one peaking around 570 nm. The experimental map (Figure 5.10 (d)), instead, shows a single, very broad $S_2$ ESA signal (i.e. with instantaneous rise and 200 fs decay) at 580 nm, which probably includes both simulated peaks. The experimental long-lived ESA bands peaking at 515 and 470 nm, are instead assigned to transitions from $S_1$ and are present also in the simulated map, with the former being partially overlapped with the $S_2$ ESA at early times.

Figure 5.11 shows the simulated ((b), using $\mathrm{LVC}_{\mathrm{MS}(16)}$ population dynamics) and experimental (a) pump-probe maps obtained pumping $S_5$ and probing in the visible range. The early (and very short living) negative ESA signals observed in the experimental map at 350 and 550 nm are well reproduced by our simulations, although the latter is blue-shifted by ca. 50 nm (which corresponds to a 0.2 eV error). This signal can therefore be assigned to an ESA from the rapidly decaying $S_5$ state. After $S_5$ depopulation, the experimental spectrum shows the $S_2$ ESA signal at 580 nm discussed previously, together with another weaker $S_2$ signal at 400 nm, that was out of the experimental window used for the 340 nm excitation (see Figure 5.10). The simulated $S_2$ ESA live much longer, due to the slower decay predicted by our LVC model (see the population plateau in Figure 5.6, right) and are therefore difficult to distinguish from the $S_1$ signals. Taking advantage of the possibility, in simulations, to selectively

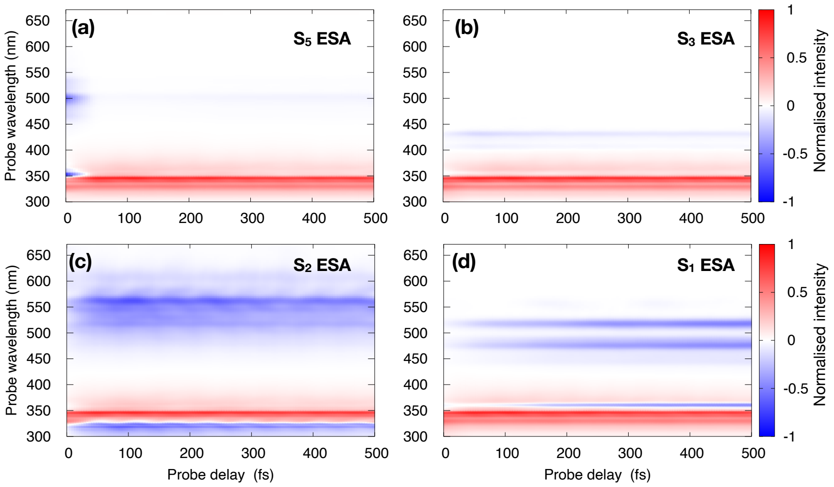

**Figure 5.12:** Simulated pyrene transient absorption maps (using $\mathrm{LVC}_{\mathrm{MS}(16)}$ population dynamics) after $S_5$ excitation with selectively-suppressed dipole moments to isolate ESA signals from $S_5$ (a), $S_3$ (b), $S_2$ (c) or $S_1$ (d).

suppress signals by setting the corresponding dipole moment to zero, we have isolated signals for each state of the first excitation manifold. The results are shown in Figure 5.12 ($S_6$ and $S_4$ do not show detectable ESA in the selected window and are not plotted). The long-living signals are then assigned to $S_1$, $S_2$ and $S_3$. The former gives rise to the characteristic peaks at 370, 470 and 515 nm, already observed when pumping $S_2$. Also for $S_2$, we found the same peaks described before, even though they live longer. Eventually, $S_3$, which gains a small but non negligible population in the MCTDH dynamics, originates a weak, long-living signal around 430 nm. This is not distinguishable in the experimental spectrum where it is probably too short-living and too weak to be detected and/or buried under the $S_1$ stronger signals.

## 5.6 Conclusions

We have successfully developed a protocol that combines highly accurate, multiconfigurational electronic structure methods such as RASPT2/RASSCF, with a maximum-overlap diabatisation technique to parameterise a LVC Hamiltonian for QD. We have identified the ideal candidate to assess our protocol with the pyrene molecule, whose rigidity justifies the LVC approximation for the PESs and which shows an interesting photophysics after excitation to either the first or the second bright states. To the best of our knowledge, this is the first reported example of LVC parameterisation based on energies and wavefunctions overlaps computed with RASPT2/RASSCF electronic structure calculations. While, in principle, the RASTP2/RASSCF protocol is able to describe states with different nature on an equal footing, the electronic structure can show a significant dependence on the QM parameters (e.g. active space size, state averaging, use of symmetry, type of perturbative correction), especially in the presence of a manifold of close-lying interacting excited states. Therefore, benchmarking is essential for assuring the convergence of the excited state energies with respect to the active space size[71], and our protocol is not a "black-box" procedure. An accurate description of the wavefunctions is particularly important to obtain reliable diabatic couplings, which require (X)MS-RASPT2 corrections and an active space wide enough in case of state-mixing at lower level. This is best testified by the results of the $\mathrm{LVC}_{\mathrm{XMS}(12)}$ Hamiltonian, that leads to erroneous results due to a bad description of the close-lying $S_5$/$S_4$ states. Benchmarking against RASPT2 calculations has proven that the LVC Hamiltonian can be highly accurate, and our $\mathrm{LVC}_{\mathrm{MS}(16)}$ and $\mathrm{LVC}_{\mathrm{XMS}(16)}$ models are also able to predict the structure and energy of both excited state minima and crossings between the states included in the model.

The QD simulations are in good agreements with the experiments[36, 38], especially for the deactivation of $S_2$, for which we obtained a perfect agreement with the reported time constant of 85 fs[38] for the flow of population to the long-living $S_1$. Despite the apparent simplicity of the case, we were able to reveal the important role of the $S_3$ state which, even if it lyes higher in energy, is strongly coupled to both $S_2$ and $S_1$, and effectively acts as a fast population bridge between them. This finding highlights that, in order to obtain robust QD results, it is necessary to adopt LVC models including a sufficiently large number of diabatic states. Direct excitation of the second bright state $2B_{3u}$ ($S_5$) leads to a more complicated mechanism, involving a smooth flow of population to a number of intermediate states which progressively decay to $S_1$. The ultrafast but smooth decay of the upper states is better explained by coupling between vibrational levels, rather than ballistic motion towards a CI. In the light of this finding the question arises whether semi-classical trajectory-based approaches, which treat nuclei classically, are capable of capturing the ultrafast nature of the internal conversion.

The results of our MCTDH dynamics were also used to simulate transient absorption signals originated from the excited states populated during the dynamics. The obtained spectra show a qualitative match with the experimental transient absorption maps[38], except for a high-energy $S_2$ ESA signal which is not experimentally detected and for which a specific lifetime broadening is probably needed to reduce the peak intensity. Also the transient spectra obtained pumping $S_5$ show a remarkable accuracy of the ESA signals position, even though the $S_2$ simulated signals are too long living. Improvements to the spectroscopic simulations based on MCTDH dynamics are currently in progress.

Finally, it is noteworthy that the protocol for the parameterisation of LVC Hamiltonians from RASPT2/RASSCF is fully general and ready to be applied to other interesting problems, like the ultrafast internal conversion in photoexcited nucleobases[10]. Furthermore, the protocol is straight-forwardly extendable to incorporate spin-orbit couplings to describe inter-system crossing[72].

## References

[1] H. Köppel, W. Domcke, and L. S. Cederbaum, "Multi-mode Molecular Dynamics Beyond the Born-Oppenheimer Approximation," *Advances in Chemical Physics*, vol. 57, p. 59, **1984**.

[2] H. Köppel, "Diabatic Representation: Methods for the Construction of Diabatic Electronic State," in *Conical Intersections, Electronic Structure, Dynamics and*

*Spectroscopy*, W. Domcke, R. Yarkony, and H. Köppel, Eds., World Scientific Publishing Co. Singapore, **2004**, pp. 175–204.

[3] T. J. Penfold, E. Gindensperger, C. Daniel, and C. M. Marian, "Spin-Vibronic Mechanism for Intersystem Crossing," *Chemical Reviews*, vol. 118 (15), pp. 6975–7025, **2018**.

[4] M. Fumanal, E. Gindensperger, and C. Daniel, "Ultrafast Intersystem Crossing vs Internal Conversion in $\alpha$-Diimine Transition Metal Complexes: Quantum Evidence," *The Journal of Physical Chemistry Letters*, vol. 9 (17), pp. 5189–5195, **2018**.

[5] F. Plasser, S. Gómez, M. F. S. J. Menger, S. Mai, and L. González, "Highly efficient surface hopping dynamics using a linear vibronic coupling model," *Physical Chemistry Chemical Physics*, vol. 21, pp. 57–69, 1 **2019**.

[6] S. Mai and L. González, "Identification of important normal modes in nonadiabatic dynamics simulations by coherence, correlation, and frequency analyses," *The Journal of Chemical Physics*, vol. 151 (24), p. 244 115, **2019**.

[7] D. Picconi, A. Lami, and F. Santoro, "Hierarchical transformation of Hamiltonians with linear and quadratic couplings for nonadiabatic quantum dynamics: Application to the $\pi\pi^*/n\pi^*$ internal conversion in thymine," *The Journal of Chemical Physics*, vol. 136, p. 244 104, **2012**.

[8] D. Picconi, F. J. Avila Ferrer, R. Improta, A. Lami, and F. Santoro, "Quantum-classical effective-modes dynamics of the $\pi\pi^* \longrightarrow \mathrm{n}\pi^*$ decay in 9H-adenine. A quadratic vibronic coupling model," *Faraday Discussions*, vol. 163, pp. 223–242, **2013**.

[9] J. Cerezo, Y. Liu, N. Lin, X. Zhao, R. Improta, and F. Santoro, "Mixed Quantum/Classical Method for Nonadiabatic Quantum Dynamics in Explicit Solvent Models: The $\pi\pi^*/\mathrm{n}\pi^*$ Decay of Thymine in Water as a Test Case," *Journal of Chemical Theory and Computation*, vol. 14, pp. 820–832, **2018**.

[10] M. Yaghoubi Jouybari, Y. Liu, R. Improta, and F. Santoro, "The Ultrafast Dynamics of the Two Lowest Bright Excited States of Cytosine and 1-Methyl-Cytosine: A Quantum Dynamical Study," *Journal of Chemical Theory and Computation*, vol. 16 (9), pp. 5792–5808, **2020**.

[11] M. Yaghoubi Jouybari, Y. Liu, R. Improta, and F. Santoro, "Quantum dynamics of the $\pi\pi^*/\mathrm{n}\pi^*$ decay of the epigenetic nucleobase 1,5-dimethyl-cytosine in the gas phase," *Physical Chemistry Chemical Physics*, vol. 22, pp. 26 525–26 535, 45 **2020**.

[12] M. Pápai, M. Abedi, G. Levi, E. Biasin, M. M. Nielsen, and K. B. Møller, "Theoretical Evidence of Solvent-Mediated Excited-State Dynamics in a Functionalized Iron Sensitizer," *The Journal of Physical Chemistry C*, vol. 123 (4), pp. 2056–2065, **2019**.

[13] D. Aranda and F. Santoro, "Vibronic Spectra of π-Conjugated Systems with a Multitude of Coupled States: A Protocol Based on Linear Vibronic Coupling Models and Quantum Dynamics Tested on Hexahelicene," *Journal of Chemical Theory and Computation*, vol. 17 (3), pp. 1691–1700, **2021**.

[14] F. Aleotti, D. Aranda, M. Yaghoubi Jouybari, M. Garavelli, A. Nenov, and F. Santoro, “Parameterization of a linear vibronic coupling model with multiconfigurational electronic structure methods to study the quantum dynamics of photoexcited pyrene,” *The Journal of Chemical Physics*, vol. 154 (10), p. 104 106, **2021**.

[15] M. Randić, “Aromaticity of Polycyclic Conjugated Hydrocarbons,” *Chemical Reviews*, vol. 103 (9), pp. 3449–3606, **2003**.

[16] T. Forster and K. Kasper, “Concentration reversal of the fluorescence of pyrene,” *Z. Elektrochem. Angew. Phys. Chem*, vol. 59, pp. 976–980, **1955**.

[17] J. B. Birks, *Photophysics of Aromatic Molecules*, J. B. Birks, Ed. Wiley, **1970**.

[18] K. Kalyanasundaram and J. K. Thomas, “Environmental effects on vibronic band intensities in pyrene monomer fluorescence and their application in studies of micellar systems,” *Journal of the American Chemical Society*, vol. 99 (7), pp. 2039–2044, **1977**.

[19] F. M. Winnik, “Photophysics of preassociated pyrenes in aqueous polymer solutions and in other organized media,” *Chemical reviews*, vol. 93 (2), pp. 587–614, **1993**.

[20] J. Aguiar, P. Carpena, J. A. Molina-Bolívar, and C. Carnero-Ruiz, “On the determination of the critical micelle concentration by the pyrene 1:3 ratio method,” *Journal of Colloid and Interface Science*, vol. 258 (1), pp. 116–122, **2003**.

[21] M. Goedeweeck, M. Van der Auweraer, and F. C. De Schryver, “Molecular dynamics of a peptide chain, studied by intramolecular excimer formation,” *Journal of the American Chemical Society*, vol. 107 (8), pp. 2334–2341, **1985**.

[22] P. Hammarström, B. Kalman, B.-H. Jonsson, and U. Carlsson, “Pyrene excimer fluorescence as a proximity probe for investigation of residual structure in the unfolded state of human carbonic anhydrase II,” *FEBS Letters*, vol. 420 (1), pp. 63–68, **1997**.

[23] D. Sahoo, V. Narayanaswami, C. M. Kay, and R. O. Ryan, “Pyrene Excimer Fluorescence: A Spatially Sensitive Probe To Monitor Lipid-Induced Helical Rearrangement of Apolipophorin III,” *Biochemistry*, vol. 39 (22), pp. 6594–6601, **2000**.

[24] P. L. Paris, J. M. Langenhan, and E. T. Kool, “Probing DNA sequences in solution with a monomer-excimer fluorescence color change,” *Nucleic Acids Research*, vol. 26 (16), pp. 3789–3793, **1998**.

[25] F. D. Lewis, Y. Zhang, and R. L. Letsinger, “Bispyrenyl Excimer Fluorescence: A Sensitive Oligonucleotide Probe,” *Journal of the American Chemical Society*, vol. 119 (23), pp. 5451–5452, **1997**.

[26] K. Yamana, T. Iwai, Y. Ohtani, S. Sato, M. Nakamura, and H. Nakano, “Bis-Pyrene-Labeled Oligonucleotides: Sequence Specificity of Excimer and Monomer Fluorescence Changes upon Hybridization with DNA,” *Bioconjugate Chemistry*, vol. 13 (6), pp. 1266–1273, **2002**.

[27] M. Ollmann, G. Schwarzmann, K. Sandhoff, and H. J. Galla, "Pyrene-labeled gangliosides: Micelle formation in aqueous solution, lateral diffusion, and thermotropic behavior in phosphatidylcholine bilayers," *Biochemistry*, vol. 26 (18), pp. 5943–5952, **1987**.

[28] P. Somerharju, "Pyrene-labeled lipids as tools in membrane biophysics and cell biology," *Chemistry and Physics of Lipids*, vol. 116 (1), pp. 57–74, **2002**.

[29] N. P. E. Barry and B. Therrien, "Chapter 13 - Pyrene: The Guest of Honor," in *Organic Nanoreactors*, S. Sadjadi, Ed., Boston: Academic Press, **2016**, pp. 421–461.

[30] T. M. Figueira-Duarte and K. Müllen, "Pyrene-Based Materials for Organic Electronics," *Chemical Reviews*, vol. 111 (11), pp. 7260–7314, **2011**.

[31] I. Berlman, *Handbook of florescence spectra of Aromatic Molecules*, Second Edition. Elsevirer, **1971**.

[32] E. L. Graef and J. B. L. Martins, "Analysis of lowest energy transitions at TD-DFT of pyrene in vacuum and solvent," *Journal of Molecular Modeling*, vol. 25 (7), **2019**.

[33] B. Shi, D. Nachtigallová, A. J. A. Aquino, F. B. C. Machado, and H. Lischka, "High-level theoretical benchmark investigations of the UV-vis absorption spectra of paradigmatic polycyclic aromatic hydrocarbons as models for graphene quantum dots," *The Journal of Chemical Physics*, vol. 150 (12), p. 124 302, **2019**.

[34] F. J. Avila Ferrer, V. Barone, C. Cappelli, and F. Santoro, "Duschinsky, Herzberg–Teller, and Multiple Electronic Resonance Interferential Effects in Resonance Raman Spectra and Excitation Profiles. The Case of Pyrene," *Journal of Chemical Theory and Computation*, vol. 9 (8), pp. 3597–3611, **2013**.

[35] P. Foggi, L. Pettini, I. Santa, R. Righini, and S. Califano, "Transient absorption and vibrational relaxation dynamics of the lowest excited singlet state of pyrene in solution," *The Journal of Physical Chemistry*, vol. 99 (19), pp. 7439–7445, **1995**.

[36] F. V. R. Neuwahl and P. Foggi, "Direct Observation of S2–S1 Internal Conversion in Pyrene by Femtosecond Transient Absorption," *Laser Chemistry*, vol. 19 (1-4), pp. 375–379, **1999**.

[37] M. Raytchev, E. Pandurski, I. Buchvarov, C. Modrakowski, and T. Fiebig, "Bichromophoric Interactions and Time-Dependent Excited State Mixing in Pyrene Derivatives. A Femtosecond Broad-Band Pump-Probe Study," *The Journal of Physical Chemistry A*, vol. 107 (23), pp. 4592–4600, **2003**.

[38] R. Borrego-Varillas, L. Ganzer, G. Cerullo, and C. Manzoni, "Ultraviolet Transient Absorption Spectrometer with Sub-20-fs Time Resolution," *Applied Sciences*, vol. 8 (6), p. 989, **2018**.

[39] A. Nenov, A. Giussani, B. P. Fingerhut, I. Rivalta, E. Dumont, S. Mukamel, and M. Garavelli, "Spectral lineshapes in nonlinear electronic spectroscopy," *Physical Chemistry Chemical Physics*, vol. 17 (46), pp. 30 925–30 936, **2015**.

[40] M. K. Roos, S. Reiter, and R. de Vivie-Riedle, "Ultrafast relaxation from 1La to 1Lb in pyrene: A theoretical study," *Chemical Physics*, vol. 515, pp. 586–595, **2018**.

[41] A. Picchiotti, A. Nenov, A. Giussani, V. I. Prokhorenko, R. J. D. Miller, S. Mukamel, and M. Garavelli, "Pyrene, a Test Case for Deep-Ultraviolet Molecular Photophysics," *The Journal of Physical Chemistry Letters*, vol. 10 (12), pp. 3481–3487, **2019**.

[42] J. A. Noble, C. Aupetit, D. Descamps, S. Petit, A. Simon, J. Mascetti, N. B. Amor, and V. Blanchet, "Ultrafast electronic relaxations from the S3 state of pyrene," *Physical Chemistry Chemical Physics*, vol. 21 (26), pp. 14 111–14 125, **2019**.

[43] R. Cimiraglia, J. P. Malrieu, M. Persico, and F. Spiegelmann, "Quasi-diabatic states and dynamical couplings from ab initio CI calculations: a new proposal," *Journal of Physics B: Atomic and Molecular Physics*, vol. 18 (15), p. 3073, **1985**.

[44] J. Neugebauer, E. J. Baerends, and M. Nooijen, "Vibronic coupling and double excitations in linear response time-dependent density functional calculations: Dipole-allowed states of $N_2$," *The Journal of Chemical Physics*, vol. 121 (13), pp. 6155–6166, **2004**.

[45] Y. Liu, L. Martínez Fernández, J. Cerezo, G. Prampolini, R. Improta, and F. Santoro, "Multistate coupled quantum dynamics of photoexcited cytosine in gas-phase: Nonadiabatic absorption spectrum and ultrafast internal conversions.," *Chemical Physics*, vol. 515, pp. 452–463, **2018**.

[46] H. Köppel, W. Domcke, and L. Cederbaum, "The Multi-mode vibronic-coupling approach," in *Conical Intersections, Electronic Structure, Dynamics and Spectroscopy*, W. Domcke, R. Yarkony, and H. Köppel, Eds., World Scientific Publishing Co. Singapore, **2004**, pp. 323–368.

[47] B. Gonon, B. Lasorne, G. Karras, L. Joubert-Doriol, D. Lauvergnat, F. Billard, B. Lavorel, O. Faucher, S. Guérin, E. Hertz, and F. Gatti, "A generalized vibronic-coupling Hamiltonian for molecules without symmetry: Application to the photoisomerization of benzopyran," *The Journal of Chemical Physics*, vol. 150 (12), p. 124 109, **2019**.

[48] M. Sala, B. Lasorne, F. Gatti, and S. Guérin, "The role of the low-lying dark n$\pi$* states in the photophysics of pyrazine: A quantum dynamics study," *Physical Chemistry Chemical Physics*, vol. 16, pp. 15 957–15 967, 30 **2014**.

[49] A. Lehr, S. Gómez, M. A. Parkes, and G. A. Worth, "The role of vibronic coupling in the electronic spectroscopy of maleimide: A multi-mode and multi-state quantum dynamics study," *Physical Chemistry Chemical Physics*, vol. 22, pp. 25 272–25 283, 43 **2020**.

[50] V. Sauri, L. Serrano-Andrés, A. R. M. Shahi, L. Gagliardi, S. Vancoillie, and K. Pierloot, "Multiconfigurational Second-Order Perturbation Theory Restricted Active Space (RASPT2) Method for Electronic Excited States: A Benchmark Study," *Journal of Chemical Theory and Computation*, vol. 7 (1), pp. 153–168, **2010**.

[51] A. Nenov, S. Mukamel, M. Garavelli, and I. Rivalta, "Two-Dimensional Electronic Spectroscopy of Benzene, Phenol, and Their Dimer: An Efficient First-Principles Simulation Protocol," *Journal of Chemical Theory and Computation*, vol. 11 (8), pp. 3755–3771, **2015**.

[52] A. Nenov, A. Giussani, J. Segarra-Martí, V. K. Jaiswal, I. Rivalta, G. Cerullo, S. Mukamel, and M. Garavelli, "Modeling the high-energy electronic state manifold of adenine: Calibration for nonlinear electronic spectroscopy," *The Journal of Chemical Physics*, vol. 142 (21), p. 212 443, **2015**.

[53] A. Nenov, I. Rivalta, S. Mukamel, and M. Garavelli, "Bidimensional electronic spectroscopy on indole in gas phase and in water from first principles," *Computational and Theoretical Chemistry*, vol. 1040-1041, pp. 295–303, **2014**.

[54] I. Fdez. Galván, M. Vacher, A. Alavi, C. Angeli, F. Aquilante, J. Autschbach, J. J. Bao, S. I. Bokarev, N. A. Bogdanov, R. K. Carlson, L. F. Chibotaru, J. Creutzberg, N. Dattani, M. G. Delcey, S. S. Dong, A. Dreuw, L. Freitag, L. M. Frutos, L. Gagliardi, F. Gendron, A. Giussani, L. González, G. Grell, M. Guo, C. E. Hoyer, M. Johansson, S. Keller, S. Knecht, G. Kovačević, E. Källman, G. Li Manni, M. Lundberg, Y. Ma, S. Mai, J. P. Malhado, P. Å. Malmqvist, P. Marquetand, S. A. Mewes, J. Norell, M. Olivucci, M. Oppel, Q. M. Phung, K. Pierloot, F. Plasser, M. Reiher, A. M. Sand, I. Schapiro, P. Sharma, C. J. Stein, L. K. Sørensen, D. G. Truhlar, M. Ugandi, L. Ungur, A. Valentini, S. Vancoillie, V. Veryazov, O. Weser, T. A. Wesołowski, P.-O. Widmark, S. Wouters, A. Zech, J. P. Zobel, and R. Lindh, "OpenMolcas: From Source Code to Insight," vol. 15 (11), pp. 5925–5964, **2019**.

[55] F. Aquilante, J. Autschbach, A. Baiardi, S. Battaglia, V. A. Borin, L. F. Chibotaru, I. Conti, L. D. Vico, M. Delcey, I. F. Galván, N. Ferré, L. Freitag, M. Garavelli, X. Gong, S. Knecht, E. D. Larsson, R. Lindh, M. Lundberg, P. Å. Malmqvist, A. Nenov, J. Norell, M. Odelius, M. Olivucci, T. B. Pedersen, L. Pedraza-González, Q. M. Phung, K. Pierloot, M. Reiher, I. Schapiro, J. Segarra-Martí, F. Segatta, L. Seijo, S. Sen, D.-C. Sergentu, C. J. Stein, L. Ungur, M. Vacher, A. Valentini, and V. Veryazov, "Modern quantum chemistry with [Open]Molcas," *The Journal of Chemical Physics*, vol. 152 (21), p. 214 117, **2020**.

[56] G. A. Worth, K. Giri, G. W. Richings, M. H. Beck, A. Jäckle, and H.-D. Meyer, *The QUANTICS Package, Version 1.1, (2015), University of Birmingham, Birmingham, U.K.*

[57] G. A. Worth, "Quantics: A general purpose package for Quantum molecular dynamics simulations," *Computer Physics Communications*, vol. 248, p. 107 040, **2020**.

[58] D. S. Karpovich and G. J. Blanchard, "Relating the polarity-dependent fluorescence response of pyrene to vibronic coupling. Achieving a fundamental understanding of the py polarity scale," *The Journal of Physical Chemistry*, vol. 99 (12), pp. 3951–3958, **1995**.

[59] A. Y. Freidzon, R. R. Valiev, and A. A. Berezhnoy, "Ab initio simulation of pyrene spectra in water matrices," *RSC Advances*, vol. 4 (79), pp. 42 054–42 065, **2014**.

[60] J. Ferguson, L. W. Reeves, and W. G. Schneider, "Vapor absorption spectra of naphthalene, anthracene and pyrene," *Canadian Journal of Chemistry*, vol. 35 (10), pp. 1117–1136, **1957**.

[61] H. Baba and M. Aoi, "Vapor-phase fluorescence spectra from the second excited singlet state of pyrene and its derivatives," *Journal of Molecular Spectroscopy*, vol. 46 (2), pp. 214–222, **1973**.

[62] P. R. Salvi, P. Foggi, and E. Castellucci, "The two-photon excitation spectrum of pyrene," *Chemical Physics Letters*, vol. 98 (3), pp. 206–211, **1983**.

[63] S. Sen and I. Schapiro, "A comprehensive benchmark of the XMS-CASPT2 method for the photochemistry of a retinal chromophore model," *Molecular Physics*, vol. 116 (19-20), pp. 2571–2582, **2018**.

[64] C. A. Farfan and D. B. Turner, "Nonadiabatic Photochemistry Induced by Inaccessible Conical Intersections," *The Journal of Physical Chemistry A*, vol. 123 (36), pp. 7768–7776, **2019**.

[65] C. M. Jones and S. A. Asher, "Ultraviolet resonance Raman study of the pyrene S4, S3, and S2 excited electronic states," *The Journal of Chemical Physics*, vol. 89 (5), pp. 2649–2661, **1988**.

[66] H. Shinohara, Y. Yamakita, and K. Ohno, "Raman spectra of polycyclic aromatic hydrocarbons. Comparison of calculated Raman intensity distributions with observed spectra for naphthalene, anthracene, pyrene, and perylene," *Journal of Molecular Structure*, vol. 442 (1-3), pp. 221–234, **1998**.

[67] J. Segarra-Martí, S. Mukamel, M. Garavelli, A. Nenov, and I. Rivalta, "Towards Accurate Simulation of Two-Dimensional Electronic Spectroscopy," in *Topics in Current Chemistry Collections*, Springer International Publishing, **2018**, pp. 63–112.

[68] W. Zhuang, D. Abramavicius, T. Hayashi, and S. Mukamel, "Simulation Protocols for Coherent Femtosecond Vibrational Spectra of Peptides," *The Journal of Physical Chemistry B*, vol. 110 (7), pp. 3362–3374, **2006**.

[69] F. Segatta, A. Nenov, D. R. Nascimento, N. Govind, S. Mukamel, and M. Garavelli, "iSPECTRON : A simulation interface for linear and nonlinear spectra with ab-initio quantum chemistry software," *Journal of Computational Chemistry*, vol. 42 (9), pp. 644–659, **2021**.

[70] J. W. Hager and S. C. Wallace, "Two-laser photoionization supersonic jet mass spectrometry of aromatic molecules," *Analytical Chemistry*, vol. 60 (1), pp. 5–10, **1988**.

[71] S. Shirai and S. Inagaki, "Ab initio study on the excited states of pyrene and its derivatives using multi-reference perturbation theory methods," *RSC Advances*, vol. 10 (22), pp. 12 988–12 998, **2020**.

[72] J. Eng, C. Gourlaouen, E. Gindensperger, and C. Daniel, "Spin-Vibronic Quantum Dynamics for Ultrafast Excited-State Processes," *Accounts of Chemical Research*, vol. 48 (3), pp. 809–817, **2015**.

# Chapter 6

# Rhodopsin

## 6.1 Introduction

Rhodopsin (also known as visual purple) is a light-sensitive receptor protein involved in visual phototransduction. It is a biological pigment found in the rods of the retina and belongs to the family of light-activatable G-protein-coupled receptors (GPCRs), also called opsins. Rhodopsin is extremely sensitive to light, and thus enables vision in low-light conditions. When rhodopsin is exposed to light, it immediately photobleaches. In humans, it is regenerated fully in about 30 minutes, after which rods are more sensitive. Thousands of rhodopsin molecules are found in each outer segment disc of the host rod cell.

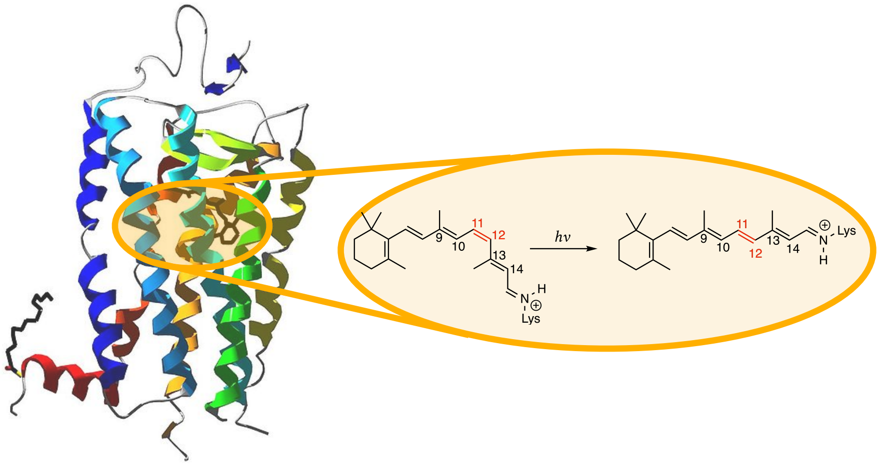

**Figure 6.1:** Structures of the rhodopsin protein (left) with a zoom on the retinal chromophore showing a scheme of the photoisomerization leading from the 11-*cis* to the all-*trans* configuration. The isomerizing C11=C12 bond is highlighted in red.

Rhodopsin consists of two components, a protein molecule called scotopsin and a covalently-bound cofactor called retinal, which is produced in the retina from vitamin A, obtained from dietary beta-carotene. Scotopsin is the GPCR that is embedded in the lipid bilayer of cell membranes using seven protein transmembrane domains (Figure 6.1). These domains form a pocket where the photoreactive chromophore, the retinal, lies horizontally to the cell membrane. The aldehyde group of retinal is covalently linked to the amino group of a lysine residue of the protein forming a protonated Schiff base ($-NH^{+}=CH-$, see Figure 6.1). When rhodopsin absorbs light, its retinal cofactor isomerizes from the 11-*cis* to the all-*trans* configuration, and the protein subsequently undergoes a series of conformational changes to accommodate the altered shape of the isomerized cofactor, which eventually lead to stimulation of the optic nerve. Indeed, the protein structure modification triggers the closure of some membrane ion channels, with a consequent reduction of cation influx and a decrease or cessation of neurotransmitter release at the synaptic terminal, which is the message that is relayed to the retinal neurones. Immediately after the photoisomerization, the Schiff base link is hydrolyzed by the enzyme rhodopsin kinease, yielding the photobleached rhodopsin. The rhodopsin pigment must therefore be regenerated for further phototransduction to occur.

Rhodopsin of the rods most strongly absorbs green-blue light and, therefore, appears reddish-purple, which is why it is also called “visual purple”. It is responsible for monochromatic vision in the dark. Color vision in humans is instead achieved by three opsin proteins which tune the electronic energy levels of the chromophore to different wavelength sensitivities. Figure 6.2 shows the absorption spectra of visual rhodopsin before and after photobleach, reported in 1958[1]. The protein absorption spectrum is significantly blue-shifted with respect to that of the protonated Schiff base in vacuo, which is experimentally measured to peak at 610 nm[2]. This shift highlights the first important role of the protein for the process of vision: the optimal tuning of the chromophore absorption. In particular, the high sensitivity of the retinal excitation energy to the electrostatic potential of the surrounding environment is associated with the charge-transfer (CT) character of the first optically bright excited state. Upon absorption of a photon, the electron density shifts from the $\beta$-ionone ring

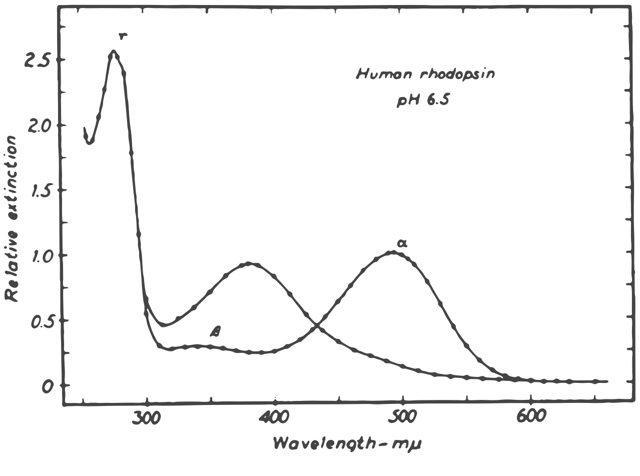

**Figure 6.2:** Absorption spectra of human rhodopsin before and after bleaching in aqueous digitonin solution[1]. Upon irradiation, the $\alpha$ (493 nm) and $\beta$ (340 nm) bands of rhodopsin are replaced by the absorption band of the photobleach prduct (380 nm). The $\gamma$ or opsin band at 278 nm remains unchanged.

to the nitrogen atom of the protonated Schiff base. In visual rhodopsins, the positively charged nitrogen atom interacts with a negatively charged counterion, leading to the stabilisation of the ground electronic state of the chromophore with respect to the gas phase and, consequently, to a blue shift of the absorption maximum[3].

Besides the influence on the spectral properties, the protein environment also plays a crucial role on the speed and final outcome of the photoisomerization dynamics. In rhodopsin, the retinal 11-*cis* ⟶ all-*trans* conversion is ultrafast and highly specific, and occurs with 65% quantum yield[4]. Femtosecond transient absorption experiments performed in the 1990's revealed that the photoreaction is completed within 200 fs[5] and that it proceeds in a vibrationally coherent manner[6]. More recent transient grating experiments revealed an even faster photoproduct formation, whose signals were observed only ~30 fs after photoexcitation[7]. In contrast, photoisomerization in solution leads to a mixture of isomers due to loss of selectivity, with a quantum yield of only a few percent for each subproduct and at a much slower rate (2–10 ps)[8]. The protein embedding is therefore a mandatory ingredient for accurate modelling of the rhodopsin isomerization, and the advent of QM/MM methods was game-changing for the computational studies on this interesting process. Indeed, the entire protein is too big for a whole quantum chemical treatment, and the first ab initio studies employed a minimal retinal model in the gas phase[9, 10]. QM/MM methods (which are introduced in section 6.2) allow to treat only the retinal chromophore (which constitutes a small part of the system) at QM level, while the remaining protein embedding can be treated at a lower level of theory (classical MM). Application of QM/MM schemes to the study of rhodopsin has revealed important aspects of the photoisomerization processes, allowing to account for the steric and electrostatic interaction with the protein and to get more accurate models.

Concerning the reaction mechanism, it was shown that a barrierless coordinate connects the FC region to the $S_1/S_0$ CI located at the bottom of the excited-state PES[11–13]. Over time, several mechanisms were proposed for the retinal photoisomerization inside rhodopsin, that has been the subject of a plethora of experimental an theoretical studies (both in vacuo and inside the protein, see reference[14] for a comprehensive review of all proposed mechanisms). Nowadays, it is widely accepted that the process is best described by a two-states, three-modes model, that is analysed in the following. The first and most intuitive model coordinate is represented by torsion of the C11=C12 bond, which however is too space demanding to happen in a pure "one-bond-flip" way inside the protein embedding . Inside rhodopsin, instead, C11=C12 rotation is accompanied by torsion around other double bonds along the polyene chain and, in particular, partial torsion of the C9=C10 bond (which results in the famous "bicycle-pedal" mechanism[14]). The second coordinate is represented by the bond length alternation (BLA), i.e. a concerted stretching mode of the carbon-carbon bonds along the chain, resulting in the inversion of the bond order in the excited molecule, with respect to the ground state pattern. BLA can be quantified through the difference between the "average single-bond" and the "average double-bond" lengths:

$$\mathrm{BLA} = \frac{\mathrm{C6C7 + C8C9 + C10C11 + C12C13 + C14C15}}{5} - \frac{\mathrm{C5C6 + C7C8 + C9C10 + C11C12 + C13C14 + C15N}}{6} \tag{6.1}$$

The BLA value is positive at the ground state *cis* and *trans* isomers, with a value around 0.1 Å[15]. As the stretching proceeds, its value decreases towards zero or

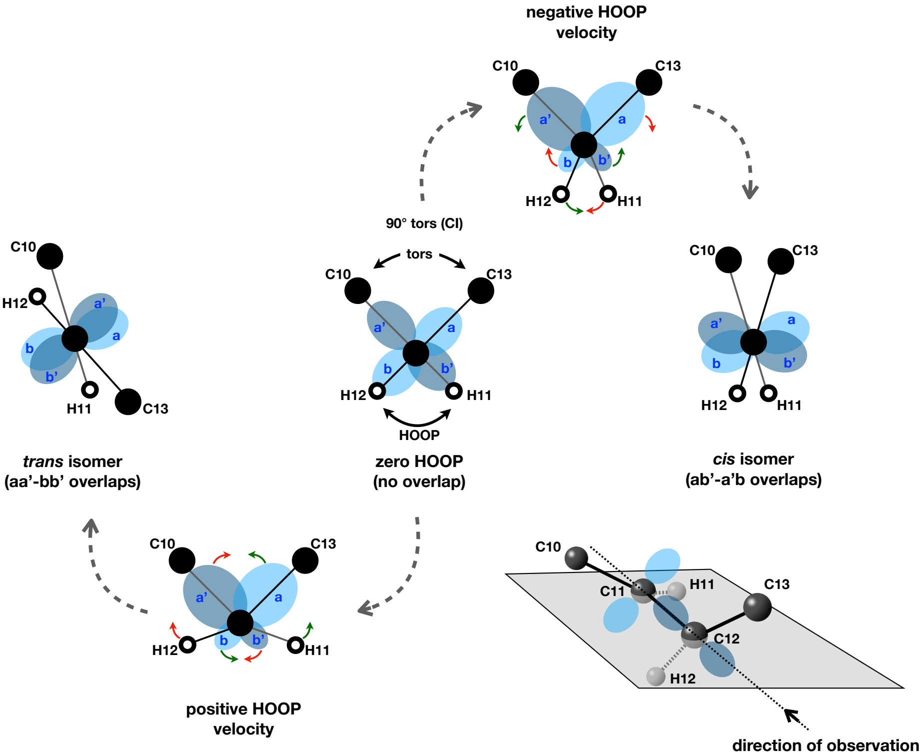

**Figure 6.3:** Rationalisation of the role of the HOOP velocity in determining the isomerization product: at the CI (~90° tors) and when the HOOP is zero (middle), the overlap between the carbon p orbitals is at its minimum. A negative HOOP velocity is reflected in a rotation of the orbitals which favours the overlap of the ab'-a'b lobes (top), leading to the *cis* isomer (right). In contrast, a positive HOOP velocity favours the overlap of the aa'-bb' lobes (bottom), leading to the *trans* isomer (left).

even negative values when the inversion is complete. The BLA mode is the first to be activated after photoexcitation, while the torsion only starts after the stretchings have relaxed[16]. Only in more recent years the relevance of a third coordinate was suggested, which is the C11−H11 and C12−H12 hydrogens out-of-plane wagging (HOOP). Participation of the HOOP mode was first supposed by Mathies et al. based on the analysis of Raman spectra[17], and its relevance was further confirmed by several experimental[18, 19] and theoretical studies[18, 20–22]. The HOOP coordinate acts as an efficient coupling mode between the electronic states, as demonstrated by the slower photoisomerization rates obtained when it is excluded from the model[23]. Moreover, and maybe more importantly, the coherence between the HOOP and torsional motion at the moment of the non adiabatic event was found to play a crucial role in determining the fate of the isomerization. The proposed explanation for this observation is that the HOOP value provides a measure of the pyramidalization of the C11 and C12 centres (determining the $sp^3$ character of the p-orbitals) and its velocity (i.e. magnitude and direction of the motion) is directly reflected in the evolution of the p orbitals overlap on the ground state, leading to either the *cis* or *trans* isomer (see Figure 6.3). Deuteration experiments on the H11−C11=C12−H12 double-bond[19] have brought evidence of the HOOP participation in the dynamics: the presence of heavier hydrogen isotopes significantly and unexpectedly alters the photoisomerization yield, while inducing smaller changes in the ultrafast isomerization dynamics assignable to known isotope effects (i.e. delayed appearance of the photoproduct for deuterated isotopomers). More importantly, the yield effect is different in the case of symmetric or asymmetric deuteration: the former produces a higher isomerization quantum yield (69%) compared to the original compound, whereas asymmetric isotopic substitution results in a significantly lower yield (45% and 48% for 11D and 12D, respectively), indicating that a successful isomerization requires a cooperative effect of both vibrations in a well-defined manner. The observed HOOP phase dependence of the outcome of the non adiabatic event endorses the development of accurate quantum models for the simulation of the photosiomerization.

Regarding the number of states included in the model, the involvement of a third state ($S_2$) in the reaction dynamics was proposed in the 90s[24–26], however, evidence for the two-state model was reported in subsequent works[16, 27, 28] and is now widely accepted. Recent works suggest that including a third electronic state is necessary to simulate absorptive features in two-dimensional electronic spectra of rhodopsin[29, 30]. Nevertheless, in this case, the third electronic state does not influence the photoisomerization dynamics but acts as a higher excited state used as a probe, and is thus only needed for the simulation of transient spectroscopic signals.

Based on the model described above (and its historical evolutions), a plethora of dynamics simulations of rhodopsin photoisomerization are reported in the literature, mainly based on the mixed quantum/classical trajectory approach[15, 19, 21, 22, 31]. Such studies have provided impressive information about the time evolution of the system, however, purely quantum effects (that the HOOP experiments suggest may play a role in the dynamics), are neglected. Reported quantum dynamics studies are less frequent, and based on approximated models. Most QD studies rely on the model proposed by Hahn and Stock[32] (and its variants), in which two diabatic states are coupled along two main modes: a reaction coordinate $\phi$, which reflects the large amplitude torsional motion of the molecule during the isomerization, and a vibronically active coupling mode $q_c$, that can mainly be identified with the BLA stretching. This original two-states, two-modes model was later augmented with a larger group of low frequency modes (usually 23) that is treated at a lower level and acts as a bath, accounting in a generic fashion for the effect of the protein environment. The diabatic and simple potential, together with the high number of bath modes, make this model particularly suitable for (ML-)MCTDH dynamics (that is, indeed, the most employed method[29, 33, 34]), but other propagation schemes have also been used[35, 36]. It is worth stressing that the 2D Hahn-Stock model is not an analytical model for rhodopsin but rather for "the photoinduced 11-*cis* ⟶ all-*trans* isomerization of retinal in rhodopsin". Indeed, its parameters have been empirically tuned to reproduce the experimental lifetime and quantum yield, and they have also been revised several times according to the new experimental findings. Thus, the used coordinates are to be considered as "effective modes" and do not correspond exactly to the torsion and BLA coordinates of the three-dimensional model. The Hahn-Stock model, besides being widely employed, is very approximated, and its robustness has recently been argued[34]. The two-state model ignores the effect of the HOOP mode and, in particular, its correlation with the reactive torsional motion. The impact of the

HOOP coordinate has been recently demonstrated by a pioneering work of Agostini and coworkers[23], who performed exact quantum dynamics on a minimal retinal model in the gas phase, based on recently published ab initio multiconfigurational PESs[37] spanning the torsion, BLA and HOOP coordinates. Despite the minimal model, the obtained results significantly improve the two-state model ones, in particular concerning the early photoproduct formation experimentally observed[7]. These promising results encourage the development of more accurate models for the QD simulation of the retinal chromophore inside rhodopsin, which are still missing. For this reason, and given the long experience in the study of rhodopsin developed in our group, we have decided to apply our parameterisation protocol to such fascinating system, with the final goal to simulate with accurate QD methods its photoisomerization inside the protein environment. The work presented here is preliminary, and the QD simulations are still missing but, even prior to dynamics results, the QM/MM parameterisation inside the protein embedding is a non trivial task which is worth a detailed analysis.

## 6.2 The QM/MM scheme

In the quantum mechanics/molecular mechanics (QM/MM) method a small part of the system (which is typically the most involved in the electronic dynamics) is treated at a high QM level, while the surrounding environment is explicitly accounted for but at a lower level (molecular mechanics, MM). Sometimes, a boundary region connecting the "high layer" (QM part) and "low layer" (MM part) exists, called "medium layer", whose atoms are treated either at "low-QM level" (i.e. QM with a lower level of theory), or at "high-MM level" (e.g. MM with a more accurate optimisation algorithm). A general QM/MM partitioning is shown in Figure 6.4. The method was first introduced by Warshel and Levitt in 1976[38], and its introduction paved the way for the accurate and efficient simulation of complex systems.

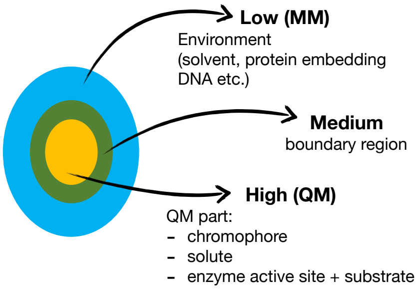

**Figure 6.4:** Graphical representation of the QM/MM partitioning scheme.

The overall accuracy of the QM/MM model depends on

- the type of embedding;
- the energy scheme;
- the partitioning scheme;
- the quality of the QM method used to describe the active site of the system.

The embedding refers to the description of the interaction between the QM and the MM parts. Three main schemes are available[39]: mechanical, electrostatic, and polarisable embedding. In a mechanical embedding, the QM subsystem is represented by point charges at MM level, thus only an MM electrostatic interaction is considered. This is the simplest type of embedding and is the least accurate among the three schemes. The most popular scheme is now the electrostatic embedding, in which the electrostatic interaction is also accounted for at QM level, and the electronic structure of the QM region changes due to the point charges of the MM part (and gets polarised by it). The polarisable embedding scheme can instead be employed in order to make the polarisation between the two regions reciprocal and requires the use of polarisable force fields.

The energy scheme refers to the combination of QM and MM results for the calculation of the total energy of the system. This can be done either by an additive or a subtractive scheme. The additive scheme comprises two calculations: a QM calculation for the QM part and one single MM calculation which accounts for the MM energy and the QM-MM interface energy[40]. In this case, it is up to the developer to ensure that no interactions are omitted or double-counted, therefore, an additive scheme requires special MM softwares that allow to selectively include/exclude MM terms. In the subtractive scheme, instead, three separate calculations are performed: one QM calculation for the QM part (yielding $E_{\mathrm{QM}}(\mathrm{QM})$) and two MM calculations, one for the entire system (yielding $E_{\mathrm{MM}}(\mathrm{MM}+\mathrm{QM})$) and one for the QM region (yielding $E_{\mathrm{MM}}(\mathrm{QM})$). The final QM/MM energy is obtained as

$$E_{\mathrm{QM/MM}} = E_{\mathrm{QM}}(\mathrm{QM}) + E_{\mathrm{MM}}(\mathrm{MM} + \mathrm{QM}) - E_{\mathrm{MM}}(\mathrm{QM}) \tag{6.2}$$

The main advantage of the subtractive scheme is its simplicity: it automatically ensures that no interactions are double-counted and it can be set up to interface any QM and MM softwares (provided that they can write out energies and forces). Moreover, it can be easily extended to more than two computational methods and regions.

The choice of the partitioning scheme and the QM level of theory is the user-defined part of the calculation, and it is crucial to obtain reliable results. A wrong partitioning could mean a too small QM part, which excludes some photochemically/photophysically relevant atoms that would require a QM description. At the same time, an appropriate basis set and level of theory are fundamental in order to get physically meaningful results and must be carefully selected for each specific problem.

## 6.3 Selection of the reference geometries and reactive coordinates

The electronic PESs serve as basis for subsequent dynamics simulation (either quantum or mixed quantum/classical). Therefore, they should include all most relevant geometries for the process description. In the case of rhodopsin, we have identified four key geometries for the model:

- $S_0$ 11-*cis* minimum (FC point);
- $S_1$ “planar” minimum;

- lowest $S_1/S_0$ CI;
- $S_0$ all-*trans* photoproduct.

The two ground state minima represent the starting and final points of the dynamics, while the $S_1/S_0$ CI is the most relevant structure determining the non adiabatic event. Besides these three geometries, the "BLA-relaxed" structure on the excited state (i.e. $S_1$ minimum along BLA starting from the *cis* FC point) is also important, as it represents an intermediate structure before the activation of torsion and HOOP. It is referred to as $S_1$ "planar" minimum (i.e. prior to torsion activation), and it had already been reported in the literature[41]. Such structures are all connected by the three model coordinates detailed in the previous section, namely

- a complex C10−C11=C12−C13 torsional motion involving partial rotation of several others dihedrals along the carbon chain;
- BLA stretching, defined as in equation (6.1);
- HOOP wagging.

## 6.4 Computational details

All the electronic structure calculations were performed using the electrostatic embedding, subtractive scheme QM/MM framework provided by the COBRAMM code [42–44]. Our QM/MM model for rhodopsin is based on an "high-medium-low" scheme, in which the QM/MM boundary is placed on the Lys $C\delta$–$C\epsilon$ bond (see Figure 6.5), employing the link–atom approach to model the frontier. The whole protonated Schiff base chromophore is treated quantum mechanically (54 atoms including the link atom) keeping the protein environment fixed at the crystal structure atomic positions, except for the closest nine atoms of the lysine side–chain connected to the retinal residue that were free to move during optimisations (M layer, see Figure 6.5). A modified AMBER[45] force field was used for the MM calculations. Such scheme has already been used and assessed for rhodopsin, providing good results[15, 46, 47].

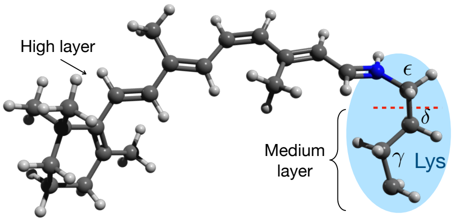

**Figure 6.5:** Partitioning between high and medium layer atoms for the QM/MM calculations on rhodopsin. The low layer includes the rest of the protein not shown in the figure.

The four reference structures listed above were all optimised at the CASSCF(12,-12)/6-31G*/AMBER level, and the energy of the optimised structure was eventually corrected at CASPT2 level. Indeed, the CASSCF method has proven to produce qualitatively accurate PESs for rhodopsin, correctly describing the relevant geometries[12,

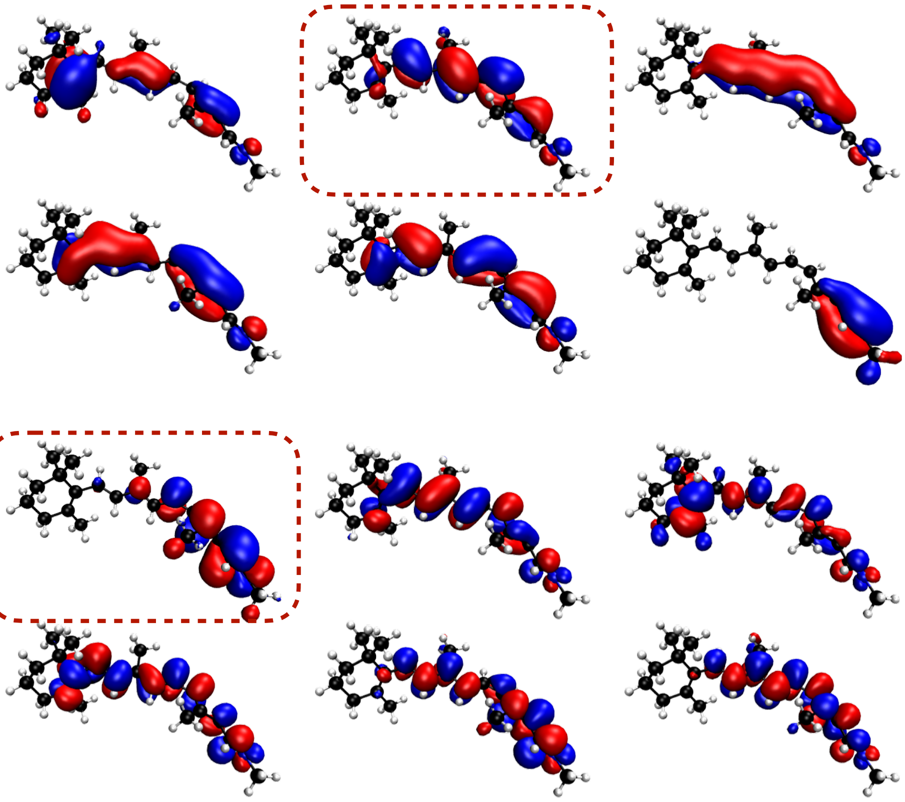

**Figure 6.6:** Active space orbitals for 11-*cis* retinal inside Rhodopsin (SA1-CASSCF(12,12)/6-31G*/AMBER). Orbitals most involved in the electronic transition describing the first excited state are highlighted by the dotted boxes. Corresponding orbitals were used for all other geometries.

15]. On the other hand, for the calculation of state energies, wavefunctions and TDMs/NACs, we rely on the dynamically-correlated CASPT2 method, using an imaginary shift of 0.2 a.u. and setting the IPEA shift to zero. This combined CASPT2/CASSCF approach has proved to return experimentally accurate energies[15, 48]. Figure 6.6 shows the CASSCF active orbitals.

The two ground state minima were optimised putting only one root in the CASSCF state averaging (i.e. SA1-CASSCF(12,12)/6-31G*/AMBER), as this showed to give a better convergence and cleaner orbitals. For comparison, the 11-*cis* structure was also optimised at the MP2/6-31G*/AMBER level. For $S_1$ and CI optimisations, instead, the ground state and the first excited state were considered (i.e. SA2-CASSCF(12,12)/6-31G*/AMBER). The structure of the $S_1$ "planar" minimum was obtained through a constrained optimisation in which all the dihedrals of the polyene chain were kept frozen at their 11-*cis* minimum value. A fully unconstrained geometry optimisation on $S_1$ was also performed at the same level of theory, that however terminated at the optimised $S_1/S_0$ CI structure. Two SA2-CASSCF(12,12)/6-31G*/ AMBER minimum energy path (MEP) calculations were also performed on the excited state, starting from either the 11-*cis* or the all-*trans* geometries.

For the subsequent parameterisation (i.e. for all single-point calculations of the final grid) the CASSCF space was extended to $S_2$ as well, as it was found to get close to $S_1$ at distorted geometries. Concerning the perturbative correction, the affordable computational cost allowed to perform the full parameterisation at both MS- and XMS-CASPT2 level, in order to appreciate final differences in the PESs and dynamics and assess the two methods. The final level of theory of the grid is therefore (X)MS-3-CASPT2/SA-3-CASSCF(12,12)/6-31G*/AMBER (referred to as MS-CASPT2 and XMS-CASPT2 in the text). NACs and TDMs across the final grid were calculated and sign-corrected using the CASPT2 energies and wavefunctions according to the procedures described in section 3.4. All calculations were performed using the COBRAMM[42–44] software, interfaced with OpenMolcas[49, 50] for the QM calculations.

### 6.4.1 Generation of the grid structures

For the generation of the 3D grid spanning the torsion, BLA and HOOP coordinates, we took advantage of the fact that the two excited state MEP define a continuous path connecting all the reference structures. Indeed, both $S_1$ MEPs (i.e. starting from 11-*cis* or all-*trans* FC point) terminate at the same $S_1/S_0$ CI structure (which matches the optimised CI structure, see below), and their union constitutes an optimised path connecting photoreactant and photoproduct via the most accessible funnel. Moreover (as will be discussed later), the initial displacement of the MEP starting from the *cis* isomer is along BLA only, until the $S_1$ “planar” minimum is reached. Therefore, the path defined by the union of the two $S_1$ MEPs includes all the four reference geometries.

The unified MEP was then sampled to have a ~5° step of the isomerizing C10−C11=C12−C13 dihedral, and the selected structures used as anchor points to scan the BLA and HOOP, so as to obtain a three-dimensional grid along complex torsion, BLA and HOOP. The MEP will explore all the three coordinates, but at each point, the BLA and HOOP scan will produce a uniform grid, in which it will be possible to move independently along the three coordinates (as illustrated in Figure 6.7). The merging of the two $S_1$ MEPs produces a smooth $S_1$ profile, with no geometrical discontinuities as both MEPs merge at the same $S_1/S_0$ CI geometry.

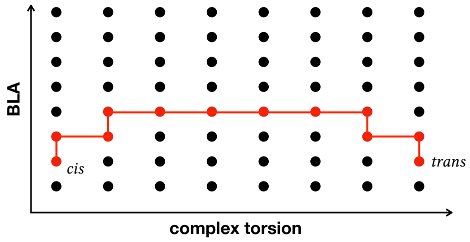

**Figure 6.7:** Scheme of the BLA-complex torsion grid anchored on the MEP points. The example MEP (red path) spans both coordinates, but the BLA scan produces a uniform grid, in which it is possible to move independently along the two coordinates.

The generation of the grid starting from the $S_1$ MEPs has, however, one important drawback: the two FC points (*trans* and *cis*) are at the edges of the grid, which is not desirable for the wavepacket dynamics. The torsion coordinate must therefore be extended beyond the *cis* and *trans* values. To this aim, we have applied the following

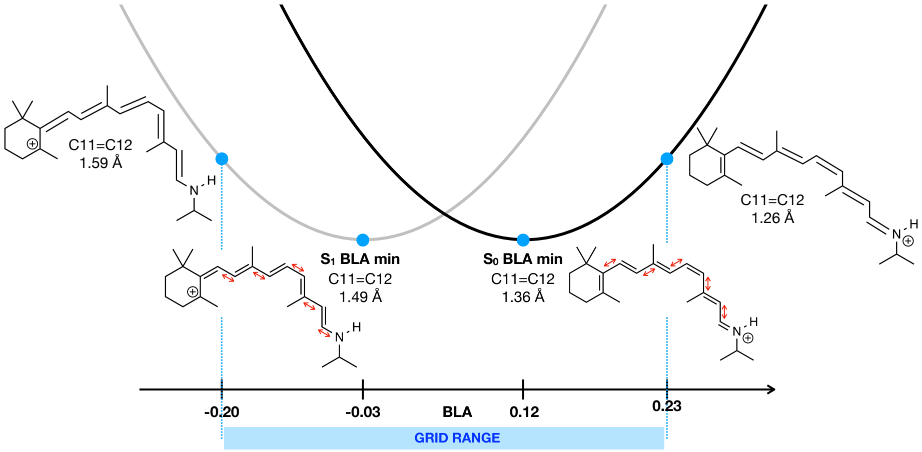

**Figure 6.8:** Schematic representation of the grid generation for the BLA coordinate.

procedure:

1. for each dihedral in the molecule we have made a linear interpolation of its value at the $S_0$ minimum and at the first optimised MEP point, using as abscissa value the norm of the cartesian difference (in Angstrom) between the two structures;
2. the "inverse-MEP" structures were extrapolated using C10−C11=C12−C13 steps of about 5° in absolute value;
3. for each geometry, we have performed an SA2-CASSCF(12,12)/6-31G*/AMBER constrained optimisation, freezing the C10−C11=C12−C13 dihedral and using a small optimisation step (3 Bohr).

The optimised geometries were then employed as new "MEP points" for the generation of BLA and HOOP grids. It is reasonable to expected that such additional grid points will not play an important role in the dynamics, being far from the non adiabatic region ($S_1/S_0$ CI). Their role is rather to prevent the wavepacket to escape the grid beyond the *cis* and *trans* minima.

The BLA coordinate is described as a concerted stretching along the retinal carbon chain, and its numerical value is defined by equation (6.1). The relative grid points were generated by linear interpolation of all the bond lengths of the QM part between their value at the $S_0$ 11-*cis* and $S_1$ "planar" minimum structures. To allow the description of wider BLA oscillations during the dynamics, the grid was extended by extrapolation in both positive and negative BLA directions (see Figure 6.8 for a schematisation of the BLA grid range). The final grid points include the BLA values [ 0.23, 0.17, 0.12, 0.05, -0.03, -0.08, -0.14, -0.20 ] Å, but the scan was made denser close to $S_1/S_0$ crossing points.

The HOOP coordinate is defined as the out-of-plane movement of the two hydrogen atoms liked to C11 and C12. More precisely, the HOOP is defined as the difference between the C10−C11=C12−C13 and H11−C11=C12−H12 dihedrals, since the latter (considered alone) changes a lot during the photoisomerization even without HOOP displacement, as a consequence of the C11=C12 torsional movement.

$$\text{HOOP} = \text{C10C11C12C13} - \text{H11C11C12H12} \tag{6.3}$$

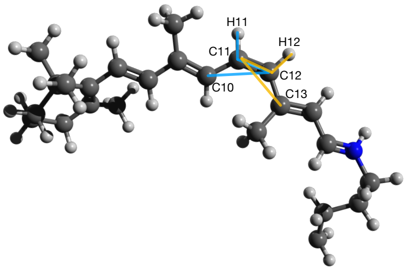

**Figure 6.9:** H11−C11=C12···C10 (blue) and H12−C12=C11···C13 (yellow) dihedrals defining the HOOP.

The definition of the dihedral angles for the HOOP scan is not unique. Indeed, the same HOOP displacement can be obtained e.g. editing the two H11−C11=C12−C13 and H12−C12=C11−C10 dihedrals together, or directly the H11−C11=C12−H12 value. However, varying these dihedrals could be tricky, since the atoms are all involved in the definition of nearby dihedrals and angles, which change consequently. Instead, a variation of the two H11−C11=C12···C10 and H12−C12=C11···C13 dihedrals (see Figure 6.9) perfectly describes the out-of-plane hydrogen movement. When both such dihedrals are equal to 180°, the two hydrogens lie in the same plane as the three carbon atoms (C10−C11=C12 or C11=C12−C13, respectively) and the HOOP value is 0. Instead, if they are coherently moved of $\pm x°$, the final HOOP value is equal to $\pm 2x°$. The HOOP was scanned for each BLA-MEP grid point from -80° to +80° with step 20°. For each BLA-torsion coordinate, 10 HOOP structures will therefore be available: the 9 scan values plus the "natural" HOOP value at the MEP anchor point.

The calculation of NACs in internal coordinates using the COBRAMM protocol described in section 3.4.1 requires cartesian displacements along the three reactive coordinates. For each grid point, we have defined three orthonormal vectors pointing in the complex torsion, BLA and HOOP directions and created the relative displacements by a shift of ±0.005 Å of magnitude. More details about the generation of the orthonormal cartesian vectors can be found in Appendix A.

## 6.5 Results and discussion

### 6.5.1 Reference geometries

The CASSCF(12,12)/6-31G*/AMBER optimised structures of the four reference geometries are shown in Figure 6.10, with the most relevant geometrical parameters collected in Table 6.1. Table 6.2 shows the CASSCF and CASPT2 energies of the lowest three electronic states at each geometry.

The differences between the bond lengths in the ground and excited state optimised structures indicates a clear displacement along the BLA coordinate, that changes from 0.12 Å of the 11-*cis* and all-*trans* minima to slightly negative values at the $S_1/S_0$ CI and $S_1$ "planar" minimum (see Table 6.1). The latter is in fact reached from the 11-*cis* minimum by a relaxation of C-C stretchings (i.e. BLA), and differs from it

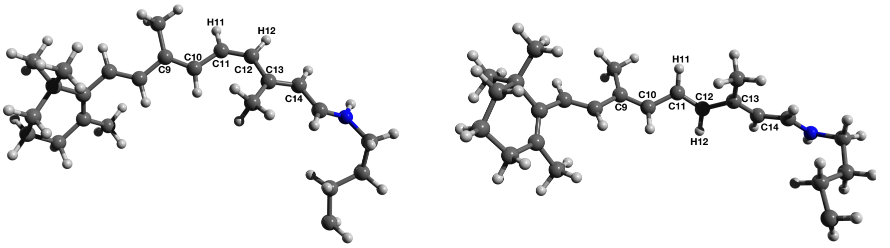

(a) 11-*cis* $S_0$ min

(b) all-*trans* $S_0$ min

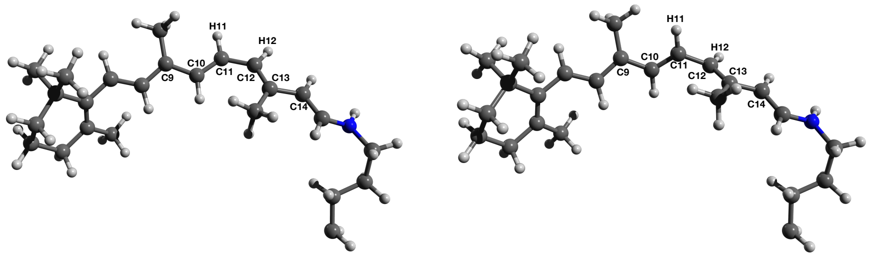

(c) $S_1$ “planar” min

(d) $S_1/S_0$ CI

**Figure 6.10:** CASSCF(12,12)/6-31G*/AMBER optimised structures of the four reference geometries for the parameterisation of the retinal chromophore inside Rhodopsin.

mainly in the bond lengths. The BLA relaxation actually stabilises both excited states, as demonstrated by the $S_1$ and $S_2$ energies at the $S_1$ “planar” minimum (see Table 6.2).

The optimised $S_1/S_0$ crossing point shows a twisted geometry (C10−C11=C12−C13 = −89.06°), with a partial rotation around the adjacent double bonds (C9=C10 in particular, see Table 6.1), addressed to the bicycle pedal mechanism discussed previously. The all-*trans* minimum optimised inside rhodopsin, instead, is not perfectly planar, but rather shows carbon chain dihedrals between −140° and −150°. Indeed, the the most stable structure in the protein is a partially rotated conformer called bathorhodopsin, that was experimentally found to show dihedral values around 150° along the carbon chain[51, 52], and our results also agree with some optimised structures reported in the literature at a very similar level of theory[22].

Concerning the HOOP coordinate, it does not change significantly on passing from the $S_0$ 11-*cis* geometry to the CI, and it shows small values in both these structures. In the all-*trans* minimum, instead, the “CCCC” and “HCCH” dihedrals differ significantly, resulting in a HOOP value of ~ 33° (see Table 6.1), as a consequence of the spatial constraints imposed by the protein embedding.

The last geometrical parameter reported in Table 6.1 is the planarization of the $\beta$-ionone ring (i.e. C5=C6−C7=C8 dihedral), which stabilise $S_1$: indeed, the C6-C7 link becomes a double bond after BLA relaxation on the excited state, therefore aiming to planarise the C5=C6−C7=C8 dihedral (as testified by the values in Table 6.1).

Although a full CASPT2 optimisation would be very expensive (due to the lack of analytical gradients), the CASSCF structures can be compared with the CASPT2 minima/CIs from the 3D grid. The geometrical parameters of the resulting SS, MS and XMS-CASPT2 $S_0$ *cis*, *trans* and $S_1$ “planar” minima are reported in Table 6.1, while a detailed analysis of the (X)MS-CASPT2 crossing seam is given later (see Table 6.3

**Table 6.1:** Geometrical parameters of the four CASSCF-optimised reference structures for the parameterisation of the retinal chromophore inside Rhodopsin and their SS-, MS- and XMS-CASPT2 analogues from the grid. The MP2-*cis* optimised structure is also reported for comparison.

| | | Torsion (°) | | | HOOP | BLA | Ring pl. (°) |
|---|---|---|---|---|---|---|---|
| | | C10C11C12C13 | C8C9C10C11 | C12C13C14C15 | (°) | (Å) | C5C6C7C8 |
| MP2 | MP2-*cis* min | −9.90 | 175.60 | −179.30 | −7.20 | 0.07 | −49.40 |
| CASSCF | $S_0$ 11-*cis* min | −5.65 | 174.29 | −178.81 | −5.14 | 0.12 | −55.14 |
| | $S_1$ pl. min | −5.65 | 174.29 | −178.81 | −5.14 | −0.03 | −51.95 |
| | $S_1/S_0$ CI | −89.06 | −153.87 | −167.10 | −3.09 | −0.01 | −39.86 |
| | $S_0$ all-*trans* min | −140.98 | −150.94 | −154.90 | 32.92 | 0.12 | −46.57 |
| SS | SS-*cis*-min | −5.65 | 174.29 | −178.81 | −5.14 | 0.12 | −55.14 |
| | SS-$S_1$ pl. min | −5.65 | 174.29 | −178.81 | −5.14 | 0.05 | −55.14 |
| | SS-*trans* | −140.98 | −150.94 | −154.90 | 32.92 | 0.12 | −46.57 |
| MS | MS-*cis*-min | −10.47 | 174.30 | −176.81 | 0.82 | 0.05 | −53.76 |
| | MS-$S_1$ pl. min | −10.47 | 174.30 | −176.81 | 0.82 | −0.03 | −53.76 |
| | MS-*trans* | −135.88 | −152.27 | −155.42 | 20.00 | 0.05 | −45.37 |
| XMS | XMS-*cis*-min | −5.65 | 174.29 | −178.81 | −5.14 | 0.12 | −55.14 |
| | XMS-$S_1$ pl. min | −5.65 | 174.29 | −178.81 | −5.14 | 0.05 | −55.14 |
| | XMS-*trans* | −140.98 | −150.94 | −154.90 | 32.92 | 0.12 | −46.57 |

and relative discussion). Concerning the $S_0$ minima, the SS and XMS structures perfectly match the CASSCF ones, while MS-CASPT2 minima are a bit more rotated, with C10−C11=C12−C13 torsional values around −10° and −135° for *cis* and *trans*, respectively. Also, their BLA value is smaller compared to the CASSCF ground state minima, while the HOOP shows a better agreement, considering the discretised HOOP grid does not allow for a perfect match. The MP2-*cis* minimum is similar to the MS-CASPT2 one, with a torsional value of ~ −10° and a less pronounced difference in the single and double bond lengths, resulting in a smaller BLA value (i.e. 0.07 Å)

The CASPT2 vertical transition energies at the optimised 11-*cis* minimum can be compared to the experimental $S_0 \longrightarrow S_1$ and $S_0 \longrightarrow S_2$ values ($\lambda_{max}$ = 493 and 340 nm, respectively[1]). SS-CASPT2 shows the best agreement, with energy gaps corresponding to 482 nm ($S_1$) and 332 nm ($S_2$), while MS- and XMS-CASPT2 slightly overestimate the energy of both excited states ($S_1$ $\lambda_{max}$: 466/446 nm for MS/XMS, respectively; $S_2$ $\lambda_{max}$:310 nm for both MS and XMS). The MS-CASPT2 match, however, is improved if the corresponding MS-*cis* minimum is considered (see Table 6.2): here, the $S_0 \longrightarrow S_1$ energy (2.56 eV = 484 nm) is close to the experimental value, while the $S_0 \longrightarrow S_2$ excitation is now underestimated (396 nm). It is worth to notice that the difference in the MS ground state energy between the two *cis* structures is very small (< 0.1 eV, i.e. the two structures are virtually isoenergetic on $S_0$), and the improved $S_1$-$S_0$ gap energy is mostly due to $S_1$ stabilisation for more rotated structures. The MS-CASPT2 predictions improve even more at the MP2-optimised *cis* minimum (whose structure is indeed very similar to the MS one, se Table 6.1), with $S_0 \longrightarrow S_1$ and $S_0 \longrightarrow S_2$ expected at 502 and 347 nm, respectively. The similarity between the MS-CASPT2 (from the grid) and the MP2 (optimised) structures and the good agreement with the experimental value suggests that the MS-CASPT2 minimum might be well captured by our grid, and that it should not be too different from the MP2 equilibrium geometry.

The same trends are observed at the *trans* geometry, with the SS-CASPT2 energy gap reproducing better the experimental bathorhodopsin $\lambda_{max}$ of 535 nm[53] at the CASSCF structure (calculated $\lambda_{\text{max}}$ = 508, 484 and 494 nm for SS-, MS- and XMS-CASPT2, respectively). Again, the MS-CASPT2 agreement improves at the corresponding minimum (from the 3D grid) due to $S_1$ stabilisation (while the $S_0$ energy is close to the CASSCF-optimised structure), with a calculated $\lambda_{\text{max}}$ of 563 nm. Experimentally, an intermediate species (called photorhodopsin) with a red-shifted absorption (i.e. 590 nm[53]) is observed prior to the formation of all-*trans* photproduct. Photorhodopsin was found to be even more distorted in the dihedral values[17], and it rapidly converts to the more stable bathorhodopsin.

The CASSCF-optimised structure of the $S_1$ "planar" minimum (reported in Tables 6.1 and 6.2) is not perfectly reproduced in the 3D grid (due to the fact that the MEP used for the grid construction reaches a similar, although not identical structure), which does not allow for a one-to-one comparison as in the case of the $S_0$ minima. However, the MS-$S_1$ "planar" minimum shows state energies which are very similar to those at the CASSCF-optimised structure. On the other hand, the stabilisation along BLA is smaller according to SS- and XMS-CASPT2, whose $S_1$ "planar" minimum is only ~ 0.15 eV below the *cis* FC point.

The better performance of the single state correction in cases where the reference states are well separated in energy is a known feature of CASPT2 (see section 2.1.12). However, in case of (quasi)degenerate CASSCF states, SS-CASPT2 has shown to be unreliable due to the neglect of state mixing of the reference states. For this reason, considering that our PESs span distorted geometries including wide avoided crossing regions, the parameterisation was eventually carried out at MS- and XMS-CASPT2 level (some cuts of the SS-CASPT2 PESs are shown in Appendix B, together with a comparison of the crossing seam at the different CASPT2 levels). Concerning the choice of the level of theory (detailed in section 6.4), more explanation is needed for the $S_1/S_0$ CI case. The $S_1/S_0$ CI geometry was optimised at the SA-2-CASSCF(12,12)/6-31G*/AMBER level of theory, yielding a perfect degeneracy of the two CASSCF states at 2.49 eV above the 11-*cis* minimum. Subsequent (X)MS-2-CASPT2 corrections on the two states resulted in a small splitting of the states (~ 0.2 eV). Only later we decided to include $S_2$ in the parameterisation, as a consequence of its approach to $S_1$ at CASSCF level for distorted geometries (especially along BLA). The recalculation of the same CI structure at the new level of theory removed the degeneracy at CASSCF level (see Table 6.2), however, the states are still degenerate or very close at CASPT2 level (with a maximum gap of 0.3 eV observed in the case of XMS-CASPT2, while at SS- and MS-CASPT2 level they are perfectly degenerate). For this reason, we decided to retain the SA-2 optimised CI structure for the scan.

Upon $S_1$ excitation, the positive charge is partially transferred from the Schiff base unit to the $\beta$-ionone ring, therefore the first excited state has a charge transfer (CT) character. Figure 6.11 shows the charge distribution in $S_0$ and $S_1$ at the four reference structures. A quick parameter to compare the charge distribution is the total charge on the C1-C11 terminus and on the C12-NH-Lys terminus[15], shown in Figure 6.11 as orange circles around the two moieties. In the ground state, the +1 charge is almost completely localised on the C12-NH-Lys terminus, while on $S_1$ at least 50% of the charge is localised on the C1-C11 terminus at all four geometries. This is particularly evident at the twisted $S_1/S_0$ CI, where the charges are almost 0, +1 ($S_0$) and +1, 0 ($S_1$) on the C1-C11 and C12-NH-Lys terminus, respectively (see Figure 6.11).

**Table 6.2:** Vertical excitation QM/MM energies (eV) of the retinal chromophore inside rhodopsin at the CASSCF and MP2 optimised structures and and their CASPT2 analogues from the grid (SS and XMS *cis* and *trans* minima correspond to the CASSCF ones). All energies are given relative to the $S_0$ 11-*cis* minimum at the corresponding level of theory.

| **Geometry** | **CASSCF** | | | **SS-CASPT2** | | | **MS-CASPT2** | | | **XMS-CASPT2** | | |
|---|---|---|---|---|---|---|---|---|---|---|---|---|
| | $S_0$ | $S_1$ | $S_2$ | $S_0$ | $S_1$ | $S_2$ | $S_0$ | $S_1$ | $S_2$ | $S_0$ | $S_1$ | $S_2$ |
| $S_0$ 11-*cis* min | 0.00 | 3.86 | 4.64 | 0.00 | 2.57 | 3.74 | 0.00 | 2.66 | 4.00 | 0.00 | 2.78 | 4.00 |
| $S_1$ “planar” min | 1.14 | 3.16 | 4.05 | 0.62 | 2.23 | 2.98 | 0.32 | 2.40 | 3.44 | 0.68 | 2.38 | 3.40 |
| $S_1/S_0$ CI | 2.27 | 2.92 | 4.94 | 1.81 | 1.83 | 4.17 | 1.91 | 1.95 | 4.29 | 1.63 | 1.95 | 4.39 |
| $S_0$ all-*trans* min | 1.18 | 5.02 | 5.78 | 1.09 | 3.53 | 4.78 | 1.05 | 3.61 | 5.06 | 1.07 | 3.58 | 4.90 |
| MS-*cis* min | 0.37 | 3.54 | 3.64 | 0.13 | 2.39 | 2.84 | −0.08 | 2.48 | 3.05 | 0.16 | 2.53 | 3.18 |
| MS-$S_1$ pl. min | 1.13 | 3.31 | 4.10 | 0.66 | 2.41 | 3.03 | 0.39 | 2.51 | 3.53 | 0.72 | 2.55 | 3.46 |
| MS-*trans* min | 1.58 | 4.23 | 4.60 | 1.19 | 3.21 | 3.43 | 0.91 | 3.11 | 4.14 | 1.21 | 3.26 | 3.99 |
| SS/XMS-$S_1$ pl. min | 0.35 | 3.68 | 3.77 | 0.16 | 2.40 | 3.02 | 0.06 | 2.46 | 3.40 | 0.18 | 2.64 | 3.33 |
| MP2-*cis* min | 0.00 | 3.50 | 3.91 | 0.00 | 2.34 | 3.19 | 0.00 | 2.47 | 3.57 | 0.00 | 2.57 | 3.46 |

### 6.5.2 Minimum energy paths

Two MEP calculations were performed at CASSCF level on the first excited state ($S_1$), starting at the 11-*cis* or all-*trans* geometry, respectively. The (X)MS-3-CASPT2/SA3-CASSCF(12,12)/6-31G*/AMBER energies were calculated every five MEP steps. Figure 6.12 shows the energy profiles along the union of the two MEPs as a function of the isomerizing dihedral. The CASSCF profiles are qualitatively preserved at (X)MS-CASPT2 level, with a stabilisation of $S_1$ towards ~−90° torsion, where it become almost degenerate to $S_0$. On the other hand, the ground state is highly destabilised along the MEP. The main difference between the two perturbative corrections is observed between −85° and −110° torsion: the $S_1$-$S_0$ degeneracy is preserved by MS-CASPT2, while at XMS-CASPT2 level the two states split, and are separated by a ~0.3 eV gap. The second excited state $S_2$ lies higher in energy in all points at (X)MS-CASPT2 level, except close to the *trans* structure where it approaches $S_1$.

The two MEPs end at very similar structures, which are also very similar to the optimised $S_1/S_0$ CI.

Starting from the corresponding $S_0$ minimum, the main geometrical deformations are along the BLA and torsion coordinates, whose profiles are shown in Figure 6.13 (a) and (b) as a function of the C10−C11=C12−C13 dihedral along the two MEPs. Both MEPs show an initial decrease of the BLA value, while the C10−C11=C12−C13 remains almost unchanged (see Figure 6.13 (a)). The BLA decreases from the initial value of 0.12 Å (of both *trans* and *cis* isomers) to the negative value at the $S_1$ “planar” minimum (−0.03 Å), which is reached after the first MEP steps on the *cis* side. In both MEPs, the BLA value increases a bit as torsion proceeds towards the $S_1/S_0$ CI at −89°, to ebentually reach the −0.01 Å value of the crossing point.

After BLA relaxation, the C10−C11=C12−C13 torsion is started. As discussed previously, rotation of the adjacent double bonds accompanies the isomerization inside the protein embedding (as testified by the C8−C9=C10−C11 and C12−C13-=C14−C15 dihedral variation shown in Figure 6.13 (b)), in which the simple “one-bond flip” mechanism would be too space demanding. However, torsion of the corresponding dihedrals is only partial, with a maximum displacement form the FC values of ~ 20°-30°.

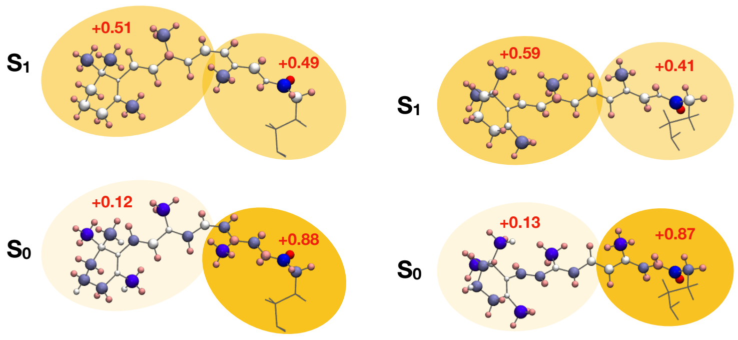

(a) 11-*cis* $S_0$ min (b) all-*trans* $S_0$ min

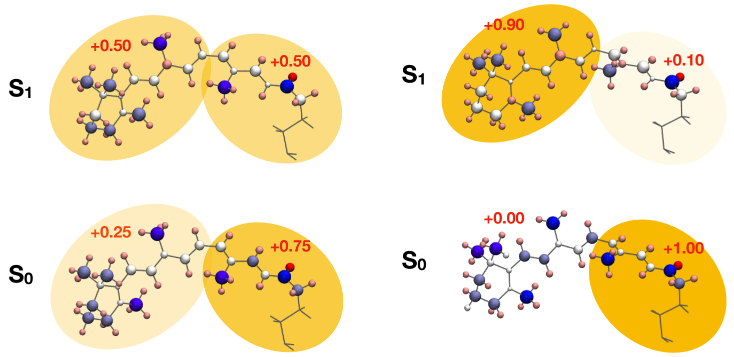

(c) $S_1$ “planar” min (d) $S_1/S_0$ CI

**Figure 6.11:** CASSCF(12,12)/6-31G*/AMBER charge distribution (Mulliken) at the four reference geometries. The size and colour of the atom spheres is proportional to the corresponding charge (blue = negative, red = positive), while the total charges of the C1-C11 terminus and C12-N-Lys terminus are represented by the orange circles, with colour opacity proportional to the charge value.

Figure 6.13 (c) shows the HOOP and H11−C11=C12−H12 dihedral profiles along the path defined by the union of the two MEPs. On the “*cis*-side” of the path, the HOOP is always close to zero (i.e. the two H11−C11=C12−H12 and C10−C11=C12−C13 dihedrals are similar, with only small out-of-plane oscillations of the two hydrogens). In the path connecting the $S_1/S_0$ CI to the *trans* isomer (or vice versa), instead, the HOOP varies significantly, reaching a value of approximately −30° at −120° torsion and 30° at the all-*trans* isomer.

The union of the two MEPs creates a smooth path connecting all the four reference geometries, that can conveniently be used to build the BLA and HOOP grid for our model. The MEP spans all three reactive coordinates (BLA, HOOP, complex torsion), however, the construction of the grid will allow to move independently along each of them (see Figure 6.7), leaving in the “complex torsion” all the geometrical deformations not included in bond stretchings and hydrogen oscillations.

Figure 6.14 shows the (X)MS-CASPT2 MEP, built using the grid points. Both CASPT2 MEPs are in good agreement with the CASSCF path (smooth black line), with the only difference in the wider HOOP oscillations observed for MS-CASPT2.

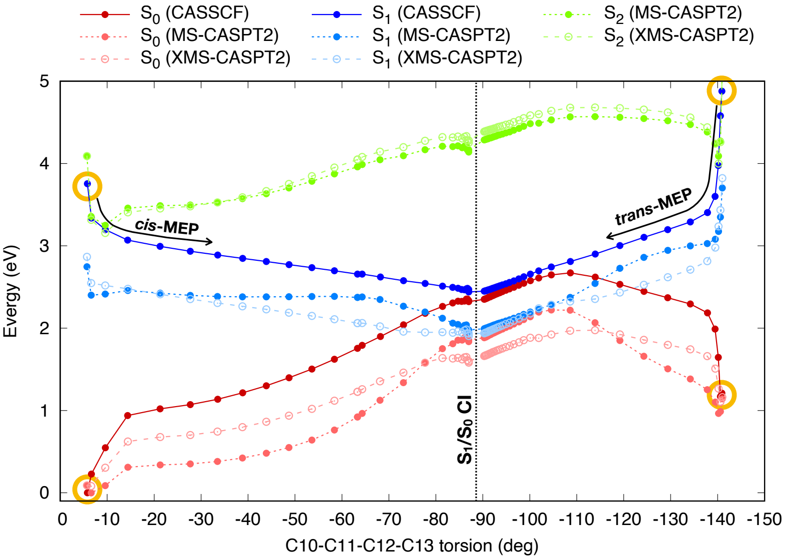

**Figure 6.12:** CASSCF and CASPT2 energies (QM/MM) along the $S_1$ MEPs starting from the 11-*cis* minimum (left branch) or all-*trans* minimum (right branch) both ending at the $S_1/S_0$ CI (C10−C11=C12−C13 ~ −90°).

Such wide fluctuations are due to the large HOOP step (20°) that was used to reduce the computational cost, since this coordinate exhibits a smooth and almost quadratic profile. Therefore, a MEP based on the grid points will necessarily suffer from possible large HOOP variation between consecutive steps. Despite not being optimised, the agreement of the CASPT2 paths with the CASSCF one is remarkable, and all the three MEPs first follow BLA starting from either *cis* or *trans* FC points, then deviate along torsion (and HOOP) to reach the $S_1/S_0$ crossing.

## 6.5.3 Potential energy surfaces

### BLA scan from MEP points

For construction of the BLA grid, the MEP geometries were sampled to get a step of approximately -5° of the central C10−C11=C12−C13 dihedral, and for each geometry we performed a BLA scan. The HOOP coordinate was left untouched at this stage and, for each BLA scan, it retains the value of each MEP “anchor” point. Figure 6.15 shows the 2D PESs of $S_0$, $S_1$ and $S_2$ at CASSCF and (X)MS-CASPT2 level, while Figures 6.16 and 6.17 show some cuts along the torsion and BLA coordinates.

As expected, the torsion is not favoured on $S_1$ whenever BLA > 0.05 Å (as demonstrated by the torsion profiles in Figure 6.16), while it shows a favourable $S_1$ gradient after the bond-order inversion is complete (i.e. BLA < 0.05 Å). The steep torsional gradient observed on all states for BLA < −0.03 Å and BLA > 0.12 Å at the 11-*cis* and all-*trans* torsional values (see orange circles in Figure 6.16) is due to the high destabilisation, inside the protein embedding, of highly-distorted BLA geometries close to FC points. Indeed, rotation around the double bonds of the carbon chain is able to accommodate/compensate the highly distorted bond lengths, which are instead

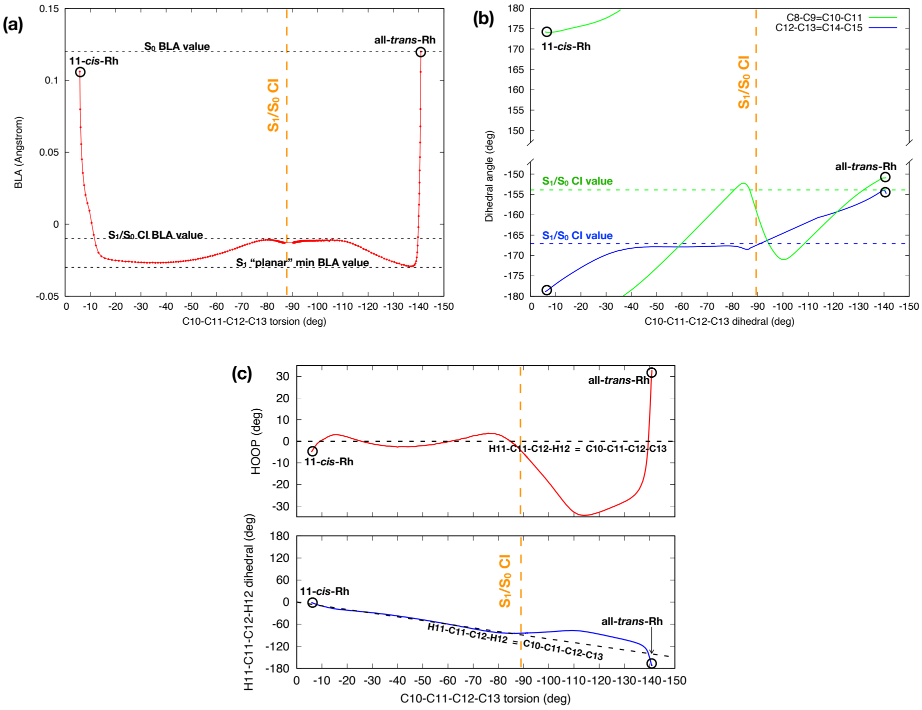

**Figure 6.13:** Variation of the BLA (a), C8-C9-C10-C11/C12-C13-C14-C15 dihedrals (b) and HOOP (c) along the MEPs starting from the 11-*cis* minimum or all-*trans* minimum and ending at the $S_1/S_0$ CI. For the HOOP coordinate both the HOOP value (panel (c), top) and the H11-C11-C12-H12 values are plotted (panel (c), bottom), together with the HOOP = 0 reference (black dashed line). In all panels, the joining point of the two MEPs ($S_1/S_0$ CI) is represented by the vertical orange line.

strongly unfavored at the *cis* and *trans* conformations. However, such discontinuities can be smoothed by appropriate PESs fitting prior to dynamics, retaining only the steep gradient that will hinder any wavepacket/trajectory to populate such distorted geometries for a long time.

The BLA coordinate shows a quadratic profile for all torsional values and for all three states (Figure 6.17). At *cis* and *trans* minima, the BLA minimum on the ground state is found at positive values, while it shifts towards 0 Å for twisted geometries. Instead, both $S_1$ and $S_2$ minima are always found at small (or negative) BLA values, originating the initial gradient at the FC point.

Besides the position of stationary points, a fundamental characteristic of the parameterised PESs is represented by the reactive $S_1$-$S_0$ crossing seam. No $S_1/S_0$ CIs are observed at CASSCF level in this scan. Indeed, even if the MEP was calculated at SA2-CASSCF level and clearly leads towards the SA2-CASSCF $S_1/S_0$ crossing, the inclusion of the third root (SA3-CASSCF) removes the degeneracy at this level of theory. However, the CI is still captured by CASPT2 (as discussed previously). The right panels of Figure 6.16 show some close-up of the CASPT2 profiles for torsion [−70°:−120°]. While MS- and XMS-CASPT2 both predict the lowest $S_1$ energies around −90° torsion, they somehow disagree on the BLA values: the lowest energy gaps $\Delta E_{S_1-S_0}$ are found at

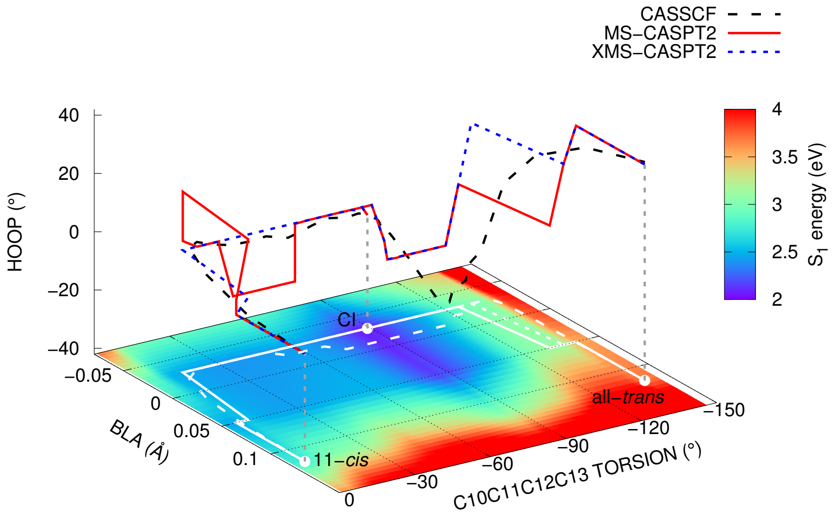

**Figure 6.14:** Comparison between the optimised CASSCF MEP on $S_1$ (black dashed line) and the (X)MS-CASPT2 MEP extrapolated from the 3D grid. The $S_1$ PES along torsion and BLA is shown on the bottom plane (at MS-CASPT2 level), together with the projection of the three MEPs on the same 2D space.

**Table 6.3:** Energies (eV) of lowest (X)MS-CASPT2 crossing points (i.e. $\Delta E_{S_1-S_0}$ < 0.15 eV) from the 3D torsion-BLA-HOOP grid.

| | Torsion (°) | BLA (Å) | HOOP (°) | MS-CASPT2 | | | XMS-CASPT2 | | |
|---|---|---|---|---|---|---|---|---|---|
| | | | | $S_0$ | $S_1$ | $S_2$ | $S_0$ | $S_1$ | $S_2$ |
| CI-MS-1 | -87.0 | −0.03 | 0.0 | **1.95** | **2.03** | 4.25 | 1.68 | 1.99 | 4.37 |
| CI-MS-2 | -85.8 | −0.03 | 0.0 | **1.93** | **2.06** | 4.27 | 1.69 | 1.99 | 4.38 |
| CI-MS-3 | -90.8 | −0.03 | −6.6 | **1.98** | **2.08** | 4.32 | 1.71 | 2.04 | 4.43 |
| CI-MS-4 | -89.1 | −0.03 | −3.1 | **2.05** | **2.10** | 4.34 | 1.75 | 2.09 | 4.46 |
| CI-XMS-1 | -85.8 | 0.05 | −0.8 | 1.89 | 2.15 | 4.12 | **1.81** | **1.96** | 4.24 |
| CI-XMS-2 | -85.8 | 0.05 | 0.0 | 1.90 | 2.15 | 4.13 | **1.83** | **1.97** | 4.24 |
| CI-XMS-3 | -90.8 | 0.05 | −6.6 | 1.93 | 2.17 | 4.16 | **1.84** | **1.98** | 4.28 |
| CI-XMS-4 | -75.9 | 0.05 | 20.0 | 1.96 | 2.26 | 4.21 | **1.93** | **2.02** | 4.32 |

slightly negative BLA values for MS-CASPT2, while the XMS-CASPT2 crossing seam is found at slightly positive BLA. Table 6.3 shows the geometrical parameters and energies of the four lowest energy $S_1/S_0$ CIs of the 3D grid for MS- and XMS-CASPT2 (where we have considered as CIs all those points in which $\Delta E_{S_1-S_0}$ < 0.15 eV). The geometries labelled CI-MS-3, CI-MS-4, CI-XMS-1 and CI-XMS-3 belong to this first BLA scan (while the other four structures are found after HOOP scan and are discussed later). All the identified CIs show similar structures, with the major differences observed in the BLA values between MS- and XMS-CASPT2 as discussed before. It is worth to notice that these crossing regions are accessible from *cis* FC point, whose energy is 2.66/2.78 eV at MS/XMS-CASPT2, respectively.

Concerning $S_2$, it is generally destabilised by torsion at all levels of theory, with the nice result that it is not interfering with $S_1$ and $S_0$ in the crossing region. However, especially for positive BLA values, it sometimes approaches $S_1$ (see Figure 6.17), especially at CASSCF level (degeneracy is then resolved by CASPT2 correction).

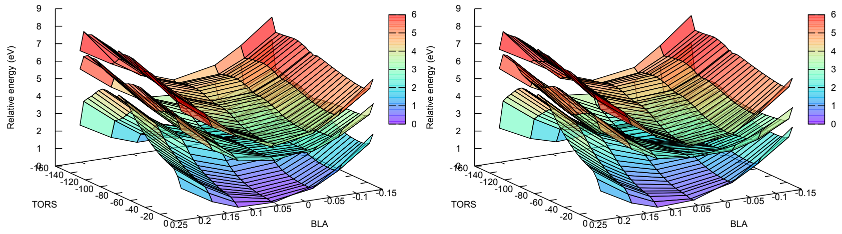

(a) MS-CASPT2 (b) XMS-CASPT2

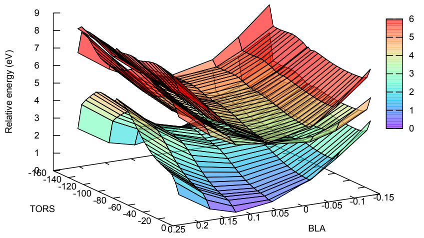

(c) CASSCF

**Figure 6.15:** Potential energy surfaces of $S_0$, $S_1$ and $S_2$ of the retinal chromophore inside rhodopsin along the complex torsion and BLA coordinates.

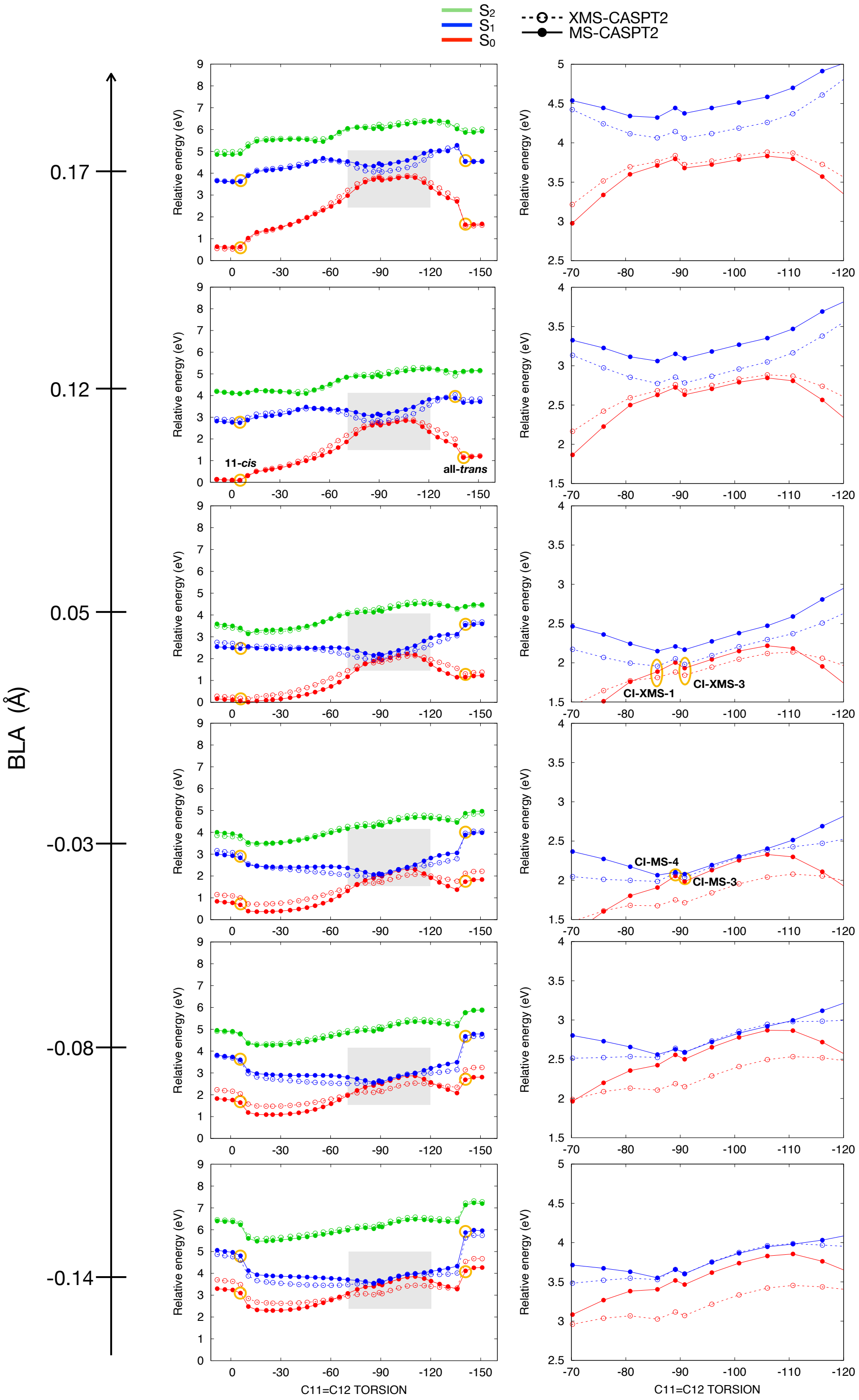

**Figure 6.16:** (X)MS-CASPT2 profiles along the torsion coordinate for fixed BLA values. The shaded area where CASPT2-S$_1$ and S$_0$ get closer in energy is zoomed on the right.

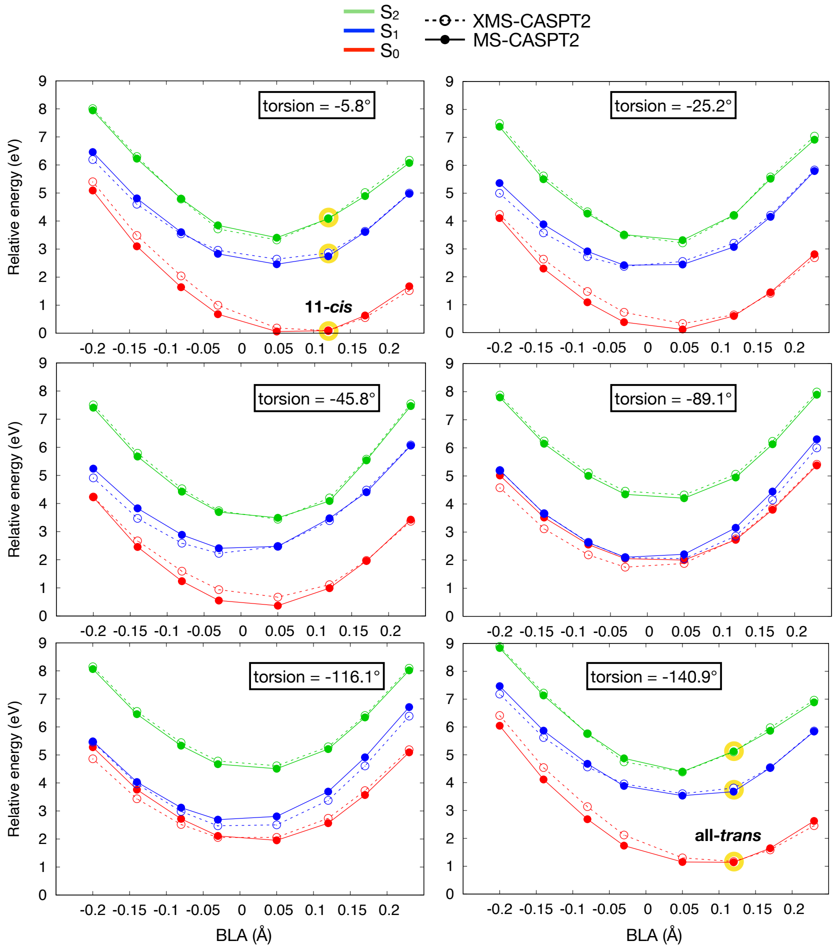

**Figure 6.17:** (X)MS-CASPT2 profiles along the BLA coordinate for selected torsional values.

### Torsion-BLA-HOOP grid

Figure 6.18 shows the $S_0$, $S_1$ and $S_2$ PESs along the torsion and HOOP coordinates for the BLA values at which $S_0$ and $S_1$ come closer in energy (i.e. BLA = 0.05 and −0.03 Å for MS-CASPT2 and BLA = 0.12 and 0.05 Å for XMS-CASPT2). The crossing between $S_1$ and $S_0$ at twisted geometries is clearly visible, while $S_2$ is always higher in energy and not interacting. For a better visualisation of the crossing seam, Figure 6.19 (left) shows the $S_1$-$S_0$ energy in the BLA-HOOP space for several torsional values. The crossing region spreads from C10−C11=C12−C13 ~ −60° to −120°, with all the lowest-energy crossings found between −75° and −91° (see Table 6.3). As discussed previously, the XMS CIs are fund for higher (more positive) BLA values compared to MS-CASPT2. Concerning the HOOP, it emerges that the MS-CASPT2 crossing region is more spread along BLA but more "peaked" along the HOOP (blue-violet region in the left panels of Figure 6.19) compared to XMS-CASPT2, which shows less real-degeneracy points, but with a broader avoided-crossing region along the HOOP. Moving from the *cis* to the *trans* side, the crossing region shifts from positive to negative HOOP values for both CASPT2 corrections, passing through HOOP = 0° around −90° torsion. This trend is testified by the geometries of the lowest crossing points in Table 6.3: CI-XMS-4 located on the "*cis* side" (−75.9° torsion) and is characterised by a significant positive HOOP value (20°), while all other structures are closer to −90° torsion and show small HOOP values.

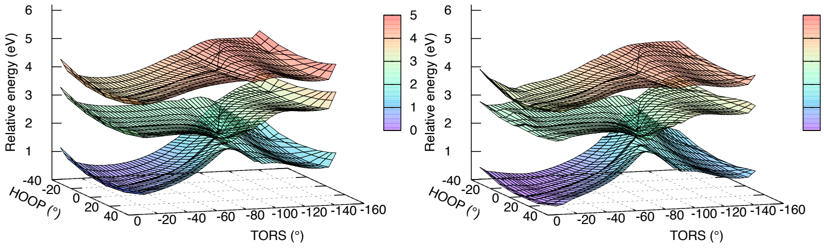

(a) BLA = −0.03 Å (MS)

(b) BLA = 0.05 Å (MS)

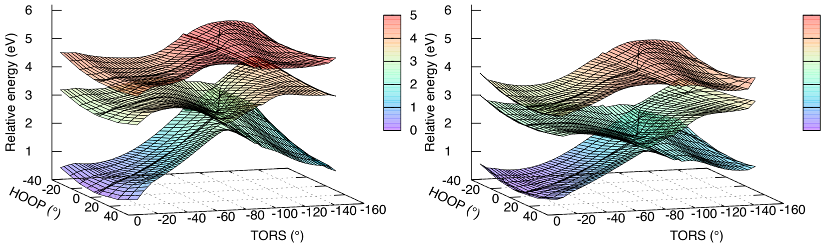

(c) BLA = 0.12 Å (XMS)

(d) BLA = 0.05 Å (XMS)

**Figure 6.18:** Potential energy surfaces of $S_0$, $S_1$ and $S_2$ of the retinal chromophore inside rhodopsin along the complex torsion and HOOP coordinates (a) MS-CASPT2 PESs for fixed BLA = −0.03 Å; (b) MS-CASPT2 PESs for fixed BLA = 0.05 Å; (c) XMS-CASPT2 PESs for fixed BLA = 0.12 Å; (d) XMS-CASPT2 PESs for fixed BLA = 0.05 Å.

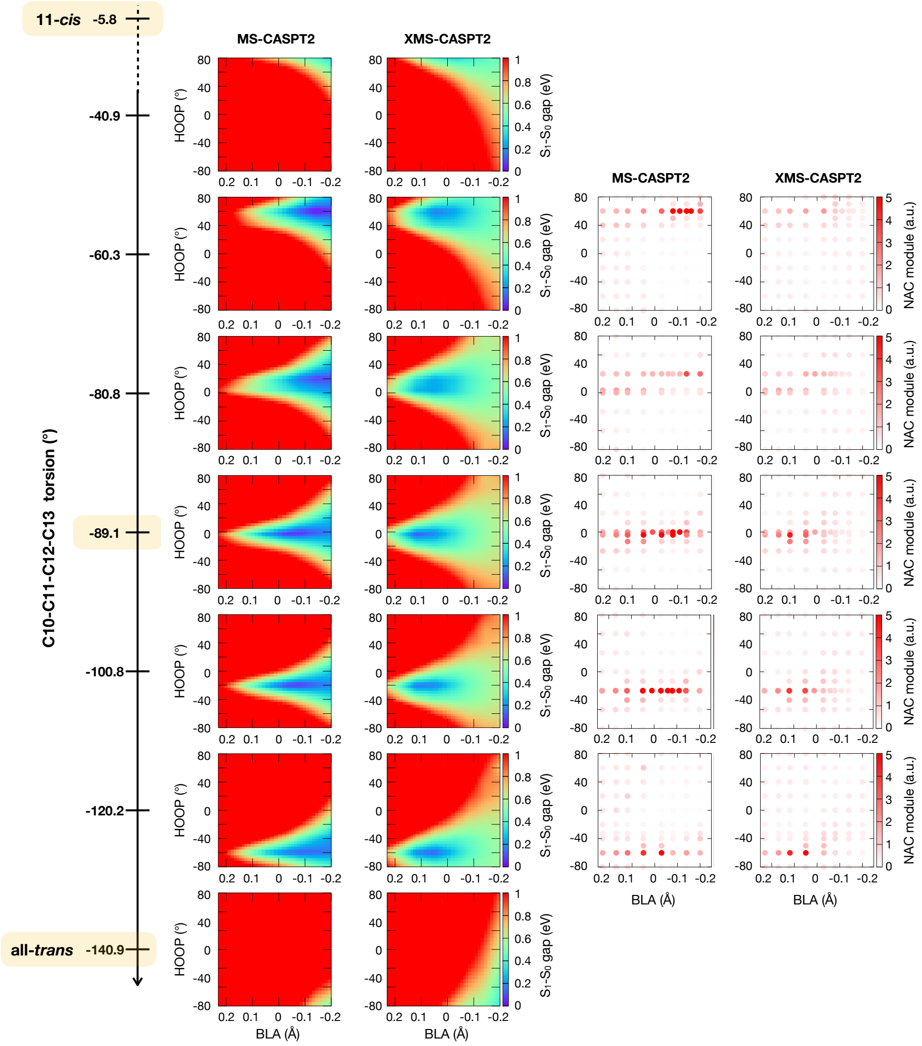

**Figure 6.19:** $S_1$-$S_0$ energy gap (left panels) and NAC module (right panels) along BLA-HOOP for selected torsional values.

### 6.5.4 Non adiabatic couplings

The (X)MS-CASPT2 NACs were calculated for all three couples of states between −10° and −135° torsion for all BLA and HOOP values. The $S_2/S_1$ and $S_2/S_0$ NACs are always small, while the $S_1/S_0$ NAC gains magnitude in the region where the two states get close in energy. The $S_1/S_0$ NAC module for selected torsional values is shown in the right panels of Figure 6.19. In agreement with the topology of the crossing seam described above, the MS-CASPT2 NAC is largest at slightly negative BLA, while the peak along the HOOP shifts from positive to negative values as the torsion proceeds from *cis* to *trans*. The same HOOP trend is observed for XMS-CASPT NACs, which however show highest values for slightly positive values of BLA (Figure 6.19).

To assess our protocol for NAC calculation, and to make sure that our three coordinates capture a sufficient portion of the full NAC (which also gives an estimate of the accuracy of the selected coordinates), the full cartesian $S_1/S_0$ MS-CASPT2 NAC was calculated for one of the torsional scans. The results are shown in Figure 6.20. Our three coordinates are able to reproduce a large part of the full NAC, especially at the crossing region, where BLA, HOOP and complex torsion account for about 70% of the total NAC vector. Away from the crossing region, the fraction of NAC reproduced is still relevant (~30%) although smaller. However, the absolute value of the coupling is small here, and it is therefore expected that the missing portion of the NAC will not affect the dynamics in a significant way.

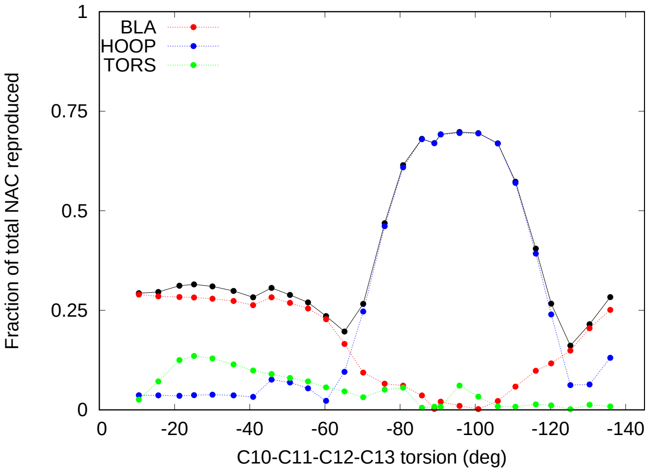

**Figure 6.20:** Fraction of the full cartesian $S_1/S_0$ MS-CASPT2 NAC vector reproduced by its components along BLA (red) HOOP (blue) and complex TORSION (green) directly computed as described in section 3.4.1 (BLA fixed at 0.12 Å, from the initial MEP-BLA scan). The black line represents fraction of total NAC reproduced by all three components.

Figure 6.20 is also representative of the general trend in the relevance of the three reactive coordinate in reproducing the $S_1/S_0$ NAC: across all the grid, the BLA component of the NAC vector is the highest close to the 11-*cis* and all-*trans* torsional values, while moving towards the twisted (crossing) region, the HOOP component always dominates. This further testifies the importance of the HOOP coordinate as coupling mode for the rhodopsin model, in agreement with previous findings[21–23, 37].

## 6.6 Conclusions

We have parameterised a three-states, three-modes model for the retinal chromophore inside rhodopsin based on accurate QM/MM calculations (i.e. (X)MS-3-CASPT2/SA3-CASSCF(12,12)/6-31G*/AMBER) that could serve as solid basis for the simulation of the photoisomerization process inside the protein by means of quantum or mixed quantum/classical dynamics. Our data could allow to perform dynamics simulations of high accuracy, especially in the case of QD for which (to the best of our knowledge) previous simulations reported in the literature are based on either accurate description of the relevant coordinates but for minimal models in the gas phase[23], or they account for the protein embedding but at the expenses of the accuracy in the coordinate description (Hahn-Stock model and its variants[29, 32–36]).

The model coordinates include the bond-length-alternation (BLA), H11 and H12 hydrogens out-of-plane wagging (HOOP) and a complex torsional motion of many dihedrals along the chain, describing the bicycle pedal mechanism previously reported[14]. For the 3D grid construction, we took advantage of the fact that the union of the two $S_1$ MEPs (starting from either *cis* or *trans* FC points) forms a continuous optimised path connecting all relevant structures for the isomerization (i.e. *cis* and *trans* $S_0$ minima, lowest $S_1/S_0$ CI and $S_1$ “planar” minimum visited through BLA relaxation after the photoexcitation) following exactly the three model coordinates. Such MEP path was sampled to obtain almost uniform steps of 5° for the isomerizing dihedral, and each sampled geometry was then used as starting point for the generation of the BLA-HOOP grid. The energies, TDMs and NACs of the three lowest electronic states were calculated across the grid, both using MS- and XMS-CASPT2 correction in order to appreciate any difference between the two methods.

The resulting PESs show a qualitative agreement between CASSCF and CASPT2 topologies, both in terms of position of the reference structures and (more importantly) in terms of MEP connecting them, thus justifying the use of the CASSCF MEP for the grid construction. The $S_1/S_0$ crossing seam spreads around the optimised CI in all three coordinates and includes twisted geometries between $-60°$ and $-120°$ of torsion. The two CASPT2 methods predict similar PESs topology, with the only difference in the BLA position of the crossing seam which, according to MS-CASPT2 is found mainly at slightly negative BLA values, while the bond-order inversion is less pronounced at XMS-CASPT2 level, whose CI seam is found at slightly positive BLA values. The HOOP coordinate is found to play a crucial role as coupling mode between $S_1$ and $S_0$ states, especially in the crossing region, where it accounts alone for more than 70% of the total NAC value. The $S_2$ state was also included in the model, due to its (almost)crossing with $S_2$ at CASSCF level for BLA-distorted geometries, which however is resolved by both CASPT2 correction, with a consequent small magnitude of the corresponding NAC in all gridpoints.

The selection of the three reactive coordinates for the description of the photoisomerization was further assessed by comparison of the full MS-CASPT2 numerical $S_1/S_0$ NAC with the reduced NAC made up of its three components along the model coordinates. The high fraction of the total NAC reproduced (~ 75 % around the crossing seam) proves their accuracy.

A complete assessment of our model can be reached only through its employment in dynamics simulations, and we are currently planning to perform QD as well as trajectory surface hopping dynamics based on the presented PESs and couplings. Accurate QD simulations of this fascinating process inside the protein embedding are still missing, and could give more insight on quantum effects related to the nonadiabatic event.

## References

[1] G. Wald and P. K. Brown, "Human Rhodopsin," *Science*, vol. 127 (3292), pp. 222–249, **1958**.

[2] L. H. Andersen, I. B. Nielsen, M. B. Kristensen, M. O. A. El Ghazaly, S. Haacke, M. B. Nielsen, and M. Å. Petersen, "Absorption of Schiff-Base Retinal Chromophores in Vacuo," *Journal of the American Chemical Society*, vol. 127 (35), pp. 12 347–12 350, **2005**.

[3] O. P. Ernst, D. T. Lodowski, M. Elstner, P. Hegemann, L. S. Brown, and H. Kandori, "Microbial and Animal Rhodopsins: Structures, Functions, and Molecular Mechanisms," *Chemical Reviews*, vol. 114 (1), pp. 126–163, **2014**.

[4] J. E. Kim, M. J. Tauber, and R. A. Mathies, "Wavelength Dependent Cis-Trans Isomerization in Vision," *Biochemistry*, vol. 40 (46), pp. 13 774–13 778, **2001**.

[5] R. W. Schoenlein, L. A. Peteanu, R. A. Mathies, and C. V. Shank, "The First Step in Vision: Femtosecond Isomerization of Rhodopsin," *Science*, vol. 254 (5030), pp. 412–415, **1991**.

[6] Q. Wang, R. W. Schoenlein, L. A. Peteanu, R. A. Mathies, and C. V. Shank, "Vibrationally Coherent Photochemistry in the Femtosecond Primary Event of Vision," *Science*, vol. 266 (5184), pp. 422–424, **1994**.

[7] P. J. M. Johnson, A. Halpin, T. Morizumi, V. I. Prokhorenko, O. P. Ernst, and R. J. D. Miller, "Local vibrational coherences drive the primary photochemistry of vision," *Nature Chemistry*, vol. 7 (12), pp. 980–986, **2015**.

[8] K. A. Freedman and R. S. Becker, "Comparative investigation of the photoisomerization of the protonated and unprotonated n-butylamine Schiff bases of 9-cis-, 11-cis-, 13-cis-, and all-trans-retinals," *Journal of the American Chemical Society*, vol. 108 (6), pp. 1245–1251, **1986**.

[9] M. Garavelli, P. Celani, F. Bernardi, M. A. Robb, and M. Olivucci, "The $C_5H_6NH_2^+$ Protonated Shiff Base: An ab Initio Minimal Model for Retinal Photoisomerization," *Journal of the American Chemical Society*, vol. 119 (29), pp. 6891–6901, **1997**.

[10] M. Garavelli, T. Vreven, P. Celani, F. Bernardi, M. A. Robb, and M. Olivucci, "Photoisomerization Path for a Realistic Retinal Chromophore Model: The Nonatetraeniminium Cation," *Journal of the American Chemical Society*, vol. 120 (6), pp. 1285–1288, **1998**.

[11] F. Bernardi, M. Olivucci, and M. A. Robb, "Potential energy surface crossings in organic photochemistry," *Chemichal Society Review*, vol. 25, pp. 321–328, 5 **1996**.

[12] I. Rivalta, A. Nenov, O. Weingart, G. Cerullo, M. Garavelli, and S. Mukamel, "Modelling Time-Resolved Two-Dimensional Electronic Spectroscopy of the Primary Photoisomerization Event in Rhodopsin," *The Journal of Physical Chemistry B*, vol. 118 (28), pp. 8396–8405, **2014**.

[13] G. Tomasello, G. Olaso-González, P. Altoè, M. Stenta, L. Serrano-Andrés, M. Merchán, G. Orlandi, A. Bottoni, and M. Garavelli, "Electrostatic Control of the Photoisomerization Efficiency and Optical Properties in Visual Pigments: On the Role of Counterion Quenching," *Journal of the American Chemical Society*, vol. 131 (14), pp. 5172–5186, **2009**.

[14] S. Sen, R. K. Kar, V. A. Borin, and I. Schapiro, "Insight into the isomerization mechanism of retinal proteins from hybrid quantum mechanics/molecular mechanics simulations," *WIRES Computational Molecular Science*, **2021**.

[15] M. M. T. El-Tahawy, A. Nenov, O. Weingart, M. Olivucci, and M. Garavelli, "Relationship between Excited State Lifetime and Isomerization Quantum Yield in Animal Rhodopsins: Beyond the One-Dimensional Landau–Zener Model," *The Journal of Physical Chemistry Letters*, vol. 9 (12), pp. 3315–3322, **2018**.

[16] S. Gozem, H. L. Luk, I. Schapiro, and M. Olivucci, "Theory and Simulation of the Ultrafast Double-Bond Isomerization of Biological Chromophores," *Chemical Reviews*, vol. 117 (22), pp. 13 502–13 565, **2017**.

[17] P. Kukura, D. W. McCamant, S. Yoon, D. B. Wandschneider, and R. A. Mathies, "Structural Observation of the Primary Isomerization in Vision with Femtosecond-Stimulated Raman," *Science*, vol. 310 (5750), pp. 1006–1009, **2005**.

[18] D. Polli, P. Altoè, O. Weingart, K. M. Spillane, C. Manzoni, D. Brida, G. Tomasello, G. Orlandi, P. Kukura, R. A. Mathies, M. Garavelli, and G. Cerullo, "Conical intersection dynamics of the primary photoisomerization event in vision," *Nature*, vol. 467 (7314), pp. 440–443, **2010**.

[19] C. Schnedermann, X. Yang, M. Liebel, K. M. Spillane, J. Lugtenburg, I. Fernández, A. Valentini, I. Schapiro, M. Olivucci, P. Kukura, and R. A. Mathies, "Evidence for a vibrational phase-dependent isotope effect on the photochemistry of vision," *Nature Chemistry*, vol. 10 (4), pp. 449–455, **2018**.

[20] S. Hayashi, E. Tajkhorshid, and K. Schulten, "Photochemical Reaction Dynamics of the Primary Event of Vision Studied by Means of a Hybrid Molecular Simulation," *Biophysical Journal*, vol. 96 (2), pp. 403–416, **2009**.

[21] O. Weingart, P. Altoè, M. Stenta, A. Bottoni, G. Orlandi, and M. Garavelli, "Product formation in rhodopsin by fast hydrogen motions," *Physical Chemistry Chemical Physics*, vol. 13, pp. 3645–3648, 9 **2011**.

[22] I. Schapiro, M. N. Ryazantsev, L. M. Frutos, N. Ferrè, R. Lindh, and M. Olivucci, "The Ultrafast Photoisomerizations of Rhodopsin and Bathorhodopsin Are Modulated by Bond Length Alternation and HOOP Driven Electronic Effects," *Journal of the American Chemical Society*, vol. 133 (10), pp. 3354–3364, **2011**.

[23] E. Marsili, M. Olivucci, D. Lauvergnat, and F. Agostini, "Quantum and Quantum-Classical Studies of the Photoisomerization of a Retinal Chromophore Model," *Journal of Chemical Theory and Computation*, vol. 16 (10), pp. 6032–6048, **2020**.

[24] K. Schulten, W. Humphrey, I. Logunov, M. Sheves, and D. Xu, “Molecular Dynamics Studies of Bacteriorhodopsin’s Photocycles,” *Israel Journal of Chemistry*, vol. 35 (3-4), pp. 447–464, **1995**.

[25] K. C. Hasson, F. Gai, and P. A. Anfinrud, “The photoisomerization of retinal in bacteriorhodopsin: Experimental evidence for a three-state model,” *Proceedings of the National Academy of Sciences*, vol. 93 (26), pp. 15 124–15 129, **1996**.

[26] F. Gai, K. C. Hasson, J. C. McDonald, and P. A. Anfinrud, “Chemical Dynamics in Proteins: The Photoisomerization of Retinal in Bacteriorhodopsin,” *Science*, vol. 279 (5358), pp. 1886–1891, **1998**.

[27] J. P. Kraack, T. Buckup, and M. Motzkus, “Evidence for the Two-State-Two-Mode model in retinal protonated Schiff-bases from pump degenerate four-wave-mixing experiments,” *Physical Chemistry Chemicl Physics*, vol. 14, pp. 13 979–13 988, 40 **2012**.

[28] R. González-Luque, M. Garavelli, F. Bernardi, M. Merchán, M. A. Robb, and M. Olivucci, “Computational evidence in favor of a two-state, two-mode model of the retinal chromophore photoisomerization,” *Proceedings of the National Academy of Sciences*, vol. 97 (17), pp. 9379–9384, **2000**.

[29] P. J. M. Johnson, M. H. Farag, A. Halpin, T. Morizumi, V. I. Prokhorenko, J. Knoester, T. L. C. Jansen, O. P. Ernst, and R. J. D. Miller, “The Primary Photochemistry of Vision Occurs at the Molecular Speed Limit,” *The Journal of Physical Chemistry B*, vol. 121 (16), pp. 4040–4047, **2017**.

[30] M. H. Farag, T. L. C. Jansen, and J. Knoester, “The origin of absorptive features in the two-dimensional electronic spectra of rhodopsin,” *Physical Chemistry Chemical Physics*, vol. 20, pp. 12 746–12 754, 18 **2018**.

[31] P. A. Kusochek, V. V. Logvinov, and A. V. Bochenkova, “Role of the Protein Environment in Photoisomerization of Type I and Type II Rhodopsins: a Theoretical Perspective,” *Moscow University Chemistry Bulletin*, vol. 76 (6), pp. 407–416, **2021**.

[32] S. Hahn and G. Stock, “Quantum-Mechanical Modeling of the Femtosecond Isomerization in Rhodopsin,” *The Journal of Physical Chemistry B*, vol. 104 (6), pp. 1146–1149, **2000**.

[33] G. Gaulier, Q. Dietschi, S. Bhattacharyya, C. Schmidt, M. Montagnese, A. Chauvet, S. Hermelin, F. Chiodini, L. Bonacina, P. L. Herrera, U. Rothlisberger, I. Rodriguez, and J.-P. Wolf, “Ultrafast pulse shaping modulates perceived visual brightness in living animals,” *Science Advances*, vol. 7 (18), eabe1911, **2021**.

[34] M. Sala and D. Egorova, “Quantum dynamics of multi-dimensional rhodopsin photoisomerization models: Approximate versus accurate treatment of the secondary modes,” *Chemical Physics*, vol. 515, pp. 164–176, **2018**.

[35] C.-Y. Lu, T.-Y. Lee, and C.-C. Chou, “Moving boundary truncated grid method for electronic nonadiabatic dynamics,” *The Journal of Chemical Physics*, vol. in press, **2021**.

[36] X. Chen and V. S. Batista, "The MP/SOFT methodology for simulations of quantum dynamics: Model study of the photoisomerization of the retinyl chromophore in visual rhodopsin," *Journal of Photochemistry and Photobiology A: Chemistry*, vol. 190 (2), pp. 274–282, **2007**.

[37] E. Marsili, M. H. Farag, X. Yang, L. De Vico, and M. Olivucci, "Two-State, Three-Mode Parametrization of the Force Field of a Retinal Chromophore Model," *The Journal of Physical Chemistry A*, vol. 123 (9), pp. 1710–1719, **2019**.

[38] A. Warshel and M. Levitt, "Theoretical studies of enzymic reactions: Dielectric, electrostatic and steric stabilization of the carbonium ion in the reaction of lysozyme," vol. 103 (2), pp. 227–249, **1976**.

[39] H. M. Senn and W. Thiel, "QM/MM Methods for Biomolecular Systems," *Angewandte Chemie International Edition*, vol. 48 (7), pp. 1198–1229, **2009**.

[40] L. Cao and U. Ryde, "On the Difference Between Additive and Subtractive QM/MM Calculations," *Frontiers in Chemistry*, vol. 6, **2018**.

[41] M. Garavelli, F. Negri, and M. Olivucci, "Initial Excited-State Relaxation of the Isolated 11-cis Protonated Schiff Base of Retinal: Evidence for in-Plane Motion from ab Initio Quantum Chemical Simulation of the Resonance Raman Spectrum," *Journal of the American Chemical Society*, vol. 121 (5), pp. 1023–1029, **1999**.

[42] O. Weingart, A. Nenov, P. Altoè, I. Rivalta, J. Segarra-Martí, I. Dokukina, and M. Garavelli, "COBRAMM 2.0 — A software interface for tailoring molecular electronic structure calculations and running nanoscale (QM/MM) simulations," vol. 24 (9), p. 271, **2018**.

[43] P. Altoè, M. Stenta, A. Bottoni, and M. Garavelli, "A tunable QM/MM approach to chemical reactivity, structure and physico-chemical properties prediction," vol. 118 (1), pp. 219–240, **2007**.

[44] Cobramm on GitLab, available at: `https://gitlab.com/cobrammgroup/cobramm/-/wikis/home`.

[45] D. A. Case, I. Y. Ben-Shalom, S. R. Brozell, D. S. Cerutti, T. Cheatham, V. Cruzeiro, T. Darden, R. Duke, D. Ghoreishi, M. Gilson, H. Gohlke, A. Goetz, D. Greene, R. Harris, N. Homeyer, Y. Huang, S. Izadi, A. Kovalenko, T. Kurtzman, T. Lee, S. LeGrand, P. Li, C. Lin, J. Liu, T. Luchko, R. Luo, D. Mermelstein, K. Merz, Y. Miao, G. Monard, C. Nguyen, H. Nguyen, I. Omelyan, A. Onufriev, F. Pan, R. Qi, D. Roe, A. Roitberg, C. Sagui, S. Schott-Verdugo, J. Shen, C. Simmerling, J. Smith, R. Salomon- Ferrer, J. Swails, R. Walker, J. Wang, H. Wei, R. Wolf, X. Wu, L. Xiao, D. York, and P. Kollman, *AMBER18*, **2018**.

[46] N. Ferré and M. Olivucci, "Probing the Rhodopsin Cavity with Reduced Retinal Models at the CASPT2//CASSCF/AMBER Level of Theory," *Journal of the American Chemical Society*, vol. 125 (23), pp. 6868–6869, **2003**.

[47] N. Ferré, A. Cembran, M. Garavelli, and M. Olivucci, "Complete-active-space self-consistent-field/Amber parameterization of the Lys296-retinal-Glu113 rhodopsin chromophore-counterion system," *Theoretical Chemistry Accounts*, vol. 112 (4), **2004**.

[48] M. M. T. El-Tahawy, A. Nenov, and M. Garavelli, "Photoelectrochromism in the Retinal Protonated Schiff Base Chromophore: Photoisomerization Speed and Selectivity under a Homogeneous Electric Field at Different Operational Regimes," *Journal of Chemical Theory and Computation*, vol. 12 (9), pp. 4460–4475, **2016**.

[49] I. Fdez. Galván, M. Vacher, A. Alavi, C. Angeli, F. Aquilante, J. Autschbach, J. J. Bao, S. I. Bokarev, N. A. Bogdanov, R. K. Carlson, L. F. Chibotaru, J. Creutzberg, N. Dattani, M. G. Delcey, S. S. Dong, A. Dreuw, L. Freitag, L. M. Frutos, L. Gagliardi, F. Gendron, A. Giussani, L. González, G. Grell, M. Guo, C. E. Hoyer, M. Johansson, S. Keller, S. Knecht, G. Kovačević, E. Källman, G. Li Manni, M. Lundberg, Y. Ma, S. Mai, J. P. Malhado, P. Å. Malmqvist, P. Marquetand, S. A. Mewes, J. Norell, M. Olivucci, M. Oppel, Q. M. Phung, K. Pierloot, F. Plasser, M. Reiher, A. M. Sand, I. Schapiro, P. Sharma, C. J. Stein, L. K. Sørensen, D. G. Truhlar, M. Ugandi, L. Ungur, A. Valentini, S. Vancoillie, V. Veryazov, O. Weser, T. A. Wesołowski, P.-O. Widmark, S. Wouters, A. Zech, J. P. Zobel, and R. Lindh, "OpenMolcas: From Source Code to Insight," vol. 15 (11), pp. 5925–5964, **2019**.

[50] F. Aquilante, J. Autschbach, A. Baiardi, S. Battaglia, V. A. Borin, L. F. Chibotaru, I. Conti, L. D. Vico, M. Delcey, I. F. Galván, N. Ferré, L. Freitag, M. Garavelli, X. Gong, S. Knecht, E. D. Larsson, R. Lindh, M. Lundberg, P. Å. Malmqvist, A. Nenov, J. Norell, M. Odelius, M. Olivucci, T. B. Pedersen, L. Pedraza-González, Q. M. Phung, K. Pierloot, M. Reiher, I. Schapiro, J. Segarra-Martí, F. Segatta, L. Seijo, S. Sen, D.-C. Sergentu, C. J. Stein, L. Ungur, M. Vacher, A. Valentini, and V. Veryazov, "Modern quantum chemistry with [Open]Molcas," vol. 152 (21), p. 214 117, **2020**.

[51] H. Nakamichi and T. Okada, "Crystallographic analysis of primary visual photochemistry," *Angewandte Chemie International Edition*, vol. 45 (26), pp. 4270–4273, **2006**.

[52] M. Schreiber, M. Sugihara, T. Okada, and V. Buss, "Quantum mechanical studies on the crystallographic model of bathorhodopsin," *Angewandte Chemie International Edition*, vol. 45 (26), pp. 4274–4277, **2006**.

[53] H. Kandori, Y. Shichida, and T. Yoshizawa, "Absolute absorption spectra of batho- and photorhodopsins at room temperature. Picosecond laser photolysis of rhodopsin in polyacrylamide," *Biophysical Journal*, vol. 56 (3), pp. 453–457, **1989**.

# Chapter 7

# Concluding remarks

During my three-years PhD research activity I have extensively used accurate wavefunction-based quantum chemistry electronic structure methods such as CASPT2/CASSCF (and their restricted version RASPT2/RASSCF) to parameterise different models for the simulation of non adiabatic events in photoactive systems. This implies both the development of general computational tools for the parameterisation of quantities like energies and non adiabatic couplings (NACs), but also a specific tailoring of the approach for each case (e.g. choice of level of theory for the electronic structure, type of dynamics simulation, selection of reduced coordinates).

The produced data allowed to simulate with high levels of accuracy the excited-state quantum dynamics of relevant photoactive systems like azobenzene, pyrene and the retinal chromophore inside rhodopsin. For each system, the first crucial step was the selection of the photochemically (or photophysically) active coordinates, represented by either few key internal coordinates (e.g. azobenzene), a subset of normal modes (e.g. pyrene) or even by complex mixtures of many degrees of freedom (e.g. rhodopsin). The second important point for the construction of accurate models is the selection of the level of theory. Indeed, it is fundamental to select the best active space and flavour of perturbative correction (e.g. single state, multistate, extended multistate, etc.) for each specific case, especially when mapping energies and wavefunctions over a wide range of geometries, which can be quite deformed and significantly different from the ground state minimum. The optimal level of theory should represent the best compromise between accuracy and computational time.

In order to obtain accurate and wide sets of data with a fair computational cost, some computational tools were developed and implemented in the computational chemistry software COBRAMM[1–3] for the direct calculation of the components of vectorial quantities (like gradients and NACs) along reactive coordinates, significantly reducing the computational cost.

Our model for the azobenzene molecule consists of two states and three internal coordinates (the central C−N=N−C dihedral and the two C−N=N bending angles) which are able to describe both proposed mechanisms for the *cis*/*trans* photoisomerization (i.e. dihedral torsion or inversion of one of the two bending angles). We have produced an extended map of the $S_0$ and $S_1$ energies and couplings that allowed to get a clear and comprehensive picture of the intersection seam between the two states.

Mixed quantum-classical dynamics using our reduced model showed that it correctly reproduces the n$\pi^*$ *trans* $\longrightarrow$ *cis* quantum yield, and confirmed the torsion as driving coordinate for the isomerization, but with a crucial role of the CNN bendings to desymmetrize the molecule and couple the two states. A similar deactivation mechanism to that of the n$\pi^*$ state of azobenzene was also observed in mixed quantum-classycal (TD-DFT) dynamics simulations of *push-pull* azobenzene derivatives excited to the higher $\pi\pi^*$ state, foreseeing an increase in the bright state quantum yield compared to the parent compound. This interesting behaviour is addresses tho the effect of the electron donating-withdrawing substituents, endorsing the use of *push-pull* derivatives for more efficient, visible-light activated switches. In the case of pure azobenzene, our extended database was employed in a collaboration with the group of Shaul Mukamel for the simulation of transient X-ray diffraction and X-ray Raman spectroscopy experiments during the non adiabatic event, making predictions about specific signatures of the conical intersection passage.

The simulation of the deactivation mechanism of pyrene, in contrast, involves many of its normal modes but with only small deformations due to the rigidity of this aromatic system. In this case, we have developed a parameterisation protocol for a linear vibronic coupling hamiltonian for quantum dynamics based on accurate wavefunction-based multiconfigurational methods. Our results evidence the dependance of the resulting model on the active space size and composition, which must be carefully tuned. Despite not being a "black-box" procedure, our protocol is fully portable and has proved to yield accurate dynamics.

An important assessment of our parameterisation strategies is represented by their application to a photoinduced process taking place in a complex environment. We were able to produce a wide and accurate data set for the photoisomerization of the 11-*cis* retinal chromophore inside rhodopsin, producing the first extended mapping of electronic energies and couplings inside the protein embedding (which was treated using the QM/MM approach). In this case, most recent literature results agree on the need of a two-states, three-modes model including two reactive coordinates (torsion of dihedrals along the carbon chain and bond length alternation) and a coupling mode (out-of-plane wagging of the two hydrogens linked to the isomerizing bond). A model for quantum dynamics simulation of rhodopsin, that accurately accounts for all three degrees of freedom and for the protein embedding at the same time, is still missing, and we hope that future simulations based on our data could add new insight into the dynamics of this fascinating system.

To summarise, we have shown useful computational protocols to produce accurate and extended databases for the simulation of photochemical reactions at a fair computational cost, and tested the resulting models through different types of dynamics simulations (ranging from semiclassical to fully quantum). The developed protocols and strategies can be applied to many small/medium size photoactive systems (both in gas phase and in complex environments) allowing for accurate simulations of ultrafast processes (including complex multi-pulse non-linear spectroscopies) which are still difficult to study experimentally.

# References

[1] P. Altoè, M. Stenta, A. Bottoni, and M. Garavelli, “A tunable QM/MM approach to chemical reactivity, structure and physico-chemical properties prediction,” vol. 118 (1), pp. 219–240, **2007**.

[2] Cobramm on GitLab, available at: `https://gitlab.com/cobrammgroup/cobramm/-/wikis/home`.

[3] O. Weingart, A. Nenov, P. Altoè, I. Rivalta, J. Segarra-Martí, I. Dokukina, and M. Garavelli, “COBRAMM 2.0 — A software interface for tailoring molecular electronic structure calculations and running nanoscale (QM/MM) simulations,” vol. 24 (9), p. 271, **2018**.

# Appendix A

# Cartesian displacements along reactive coordinates

The use of arbitrary coordinates in numerical calculations is a powerful strategy to reduce the computational cost. However, a robust procedure to correctly generate displacements along arbitrary coordinates is needed, in order to obtain structures which are consistent with the desired geometrical deformation, that are orthogonal to all other reactive coordinates and that do not contain pure rotations and translations.

In the case of the retinal chromophore inside rhodopsin described in chapter 6, the main hurdle is represented by the non-linear torsional coordinate. Indeed, the BLA stretching and HOOP wagging are well described by linear variation of single or multiple bonds/dihedrals, that allows to obtain the unit vector pointing in their direction quite easily at any grid point. In contrast, the torsional coordinate was defined through the union of two optimised MEPs connecting each GS minimum geometry (*cis* and *trans*) to the same $S_1/S_0$ CI on the excited state, and sampling geometries to have a ~5° step of the isomerizing C10−C11=C12−C13 dihedral. As a result, the variation of all other dihedrals in the chromophore is non-uniform along the path, and the definition of the vector pointing in the direction of the torsion coordinate is not straightforward.

In the following, we describe the procedure for the generation of orthonormal unit vectors along the complex torsion, BLA and HOOP coordinates for the rhodopsin case study of chapter 6, but adaptation to other cases of similar or lower complexity should be easy. The procedure was designed to be integrated with the COBRAMM package[1–3] for the calculation of numerical NACs and produces cartesian displacements removing rigid translations or rotations to satisfy Eckart conditions[4]. The latter requirement is fundamental, otherwise e.g. the wavefunction overlaps between reference and displaced geometries would necessarily be affected by these displacements as well.

The three unit vectors are eventually made orthogonal by application of Gram-Shmidt algorithm, and corresponding orthogonal displacements for numerical NAC calculation at each grid geometry can be obtained.

## A.1 Removing translations and rotations

Determining the Eckart molecule fixed-frame for an arbitrary molecule with respect to a reference geometry is a common problem in chemistry. This implies removing pure translations and rotations from the cartesian coordinates of the displaced structure, to retain only internal vibrations (i.e. geometrical deformations). Removing pure translations from displaced geometries is accomplished by subtracting the reference centre of mass coordinates, while pure rotations are more complicated to deal with.

We have applied an algorithm presented by Krasnoshchekov et al.[5], which makes use of quaternion algebra. A quaternion is a 4D vector $(q_0, q_1, q_2, q_3)$, whose components represent a scalar value $(q_0)$ and the three components of a 3D vector $(q_1, q_2, q_3)$. A quaternions is usually represented as $\left[q_0, \bar{q}\right]$, and it can also be considered as a rotation of the three-dimensional space about the axis specified by the vector of the quaternion $\bar{q}$, by the angle specified by its scalar part $q_0$. The applied algorithm makes use of quaternions to find the rotational matrix that minimises the sum of mass-weighted squared deviations (MWSD) between the reference and displaced geometry. The authors of reference[5] prove that such minimisation ensures satisfying the rotational Eckart conditions.

## A.2 Stretching: bond length alternation

The BLA coordinate is described by a concerted stretching of all carbon-carbon bonds along the chain (see section 6.4.1). However, the range of the C−C oscillation is non uniform, with the central bonds showing the larger differences in the initial and final values. In order to get the most accurate BLA oscillation, we have performed a linear interpolation of each bond length in the retinal chromophore between the two limit structures of BLA, i.e. the 11-*cis* minimum and the $S_1$ “planar” minimum, that show an inversion of the bond order with respect to each other.

To obtain the BLA unit vector at a generic grid point (reference structure):

1. convert the reference structure to “chemically meaningful” Z-matrix format (i.e. making sure that all distances between chemically bonded atoms are defined);
2. for each bond, find the corresponding maximum BLA variation as the difference between its values at the two extremes;
3. create two copies of the reference Z-matrix (Z-mat$_+$ and Z-mat$_-$) and edit each bond length adding ± the corresponding BLA variation;
4. transform back to cartesian coordinates removing translations and rotations with respect to the reference geometry obtaining $xyz_+$ and $xyz_-$;
5. find the BLA unit vector as the normalised cartesian difference between $xyz_+$ and $xyz_-$.

## A.3 Simple torsion: hydrogen out-of-plane wagging

As discussed in section 6.4.1, the HOOP coordinate is numerically evaluated as the difference between the C10−C11=C12−C13 and H11−C11=C12−H12 dihedrals of the retinal chromophore, but a deformation along such coordinate is better achieved by a simultaneous variation of the two H11−C11=C12···C10 and H12−C12=C11···C13 dihedrals (see Figure 6.9).

Deformation along the HOOP for a generic reference geometry is therefore defined by the simple variation of the two dihedrals in the Z-matrix:

- convert the reference structure to Z-matrix format making sure that the two H11−C11=C12···C10 and H12−C12=C11···C13 dihedrals are included;
- create two copies of the reference Z-matrix (Z-mat$_+$ and Z-mat$_-$) and edit the corresponding H11−C11=C12···C10 and H12−C12=C11···C13 values by ±0.001 radians;
- transform back to cartesian coordinates removing translations and rotations with respect to the reference geometry obtaining $xyz_+$ and $xyz_-$;
- find the HOOP unit vector as the normalised cartesian difference between $xyz_+$ and $xyz_-$.

The same procedure can be applied for any coordinate that can be described by a linear displacement of one or multiple angles/dihedrals.

## A.4 Complex torsion

The last and more complicated case is that of the so called "bicycle pedal" motion, that involves the simultaneous rotation around the C11=C12 and C9=C10 bonds, which is actually accompanied by torsion of several other dihedrals in the retinal chromophore. Since in our model we have defined this coordinate through the optimised MEPs connecting the GS minima to the $S_1/S_0$ CI, however, this coordinate is rather curved. Therefore, one needs to define a specific unit vector for each grid geometry. This is achieved through a quadratic interpolation of each dihedral value at each grid point along the torsional coordinate, excluding the first and last torsional values, for which a three-points interpolation was not possible.

To obtain the torsion unit vector at a generic grid point (reference structure):

1. convert the reference structure, together with the previous and following torsional grid points to "chemically meaningful" Z-matrix format (i.e. making sure that all dihedrals involving chemically bonded atoms are defined);
2. for each dihedral defined in the Z-matrix, read its value at the current, previous and following torsional grid point and find the equation of the parabola passing through these three values. In this step, the abscissa value of the current geometry is set to zero, while for the previous and following torsional points, the absolute value of the cartesian difference with the reference geometry is used (in Angstrom, with + and − sign for next and previous torsional structures, respectively);
3. create two copies of the reference Z-matrix (Z-mat$_+$ and Z-mat$_-$) and replace each dihedral value with $f(\pm 0.0001)$ where $f(x)$ is the corresponding quadratic function;

4. transform back to cartesian coordinates removing translations and rotations with respect to the reference geometry obtaining $xyz_+$ and $xyz_-$;
5. find the torsional unit vector as the normalised cartesian difference between $xyz_+$ and $xyz_-$.

## References

[1] F. Aquilante, J. Autschbach, A. Baiardi, S. Battaglia, V. A. Borin, L. F. Chibotaru, I. Conti, L. D. Vico, M. Delcey, I. F. Galván, N. Ferré, L. Freitag, M. Garavelli, X. Gong, S. Knecht, E. D. Larsson, R. Lindh, M. Lundberg, P. Å. Malmqvist, A. Nenov, J. Norell, M. Odelius, M. Olivucci, T. B. Pedersen, L. Pedraza-González, Q. M. Phung, K. Pierloot, M. Reiher, I. Schapiro, J. Segarra-Martí, F. Segatta, L. Seijo, S. Sen, D.-C. Sergentu, C. J. Stein, L. Ungur, M. Vacher, A. Valentini, and V. Veryazov, "Modern quantum chemistry with [Open]Molcas," vol. 152 (21), p. 214 117, **2020**.

[2] Cobramm on GitLab, available at: https://gitlab.com/cobrammgroup/cobramm/-/wikis/home.

[3] O. Weingart, A. Nenov, P. Altoè, I. Rivalta, J. Segarra-Martí, I. Dokukina, and M. Garavelli, "COBRAMM 2.0 — A software interface for tailoring molecular electronic structure calculations and running nanoscale (QM/MM) simulations," vol. 24 (9), p. 271, **2018**.

[4] C. Eckart, "Some Studies Concerning Rotating Axes and Polyatomic Molecules," *Physical Reviews*, vol. 47, pp. 552–558, 7 **1935**.

[5] S. V. Krasnoshchekov, E. V. Isayeva, and N. F. Stepanov, "Determination of the Eckart molecule-fixed frame by use of the apparatus of quaternion algebra," *The Journal of Chemical Physics*, vol. 140 (15), p. 154 104, **2014**.

# Appendix B

# Rhodopsin PESs

Figure B.1 shows the $S_1$-$S_0$ energy gap for selected torsional values of the 3D grid at all levels of theory (CASSCF, SS-, MS- and XMS-CASPT2). The SS-CASPT2 clearly suffers from the neglect of state mixing, resulting in a very wide crossing region. Most of such artificial crossing points are resolved by MS- or XMS-CASPT2 corrections, which are best suited for strongly interacting states in avoided crossing regions. Figure B.2 shows the torsional profiles at SS-, MS- and XMS-CASPT2 for fixed BLA values of the initial BLA scan starting from the MEP points.

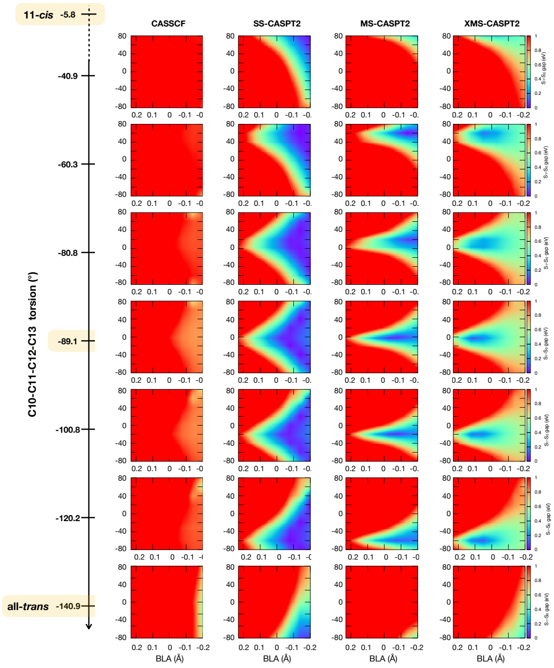

**Figure B.1:** $S_1$-$S_0$ energy gap along BLA-HOOP for selected torsional values and at different levels of theory.

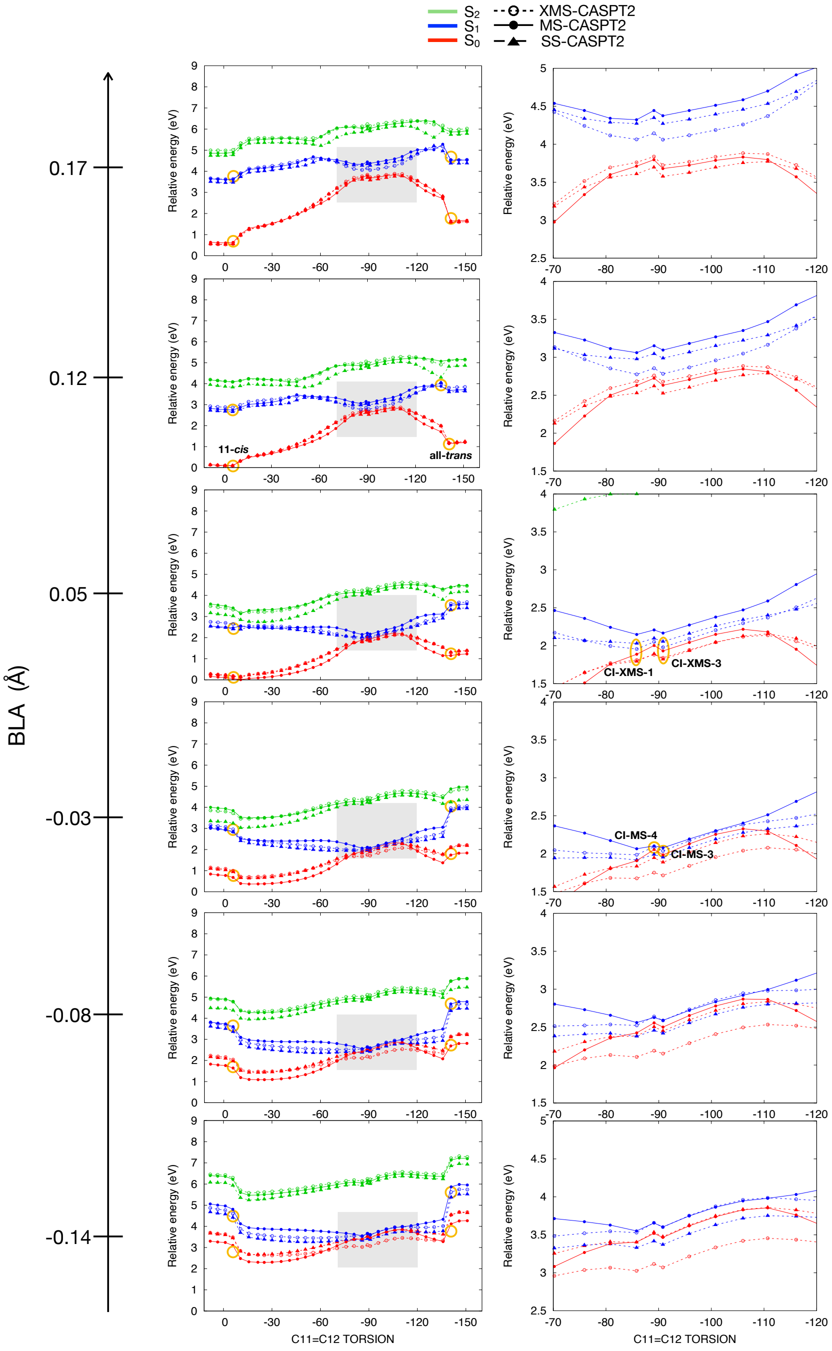

**Figure B.2:** SS-, MS- and XMS-CASPT2 profiles along the torsion coordinate for fixed BLA values. The shaded area where CASPT2-$S_1$ and $S_0$ get closer in energy is zoomed on the right.